DEFORMATION AND FRACTURE BEHAVIOR OF TI-AL-NB-(CR,MO) ALLOYS WITH A $\gamma+\sigma$ MICROSTRUCTURE AT AMBIENT TEMPERATURE

By

MICHAEL STEINER KESLER

A DISSERTATION PRESENTED TO THE GRADUATE SCHOOL
OF THE UNIVERSITY OF FLORIDA IN PARTIAL FULFILLMENT
OF THE REQUIREMENTS FOR THE DEGREE OF
DOCTOR OF PHILOSOPHY

UNIVERSITY OF FLORIDA

2011

© 2011 Michael Steiner Kesler

To my mother, my father and Fereshteh

ACKNOWLEDGMENTS

I would like to start by thanking the members of my research group, both past and present. Firstly, I would like to acknowledge Yanli Wang. She helped me so much early on in my life as a graduate student. I think of her as both a mentor and a friend and will forever be thankful for the valuable time we spent together in the lab. A special thanks goes out to Sonalika Goyel, without whom my lab experience would have been lonelier, less eventful and surely lacking in beauty. The long talks consisting of research related topics and life in general will always hold a special place in my heart. We needed each other to survive the lows and revel in highs of life as a graduate student under the ever vigilant and demanding eye of Dr. Ebrahimi and I could not imagine going through this experience without her. In addition to Sonalika, the culture of the lab would not have been the same without the presence of Orlando Rios, and surely was not the same once he graduated. He provided endless entertainment and encouraged timely social breaks throughout the long work days and nights. He was a gracious host and friend and can roast one heck of a pig. Glenn Bean provided bright eyes and a fresh mind to the project and I enjoyed getting to know him and teaching him everything he knows. I would also like to acknowledge Mahesh, Sankara, Yan, Damian, Eboni, Jinuk, Danials (both Taiwanese and German), Tabea, Ross, David, Jon, Christian, Diego, Steven and Matthew for rounding out the research group and providing sharp minds and quality company.

To my parents who give love and encouragement to me in everything I do. There is so much I owe to them for giving me life and showing me how to live it. The emotional and financial support they provided throughout these last 5 years has been priceless. I would like to thank Corey for her love and support through the final and most difficult

stages of this process. Her encouraging cheerleading as I complete this work has been instrumental to my progress and motivation. The fact that I will see her in Hawaii when I am done helps a little, too.

A special thanks goes out to Dr. Gerhard Fuchs who accepted me into his research group upon Dr. Ebrahimi's untimely passing. I appreciate the time that he set aside to review my work and aid me in the final months of this process. I also thank Dr. Phillpot and the Department of Materials Science and Engineering for additional funding in these final months which enabled the continuation of my work.

A special acknowledgement goes out the staff of the MAIC facility, including Dr. Dempere, Kerry, Eric and Wayne who provided access and training for the characterization instrumentation for this study including SEM, EPMA, XRD, TEM and FIB.

Finally, I cannot even begin to express the level of thanks, gratitude and love that is owed to the late Dr. Fereshteh Ebrahimi. She was an instrumental figure in my life for the past 5 years and will continue to be a beacon of strength, integrity and compassion for the rest of my life. I will always remember and cherish our long individual meetings where she challenged every idea no matter how valid. Her ability to provoke critical thinking was unmatched and we, as her students, are all better for it. This was a women who was so dedicated to the wellbeing of her graduate students that she held a meeting with Dr. Fuchs and I to review my work two weeks before her passing. I believe she was aware of the imminence of her condition, though her company was not. In addition to this, she showed infinite patience and compassion for me in the most difficult time in my personal life to date. The degree that it affected my progress in the lab was immense.

Without her love, support and understanding during that time, I do not think I would be in a position to write this acknowledgement. For that, and countless other things, I will be forever grateful and indebted to Dr. Fereshteh Ebrahimi. Words cannot describe the influence she has had on my life and many others.

TABLE OF CONTENTS

page

ACKNOWLEDGMENTS 4

LIST OF TABLES 10

LIST OF FIGURES 11

ABSTRACT 17

1 INTRODUCTION 19

2 BACKGROUND 23

2.1 γ-(TiAl)-Based Alloys 23
2.1.1 Deformation in TiAl 26
2.1.2 Toughening Mechanisms in TiAl-Based Alloys 28
2.2 β-Stabilizers and Other Alloying Elements 30
2.3 γ+σ Alloys 31

3 MATERIALS AND EXPERIMENTAL PROCEDURES 37

3.1 Materials 37
3.2 Differential Thermal Analysis (DTA) 39
3.3 Heat Treatments 40
3.3.1 Solutionizing + Water Quenching Heat Treatments (Soln+WQ) 40
3.3.1.1 Quenching Furnace 41
3.3.1.2 Temperature Calibration 42
3.3.2 Aging Heat Treatments 43
3.3.2.1 Encapsulation 44
3.3.2.2 Aging Times 44
3.3.2.3 Aging Temperatures 45
3.4 Sample Preparation and Characterization 45
3.4.1 Metallographic Procedures 45
3.4.2 Optical Microscopy (OM) 46
3.4.3 Scanning Electron Microscopy (SEM) 47
3.4.4 X-Ray Diffraction (XRD) 48
3.4.5 Transmission Electron Microscopy (TEM) 49
3.4.6 Imaging Analysis 51
3.5 Mechanical Testing 52
3.5.1 Microindentation 52
3.5.2 Compression Testing 53
3.5.3 Fracture Toughness Testing 54
3.5.3.1 Single Edge Notch (SEN) 4pt Bending 54
3.5.3.2 Unnotched 3pt Bending 56

4 MICROSTRUCTURAL EVOLUTION OF TWO-PHASE γ+σ ALLOYS 65

4.1 Alloy Selection 65
4.1.1 Ternary Alloys 65
4.1.2 Alloys with β-stabilizer Additions 66
4.2 As-cast Microstructures 67
4.3 Solutionized + Water Quenched Condition 70
4.3.1 Determination of Solutionizing Temperatures 70
4.3.2 Microstructural Analysis of Soln+WQ Alloys 71
4.4 Aged Condition 73
4.4.1 Determination of the Aging Temperature Range 74
4.4.2 Microstructural Analysis of Aged Alloys 75
4.5 Effect of Composition on Quenching-in the β-phase 77
4.5.1 Effect of Cr Addition 78
4.5.2 Effect of Al-content 79
4.6 Controlling Scale and Volume Fraction in Aged Microstructures 80
4.6.1 Effect of γ-phase Formation upon Quenching on Microstructural Scale 80
4.6.2 The γ-phase formation at β-phase Grain Boundaries 81
4.6.3 Effect of Aging Temperature on Microstructural Scale 81
4.6.4 Effect of Nb-content σ-phase Volume Fraction 84

5 DEFORMATION AND FRACTURE IN γ+σ ALLOYS AGED FROM A POLYCRYSTALLINE β-PHASE MICROSTRUCTURE 124

5.1 Compression Testing on γ+σ Alloys 124
5.1.1 Compression testing to failure 124
5.1.2 Interrupted Compression tests 126
5.2 Deformation and Fracture on the Macroscopic Level 127
5.2.1 Macroscopic Deformation 127
5.2.2 Macroscopic Fracture 128
5.3 Deformation and Fracture on the Microscopic Level 129
5.3.1 Deformation Near the Prior β Grain Boundaries 130
5.3.2 Deformation Away From the Prior β Grain Boundaries 132
5.3.3 Fracture Near the Prior β Grain Boundaries 133
5.3.4 Fracture Away From the Prior β Grain Boundaries 135
5.3.2.1 Refined Microstructure 135
5.3.2.1 Coarsened Microstructure 136
5.4 The Effects of Volume Fraction and Scale on Mechanical Behavior 136
5.4.1 Effect of Volume Fraction 137
5.4.2 Effect of Microstructural Scale 138

6 DEFORMATION AND FRACTURE IN γ+σ ALLOYS AGED FROM SINGLE β-PHASE CRYSTALS 167

6.1 Compression Testing on SX γ+σ Alloys 167
6.1.1 Compression testing to failure 167
6.1.2 Interrupted Compression tests 170
6.2 Fracture Toughness Testing on SX γ+σ Alloys 171

6.2.1 Vickers Microindentation Technique 171
6.2.2 Singe Edge Notch (SEN) 4pt Bending 173
6.2.3 Unnotched 3pt Bending Bars 176
6.3 Deformation and Fracture of SX alloys 178
6.3.1 Macroscopic Deformation and Fracture 178
6.3.2 Microscopic Deformation and Fracture 178
6.3.3 Effect of Microstructural Scale in SX Alloys 179
6.3.4 PX vs SX: A Comparison 181
6.4 Comparing $\gamma+\sigma$ Alloys to Other Novel γ-based Alloys 183

7 SUMMARY 206

8 FUTURE WORK 209

APPENDIX

A EPMA STATISTICS AND QUANTITATIVE MICROSCOPY 210

A-1 EPMA 210
A-2 Volume Fraction Measurements 210
A-3 Particle Size Measurements 210

B DETERMINATION OF YIELD STRENGTH AND PLASTIC STRAIN VALUES FROM EVALUATION OF STRESS-STRAIN CURVES 217

C TENSILE SAMPLE FABRICATION 219

D NOTCH DIMENSIONS AND LOAD-DISPLACEMENT CURVES 225

LIST OF REFERENCES 230

BIOGRAPHICAL SKETCH 236

LIST OF TABLES

Table		page
3-1	Alloy compositions as measured by EPMA	58
4-1	Microstructural parameters of alloys aged for mechanical testing	111
4-2	Transformation temperature estimated from DTA experiments	117
5-1	Mechanical properties of polycrystalline alloys under compression	143
6-1	Mechanical properties of SX alloys under compression	185
6-2	Sample dimensions and SEN fracture toughness results	192
6-2	Sample dimensions and unnotched 3pt bend test results	195
A-1	EPMA from random spots on Alloy 11	212
A-2	EPMA from random spots on Alloy 12	212
A-3	EPMA from random spots on Alloy 12Cr	212
A-4	EPMA from random spots on Alloy 12.5CrMo	213
A-5	EPMA from random spots on Alloy 13CrMo	213
A-6	Volume fraction measurements from Alloy 11	214
A-7	Volume fraction measurements from Alloy 12Cr	214
A-8	Volume fraction measurements from Alloy 12.5CrMo	215
A-9	Volume fraction measurements from Alloy 13CrMo	215
A-10	Particle size measurements from Alloy 13CrMo	215

LIST OF FIGURES

Figure		page
2-1	TiAl-$L1_0$ unit cell	35
2-2	Crack tip orientations in TiAl alloys	36
3-1	Examples of an arc melted 5g button and 25g bar	58
3-2	BSE images showing the effects of inhomogeneous melting of Nb on aged microstructures	59
3-3	Illistration of the slicing direction	60
3-4	Examples of the heat treatment schedules	60
3-5	Quenching furnace components	61
3-6	Alumina top hat components	62
3-7	Removable plug for pumping/purging, flowing gas relief and drop quenching	62
3-8	Thermocouple position and temperature calibration	63
3-9	Schematic showing where a SX compression sample was cut from a soln+WQ slice	63
3-10	Schematic of bending test setup and nominal dimensions	64
4-1	TiAlNb phase diagrams.	86
4-2	Micrographs of as-cast Alloy 11	87
4-3	The XRD profile of Alloy 11 in the as-cast condition	88
4-4	Micrographs of as-cast Alloy 11Cr	89
4-5	The XRD profile of Alloy 11Cr in the as-cast condition	90
4-6	Images of as-cast Alloy 12	91
4-7	The XRD profile of Alloy 12 in the as-cast condition	92
4-8	Images of as-cast Alloy 12Cr	93
4-9	The XRD profile of Alloy 12Cr in the as-cast condition	94
4-10	DTA plot of Alloy 11	95

4-11 DTA plot of Alloy 12 96

4-12 DTA plot of Alloy 11Cr 97

4-13 DTA plot of Alloy 12Cr 98

4-14 Images of Alloy 11 in the soln+WQ condition 99

4-15 The XRD profile of Alloy 11 in the soln+WQ condition 100

4-16 Images of Alloy 11Cr in the soln+WQ condition 101

4-17 The XRD profile of Alloy 11Cr in the soln+WQ condition 102

4-18 Images of Alloy 12 in the soln+WQ condition 103

4-19 The XRD profile of Alloy 12 in the soln+WQ condition 104

4-20 Images of Alloy 12Cr in the soln+WQ condition 105

4-21 The XRD profile of Alloy 12Cr in the soln+WQ condition 106

4-22 Images of Alloy 12.5CrMo in the soln+WQ condition 107

4-23 The XRD profile of Alloy 12.5CrMo in the soln+WQ condition 107

4-24. Optical micrograph of Alloy 13CrMo in the soln+WQ condition 108

4-25 The XRD profile of Alloy 13CrMo in the soln+WQ condition 108

4-26 DTA curves 109

4-27 BSE micrographs of Alloy 12Cr which had been aged 110

4-28 BSE micrographs of the two-phase $\gamma+\sigma$ microstructures formed in Alloy 12Cr after aging 111

4-29 BSE micrographs of aged Alloy 12Cr showing regions of relatively coarse γ-phase due to 'early' formation of this phase upon aging 112

4-30 BSE micrograph of the Widmanstätten γ-phase formation upon aging at the prior β-phase grain boundaries in Alloy 12Cr-1050 113

4-31 BSE micrographs of the two-phase $\gamma+\sigma$ microstructures formed in Alloy 12.5CrMo after aging 114

4-32 BSE micrographs of the two-phase $\gamma+\sigma$ microstructures formed in Alloy 13CrMo after aging 115

4-33 BSE micrographs of the two-phase γ+σ microstructures formed in Alloy 11 after aging at 1100ºC, then furnace cooling to room temperature 116

4-34 BSE micrographs of soln+ WQ Alloy 12Cr 117

4-35 BSE micrographs of the soln+WQ microstructures in Alloy 12Cr 118

4-36 BSE micrographs of Alloy 12.5CrMo-1000 revealing fine and coarse microstructures as a result of inconsistent cooling rates 119

4-37 BSE micrograph of Alloy 13CrMo revealing the coarse Widmanstätten γ-phase which formed at the prior β-phase grain boundaries upon quenching ... 120

4-38 The DTA curve of Alloy 12Cr (top) with vertical lines marking the aging temperatures and arrows denoting the resulting microstructures 120

4-39 Higher magnification BSE micrographs of Alloy 12Cr..... 121

4-40 A phase fraction diagram of the base ternary alloy, Alloy 12, revealing limited changes in volume fraction 122

4-41 1000ºC isothermal section of the Ti-Al-Nb phase diagram with Alloys 12Cr, 12.5CrMo and 13CrMo plotted by nominal Nb-content..... 123

5-1 Engineering stress vs. strain curves 142

5-2 Engineering stress vs. strain curves 144

5-3 Engineering stress vs. strain curves 145

5-4 Engineering stress vs. strain curve for Alloy 11-1100 tested at room temperature in compression 146

5-5 Stress strain curve of a room temperature interrupted compression test at 1.4% plastic strain on Alloy 13CrMo-1000 146

5-6 Stress strain curve of room temperature interrupted compression tests at 0.5% and at 3.7% plastic strain on Alloy 11-1100..... 147

5-7 Surface deformation after interrupted compression 147

5-8 Micrographs of fractured compression samples 148

5-9 Surface deformation after interrupted compression 149

5-10 SE micrographs showing slip and microcracking in the vicinity of the prior β-phase grain boundary from region ‘A’ in Figure 5-7a..... 150

5-11 SE micrographs of the sample surface after interrupted compression 151

5-12 TEM micrographs of the FIB foil 152

5-13 TEM micrograph and SAD pattern..... 153

5-14 A TEM micrograph and SAD pattern 154

5-15 TEM micrograph of the inside of a γ-lath showing many dislocations interacting with σ-particles 155

5-16 An OM image (left) taken from region 'B'..... 156

5-17 SE micrographs of an area of localized 157

5-18 SE micrographs of the localized deformation 158

5-19 SE micrographs showing extensive microcracking..... 159

5-20 SEM micrographs of Alloy 11-1100-3.7%ε_p 160

5-21 Alloy 13CrMo-1000-1.4%ε_p..... 161

5-22 SE micrographs showing interfacial microcracks which formed in the areas of localized deformation in region 'B' 162

5-23 An area in region 'B' which has undergone significant microcracking 163

5-24 The coarsened s-particles in Alloy 11-1100-3.7%ε_p were the primary source of microcracking in this alloy..... 163

5-25 The plots of yield strength 164

5-26 The plots of yield strength 165

5-27 The plots of ductility (plastic deformation to failure) vs. yield strength 166

6-1 The engineering stress-strain curves generated from compression of Alloy 12Cr-865 185

6-2 The engineering stress-strain curves generated from compression of Alloy 12Cr-1050 in the PX (black) and SX (blue) conditions 186

6-3 The engineering stress-strain curves generated from compression of Alloy 13Cr-865 in the PX (black) and SX (green) conditions..... 186

6-4 The engineering stress-strain curves generated from compression of Alloy 13Cr-1000 in the PX (black) and SX (green) conditions..... 187

6-5 The engineering stress-strain curves generated from compression of Alloy 13Cr-1050 in the PX (black) and SX (green) conditions..... 187

6-6 Stress-strain curves of room temperature interrupted compression tests at 1.4% plastic strain 188

6-7 Interrupted compression tests 189

6-8 OM images of Vickers indents applied with 20kgf 189

6-9 OM images of Vickers indents applied with 30kgf 190

6-10 SE images from Alloy 12Cr-1050 191

6-11 SEM micrographs revealing the scales of the microstructures in Alloy 13CrMo at different aging temperatures and times..... 192

6-12 Fracture surfaces from SEN bending samples 193

6-13 SE micrographs from Alloy 13CrMo-1000 194

6-14 Load-displacement curves for bending of unnotched samples of Alloy 13CrMo-1000-2hrs 194

6-15 The fracture surface of an unnotched sample of Alloy 13CrMo-1000-2hrs at increasing magnification 195

6-16 Compilations of OM images of Alloy 13CrMo-1000-SX revealing surface damage 196

6-17 SE micrographs from a,b) the surface of Alloy 13CrMo-1000-SX-1.4% of a region of localized deformation..... 197

6-18 SE (left) and BSE (right) micrographs from Alloy 13CrMo-1000-SX-1.4% showing the interfacial microcrack formation at the σ-particles 198

6-19 SEM micrographs taken from Alloy 13CrMo-1000-SX loaded to fracture..... 199

6-20 Plot of yield strength versus mean diameter of σ-particles 200

6-21 SE micrographs of surface damage 201

6-22 Compilations of OM images from the sample surfaces 202

6-23 SE micrographs comparing the surface damage..... 203

6-24 Plots of ductility..... 204

6-25 A comparison of the compressive ductility (plastic deformation to failure) vs. yield strength 205

A-1 BSE (top) and corresponding threshold enhanced (bottom) images of Alloy 11 for volume fraction measurements 214

A-2 BSE images with lines intersecting σ-phase particles in Alloy 13CrMo 215

A-3 Schematic showing that (σ_r-λ) equals the mean diameter 216

A-4 Raw compression stress-strain curves showing the procedure for measuring 0.2% off-set yield strength and plastic strain to failure 218

A-5 Schematic of the tensile specimen designed for the collared fixture 223

A-6 Schematic of the tensile specimen designed for the cylindrical threaded fixture 223

A-7 Schematic (top) of the tensile specimen designed for the hydraulic grips and images of the fabricated tensile sample (bottom) 224

A-8 OM images of the notch cut into the sample Alloy 13CrMo-1000-2hrs-1 with labeled dimensions 226

A-9 Images showing a) the fracture surface and b) side view of the fracture path from the sample Alloy 13CrMo-1000-2hrs-2 227

A-10 Load-displacement curve of Alloy 13CrMo-865-2hrs 228

A-11 Load-displacement curve of Alloy 13CrMo-1000-2hrs 228

A-12 Load-displacement curve of Alloy 13CrMo-1050-20hrs 229

Abstract of Dissertation Presented to the Graduate School
of the University of Florida in Partial Fulfillment of the
Requirements for the Degree of Doctor of Philosophy

DEFORMATION AND FRACTURE BEHAVIOR OF TI-AL-NB-(CR,MO) ALLOYS WITH A $\gamma+\sigma$ MICROSTRUCTURE AT AMBIENT TEMPERATURE

By

Michael Steiner Kesler

December 2011

Chair: Fereshteh Ebrahimi
Major: Materials Science and Engineering

Titanium aluminides are of interest as a candidate material for aerospace turbine applications due to their high strength to weight ratio. γ-TiAl + α_2-Ti_3Al alloys have recently been incorporated in the low pressure turbine region but their loss of strength near 750C limits their high temperature use. Additions of Nb have been shown to have several beneficial effects in $\gamma+\alpha_2$ alloys, including enhancements in strength and ductility of the γ-phase, along with the stabilization of the cubic BCC β-phase at forging temperatures allowing for thermomechanical processing.

In the ternary Ti-Al-Nb system at high Nb-contents above approximately 10at%, there exists a two-phase γ-TiAl + σ-Nb_2Al region at and above current service temperature for the target application. Limited research has been conducted on the mechanical properties of alloys with this microstructure, though they have demonstrated excellent high temperature strength, superior to that of $\gamma+\alpha_2$ alloys. Because the σ-phase does not deform at room temperature, high volume fractions of this phase result in poor toughness and no tensile elongation. Controlling the microstructural morphology

by disconnecting the brittle matrix through heat treatments has improved the toughness at room temperature.

In this study, attempts to further improve the mechanical properties of these alloys were undertaken by reducing the volume fraction of the σ-phase and controlling the scale of the γ+σ microstructure through the aging of a meta-stable parent phase, the β-phase, that was quenched-in to room temperature. Additions of β-stabilizing elements, Cr and Mo, were needed in order to quench-in the β-phase. The room temperature mechanical properties were evaluated by compression, Vickers' indentation and single edge notch bend tests at room temperature. The formation of the large γ-laths at prior β-phase grain boundaries was found to be detrimental to ductility due to strain localization in this coarsened region of the microstructure. Furthermore, samples aged from β-phase single crystals proved to have excellent combinations of strength and ductility under compression. In the single crystals, microcracking did not develop until much larger plastic strains were reached. Lowering the volume fraction of the σ-phase proved to enhance the fracture toughness in these alloys.

CHAPTER 1
INTRODUCTION

The advancement in efficiency of the gas turbine engine for aerospace application is highly dependant on the strength-to-weight ratio and temperature capabilities of the materials therein. For decades, Ni-base superalloys have been the dominant material of choice for turbine blades due to the excellent creep properties, oxidation resistance and anomalous strength at the homologous temperature [1]. The relative high density (8-9g/cm^3) of these Ni-base superalloys requires accommodation of the extra weight resulting in a larger and heavier engine overall. Incremental steps to improve the performance of superalloys have been made, which include advancements in processing (directional solidification and single crystal casting) and development of thermal barrier coatings, though there is a need to develop alternate materials if a leap in efficiency is expected to be achieved.

Titanium aluminides are of interest due to their high specific strength (density ranges from 3-4g/cm^3) and potential for excellent high temperature properties [2, 3]. Recent developments in the manufacturing of advanced TiAl-based alloys have progressed to the point that they are now being incorporated into areas of commercial aerospace turbines. These alloys, which consist of a two-phase γ-TiAl + α_2-Ti_3Al microstructure, have a maximum use temperature approaching 750ºC which limits application to less severe environments in the turbine, including the last two rows of turbine blades in the GEnX engine [3-5]. Additions of Nb to $\gamma+\alpha_2$ alloys have become common-place due to several beneficial affects including strengthening and room temperature ductilization of the γ-phase along with improved forgeability through the stabilization of the BCC β-(Ti,Nb) at high temperature [6, 7]. For these materials to

move further into the turbine, and therefore operate at higher temperatures, retention of strength to higher temperatures is necessary. Implementation of a TiAl-based material which is suitable for use at higher temperatures has been limited by the mechanical properties at room temperature due to poor toughness and ductility. Optimization of high temperature strength and room temperature mechanical properties are the challenges in producing a viable component.

Several approaches have been undertaken for achieving greater high temperature strength including the incorporation of hard particles such as oxides, borides and silicides into the various TiAl-based alloys [8-13]. Developing the target microstructure for these alloys is difficult and requires processing routes such as powder metallurgy with preexisting oxide and silicide particles, or precipitation of borides. In the case of preexisting particles, the particle/matrix interface is incoherent and fracture is usually initiated at the matrix/particle interface resulting in poor toughness and tensile elongation [10]. For the cases of TiAl/alumina composites and boride precipitation, difficulty arises due to the agglomeration of alumina particles around grain boundaries [13], and the formation of primary borides from the melt which coarsen and cluster around grain boundaries in as-cast microstructures. Once formed, the morphology and dispersion of particles is difficult to control which limits the ability to develop target microstructures.

In the ternary Ti-Al-Nb system, there exists a two-phase γ-TiAl + σ-Nb_2Al region over a temperature range of 850-1250ºC at Nb concentrations above 10at%. The σ-phase is hard and brittle at room temperature, but has the potential to impart excellent properties at elevated temperature. It has been shown that $\gamma+\sigma$ alloys exhibit superior

creep properties as compared to $\gamma+\alpha_2$ alloys at temperatures up to 1000ºC [14]. The main issue facing the advancement of these alloys is a high volume fraction of the connected σ-phase which acts as a brittle matrix resulting in low fracture toughness (4.4MPam^{½}) and no ductility at room temperature [15, 16]. Dramatic improvements in toughness are needed for this material to compare to the more common $\gamma+\alpha_2$ alloys, which have a toughness range from 5 to 35MPam^{½}. The toughness of these alloys is highly dependant on the microstructure [17-28]. For an alloy to be considered for these structural applications a minimum toughness value of ~20MPam^{½} must be attained. Enhancements in toughness in $\gamma+\sigma$ alloys have been achieved by heat treatments that result in a disconnected σ-phase which prevent cracks from propagating continuously though the brittle medium [16, 29]. Even with the improved toughness (6.3 MPam^{½}), the high volume fraction of the σ-phase is still detrimental to room temperature mechanical properties.

Improving room temperature properties could be achieved by reducing the volume fraction of the σ-phase and refining the microstructure. A second phase hard particle can provide strengthening and, if properly refined, the adverse affect on fracture toughness can be limited. Refinement of the microstructure can be achieved through controlled precipitation of the γ and σ phases from a high temperature parent phase, the β-phase, after being quenched-in by rapidly cooling to room temperature.

A major issue arises when attempting to develop this microstructure. When a ternary composition is selected that would yield a low volume fraction of the σ-phase, it is not possible to fully quench-in the parent β-phase to room temperature, thus resulting

in a coarsened microstructure after heat treating. β-stabilizing elements can be used to kinetically stabilize the β-phase to room temperature upon quenching.

In the following study, several two-phase γ+σ Ti-Al-Nb-(Cr, Mo) alloys were developed and the effects of microstructural parameters on the mechanical properties have been evaluated. Variation in the volume fraction of the phases was accomplished through adjustments in compositions based on the most recently calculated ternary Ti-Al-Nb phase diagrams and differing microstructural scale was accomplished through successful quenching experiments and controlled heat treatment schedules. The aim of the current work was to compare mechanical properties between alloys and come closer to developing a microstructure that results in the optimization of both strength and fracture toughness at room temperature. Understanding deformation and fracture behavior as it relates to the microstructure on both a microscopic and macroscopic level was a focus of this investigation.

CHAPTER 2
BACKGROUND

Over the past three decades, there has been a push for higher efficiency in power generation due to ever-depleting resources. In the case of aerospace turbines, significant improvements can be made by reducing the weight and/or increasing the operating temperature of the engine. Both of these methods for improvement are limited by the materials therein. Over the last half-century, Ni-base superalloys have been incrementally improved through alloying, cutting edge processing techniques and protective coatings, but are now reaching a plateau in further advancement. Alternative materials are being looked into, with titanium aluminides receiving considerable attention for the high specific strength they exhibit. This class of material has come a long way in the past fifteen years through exploration of alloying additions and processing routes.

2.1 γ-(TiAl)-Based Alloys

Over the past three decades, there has been a push for higher efficiency in power generation due to ever-depleting resources, fuel cost and emissions. In the case of aerospace turbines, significant improvements can be made by reducing the weight and/or increasing the operating temperature of the engine. Both of these methods for improvement are limited by the materials therein. Over the last half-century, Ni-base superalloys have been incrementally improved through alloying, cutting edge processing techniques and protective coatings, but are now reaching a plateau in further advancement. Alternative materials are being looked into, with titanium aluminides receiving considerable attention for the high specific strength they exhibit.

This class of material has come a long way in the past fifteen years through exploration of alloying additions and processing routes.

The titanium aluminides which have drawn the most attention to date are the alloys which are based on two-phase γ-TiAl+α_2-Ti_3Al microstructures. The γ-phase has a tetragonal $L1_0$ structure in which layers of Ti atoms with intermittent Al layers are the sublattices of this material and this is shown in Figure 2-1. The c/a ratio equals 1.015 with a=4.00Å and c=4.06Å when the compound is stoichiometric. The c/a ratio varies with Al content, such that when Al is at a minimum (~35at%), c/a=1.01, and when Al is at a maximum (~57at%), c/a=1.03 [30].

Ordinary dislocations of the ½[110] type, deformation twins on the {111}<112] type and superdislocations of the <101] type are active in TiAl depending on load orientation and temperature [3, 31]. At low temperatures, these materials exhibit high yield strength, ranging from ~300-650MPa, which arises from the high Peierls stresses of dislocations leading to a lack of slip systems available for plastic deformation. At high temperatures, more slip systems are available due to greater activation of superdislocations, so yielding occurs more readily giving way for strain hardening and recrystallization [3, 32, 33].

The α_2-phase has a $D0_{19}$ structure that imparts enhanced ductility to the γ-phase. Several microstructures are beneficial in these materials, the most common of which include Duplex (DP) and Fully Lamellar (FL). The DP microstructure is a combination of lamellar $\gamma+\alpha_2$ colonies and equiaxed γ-phase regions. The highest toughness values have been attained with FL microstructures, but RT ductility is poor and creep properties wane above the service temperature of ~700ºC [5]. Improvements in tensile

elongation are found in these alloys when the DP microstructure is achieved, although, this is at the expense of toughness [5, 19, 20]. In equiaxed and DP structures, these materials follow a Hall-Petch relationship and a modified Hall-Petch relationship relating the GS to lamellar spacing has been found for the FL microstructure. The colony size follows the same relationship, although the lamellar spacing and colony size are difficult to alter independently [5, 19, 20]. The strain to failure of $\gamma+\alpha_2$ alloys at RT ranges from below 1% up to 4% depending on the microstructure, alloying and load level. Hot working processes have been shown to greatly improve RT strain to values >2% and high temperature strain to values approaching 60%. This is due to microstructural changes from FL to DP [34]. Toughness and ductility have an opposing relationship in the two phase $\gamma+\alpha_2$ materials as grain or colony size varies. As grain size decreases, the ductility increases, but conversely, the toughness decreases [3, 17, 19, 20]. To understand this apparent inconsistency it is necessary to differentiate between processes that occur prior to crack initiation (ductility and stress level in tension) and processes occurring in the presence of a existing crack (fracture toughness testing). Creep properties in the FL alloys are satisfactory up to ~750ºC. Above this temperature, diffusion processes, such as climb, dominate and recovery and recrystallization occur [35-37]. The temperature at which these processes occur needs to be increased. A balance between toughness, creep and RT tensile elongation is necessary for the success of these alloys.

The FL structure can be obtained by cooling through the β+L region, then after dwelling in the single-phase α region $\rightarrow \alpha+\gamma\rightarrow\alpha_2+\gamma$. The interlamellar spacing and colony size can be controlled by the cooling rate from the α region, where a faster

cooling rate results in finer lamellae. These materials are usually annealed in the $\alpha_2+\gamma$ region to enhance RT toughness. The refinement of the lamellae increases strength more so than refining the grains of this microstructure. Refinement of both grain size and lamellar spacing lead to a high RT yield strength above 800MPa and is termed refined fully lamellar (RFL). This microstructure can then be transformed to the DP microstructure by either aging or hot working in the $\alpha+\gamma$ region, resulting in coarser and finer structures, respectively [3, 5, 38-40].

2.1.1 Deformation in TiAl

There are 3 main dislocations active in TiAl and its alloys. Ordinary dislocations of the ½<110]{111} type, twins with 1/6<112]{111} partial dislocations and superdislocations of type <101]{111} are responsible for the majority of the deformation of these alloys, and while ½<112]{111} superdislocations have been observed, the extent of their contribution to plastic deformation is miniscule. It is important to note that superdislocations, of both types mentioned above, dissociate asymmetrically [3, 31]. The consequence of this phenomenon is the polarization of the superdislocations. In addition, the behavior in compression is different than their behavior in tension. Depending on the orientation of the superdislocations, they could be sessile, due to a Wilsdorf locking mechanism, upon compression and glissile upon tension, or vice-versa. Theoretically, superdislocations could dissociate symmetrically on a single {111}, but due to anisotropy, the energy of the CSFs and APBs that would be necessary for those reactions are too high for this $L1_0$ structure and they have not been observed to dissociate in this manner. The asymmetrical dissociations are energetically favorable. The [011] superdislocation in screw orientation has been observed in HRTEM to

dissociate symmetrically with SESF and SISF ribbons, but this occurs on two adjacent {111} planes and the partials are sessile. The energy of CSFs in this system is too high, so dissociation is not resolvable by TEM techniques. Twinning in this system is also loading sense dependant. When the 1/6[112] twin propagates in one direction, the ordering of $L1_0$ is conserved, while in the other direction, it is not. The latter is termed the anti-twinning mode [3, 31].

In single phase γ-TiAl, the ordinary ½<110] dislocations have high CRSS due to screw orientation, oxygen segregation and high Peierls stress [3, 31, 41]. In these alloys, twinning and superdislocations are responsible for the majority of deformation at RT. On the other hand, in the two phase alloys, $\gamma+\alpha_2$, ordinary dislocations and twinning dominate. This has been mainly attributed to the α_2 phase gettering the oxygen from γ and thereby freeing up the ordinary dislocations [3, 31, 41]. As mentioned in the oxidation section, O interstitials settle at ordinary dislocations and stabilized them, effectively increasing the CRSS required for activation of their slip planes[41]. Upon the addition of Nb to the two phase system, the effect of gettering in α_2 is nullified by the lattice distortion and lowering of SFE in the γ-phase, leading to more superdislocation motion. Nb contribution is two-fold: 1) Nb increases the c/a ratio of γ and contributes solid solution strengthening and 2) Nb reduces the SFE, thereby allowing the dissociation of the ordinary dislocations effectively raising the Peierls stress. This results in superior YS retention at elevated temperatures by changing the deformation mechanism from ordinary dislocation motion and twin activation, to a combination of super-, ordinary and twin dislocation motion at RT and elevated temperatures [7, 31, 41, 42]. At elevated temperatures, a thermally activated ductile-to-brittle transition occurs

where the degradation of mechanical properties takes place. This occurs in the temperature range of ~650-800ºC [3, 43, 44].

2.1.2 Toughening Mechanisms in TiAl-Based Alloys

The toughening mechanisms in TiAl are extremely microstructure dependant and a brief overview of how these materials fracture is important for knowing how to increase the toughness effectively. For the equiaxed and DP structures, intergranular fracture and cleavage dominate the fracture process. Intergranular fracture increases the toughness due to the deflection of the crack around grains [17, 18]. This is usually seen in concert with brittle transgranular cleavage, where the cleavage plane of one grain is not oriented favorably for cleavage in the adjacent grain, so the grain boundary is the weak link and the crack goes intergranular increasing the crack path distance. In FL structures, translamellar fracture, crack dividing and lamellar debonding are all manners in which this microstructure can fracture. The orientation of the crack with respect to the lamella is important (Figure 2-2) [45]. All three orientations are possible for a single crack when propagating from colony to colony and the fracture surfaces that the different orientations yield are distinctly identifiable [3, 17].

In TiAl at RT, when a γ grain slips, either grain boundary decohesion or slip band cracking occur due to a limited number of slip systems. The adjacent γ grain is unable to accommodate the strain, thus a crack is formed. If a second more ductile phase is introduced at the interfaces (GB or lamellar), this phase can help distribute the strain by forming geometrically necessary dislocations that satisfy the degree of plastic deformation. When a crack is formed in γ, a ductile phase can provide a more diffuse plastic zone, thereby, resisting the formation of microcracks which would ultimately link

to the main crack and, thus, increase toughness. This mechanism is referred to as *ductile-phase accommodation* [3, 17].

For lamellar microstructures, lamellar debonding is not only a fracture mechanism, but also a means by which to deflect the crack, and therefore is a toughening mechanism. When a crack is propagating normal to the lamella, the crack tip approaches the γ/α_2 interface and separates one phase from the other. This reduces the normal stress at the crack tip by redistributing the stress to areas ahead of the crack tip. This mechanism, referred to as *crack-tip interface debonding*, essentially blunts the tip of the crack by not allowing a high degree of stress intensification to occur at the incident lamellae [3, 17].

In $\gamma+\alpha_2$ alloys with lamellar microstructures, a fracture process has been observed where a crack propagates and encounters other colonies, where a discontinuous crack can form due to fracture plane misalignment. The material between the main crack and the new crack is called a ligament. This ligament experiences a shear and eventual fracture connecting the cracks, but not before acting as a toughening mechanism referred to as *shear-ligament toughening*. This process not only deflects the main crack, but absorbs energy through shearing of the ligament, thereby improving toughness. These ligaments act similar to the crack bridging mechanism observed in ceramic/ductile-phase composites where a crack will propagate through the ceramic, but the crack opening is resisted by the unfractured ductile phase, thereby lowering the stress intensity at the crack tip. As colony size increases, the ligament size increase and toughness is increased. A competing element to this process is that as the colony size increases, so does the interlamellar spacing. The refining of lamellae has proven to

toughen the material, so a balance between colony size and interlamellar spacing must be achieved [3, 5, 17].

When slip is not favorable, a material has two options, 1) fracture, or 2) twin. Twinning is observed in many TiAl-based alloys and can be responsible for a significant amount of plastic deformation. Twinning occurs at RT and elevated temperatures in TiAl alloys. Several researchers have found evidence of a *twin toughening* mechanism where the majority of twins were observed in the wake of the crack [3, 17, 33, 46]. In general, twinning is observed to be more prevalent at elevated temperatures once dislocation motion has been exhausted [47].

2.2 β-Stabilizers and Other Alloying Elements

There are several elements that have been found to stabilize the β-Ti BCC solid solution, some of which include Mo, Si, Ta, W and Cr [48-52]. As the preliminary work will show, Cr has successfully been added to a TiAlNb alloy and stabilized β. When adding an element to an alloy, several factors must be considered: a) stability, b) properties including melting point, creep and tensile elongation, c) phase formation and d) c/a ratio of γ. The main purpose of adding a fourth element to the system is to stabilize β, but the element could, also, stabilize or destabilize other phases in the system that could inhibit the control of the microstructure. Properties can be affected positively or negatively through the incorporation of other elements. For example, the melting temperature can be suppressed, as was the case with Cr, and for the long term goals of this research, that would be negative. Conversely, in the case of Mo and W, the kinetics of the system is slowed and it could effectively stabilize the final microstructure and for a material that goes through many thermal cycles, this affect is desired. New

phases can, also, result from the addition of a fourth element. Carbides or other intermetallics could form and have a deleterious effect on mechanical properties, so it is important to consider all of the possibilities.

In an effort to increase RT ductility of γ, two major factors must be considered. The tetragonality of γ has an effect on its ability to undergo plastic deformation in the c-axis directions. The c/a ratio must be minimized in order to increase plastic deformation in the c≠0 directions. Nb additions, when substituted for Ti, increase the c-axis lattice parameter in γ. This anisotropic effect is proposed to be one reason for Nb strengthening γ, but also could account for a loss of toughness [53]. Another factor to consider is the affects of alloying on stacking fault energy (SFE). Several studies have been conducted and based on the results, it is proposed that Nb decreases the SFE of γ due to higher measured yield strength at elevated temperatures [7, 53]. Al is known to have a great affect on the SFE of γ in the binary system, but with the addition of Nb, the SFE is independent of Al concentration [7]. Climb of dislocations is responsible for a great deal of plastic deformation in γ at elevated temperatures, and a reduction in climb is observed with the additions of Nb [54]. The lattice distortion along with SFE effects of Nb could all contribute to strengthening at high temperature along with embrittlement [7, 53, 54].

2.3 γ+σ Alloys

In previous work [55, 56] two alloys were tested by microindentation, compression, creep and 4-Pt bending. One of the alloys, Ti-40Al-27Nb, was heat treated into two microstructures: 1) single aged with continuous σ matrix with fine γ precipitates, and 2) double aged with disconnected coarse and fine σ in a γ matrix. The phase fractions in

each microstructure were approximately equal at 60% σ and 40% γ. During high temperature compression, a maximum stress was achieved before softening ensued. The softening was due to dynamic recrystallization of γ. σ-grains were not observed to have deformed, but 'fragmentation' occurred leading to the assumption that grain boundary sliding was part of the deformation process. These phenomena were observed in both microstructures, but to differing extents. Grain boundary sliding was greater in the finer single aged material, which is to be expected, due to the greater amount of σ/σ interface. Although the finer structure had a lower peak stress, the work hardening rates were greater and led to recrystallization at lower stress levels.

Toughness measurements were conducted by microindentation and 4-pt bending with a chevron notch. Indentation was found to be accurate within 20% of the values measured by bending. The closest values to the 4-pt bending were calculated through the curve fitting model [56, 57]. This technique resulted in reasonable approximations (slight overestimations) of fracture toughness for the alloys with high s-phase volume fraction. Results show an increased K_{1C} value from the single aged to the double aged specimen from 4.4MPam$^{1/2}$ to 6.3MPam$^{1/2}$, respectively [29]. The discontinuous brittle phase, σ, was unable to continuously propagate a crack in the double aged sample. Gomez proposes that indentation would not be valid for a material with a ductile matrix due to over estimations. The scale of the microstructure will have an impact on the toughness value using this technique, along with the chances of hitting a brittle σ particle with the corner of the indenter. Toughness measurements through Vickers indentation were designed for brittle materials, so if a material is too tough, this method would not be valid.

Fractographic analysis through observation of several BSE micrographs showed that cracks propagated intergranularly through the σ/γ boundaries, but transgranularly through the grains when large amounts of σ could not be avoided. This observation led to the conclusion that there are large internal stresses in the material between σ and γ. The deflection of the crack which occurs due to intergranular fracture was proposed as a mechanism for toughening. The promising results from this study are that the toughness of these materials can be increased with microstructural modification [55, 56].

Very little research has been conducted on the mechanical properties of σ+γ microstructures. Some of what has been found for σ+γ microstructures is the following: a) in a σ matrix with γ precipitates, γ acts as an impediment to crack propagation, b) under compression at elevated temperatures, grain boundary sliding of σ/σ interfaces occurred until σ particles separated and γ underwent recrystallization, while in creep, γ primarily deformed do to dislocation motion and twinning c) under compression, a decrease in yield temperature resulted as the volume fraction of γ increased and d) indentation-induced plastic deformation yields intergranular fracture [14, 15, 55, 56].

When the volume fraction of the dispersed σ-phase reaches a low enough value, <30%, this material may essentially act like a dispersion strengthened material where the volume fraction, particle size and interparticle spacing must be optimized to obtain the best combination of properties, including creep, toughness and tensile elongation. The particle size needs to be sufficiently small in γ+σ materials, so as to decrease the initial crack size and improve toughness. It has been shown for some dispersion

strengthened materials that reducing interparticle spacing reduces minimum creep rate. When interparticle spacing and particle size are both controlled, the volume fraction is set, so varying either of those factors independently varies the volume fraction. Finding a dependence of just one of the factors is difficult and depends on the property being evaluated, so measures must be taken to control these microstructures. For example, creep rate may be a minimum when interparticle spacing is minimized and particle size is maximized (high volume fraction), but this may have a deleterious effect on toughness and tensile elongation [58].

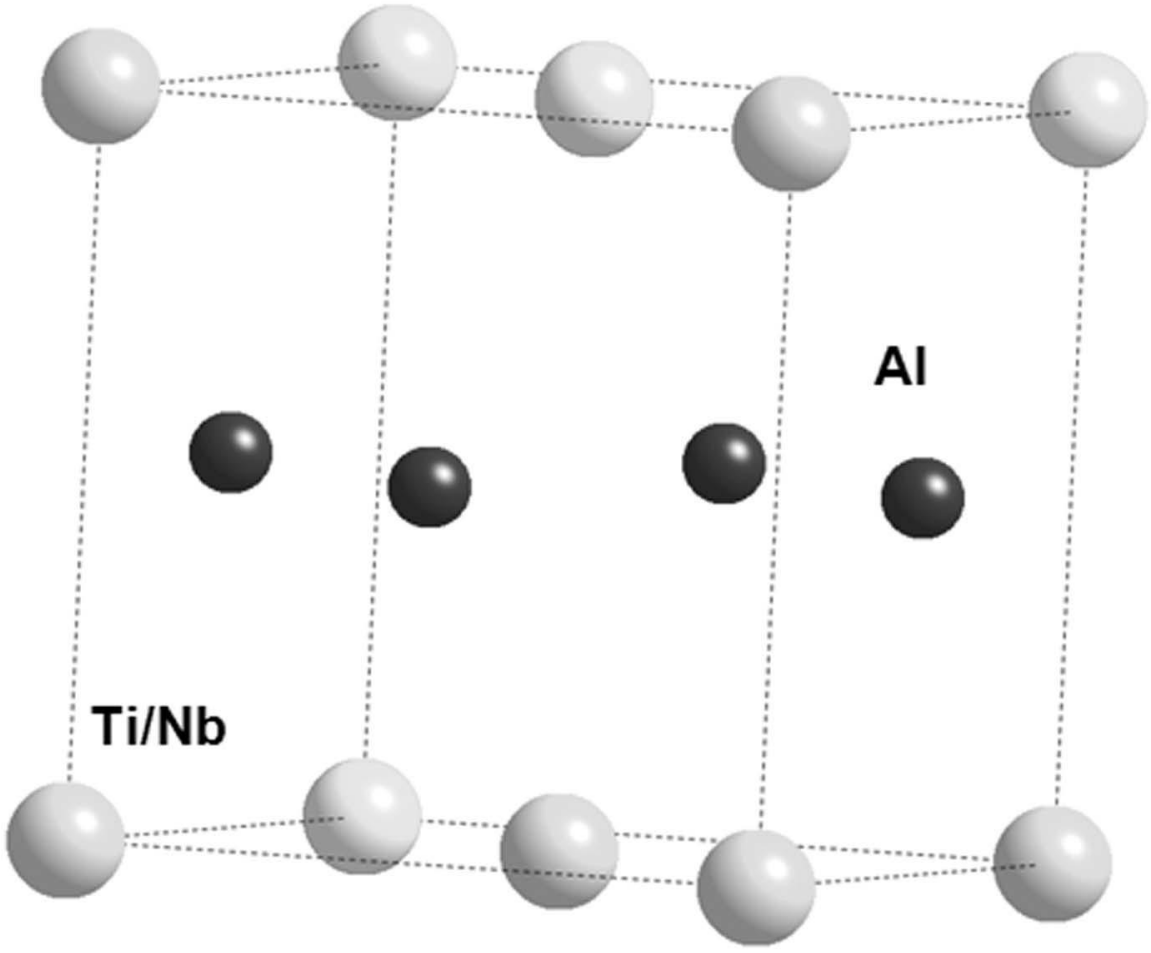

Figure 2-1. TiAl-$L1_0$ unit cell (Courtesy of Michael S. Kesler)

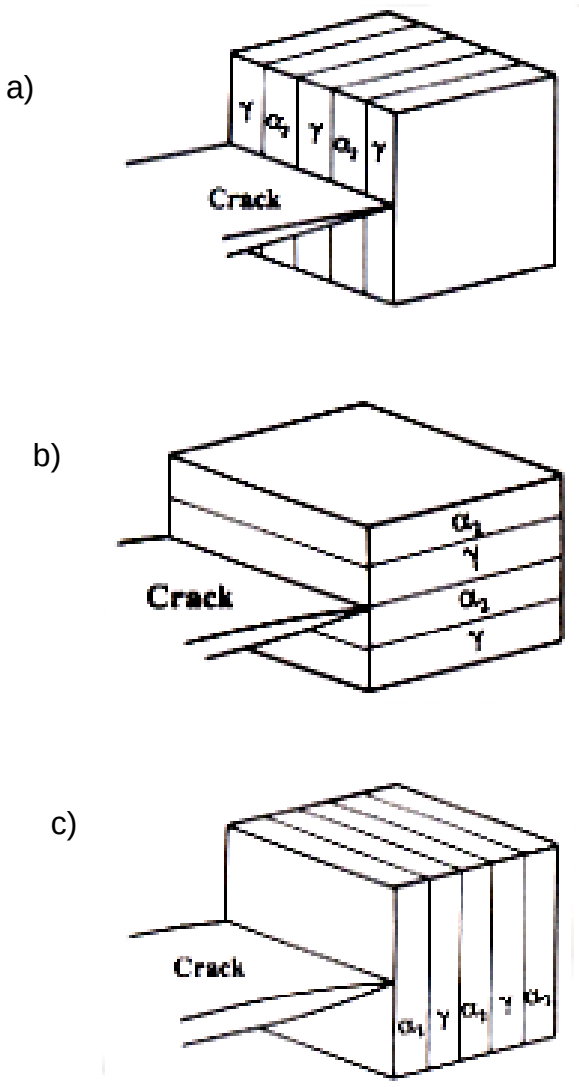

Figure 2-2. Crack tip orientations in TiAl alloys. a) Crack divider orientation, b) Crack delamination orientation, c) Crack arrester orientation (KS Chan, JOM 44 308 (1992).)

CHAPTER 3
MATERIALS AND EXPERIMENTAL PROCEDURES

3.1 Materials

Alloys investigated in this study were produced in an MRF Inc. custom arc-melter using a Miller Gold Star 652 welding unit with a non-consumable tungsten electrode under flowing ultra high purity Ar gas. The purity of each element was as follows: 99.995%Ti, 99.99%Al, 99.99%Nb, 99.95%Cr, 99.99%Mo. The alloy compositions selected for this study are listed in at% and can be found in Table 3-1. It should be notes that the names of the alloys, i.e. Alloy 11, was based on the order in which they were chosen and has no relevance to the composition therein. Details of alloy design and selection will be discussed in Chapter 4. The elements were in several forms including granules (Ti, Al and Cr), wire (Mo) and plate that was chipped to fine flakes (Nb). They were precisely weighed within ±0.001g. The elements were acid washed (with the exception of Molybdenum) in a Nital (3% HNO3 + Methanol) then rinsed and ultra-sonicated in isopropyl alcohol. Molybdenum wire was ground with sand paper to clean the surface, and then rinsed in isopropyl alcohol and cut into small pieces. Acid washing of Mo was avoided due to a reaction which causes the surface to oxidize. After cleaning, the elements were re-weighed, and then arranged in the arc-melter. Fine Nb flakes were placed in the bottom of the cavity, then Ti would be placed on top followed by the rest of the elements. This arrangement had two benefits: 1) to prevent the fine Nb flakes from scattering about the chamber during the initial agglomeration of the sample, and 2) because of the 100% solubility of Nb in Ti, this arrangement increased the chance of homogeneous melting. The chamber was evacuated 3 times (<60mTorr) and purged with argon after each pump down to a pressure just below 1atm, keeping a

slight negative pressure in order to conserve the seal. The chamber achieved a minimum pressure of 10mTorr while pumping and the chamber was kept at an overpressure of 2psi with flowing argon using a relief valve during the melting process. In order to minimize oxygen contamination, a small piece of Ti (~1g) was employed as a getter, which was melted prior to each successive melting and visually inspected for oxidation on the surface. Inside the bell jar of the arc-melter was a water-cooled copper hearth with cavities of varying sizes and shapes. Buttons of 5g, shown in Figure 3-1, were melted in cavities which were 2.54cm in diameter. 10g buttons were produced from the consolidation of 2 5g buttons which were also melted in a 2.54cm cavity. 25g rods, shown in Figure 3-1, were produced from the consolidation of 5 5g buttons and were melted in an elongated cavity resulting in a rod with approximate dimensions of 50mm x 12mm x 12mm. The 5g buttons were melted and flipped 6 times to ensure compositional homogeneity. The larger samples (10 and 25g) were melted twice more for consolidation and uniformity of shape. In some samples, problems with the melting of Nb and Mo were encountered resulting in regions of un-melted and/or the inhomogeneous distribution of elements. Figure 3-2 shows an example of an aged sample with an inhomogeneous distribution of Nb. The result was a localized high volume fraction of significantly coarsened σ-phase (lighter phase) in a particular region of the sample. These samples were discarded and once this issue of inhomogeneous melting was recognized, each sample was inspected after melting to insure homogeneity by sectioning and LOM/SEM analysis. This issue has many factors including, initial size of Nb and Mo, sinking of heavy/high melting point elements in the melt and human error in the melting process. Measures were taken to insure a

consistent melting process such as a consistent melting time (~15secs per melt) and technique. This consistency in the melting process is also important for the controlled vaporization of Al during melting. An amperage of 300 resulted in the loss of approximately 1% of the total weight in Al during melting, i.e. 0.45at% Al was lost from a total Al concentration of 45at%.

3.2 Differential Thermal Analysis (DTA)

DTA using a Setaram Setsys Evolution 1750 with a DSC1600 rod was conducted on as-cast materials in order to estimate transformation temperatures as well as on solutionized and water quenched samples to evaluate the evolution of phases upon aging. In DTA, phase transformations are identified through the measurement of heat flow to and from a reference sample (an empty alumina crucible, in this study), and to and from the sample being tested. When differences in heat flow between the sample and reference are observed, a phase transformation is taking place. When an exothermic reaction occurs in the test sample, energy is released to the surroundings and a peak is observed on the DTA curve. Endothermic reactions in the test sample, on the other hand, absorb energy from the surroundings resulting in a valley in the DTA curve. Analysis of DTA data aided in selecting solutionizing and aging temperatures.

Samples of 20–50mgs were heated at rates of 5 K/min and 10 K/min inside covered alumina crucibles in a He atmosphere. Temperature calibrations were performed by melting high purity standards of Cu, Ni (from NIST) and Al (from Alfa Aesar) at scan rates of 2 K/min, 5 K/min and 10 K/min. All DTA experiments were run using experimental procedures reported by Rios [59].

3.3 Heat Treatments

The goal of the heat treatments in this study was to precipitate a fine $\gamma+\sigma$ microstructure from the β-phase. This was achieved by retaining the β-phase to room temperature via solutionizing and water quenching, followed by subsequent aging heat treatments for precipitation of the γ and σ phases. In the composition range of this study, the β-phase is in equilibrium as a single phase at higher temperatures (>1400ºC) and the desired two-phase region of $\gamma+\sigma$ is present at temperatures between ~850-1200ºC. The following describes the instrumentation and heat treatment schedules of solutionizing and aging of the alloys.

3.3.1 Solutionizing + Water Quenching Heat Treatments (Soln+WQ)

These alloys require a solutionizing heat treatment for dissolution of the dendritic as-cast structure and formation of a single β-phase, then water quenching to retain the β-phase. Prior to the soln+WQ heat treatment, buttons and rods in the as-cast condition were cut into slices, rectangular compression samples or bending bars, using a Allied TECHCUT 4 slow speed diamond saw. Figure 3-3 shows the cutting direction for slices which is the same as the cooling direction. The rounded ends of the buttons were discarded. Samples were then wrapped in Ta foil for oxygen gettering during heat treatment. Samples were inserted into a CM 1700 split vertical tube furnace capable of reaching 1600ºC. The furnace had a sealed alumina tube which allowed for an inert flowing argon atmosphere and drop quenching capability. A small amount of Ta wire was used (~7.5cm) as a basket for the samples and was hooked to a braided alumina-borica-silica rope which suspended the samples in the hot zone of the furnace. Outside of the hot zone, the braided rope was attached to a steel wire that was looped around a

latch which was used to drop the samples for quenching. The samples were dropped by switching a lever attached to a rotating bar which released the steel wire from the latch. The bottom of the furnace was opened nearly simultaneously with the turning of the lever for the purpose of minimizing oxygen contamination while at high temperature prior to quenching. All samples in this study were drop quenched from the solutionizing temperature into water. Figure 3-4 shows examples of the heat treatment schedules for the alloys. For large samples, including bending bars, the water was agitated using a small water pump. This process aided in slowing the transformation of the β-phase to the γ-phase upon quenching. Once samples were hung inside the furnace and the furnace was sealed, a roughing pump was applied to evacuate the alumina tube and the system was purged with Ti-gettered ultra high purity Ar gas via a Centorr gettering furnace Model 2G-100-SS. The gettered gas flowed through the system for the duration of the heat treatments.

After pumping and purging, the furnace was ramped up to the solutionizing temperature (1400-1500ºC) at a rate of 9ºC/min. Samples were then held for 1hr at the solutionizing temperature, then WQ. After quenching, the furnace was ramped down at 9ºC/min. The ramp rates are low in order to limit the thermal shock on the alumina tube.

3.3.1.1 Quenching Furnace

Figure 3-5 displays the components of the sealed alumina tube. Due to the extreme temperatures of the furnace, a cooling system was necessary for safe handling during quenching experiments. Copper cooling caps were attached to the alumina tube with Ceramabond by inserting the tube into the inner diameter of each cooling cap. The tube was seated against a lip inside the copper cap which stabilized the tube. TorrSeal

was applied over the gap between the alumina tube and the cooling cap because the Ceramabond does not provide an acceptable seal for pumping down. The caps are cooled by the ‘water jacket’ that flows around a cavity in the copper cylinders keeping them near ambient temperature. This is necessary for removal of the plug and turning of the steel quenching lever.

The aluminum ‘top hat’, shown in Figure 3-6, provides the gas inlet, the quenching lever and two ports for the internal thermocouple (B-type) and pressure gauge. The quenching lever is a Swagelok part that allows for a bar to be rotatable inside the system while still providing a seal. The top hat is fitted to the top of the cooling cap and provides a seal with an o-ring which lies in a channel around the cooling cap.

The removable plug, shown in Figure 3-7, provides a sealed interface with the rest of the bottom cooling cap. Beneath the plug is the isolation valve which determines where the chamber releases gas. It has three settings; 1) pointing left for evacuating the system, 2) pointing up for sealing the tube and backfilling with argon, and 3) pointing right (current setting) for relieving the flowing argon gas for the duration of an experiment. The gas exits through a relief valve keeping a constant over pressure of 2psi for these experiments.

3.3.1.2 Temperature Calibration

The internal thermocouple was inserted in the tube level with the furnace thermocouple that lies outside of the sealed system directly adjacent to the furnaces heating elements. Samples were hung directly adjacent to the internal thermocouple to measure the temperature accurately. A calibration was necessary for setting the furnace controller temperature such that the sample would experience a target temperature. Figure 3-8 shows a schematic of the internal and furnace thermocouples (both B-type)

along with the resulting temperatures upon heating the furnace through the range of temperatures needed for this experimentation. The temperature recorded at the sample was lower than the furnace thermocouple because of the relative distances from the elements along with the flowing argon gas through the tube. The temperature at the sample (measured by the internal thermocouple) was monitored in every test. This calibration process was repeated every time a furnace element was changed or any other change was made to the furnace or alumina tube set up.

3.3.2 Aging Heat Treatments

After soln+WQ, aging heat treatments were performed in order to precipitate two-phase $\gamma+\sigma$ microstructures. Figure 3-4 shows the heat treatment schedules. Aging heat treatments were conducted in an ATS box furnace over a temperature range of 500-1200ºC. Samples were encapsulated in quartz tubes that were pumped down, then backfilled with argon gas. For all aging experiments, the furnace was at the aging temperature prior to the insertion of a sample in order to rapidly bring the sample to the aging temperature. This method was used to limit the amount of nucleation and growth during heating prior to reaching the aging temperature. Samples were placed directly adjacent to the thermocouple inside the furnace to ensure an accurate temperature. Early experiments conducted with two K-type thermocouples established that this positioning resulted in the sample temperature being consistent with the controlling thermocouple measurement within ±3ºC. All samples used for mechanical testing were furnace cooled after aging, while samples used to elucidate phase evolution were water quenched by removing the encapsulated sample and simultaneously submersing the sample and breaking the encapsulation with a hammer to maximize the cooling rate.

3.3.2.1 Encapsulation

An encapsulation unit was designed and samples were placed inside a quartz tube with an outer diameter of 12mm and one sealed end. The system allowed for pumping and purging of the tube using a roughing pump and then back-filling with argon gas. This was repeated 3 times. The chamber was able to be pumped to a pressure of 60mTorr prior to back-filling. Once the tube had been properly evacuated, a hydrogen torch was used to seal the open end of the tube. Depending on aging temperature, a pressure from -5 to -10Torr was sustained inside the tube after sealing to ensure that the tube would not burst when heated to the aging temperature. To select the proper pressure inside the tube, the following equation was employed:

$$P_{RT}/T_{RT} = P_{age}/T_{age} \qquad \text{Equation (3-1)}$$

where,
P_{RT}: Pressure at room temperature
T_{RT}: Ambient temperature
P_{age}: Pressure at the aging temperature
T_{age}: Aging temperature

In this particular case, the volume of the gas inside the tube is held constant. For practical purposes, the pressure at the aging temperature, P_{age}, is 1atm inside the tube, thus resulting in a negative pressure at room temperature, P_{RT}.

3.3.2.2 Aging Times

For all samples aged for mechanical testing, an aging time of 2hrs was selected. This was chosen so that the samples would have enough time to fully transform to the 2-phase $\gamma+\sigma$ microstructures. It was shown that the $\gamma+\sigma$ microstructure forms in under 5 minutes upon aging and once the $\gamma+\sigma$ microstructure forms at a given temperature, it is a very stable structure and coarsening is slow [56].

3.3.2.3 Aging Temperatures

Aging temperatures were selected based on DTA experiments conducted on soln+WQ samples. Temperatures of 865ºC, 1000ºC and 1050ºC were selected with the objective of varying scales of the γ and σ phases. To further understand the nature and order of precipitation of phases, aging temperatures of 500ºC, 600ºC, 800ºC and 1200ºC were also used.

3.4 Sample Preparation and Characterization

3.4.1 Metallographic Procedures

Samples in all conditions were prepared by conventional metallographic procedures. Carbon black epoxy was used as a mounting material for the initial microstructural evaluations of sliced specimens. Because of oxygen contamination on the surface, the slices were cut in half using the slow speed diamond saw and the cross section was inspected to ensure an evaluation of the uncontaminated material. For samples that were used in mechanical testing, i.e. bars and rectangular compression samples, it was not practical to mount in epoxy, so they were either held in a planar or polished manually by hand. The planar consisted of a 90º angle and a machined block which were used to create and/or maintain parallel surfaces on sample used in mechanical testing. After soln+WQ, the mechanical testing samples surfaces were ground down 200μm to remove the 'environmentally affected zone'. Aging resulted in negligible surface contamination and served as a means of relieving residual stresses associated with grinding.

Grinding and polishing operations were conducted using SiC paper and alumina slurries, respectively. The grinding paper ranged from 240 to 1200 grit, then slurries of 5μm, 1μm and 0.3μm were applied to a designated Buehler Microcloth for final

polishing. Samples that were used for compositional analysis were put through a finishing polish in a Vibromet I Polisher with a 0.06μm SiO_2 slurry to avoid contamination from alumina which could alter the Al composition measurement. Cleaning the samples with alcohol left a residue on the sample surfaces which resulted in inconsistent metallographic results. The most affective means of cleaning the samples was the use of running water and a cotton swab. Macro- and micro-etchants, 55%H_2O+25%HF +20%HNO_3 and 75%H_2O+ 10%HF+15%HNO_3, respectively, were applied to polished samples in order to reveal the unique features of the microstructure in these samples for optical microscopy. The macro-etchant was used to reveal β-phase grain boundaries and the micro-etchant was used to reveal the finer microstructural features.

3.4.2 Optical Microscopy (OM)

Two optical microscopes, a LECO and a Leica DM2500M, were used in this study. These microscopes were employed for the observation of as-cast microstructures, soln+WQ microstructures, macroscopic observations of deformed sample surfaces and fractured samples. The micro-etchant was used for observing the finer as-cast microstructures, while the macro-etchant was used for revealing the coarse β grain boundaries in soln+WQ samples. No etchant was used on the deformed sample surfaces. OM was also used to observe and measure the indents for hardness testing, incremental observations during the polishing process and examination of sliced samples after arc-melting to ensure complete melting of pure elements.

3.4.3 Scanning Electron Microscopy (SEM)

A Philips xl40 field emission scanning electron microscope (SEM) was used for observation of samples in the as-cast, soln+WQ, aged conditions. Mechanically tested sample surfaces and fracture surfaces were also viewed using the SEM. Mounted samples were coated with carbon paint, while unmounted samples were held by an aluminum stub mount using carbon tape. A range of conditions were used to observe samples.

Secondary electron imaging (SE) was employed for observation of the topographical features including deformation/microcracking on sample surfaces and fracture surfaces. Generally, deformed sample surfaces had shallow features, so a working distance of 10mm was used, while tortuous fracture surfaces were viewed using working distances in the range of 15-25mm.

Backscattered electron imaging (BSE) was employed for observing phase contrast. This was an effective means of viewing the two-phase $\gamma+\sigma$ microstructures of aged materials, the precise positions of localized deformation/microcracks on sample surfaces and the location of particles on fracture surfaces. In $\gamma+\sigma$ microstructures, the γ-phase is dark due to relatively high Al and low Nb contents (~55at% and 10at%, respectively) and the σ-phase appears white due to the low Al and high Nb contents (~42at% and 30at%, respectively). For heavier elements, or elements of a higher Z, more electrons are elastically scattered which results in more electrons hitting the detector, thus yielding a brighter image.

A JEOL 733 Superprobe SEM was used for quantitative compositional analysis via wavelength dispersive spectroscopy, also referred to as electron probe microanalysis

(EPMA). For overall compositions of samples, soln+WQ specimens were used because the segregated dendritic structure of the as-cast condition had been solutioned resulting in a more homogenous sample for compositional analysis. For these samples, a large beam of 100-180μm was employed so a broad region of the material could be sampled. For buttons that were cross-sectioned, as shown in Figure 3-3, spots were taken from bottom to top and from left to right of a slice, thus covering the entirety of the button. At least 10 points were taken for each sample. A smaller spot size of 1μm was used to ensure that samples were appropriately homogenized and for compositional analysis of individual phases in aged materials, when possible. For highly refined microstructures, the individual phases were too small for accurate compositional measurements by this method. Compositional analysis data are listed in Appendix A.

3.4.4 X-Ray Diffraction (XRD)

A Philips APD 3720 powder x-ray diffraction system was used to identify the phases present at room temperature in various conditions. As-cast specimen preparation involved using a polished 1-2mm slice taped to a glass slide. The surface area of a slice was approximately $1cm^2$. It was necessary to match the eucentric height of the sample to the plane in which the instrument gripped the glass slide so that the sample was in proper alignment with the beam. This was done by applying layers of tape and pieces of glass slides to the gripped end of the glass slide until the plane of the sample was at the same height as the gripped end of the slide.

Crystallographic texturing in the large β grains in soln+WQ samples and in the $\gamma+\sigma$ microstructures of aged samples was identified in the initial XRD scans in this study. This was determined by comparing the results to standards and to the work of other

researchers. As a result, samples in the soln+WQ and in the aged conditions were ball milled until a fine flowing powder was produced and then XRD profiles expected from random polycrystalline specimens were generated. Ball milling also introduces strain into the resulting powders which often cause the widening of peaks in the powder XRD profiles. However, the effect was minimal in this study due to the strength and brittleness of the samples, especially in the soln+WQ condition.

The XRD was performed at 40kV and 20mA and used Cu Kα radiation. Most scans were run over a 2θ range from 20º to 130º at a step size of 0.07º and a dwell time of 2 seconds. Some scans were run over a smaller 2θ range from 35º to 45º with a step size of 0.04º and a dwell time of 2 seconds to see the relative changes in intensity of specific peaks from samples aged at different temperatures. All measured XRD profiles were compared with standards generated using PowderCell software along with CrystalMaker software.

XRD is not reliable for identifying the presence of relatively fine phases which exist in the material under approximately 5vol%. Often times the meta-stable Orthorhombic phase was not identified in soln+WQ XRD profiles, though could be observed in OM, SEM and TEM micrographs. However, it should be noted that this phase dissolves upon aging in the two phase $\gamma+\sigma$ region.

3.4.5 Transmission Electron Microscopy (TEM)

Samples for transmission electron microscopy (TEM) were selected from specific regions on deformed samples using an FEI DB352 Focused Ion Beam (FIB). For this technique, a field emission SEM is used to view and select specific areas of a material, and then a Gallium ion source is used to mill out a TEM foil. The milling procedure was

as follows: a 18μm x 1.5μm x 2.5μm (length x width x depth) strip of Pt was deposited on the sample surface at a current of 300pA. Two large 20μm x 8μm x 7μm trenches were milled on either side of the Pt strip at a current of 5000pA. The material was then thinned at a current of 1000pA until the film was 1μm thick. An undercut was made and thinning resumed at a current of 300pA until the film was ~300nm in thickness. Because of tapering of the film during milling, the sample was tilted one degree and milled, this step was repeated for the other side, then final thinning was conducted at a current of 100pA until the sample was ~100nm thick, and finally the sample was released by milling off either end of the film. A micromanipulator with a fine glass needle point was used to lift out the sample and place it on a copper TEM grid. The final dimensions of the TEM foils were approximately 15μm x 7μm x 100nm. Most foils were oriented parallel with the loading direct and transverse to the observed deformation on the surface of deformed samples. A film taken from the prior β grain boundary structure was oriented such that it cross-sectioned the Widmanstätten γ-laths.

Two TEMs, a JEOL 200CX and JEOL 2010F HRTEM, were used in this study. For samples with coarse microstructures, the JEOL 200CX was sufficient for imaging and diffraction. In order to get diffraction from a single phase in the finer microstructures, the JEOL 2010F equipped with smaller diffraction apertures was used. The JEOL 2010F was also fitted with a scanning transmission electron microscopy detector and energy dispersive x-ray spectroscopy (EDS) enabling semi-quantitative compositional analysis of phases that were too fine to be analyzed through EPMA. The beam size for EDS was approximately 1nm. The TEM aided in understanding the size, morphology and location

of phases, though primarily was used for observation and analysis of deformation substructures, i.e. twins and dislocations, and microcracks.

3.4.6 Imaging Analysis

The microstructural parameters of the alloys, including volume fraction, particle size and interparticle spacing, were measured using a combination of manual techniques and ImageJ software. The manual technique for measuring volume fraction involved using a transparent grid and tracing phases. The squares lying within the phases were totaled and then were divided by the sum total number of squares in the grid. This area fraction, when taken from several cross-sections, is comparable with the volume fraction. All quantified volume fraction measurements were taken from at least 5 BSE images and from images of at least two different relevant magnifications. Initial measurements were taken manually using the transparent grid and compared with that of the imaging software. The variation between manual techniques and the software was negligible (within 1-2vol%σ for a given image), so the majority of measurements were generated from ImageJ software. Examples of quantitative microscopy measurements are shown in Appendix A.

Mean random spacing of the σ-phase particles were measured and calculated as described by Underwood [60] using the following method: at least three BSE images were used for each measurement and intercepts were counted from 3 randomly placed lines on each image. The mean random spacing was calculated using this equation:

$$\sigma_r = 1/N_L \qquad \text{Equation (3-2)}$$

where,
σ_r: Mean random spacing of particles
N_L: Number of intercepted particles per unit length of the drawn line

The mean free path, or edge-to-edge distance between particles, was measured via the same method as the mean random spacing, but also incorporated the volume fraction measurements due to the use of the following equation:

$$\lambda = (1-V_V)/N_L \qquad \text{Equation (3-3)}$$

where,
λ: Mean free path
V_v: Volume fraction of σ-phase particles

Particle size distribution was calculated from the difference of the mean random spacing and the edge-to-edge distance (σ_r-λ) which would give the mean diameter of the σ-phase particles.

3.5 Mechanical Testing

All mechanical testing was conducted at the University of Florida. The alloys used for mechanical testing were all aged and furnace cooled to minimize residual stresses associated with thermal contraction. Sample dimensions were selected based on ASTM standards and testing conditions and were either taken from established testing procedures or designed for comparison with other researchers' results.

3.5.1 Microindentation

Microindentation testing using a Vickers diamond indenter was conducted on a Buehler Micromet II and these data were used for hardness measurements. With the assistance of Dr. Mecholsky's research group and use of their laboratory, a Zwick & Co. KG indenter was fitted with a Vickers diamond indenter and used at high loads (20-30kgf) for fracture toughness estimations.

Slices of buttons were used for all microindentation testing. Flat parallel surfaces were produced using a right angle planar to ensure uniform indents and finely polished

according to standard metallographic techniques. Slices had to have a thickness greater than 10X the diagonal length of the indents to avoid insufficient constraint during testing, so generally thicker slices (~2mm) were used for fracture toughness estimations due to an indent diagonal length ranging from ~100-200μm. Indents were applied for 15 second intervals at loads of 1kgf for hardness testing and 20-30kgf for fracture toughness estimations. Ten indentations were made on each sample from which average values were calculated.

Fracture toughness estimations were attempted using a method where cracks emanating from the corners of indents were measured. These cracks arise due to the stress field associated with the indentation. Cracks can develop during the formation of an indent and/or as a result of an elastic response upon unloading of the indenter. Fracture toughness values can be estimated using the following equation developed by Lankford's 'curve fitting model' [57]:

$$K_{1C} = 0.142(c/a)^{-1.56}(E\phi/H)^{.4}(Ha/\phi) \qquad \text{Equation (3-4)}$$

where,
c: Length from center of indent to tip of crack
a: Half the diagonal of the indent
E: Young's modulus
H: Hardness value
ϕ: Plastic constraint factor (~3)

3.5.2 Compression Testing

Compression tests were conducted on a MTS 204.63 servo-hydraulic 100kip load frame with a 22kip load cell at room temperature. All testing was run under displacement control at a constant cross-head speed of $1x10^{-4}$ inch/sec ($\dot{\varepsilon} \sim 3.9x10^{-4}$ - $4.9x10^{-4}s^{-1}$ depending upon the precise sample height). A Labview data acquisition program was used to collect load and displacement data. Molybdenum Disulfide powder

was used on the compression platens as a dry lubricant. The majority of samples were loaded to fracture in order to determine yield strength, ultimate compressive strength and plastic strain data. Other selected samples were loaded and unloaded at a low plastic strain to investigate the early stages of deformation, crack initiation and propagation. Two samples from each aging condition were loaded to fracture to ensure a level of consistency in the data.

Both polycrystalline (PX) and single crystal (SX) rectangular compression samples were tested under compression. PX samples were fabricated from 10g arc-melted buttons using the slow speed diamond saw, while SX specimens were each cut from a single soln+WQ β grain which limited the sample size. Figure 3-8 shows a schematic of how SX samples were prepared from a soln+WQ slice. The final sample dimensions were reached using 400-600grit polishing paper and a planar to ensure that the sample was orthogonal. A height to width ratio of 1.5 was employed and the nominal dimensions were 4mm x 4mm x 6mm for PX samples and 2mm x 2mm x 3mm for SX samples. The bases and at least 2 adjacent faces of the sample were polished to 0.3μm. Sample dimensions and preparations were based on ASTM E9.

3.5.3 Fracture Toughness Testing

3.5.3.1 Single Edge Notch (SEN) 4pt Bending

Fracture toughness samples were fabricated from 25g arc-melted rods by electrical discharge machining (EDM). The initial dimensions of the bars were 2.2mm x 4.3mm x 38mm. These bars had a ‘heat affected zone’ as a result of the EDM process. This zone was approximately 0.1mm thick, so the bars were ground down and polished to 0.3μm for the final dimensions of 2mm x 4mm x 38mm. Soln+WQ treatments resulted

in slight warping of the bars and in order to regain the parallel surfaces of the bar, a high speed surface grinder (courtesy of MTE) using a small 'bite' (0.00254mm) was successfully employed. The surfaces were then repolished and inspected for cracking. No microcracking was observed after surface grinding and then holding at the aging temperatures for 2hrs likely relieved residual stresses. After heat treatments, the single edge notch (SEN) was cut into the bar using a 0.15mm thick diamond wafering blade. A schematic of the bending bar and nominal dimensions are shown in Figure 3-10. Sample dimensions were selected based on ASTM E399. An important factor in cutting the notch was to ensure that the fracture was occurring through a single prior β crystal. The goal was to estimate intrinsic fracture toughness of the $\gamma+\sigma$ microstructure, so if the crack path was β grain boundary-free it would increase the accuracy of these calculations. In the soln+WQ condition when β grains were visually apparent an area was selected for testing and a mark was made by scoring the edge of the bar where the notch was to be made. The notch was not cut in the soln+WQ condition to avoid introducing microcracks into the highly stressed quenched material. The sample was then aged and the notch was cut. An annealing heat treatment was conducted at 500ºC to relieve any residual stresses associated with cutting of the notch. Two samples at each aging condition were tested. Because of time and cost constraints, the number of tests were limited. Precracking was avoided in order to conserve the limited number of samples. The absence of a pre-existing sharp crack would increase the amount of plasticity at the notch root. This would result in an overestimation of the fracture toughness values due to blunting of the crack tip that forms at the root of the notch. This effect will be discussed in Chapter 6.

A 200lbs load cell and an MTS 642.05A-1 4-point bending fixture were attached to the MTS load frame. The samples were carefully aligned such that the bar was orthogonal to the bending rollers and the notch was oriented in the center of both spans and was aligned with the center of the loading axis. Tests were run at a constant cross-head speed of $1x10^{-4}$inch/sec at room temperature. K_{1C} values were calculated based on the maximum load using the following equations:

$$K_{1C} = (P_c/BW^{1/2})Y(\alpha) \text{ [61]} \qquad \text{Equation (3-5)}$$

$$Y(\alpha) = [S_1\text{-}S_2/W][3\,\alpha^{1/2}/2(1\text{-}\alpha)^{3/2}] \times \{1.99\text{-}1.33\alpha - (3.49\text{-}0.68\alpha + 1.35\alpha^2) \times [\alpha(1\text{-}\alpha)/(1+\alpha)^2]\} \qquad \text{Equation (3-6)}$$

where,
K_{1C}: Fracture toughness
P_c: Maximum load
B: Bar thickness
W: Bar height
α: Ratio of notch length to bar height (a/W)
$Y(\alpha)$: Geometric factor

3.5.3.2 Unnotched 3pt Bending

Unnotched bars were made with the same metallographic preparation as the SEN bars with final dimensions of 2mm x 4mm x 20mm. A 3pt bending fixture was fitted to an INSTRON and tests were run at a cross-head speed of $1x10^{-4}$inch/sec. Maximum stresses and fracture toughness estimations were calculated using the following equations:

$$\sigma_{max} = (3PS)/(2bh^2) \qquad \text{Equation (3-7)}$$

where,
σ_{max}: Maximum tensile stress
P: Maximum load
S: Span
b: base

h: height

$$K_1 = Y\sigma(a)^{½} \text{ [62]} \qquad \text{Equation (3-8)}$$

where,
K_1: Fracture toughness
Y: 1.124 (geometric factor)
σ: Applied stress
a: crack size

Table 3-1. Alloy compositions as measured by EPMA

Alloy names and nominal composition (at%)	Composition (at%)				
	Ti	Al	Nb	Cr	Mo
Alloy 11 Ti-45Al-18Nb	37.0	44.7	18.3	---	---
Alloy 12 Ti-45Al-27Nb	28.3	44.0	27.7	---	---
Alloy 12Cr Ti-45Al-22Nb-5Cr	28.9	43.5	22.6	5.0	---
Alloy 12.5CrMo Ti-45Al-18Nb-5Cr-1Mo	30.7	45.5	17.9	5.0	.9
Alloy 13CrMo Ti-45Al-14Nb-5Cr-1Mo	34.9	44.7	14.3	5.1	1.0

Figure 3-1. Examples of an arc melted 5g button and 25g bar (Courtesy of Michael S. Kesler)

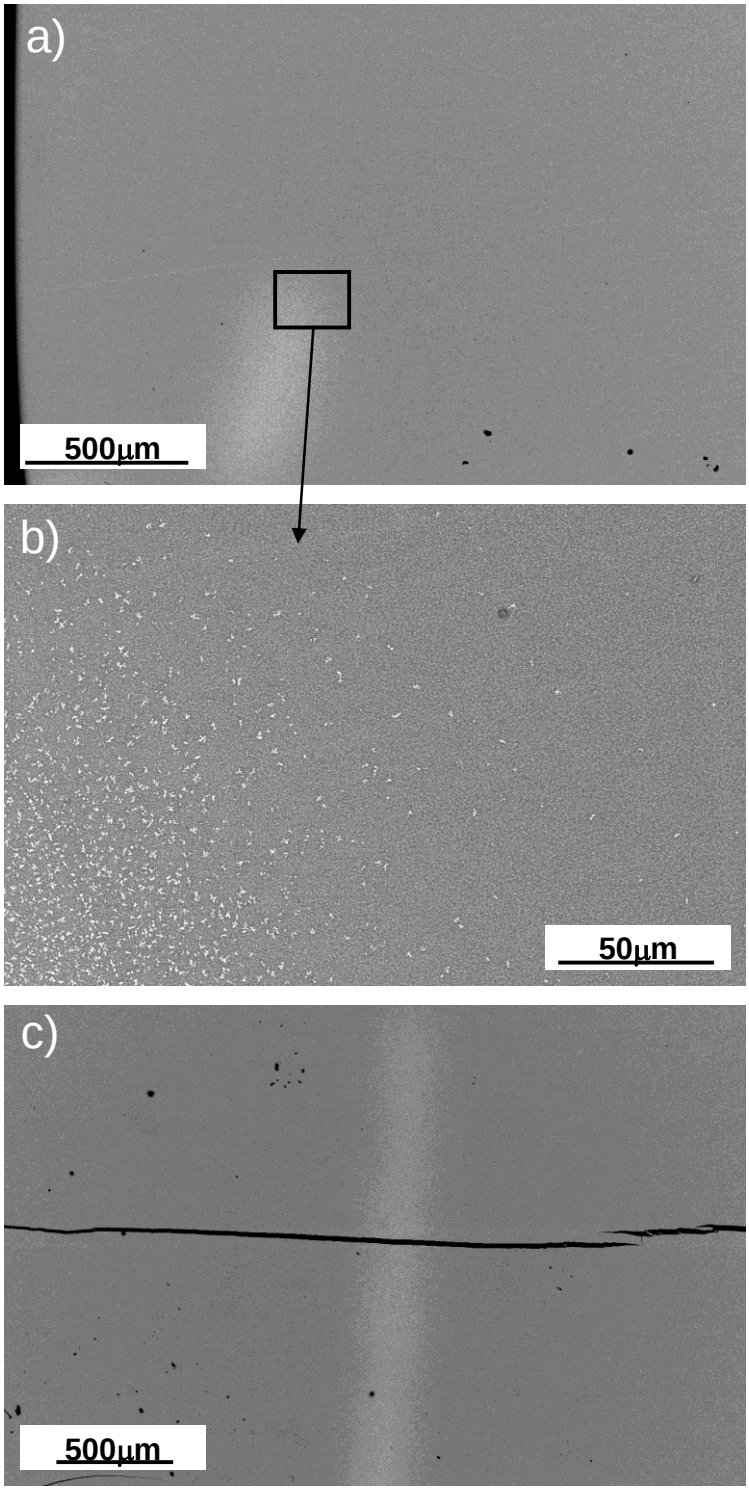

Figure 3-2. BSE images showing the effects of inhomogeneous melting of Nb on aged microstructures. a) and b) show a region with a high volume of relatively coarse σ-phase and c) a compression sample showing a large crack which initiated from an unhomogenized region (Courtesy of Michael S. Kesler)

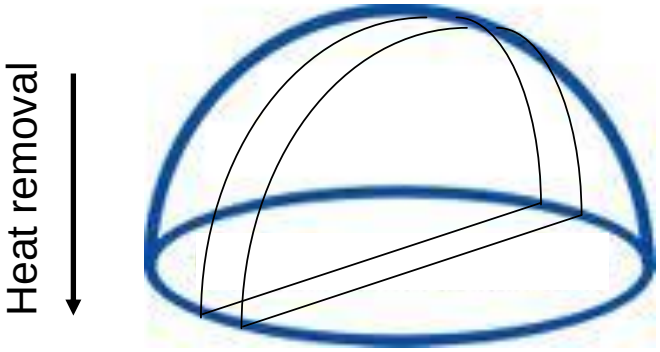

Figure 3-3. Illistration of the slicing direction (Courtesy of Michael S. Kesler)

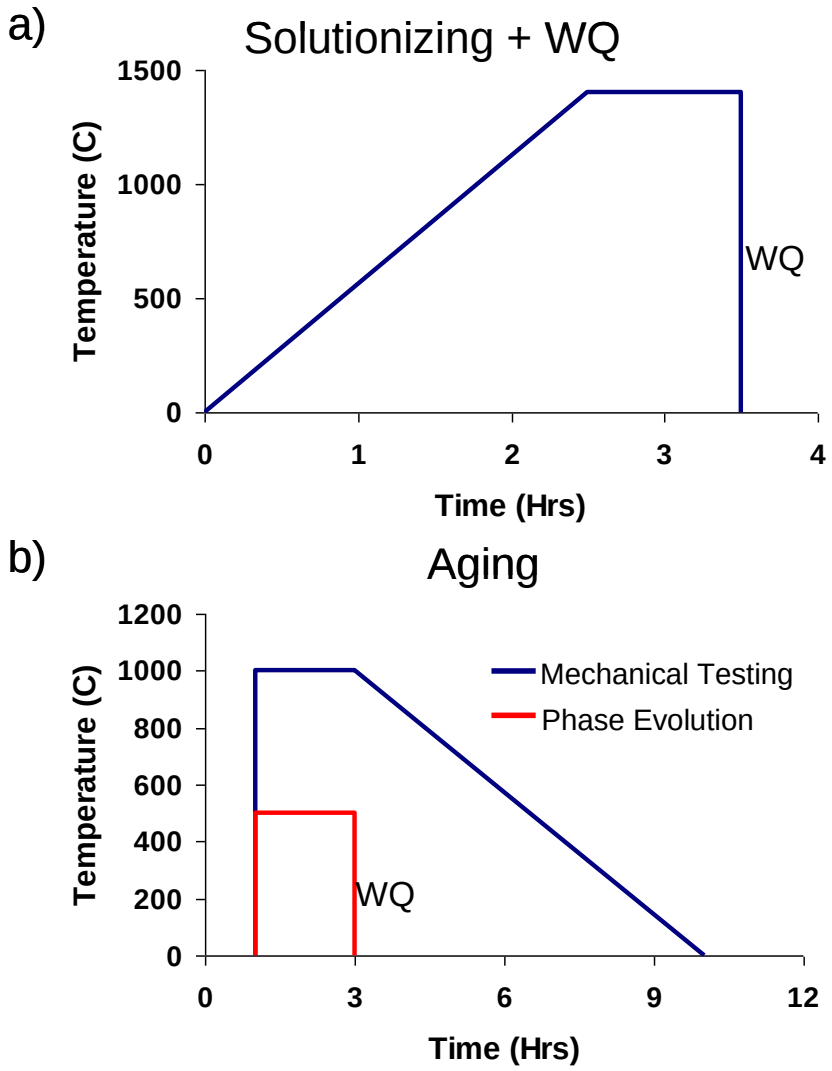

Figure 3-4. Examples of the heat treatment schedules for a) soln+WQ experiments, and b) aging experiments (Courtesy of Michael S. Kesler)

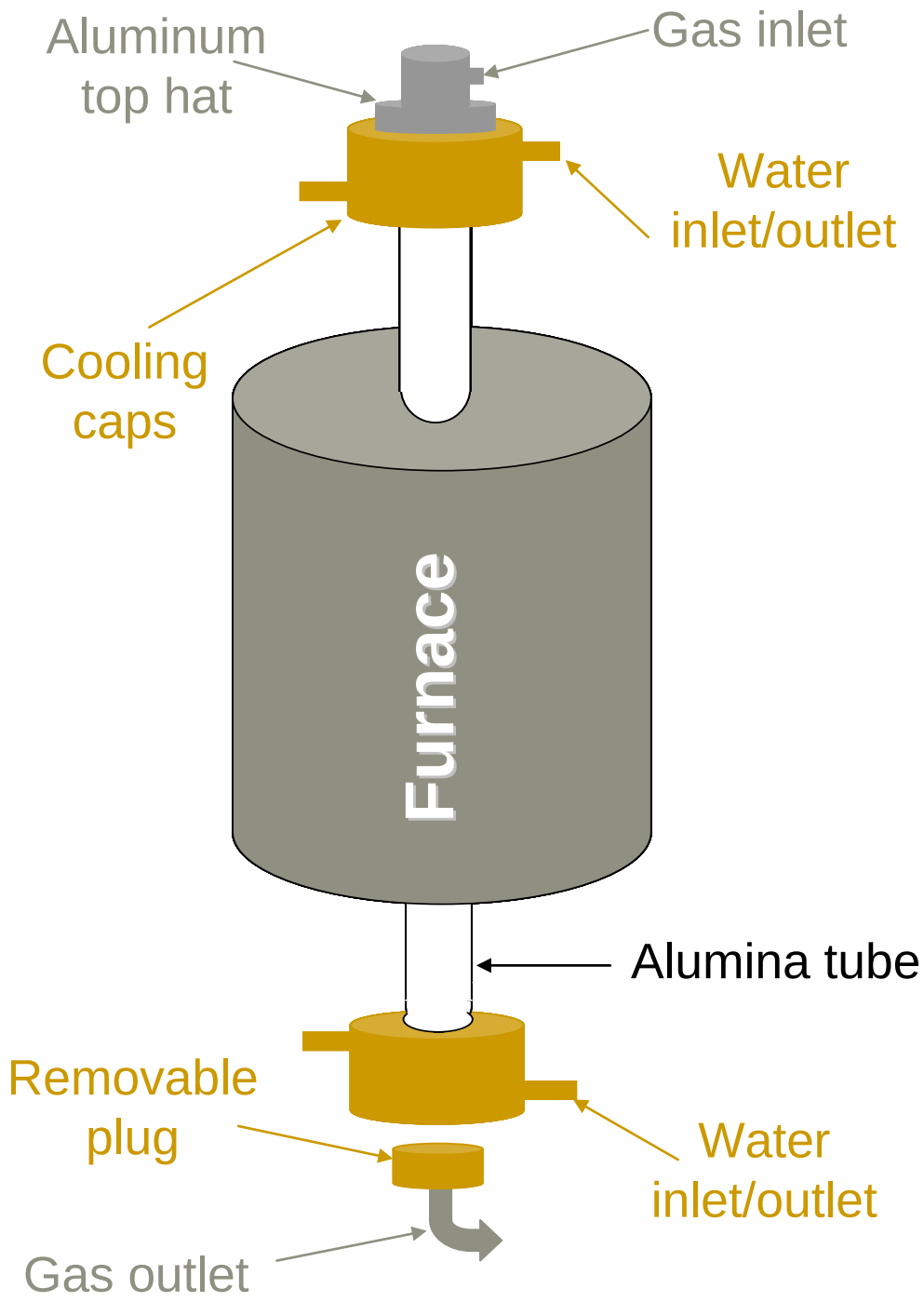

Figure 3-5. Quenching furnace components (Courtesy of Michael S. Kesler)

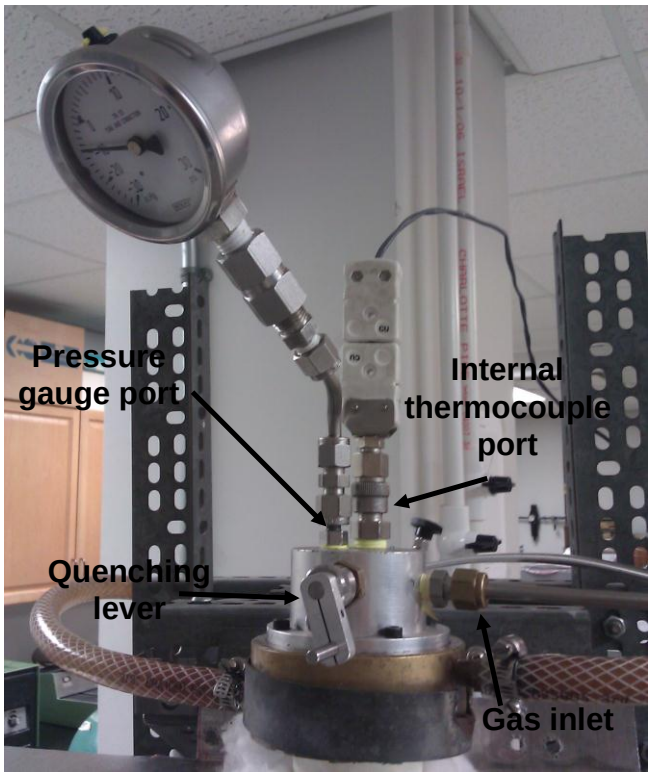

Figure 3-6. Alumina top hat components (Courtesy of Michael S. Kesler)

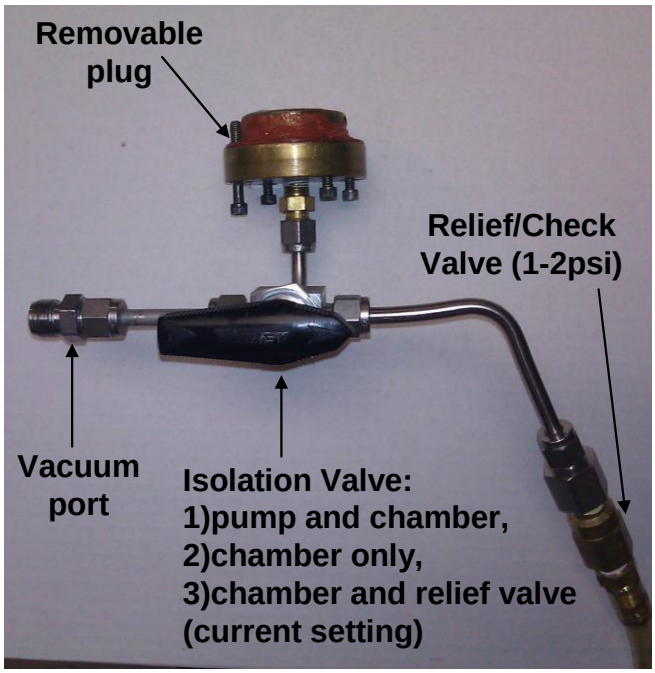

Figure 3-7. Removable plug for pumping/purging, flowing gas relief and drop quenching (Courtesy of Michael S. Kesler)

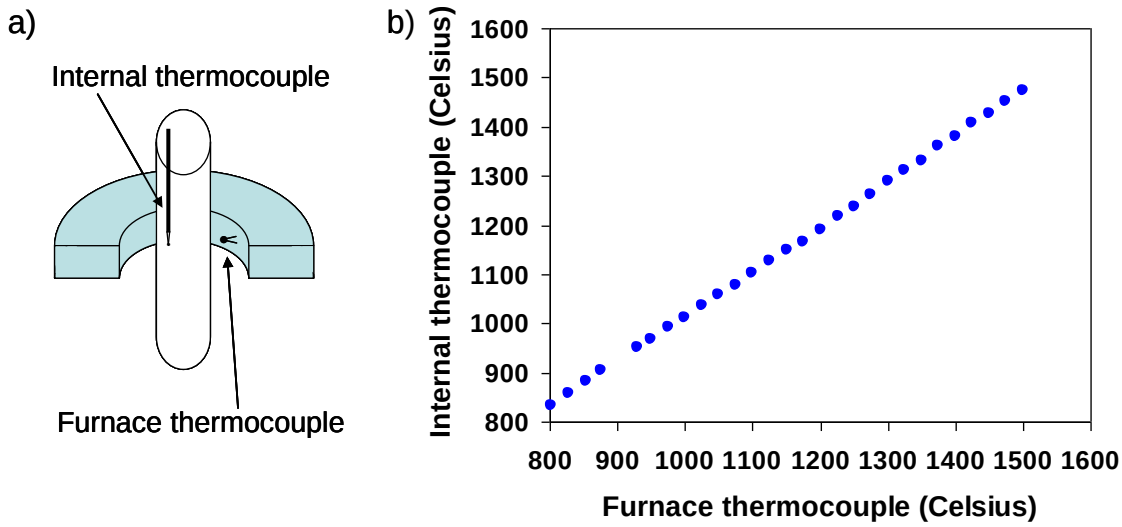

Figure 3-8. Thermocouple position and temperature calibration. a) Schematic of the thermocouple positioning and b) the temperature calibration curve (Courtesy of Michael S. Kesler)

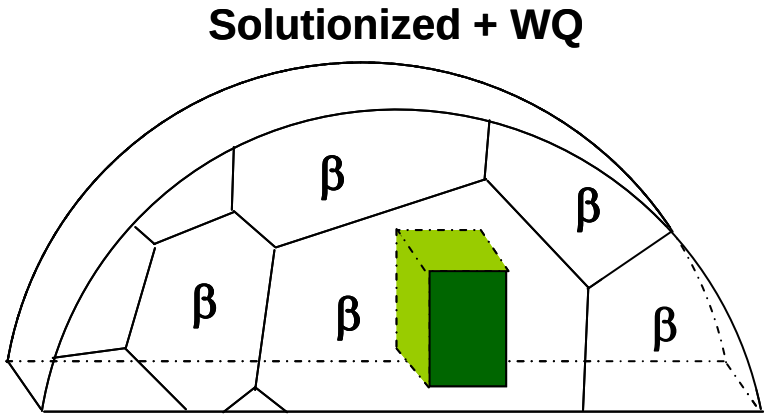

Figure 3-9. Schematic showing where a SX compression sample was cut from a soln+WQ slice (Courtesy of Michael S. Kesler)

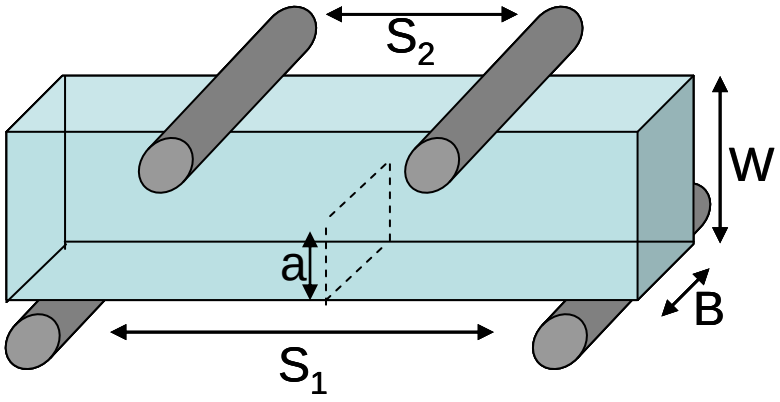

W = 4mm
a = 2mm
a/W= 0.5
B = 2mm
S1 = 20mm
S2 = 10mm

Figure 3-10. Schematic of bending test setup and nominal dimensions (Courtesy of Michael S. Kesler)

CHAPTER 4
MICROSTRUCTURAL EVOLUTION OF TWO-PHASE γ+σ ALLOYS

The goal of the work presented in this chapter was to select alloys that, when heat treated, produce a quenched-in single β-phase which could then be aged resulting in the target microstructure of ultra-fine γ grains with a low volume fraction of nano-sized σ particles distributed along the γ-phase grain boundaries.

Ternary alloys which have been shown to solidify and cool as the β-phase, have high Nb concentrations which promote the stabilization of the β-phase, but also result in high volume fractions (>60vol%) of the σ-phase[14-16, 56]. Although these alloys have excellent high temperature strength, the room temperature toughness is poor (~4-6MPam^{½}) and there is no plastic deformation prior to fracture under uniaxial compression [55]. This work, along with previously published work [63], will show that ternary alloys selected to yield low volume fractions (<30vol%) of the σ-phase do not exhibit a quenched-in single β-phase microstructure. To address this issue, a β-stabilizer, Cr, was added to alloys in order to aide in the retention of the β-phase upon quenching to room temperature. The effectiveness of stabilizing the β-phase upon quenching was dependent on the overall alloy composition.

4.1 Alloy Selection

4.1.1 Ternary Alloys

Two-phase γ+σ alloys were identified by choosing compositions based on ternary Ti-Al-Nb phase diagram at the proposed use temperature which lie in the γ-σ phase field at 800-1000ºC. Figure 4-1a and Figure 4-1b show a recently calculated 1000ºC isothermal section and the liquidus projection, respectively [64]. For all alloys, a

constant Al-content of 45at% was selected to conserve oxidation resistance, as discussed in Chapter 2 and the green line represents 45at%Al (Figure 4-1). Furthermore, the result of moving along the constant Al line is a change in σ-phase volume fraction. The blue line represents a constant volume percent line of 30vol%σ at 1000ºC and the volume percent of the σ-phase lessens when moving to the right of this line. The red line overlaid on the liquidus projection represents the β-solidus line and compositions to the left of this line solidify as 100% β-phase. These lines define the constraints in selecting γ+σ alloys which solidify as a single β-phase and result in a low volume fraction of the σ-phase upon aging. Thus, the selections of Alloys 11 and 12, with respective nominal compositions of Ti-45Al-18Nb and Ti-45Al-27Nb, were made to begin this study and they are marked with black dots along the green constant Al line in Figure 4-1.

4.1.2 Alloys with β-stabilizer Additions

The necessity of stabilizing of the β-phase for the purpose of quenching-in the phase to room temperature will be apparent based on the results and analysis from the as-cast and solutionized conditions of the ternary alloys (presented in sections 4.2 and 4.3). There are several alloying elements that are known to stabilize the β-phase, including Mo, Si, Ta, W and Cr [47-51]. Furthermore, there are factors to consider when choosing an alloying element, such as the degree of stability imparted on the β-phase, the effect on the melting point, the density, the effect on creep, the effect on ductility and possible adverse phase formation. For the purposes of this study, Cr was selected because it is one of the stronger β-stabilizers and it is not known to introduce adverse phases to this system in small concentrations [65]. 5at%Cr was chosen for each alloy

based on theoretical calculations that show the β-stabilizing effect of this element diminish above this concentration [66]. Also, 1at%Mo was added to some alloys for the purpose of phase stability of the γ+σ microstructures. Because of the importance of minimizing the weight of these alloys, Cr and Mo were added in place of Nb to offset the addition of these comparably heavy elements. The selection of Alloys 12.5CrMo and 13CrMo, of nominal compositions Ti-45Al-18Nb-5Cr-1Mo and Ti-45Al-14Nb-5Cr-1Mo, were based on the ternary phase diagram and will be elaborated upon in section 4.6.4.

In the following sections, the results from select alloys in the as-cast condition and all alloys in the soln+WQ and aged conditions will be presented and the approach and challenges in producing these microstructures will be discussed.

4.2 As-cast Microstructures

The alloys presented in this section were designed based on theoretical calculations to identify alloys that solidify as a single β-phase and lie in the γ+σ two-phase region at and above the proposed use temperature range from 800-1000ºC. Due to a lack of experimental data from the central region of this ternary system, confirmation of the theoretical work has been conducted through microstructural evaluation and XRD.

The solidification of Alloy 11 [67] has been shown to result in a microstructure with coarse columnar grains (~200-500μm in width) and a dendritic structure as seen in Figure 4-2a and Figure 4-2c, respectively. Figure 4-2b reveals evidence of a solid state transformation with a Widmanstätten-like morphology emanating from the columnar boundaries. The phases present in the as-cast condition as measured by XRD (Figure 4-3) were large amounts of the β and γ phases and possible trace amounts of the meta-

stable Orthorhombic-phase which commonly forms upon rapid cooling of the β-phase [68-70]. A typical BSE micrograph of the as-cast microstructure is shown in Figure 4-2d, wherein the darker phase is the γ-phase and the lighter phase is the β-phase. An in-depth high temperature XRD study of this alloy, reported by Rios [59, 63], resulted in the identification of a single β-phase at high temperature. Prior to this finding, an alloy of this composition was calculated to initially solidify as the γ-phase [71], though these results provide strong evidence that there exists a single β-phase at high temperature.

The addition of 5at%Cr substituted for Nb in this alloy was shown to result in a similar microstructure when compared with as-cast Alloy 11. The large columnar grains (~100-400μm in width) with Widmanstätten growth emanating from the grain boundaries are shown in Figure 4-4a and Figure 4-4b, respectively. The XRD profile in Figure 4-5 shows both the β and γ phases, though when comparing the intensity ratios of the peaks in alloy 11 and 11Cr there appears to be a greater amount of β-phase present in the Cr-containing alloy.

Alloy 12, in the as-cast condition, consisted of coarse columnar grains (~100-400μm in width) as shown in Figure 4-6a. A possible dendritic structure is evidenced by regions of high and low Z-contrast shown in the BSE image in Figure 4-6b. Figure 4-6c reveals a two-phase microstructure and the XRD profile from this sample, given in Figure 4-7, identifies these phases as γ and σ, which is consistent with the predictions based on the equilibrium phase diagram for this alloy at low temperatures [64, 71, 72]. The σ-phase, which contains a higher Nb content, appears as the lighter phase, while the γ-phase appears as the darker phase in the BSE images. Although there is a relatively high volume fraction of the σ-phase, the peak intensity in the XRD profile is

low. This is commonly observed for the σ-phase even when present in significant volume fraction [73]. The presence of the columnar grains and the dendritic growth, as shown in Figure 4-6a and Figure 4-6b, respectively, imply that this alloy initially solidified as a single phase. The Widmanstätten morphology of the γ-phase confirms that this phase developed through a solid-state phase transformation. Consequently, this alloy could not have solidified as the γ-phase as predicted by several computational studies [71, 72]. More recent optimization of the Ti-Al-Nb phase diagram (Figure 4-1) suggests that indeed this alloy lies in the field with primary β-phase solidification [64, 65]. Based on this analysis, it is suggested that Alloy 12 solidifies as single β-phase and transforms to the γ and σ phases upon cooling.

Alloy 12+Cr, of nominal composition Ti-45Al-22Nb-5Cr, exhibited large columnar grains with a two-phase microstructure similar to that of Alloy 12, as shown in Figure 4-8. However, the analysis of the XRD profile (Figure 4-9) revealed that the phases present in this alloy are β and γ. The β-phase, which appears as the lighter phase, is observed to be the matrix from which the γ-phase evolved. The presence of the β-phase matrix in this coarse columnar grained microstructure at room temperature suggests it is not only the single high temperature phase, but that the addition of Cr in place of Nb has stabilized this phase to some extent. The effect of Cr will be discussed further in section 4.5.1.

The as-cast microstructures of both alloys 11 and 12 exhibited extensive γ-phase formation, though the σ-phase is only present in Alloy 12. This was attributed to the significantly higher Nb-content in Alloy 12 (27at% in Alloy 12 vs. 18at% in Alloy 11) which is the major constituent of the σ-Nb_2Al phase. As discussed in detail by Goyel

[67], a high driving force must be attained in order to nucleate the σ-phase in Alloy 11. While the σ-phase is expected to be present based on the calculated phase diagram [65], the complex crystal structure in combination with the diffusion-controlled nucleation of this phase retard this process [74, 75].

4.3 Solutionized + Water Quenched Condition

The above analysis in section 4.2, which suggests the presence of a single β-phase upon solidification of these alloys, leads to the next stage in alloy development. The identification of transformation temperatures through DTA was used to select a solutionizing temperature in the expected single β-phase region. Because of the varying composition from alloy to alloy, the temperature range where the β-phase exists varies, so a specific solutionizing temperature was selected for each alloy. These data will be presented along with the resulting microstructures from soln+WQ experiments.

4.3.1 Determination of Solutionizing Temperatures

The results of the DTA measurements conducted on the as-cast ternary alloys, Alloys 11 and 12, are shown in Figure 4-10 and 4-11, respectively. The gray curve in Figure 4-11 represents the initial heating cycle from RT and the black curve represents the third cycle to ensure consistency in transformation temperatures. DTA curves for both alloys level off approaching the apparent baseline above 1450ºC. The baseline refers to near-linear portions of the curve where thermal events are limited to the heat flow from the sample and reference in the absence of a reaction. This is evidence of a single phase. When two or more phases are present over a temperature range, the curve will often have a slope or a curvature due to changing volume fractions and coarsening effects, but when the curve is consistent with the slope of the baseline, then

limited thermal events are taking place. Based on this analysis, a solutionizing temperature of 1500ºC was chosen for the ternary alloys.

The DTA plots for Alloys 11Cr and 12Cr are shown in Figure 4-12 and Figure 4-13, respectively. Upon the addition of 5at%Cr, the single phase region extends to lower temperatures and both alloys appear to have a single phase above 1350ºC. The solutionizing temperature for alloys with Cr addition was selected to be 1400ºC. Because of the similarity in the lower temperature range of the single phase region in these two alloys, all subsequent selected alloys were solutionized at 1400ºC. The assumption that the remaining alloys were in the single phase region at 1400ºC was based on the fact that the remaining compositions are all along the 45at%Al line and consist of compositions which lie between Alloys 11Cr and 12Cr. The selection of composition of the remaining alloys will be discussed in section 4.4.

4.3.2 Microstructural Analysis of Soln+WQ Alloys

The goal of the soln+WQ heat treatments is to solutionize single β-phase and fully retain this phase upon water quenching to room temperature. The two ternary alloys selected, Ti-45Al-18Nb (Alloy 11) and Ti-45Al-27Nb (Alloy 12), to start this study were used as reference points for further alloying and for developing other alloys.

Alloy 11 [67] was solutionized at 1500ºC and held for 1 hour before water quenching. Figure 4-14a shows the resulting microstructure consists of large equiaxed grains on the order of millimeters (~0.5-4mm) which confirm that a single phase was present at 1500ºC and grain growth occurred. The BSE image in Figure 4-14b displays a two-phase microstructure and the XRD profile (Figure 4-15) along with volume fraction measurements determined that this sample consists of ~90vol% γ-phase and ~10vol%

β-phase [67]. The elongated γ-phase (darker phase in Figure 4-14b) formed by a rapid solid-state transformation upon water quenching leaving remnants of the β-phase (lighter phase in Figure 4-14b) sandwiched between the γ-phase. The parent phase was definitively determined to be the β-phase despite the high volume fraction of the γ-phase in the quenched structure [59, 63]. The meta-stable Orthorhombic-phase was detected in this sample and among other samples to follow, but this phase dissolves upon aging and it was not found in the samples that were used in mechanical testing.

As a result of the inability to quench-in the β-phase in Alloy 11, 5at%Cr was added in place of Nb and, thus, the alloy will be identified as Alloy 11Cr [67]. The soln+WQ microstructure, after holding at 1400ºC for 1 hour, is shown in Figure 4-16a to have large equiaxed grains of the same scale as Alloy 11. The difference between the soln+WQ microstructures of these alloys is apparent when viewing Alloy 11Cr at higher magnification under BSE imaging (Figure 4-16b). A tweed-like structure, finer than that observed in Alloy 11, made up of the β-phase with Orthorhombic needles is pervasive throughout the grains [67]. The XRD profile in Figure 4-17 shows relatively high intensity peaks for the β and Orthorhombic phases, but only trace peaks for the γ-phase. The γ-phase is observed to be at the β grain boundaries forming in a Widmanstätten-like morphology. The addition of Cr resulted in nearly full retention of the β-phase upon quenching.

The soln+WQ microstructure of Alloy 12 consists of coarse equiaxed grains on the order of millimeters (~0.5-4mm) and a two-phase microstructure (Figure 4-18a and Figure 4-18b, respectively) consisting of ~80vol% γ-phase and ~20vol% β-phase. Similar to Alloy 11, in this alloy the β-phase rapidly transforms to the γ-phase upon

water quenching. With the addition of 5at%Cr to Alloy 12, a single β-phase was quenched-in to room temperature with no evidence of the γ-phase. The resulting microstructure, shown in Figure 4-20a and Figure 4-20b, shows large equiaxed β grains with clean grain boundaries and the BSE micrograph with only one phase present. Furthermore, the XRD data in Figure 4-21 detected β-phase peaks only. Alloy 12Cr was the only alloy in this study which did not exhibit detectable γ-phase formation upon quenching.

Alloys 12.5CrMo and 13CrMo both exhibited soln+WQ microstructures consisting of large equiaxed grains with significant γ-phase formation at the β-phase grain boundaries (Figure 4-22 and Figure 4-24, respectively). Similar to that of Alloy 11Cr, the XRD profiles of these two remaining alloys (Figure 4-23 and Figure 4-25) show primarily the β and Orthorhombic phases.

4.4 Aged Condition

The goal of aging experiments in this study was to precipitate two-phase γ+σ microstructures from the parent β-phase which had been quenched-in to room temperature. The importance of achieving a meta-stable parent phase lies in the ability to control the precipitation of the phases in the targeted microstructure. One of the focuses of this study is the role of microstructural scale on mechanical properties, so taking advantage of the high driving force for nucleation in the meta-stable parent phase allows for the possibility of controlling the number of nuclei by aging temperature and/or coarsening existing precipitates. In order to determine the temperature range where the two-phase γ+σ microstructure is stable, DTA experiments were conducted on soln+WQ samples and aging heat treatments were designed to aide in the analysis of DTA data.

4.4.1 Determination of the Aging Temperature Range

The study begins with Alloy 12Cr, the only alloy that was able to retain a single β-phase after quenching to room temperature. The DTA curve in Figure 4-26a was generated by heating a soln+WQ sample of 12Cr through the expected two-phase γ+σ region. Upon heating, two possible precipitation transformations were identified by the exothermic peaks between approximately 510ºC and 848ºC. At approximately 1161ºC, an endothermic peak suggesting dissolution is observed. Thus, establishing the aging temperature range as between 848ºC and 1161ºC could be undertaken and this was done by aging Alloy 12Cr at 865ºC, 1050ºC and 1200ºC, then water quenching. The microstructures that resulted from these heat treatments in coordination with the XRD profiles are shown in Figure 4-27. The samples aged at 865ºC and 1050ºC both appear to have two-phase microstructures when observing the BSE micrographs in Figure 4-27a and Figure 4-27b and both of the XRD profiles (Figure 4-27d and Figure 4-27e) reveal γ-phase and σ-phase peaks, but not the signature β-peak at 2θ ~ 40º. Whereas, the BSE micrograph in Figure 4-27c shows three distinct contrasts and the XRD profile yielded peaks from β, γ and σ phases after heat treating at 1200ºC. This confirms the temperature range of the two-phase γ+σ region upon aging above the suspected precipitation peaks and the reemergence of the β-phase at the onset of the endothermic peak above ~1150ºC.

When aging for mechanical testing, ideally all of the alloys would be aged at the same temperatures, so the two-phase γ+σ region for the alloy selected to have the highest expected volume fraction of the σ-phase (Alloy 12Cr) would have to overlap with the alloy with the lowest expected volume fraction of the σ-phase (Alloy 13CrMo).

Figure 4-26b shows the DTA curve generated from a sample of soln+WQ Alloy 13CrMo. The curve shows two low temperature peaks between 544ºC and 855ºC which are assumed to be correlated with precipitation and the onset of an endothermic peak at 1067ºC. Based on this analysis, the two-phase region for this alloy likely lies between 855ºC and 1067ºC. The overlap of the two-phase region for these two alloys allows for aging to be conducted at the same temperatures.

4.4.2 Microstructural Analysis of Aged Alloys

Soln+WQ samples of Alloy 12Cr were aged in a box furnace at 865ºC and 1050ºC for 2 hours and then furnace cooled over night to room temperature. Figure 4-28a and Figure 4-28b displays the respective microstructures which appear identical to the microstructures of the samples that were quenched from the aging temperature shown in section 4.4.1. The BSE micrographs in Figure 4-28c and Figure 4-28d are higher magnification images of the respective two-phase $\gamma+\sigma$ microstructures. The sample that was aged at 1050ºC exhibits a noticeably the coarser microstructure, though the volume fractions of the σ-phase in both microstructures were measured to be ~30%. Quantitative measurements were taken from these microstructures, as outlined in section 3.4.6. Microstructural parameters for all alloys used in mechanical testing are presented in Table 4-1 and the statistical analysis can be found in Appendix A. The morphology of the σ-phase is apparently similar between the two aging temperatures, but because of the coarsening that occurred in Alloy 12Cr-1050, the σ-phase has coalesced to some extent resulting in a connected σ-phase along with some intermittent σ-particles.

Two important observations which were consistent within the microstructures from both aging temperatures should be noted. Firstly, there were larger and smaller features within each microstructure and this is shown in the BSE micrographs in Figure 4-29a and Figure 4-29b which were observed in alloys 12Cr-865 and 12Cr-1050, respectively. The larger features (the darker γ-phase) appear coarse and elongated with a more continuous σ-phase around the perimeter. The finer regions are consistent with the descriptions of the aged microstructures for a given alloy. Secondly, there was Widmanstätten γ-phase emanating from the prior β-phase grain boundaries in both samples and an example of this is shown in Figure 4-30. The formation of coarser γ-phase within the prior β-phase grains and at the prior grain boundaries were likely the result of preferred nucleation sites. Because only the β-phase was detected in the microstructure of the soln+WQ condition of this alloy (Figure 4-20a, Figure 4-20b and Figure 4-21), it is probable that the γ-phase either nucleated upon quenching but did not grow and thus was undetectable by BSE/SEM and XRD, or the nucleation of this phase occurred at the early stages of the aging heat treatments. This finding of the formation of the Widmanstätten γ-phase at the prior β-phase grain boundaries in Alloy 12Cr brings to light the fact that, whether forming upon quenching or upon aging, the γ-phase cannot be stopped from forming at the grain boundaries of polycrystalline samples. Thus, the resulting microstructures from Alloy 12Cr will be consistent with the other alloys, 12.5CrMo and 13CrMo, such that they all have γ-phase formation at the β-phase grain boundaries.

Alloys 12.5CrMo and 13CrMo were aged at 865ºC, 1000ºC, and 1050ºC and the resulting BSE micrographs are shown in Figure 4-31 and Figure 4-32, respectively. The

volume fraction of the phases in Alloy 12.5CrMo was measured to be ~22vol%σ for each aging temperature. Likewise, the volume fraction measurements on Alloy 13CrMo were the same for each aging temperature and were ~13vol%σ. These microstructures coarsen as the aging temperature is increased and the phases appear to be of similar morphology to each other and similar to Alloy 12Cr-865. The coalescence of the σ-particles in Alloy 12Cr-1050 could be the result of the high volume fraction of the σ-phase in that particular alloy. Upon nucleation of the σ-phase, the particles are separated and remain so at an aging temperature of 865ºC, but upon coarsening, some smaller σ-particles dissolve while other larger particles grow along the γ-phase boundaries until they impinge on a neighboring σ-particle.

The final alloy aged for mechanical testing was Alloy 11. The purpose of testing this alloy was to see the effect of a significantly coarser microstructure on room temperature mechanical properties and how this compared with the alloys which quenched-in as nearly 100% β-phase. This ternary alloy exhibited a microstructure which consisted of ~90% γ-phase and ~10% β-phase after soln+WQ (Figure 4-14) and after aging at 1100ºC for 2 hours a coarsened two-phase γ+σ microstructure with ~12vol%σ was formed (Figure 4-33).

4.5 Effect of Composition on Quenching-in the β-phase

Based on these results, the composition of the alloys clearly plays a vital roll in an alloys ability to retain the β-phase upon quenching. In the following subsections the effect of Cr and Al content on the ability to quench-in the β-phase will be discussed.

4.5.1 Effect of Cr Addition

Cr is a strong β-stabilizer and has a maximum solubility limit of less than 5at% in the γ-phase in alloys close to the composition range in this study [76, 77]. The substitution of Nb for 5at% Cr in Alloy 12Cr effectively stabilized the β-phase to the extent that it was retained upon water quenching. This effect can arise from thermodynamic stabilization of the β-phase as well as the inhibition of the nucleation of the γ and σ phases due to partitioning of elements among the phases. Transformation temperatures estimated from DTA data, shown in Table 4-2, reveal that the change in the transformation temperatures for the β↔β+γ reaction were reduced minimally with the Cr additions (from 1349C without Cr to 1330ºC with Cr upon cooling and from 1382ºC without Cr to 1368ºC with Cr upon heating). Therefore, the ability to retain the β-phase from the solutionizing temperature is most likely due to kinetics effects associated with the limited solubility of Cr in the γ-phase. As described by Goyel [67], the nucleation of the γ-phase could not be prevented, but the growth of the γ-phase was limited by the addition of Cr as a result of its partitioning into the β-phase and away from the newly formed γ-phase nuclei. During the rapid cooling rates associated with water quenching, the time for this partitioning process was not sufficient for the growth of the γ-phase to occur. Additionally, the overall temperature range where the β-phase exists in the microstructure with the γ and σ phases (Figure 4-11 and Figure 4-13) has been expanded to lower temperatures which indicates that the addition of Cr has thermodynamically stabilized this phase, but only to a limited extent in the single phase region [73]. It is important to note that the thermodynamic and kinetic effects observed are highly dependent on alloy composition. For example, in Alloy 11 the effect of Cr on

transformation was more significant in the single β-phase region. More details on the effect of Cr on these alloys was reported by Goyel [67].

4.5.2 Effect of Al-content

Controlling Al-content in TiAl-based alloys is difficult due to the vaporization of Al during arc-melting caused by the relatively low melting point of this metal in comparison to the melting points of the other alloying elements. Furthermore, small variations in Al-content can move an alloy into/out of phase fields in the phase diagram in this particular system. Inconsistencies were noticed in the microstructure of some samples from Alloy 12Cr in the soln+WQ condition. Figure 4-34a shows Alloy 12Cr as a fully quenched-in β-phase, while Figure 4-34b shows another button intended to be of the same composition, but extensive formation of the γ-phase at the β-phase grain boundaries as well as in the grain away from the boundary. All conditions of these samples were identical including sample size, solutionizing time and temperature. The soln+WQ experiment was repeated and the same microstructures resulted. EPMA analysis was conducted and the results are displayed on the micrographs for the respective alloys. The ratios of all the elements are consistent except for that of Al. This difference of 0.5at% was consistent throughout the EMPA data and though it is approaching the limit of the accuracy of this technique, the precision of the measurements on each sample exhibit small standard deviation. Furthermore, arc-melting of a new button was undertaken resulting in 44.0at%Al and, again, the γ-phase formed at the boundaries of the solutionized β-phase. The volume fraction of the γ-phase in $\gamma+\alpha_2$ alloys is well known to increase as the Al-content increases [2, 78]. In addition, when increasing the Al-content in the Ti-Al-Nb ternary system (Figure 4-1), the resulting alloy moves in the

direction of increasing volume fractions of the γ-phase and approaches the β-solidus line.

4.6 Controlling Scale and Volume Fraction in Aged Microstructures

In order to understand the effect of scale and volume fraction of phases on mechanical properties of γ+σ alloys, it is necessary to understand the microstructural evolution of the alloys. In addition, microstructures must be developed in a consistent and repeatable manner. Also, understanding the way in which the phases evolve from the meta-stable parent phase is important in achieving these microstructures.

4.6.1 Effect of γ-phase Formation upon Quenching on Microstructural Scale

The existence of the γ-phase in the soln+WQ condition results in a coarser aged microstructure. Figure 4-35a shows the sample of fully quenched-in β-phase in Alloy 12Cr and the resulting fine aged microstructure formed at 865ºC. Conversely, the button which had the higher Al-content and had existing γ-phase inside the grains in the soln+WQ condition yielded a coarsened structure seen in the bottom half of Figure 4-35b. The importance of retarding the growth of the γ-phase in the soln+WQ condition is evident based on the subsequent aged microstructure.

Another issue faced when attempting to quench-in the β-phase is the cooling rate of the sample. In order to insure that samples cooled at the same rate, they must be prepared properly for the quenching process. This entails even and consistent wrapping of the Ta foil along with maintaining similar sample sizes prior to quenching. Figure 4-36 shows an example of two samples taken from the same button of Alloy 12.5CrMo and aged at 1000ºC. These samples had compositions which were identical, though the sizes of the samples were different. The BSE micrograph in Figure 4-36a represents a

sample which quenched-in as β-phase throughout the bulk of the grain and, thus, resulted in the fine, equiaxed microstructure after aging. On the other hand, Figure 4-36b shows a micrograph taken from a larger sample (roughly 1/3 of a button described in Chapter 3) which formed γ-phase upon quenching due to effectively slower cooling rates and resulted in the much coarser non-equiaxed microstructure after aging. It was imperative to stay consistent in sample preparation throughout this study to ensure that the final microstructures were consistent such that the resulting properties would correlate to the appropriate microstructural parameters.

4.6.2 The γ-phase formation at β-phase Grain Boundaries

As previously mentioned in Section 4.4.2, the γ-phase could not be stopped from forming at the β-phase grain boundaries in the Widmanstätten morphology, whether during quenching or aging. This resulted in a coarser microstructure in the vicinity of the prior β-phase grain boundaries in the aged microstructures and an example of a prior boundary of Alloy 13CrMo-1000 is shown in Figure 4-37. The coarsened microstructure at the prior boundary was present in all polycrystalline aged samples and barring grain boundary modification, this phase will inevitably form. This phenomenon will prove to have a detrimental effect on the mechanical properties of polycrystalline samples and will be presented in Chapter 5.

4.6.3 Effect of Aging Temperature on Microstructural Scale

In an attempt to further refine the microstructure of Alloy 12Cr, aging was conducted at lower temperatures near the precipitation peak, as defined by DTA experiments, which in theory would impart a higher driving force for nucleation and yield more nuclei. Samples were aged for 2 hours at temperatures of 500, 600ºC and 800ºC,

then furnace cooled, and are marked with vertical lines in Figure 4-38 on the DTA curve for quenched-in Alloy 12Cr. The resulting microstructures are displayed below the DTA curve in Figure 4-38 and arrows are directed from the respective aging temperatures. The microstructures which formed at 500ºC and 600ºC appear very similar in size and morphology, while the sample aged at 800ºC appears morphologically similar, but, interestingly, it is more refined. The γ-phase appears thicker and generally longer (on the order of 20μm) in the samples aged at 500ºC and 600ºC versus the sample aged at 800ºC where the γ-phase appears more needle-like and rarely reach a length of 20μm. Upon observation at higher magnifications (Figure 4-39a and Figure 4-39b), it became clear that the samples aged at 500ºC and 600ºC, which lie at temperatures well below the second precipitation peak result in a two-phase $\beta+\gamma$ microstructure, where the γ-phase formation, represented by the lower temperature precipitation peak, is the first transformation from the β-phase. The sample aged at 800ºC, a temperature which lies within the higher temperature precipitation peak, reveals a three-phase microstructure (Figure4-39c) consisting of the β and γ phases, along with the σ-phase which nucleated in the β-phase and at the β/γ interfaces. The nearly simultaneous kinetically driven formation of the γ and σ phases out of the meta-stable β-phase prevents the γ-phase from experiencing extensive growth as seen in the samples aged at 500ºC and 600ºC, thus refining the microstructure despite aging at a higher temperature. These experiments, though ineffective in achieving a more refined microstructure compared to the alloys aged at 865ºC, reveal an optimal temperature for obtaining the most refined structure possible by these methods. For achieving the finest microstructure, aging

should be conducted at the lowest temperature where the γ and σ phases can form nearly simultaneously.

Further evidence to support the identification of the phases present in the microstructures at a given aging temperature was gathered by conducting hardness testing using a Vickers diamond indenter. Hardness versus aging temperature is plotted in Figure 4-39d. The hardness measured from samples at 500ºC and 600ºC were 4.8 and 4.7GPa, respectively. At these temperatures, a $\gamma+\beta$ microstructure was believed to be present, though when the aging temperature increases to 800ºC, the incorporation of the harder σ-phase (which resulted in a three-phase $\gamma+\beta+\sigma$ microstructure) became apparent by a slight increase in hardness to a value of 5.0GPa. Aging at a temperature above the two precipitation peaks resulted in the complete dissolution of the β-phase giving way to a two-phase $\gamma+\sigma$ microstructure (Figure 4-28a) resulting in a significant increase in hardness to a value of 6.5GPa. The significant increase in hardness was attributed in large part to the absence of the ductile β-phase at 865ºC, though the increased volume fraction of the σ-phase likely added to the enhanced hardness values as well.

When aging at a temperature (865ºC and 1050ºC) above the peaks shown to represent precipitation of the γ and σ phases, the resulting microstructures coarsen as the aging temperature is increased, as shown in section 4.4.2. A stable microstructure over a range of temperatures is desired due to the thermal cycling that these materials would encounter in a practical application. The plot in Figure 4-40 [65] was generated from phase diagram calculations and it shows how the volume fraction of phases changes with temperature. As the temperature decreases and approaches the aging

temperatures employed in this study, the volume fraction lines for the γ and σ phases become nearly vertical, which means there is a limited change in volume fraction below approximately 1100ºC. The predicted vol%σ for the ternary alloy, Alloy 12, aged at 865ºC and 1050ºC were calculated to be 30% and 27%, respectively, which is similar to the measured volume fractions in Alloy 12Cr (~30vol%σ in each sample after aging at 865ºC and 1050ºC). Because there is no information on the quaternary phase diagram for Alloy 12Cr, the closest approximations that can be made were to compare to the results of the ternary phase diagrams for the base alloys (Alloy 12) with the alloys with minor alloying additions. The consistent volume fraction of phases observed over the temperature range from 865ºC to 1050ºC is a promising result for microstructural stability for these alloys. Additionally, for the purposes of this study, microstructures of varying scale could be compared while maintaining an approximately constant volume fraction.

4.6.4 Effect of Nb-content σ-phase Volume Fraction

Previous work [15, 16, 29, 55, 56] has shown that in an alloy of nominal composition Ti-40Al-27Nb, the high volume fraction of the σ-phase (60-65vol%σ) resulted in poor mechanical properties at room temperature, so an effort was made to reduce the σ-phase volume fraction to much lower amounts. This was accomplished to some extent with the selection of Alloy 12Cr by increasing the Al-content (from 40 to 45at%) which promotes the formation of the γ-phase and, thus, would reduce the amount of the σ-phase in the microstructure. Any increase in Al-content, beyond 45at% Al, to further reduce the σ-phase volume fraction, would produce an alloy that would fail to meet other requirement set out for this study At the higher Al-content, the alloy

cannot be heat treated to quench-in the β-phase due to rapid formation of the γ-phase upon cooling. Therefore, the approach for varying the volume fractions from alloy to alloy was to incrementally vary the Nb-content due to this elements roll in the formation of the σ-(Nb_2Al)-phase. The 1000ºC isothermal section of the ternary phase diagram is shown again in Figure 4-41 and the three main alloys used for mechanical testing are marked along the constant Al-content line and at the respective Nb-contents. Despite the additions of Cr and Mo to these alloys, the ternary phase diagram has proven to be a viable reference point for predicting volume fractions. In addition, the incremental changes in Nb-content were an affective means of systematically varying the σ-phase volume fraction.

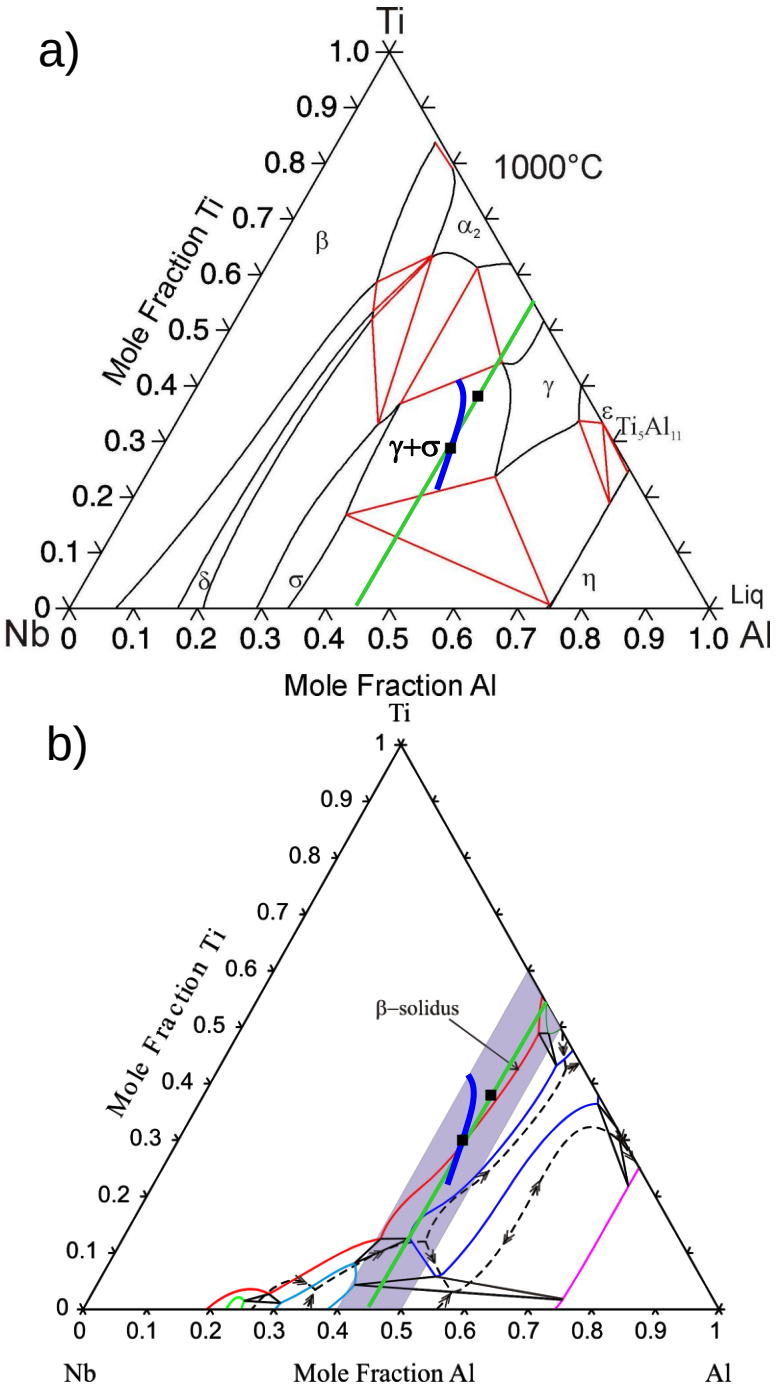

Figure 4-1. TiAlNb phase diagrams. a) The 1000ºC isotherm of the Ti-Al-NB ternary system highlighting the two-phase γ+σ region with alloys 11 and 12 marked at the respective nominal compositions, and b) the liquidus projection with overlain with the β-solidus line showing alloys 11 and 12 solidifying as a single β-phase according to recently calculated phase diagrams (Courtesy of Damian Cupid, Ph.D Dissertation, University of Florida, Gainesville, Fla., 2009.)

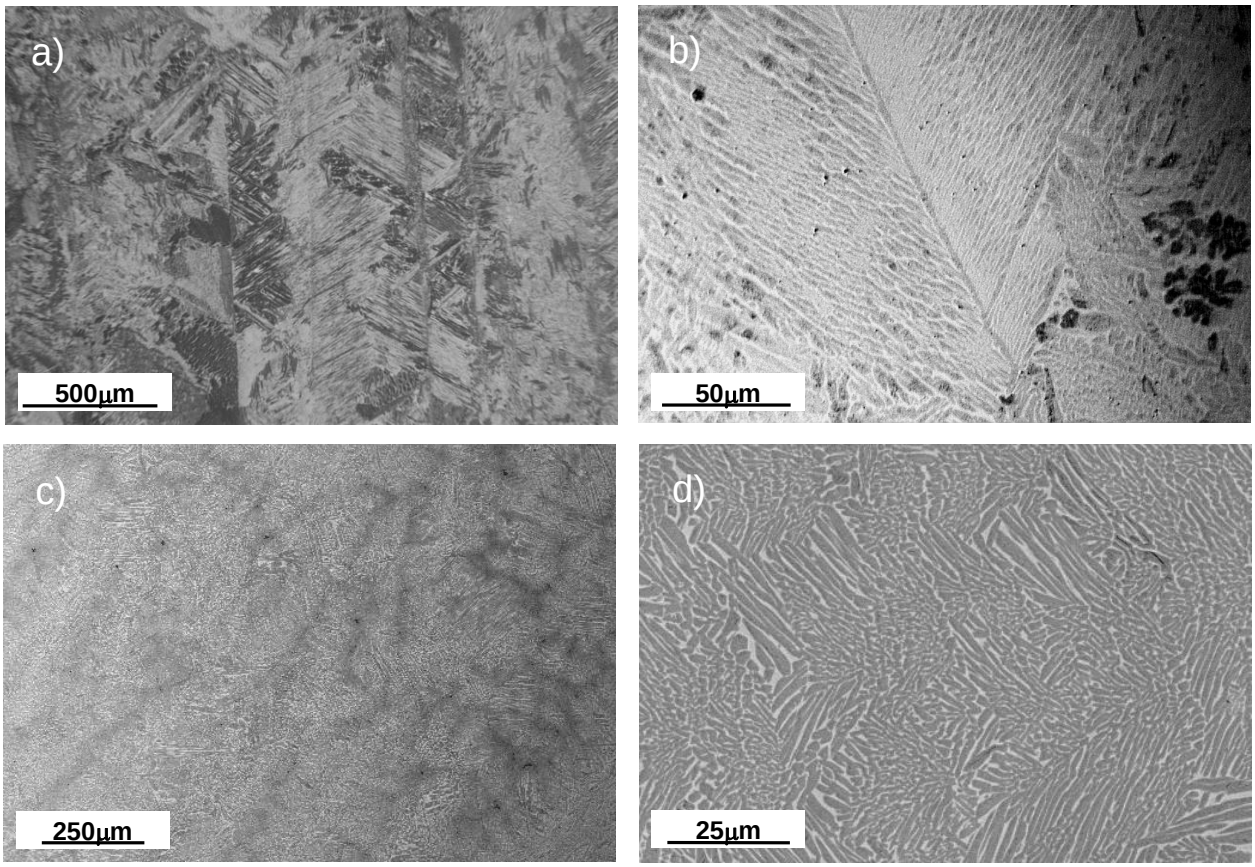

Figure 4-2. Micrographs of as-cast Alloy 11 showing a) large columnar grains (OM); b) Widmanstätten formation at the columnar grain boundaries(OM); c) apparent dendritic growth(BSE); and d) the two-phase $\beta+\gamma$ microstructure(BSE) (Courtesy of Michael S. Kesler and Sonalika Goyel)

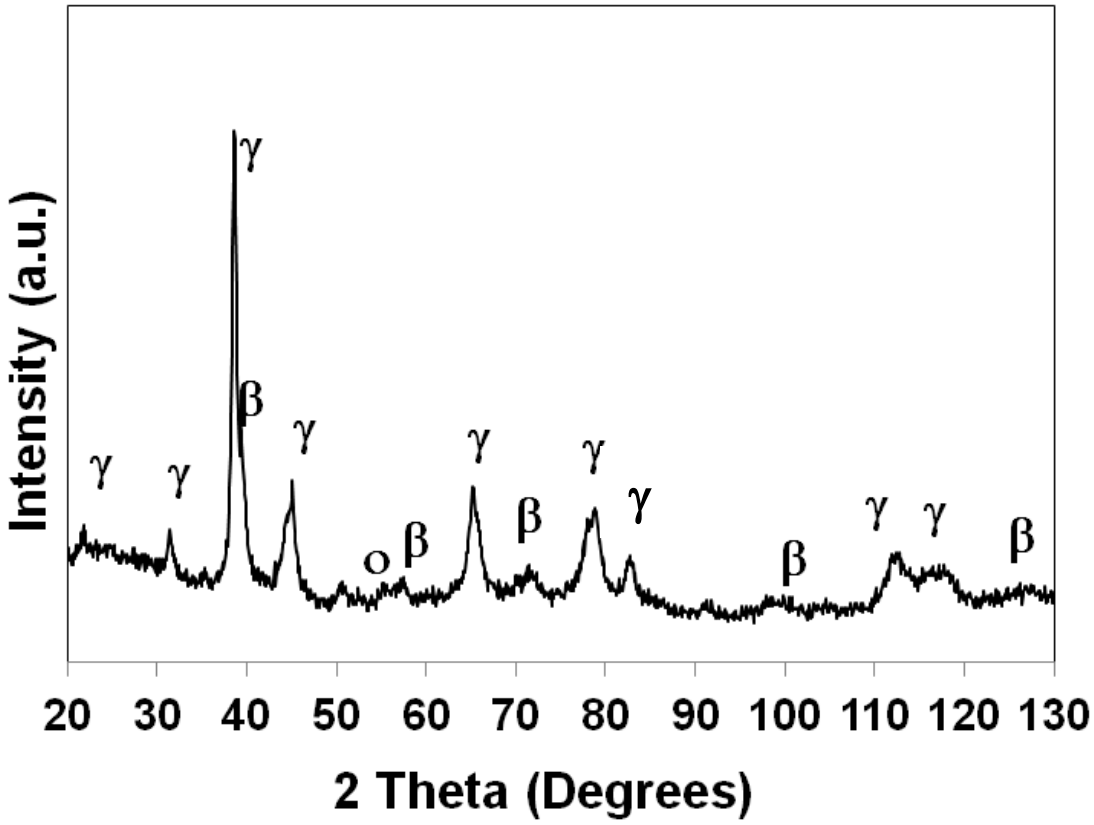

Figure 4-3. The XRD profile of Alloy 11 in the as-cast condition (Courtesy of Michael S. Kesler and Sonalika Goyel)

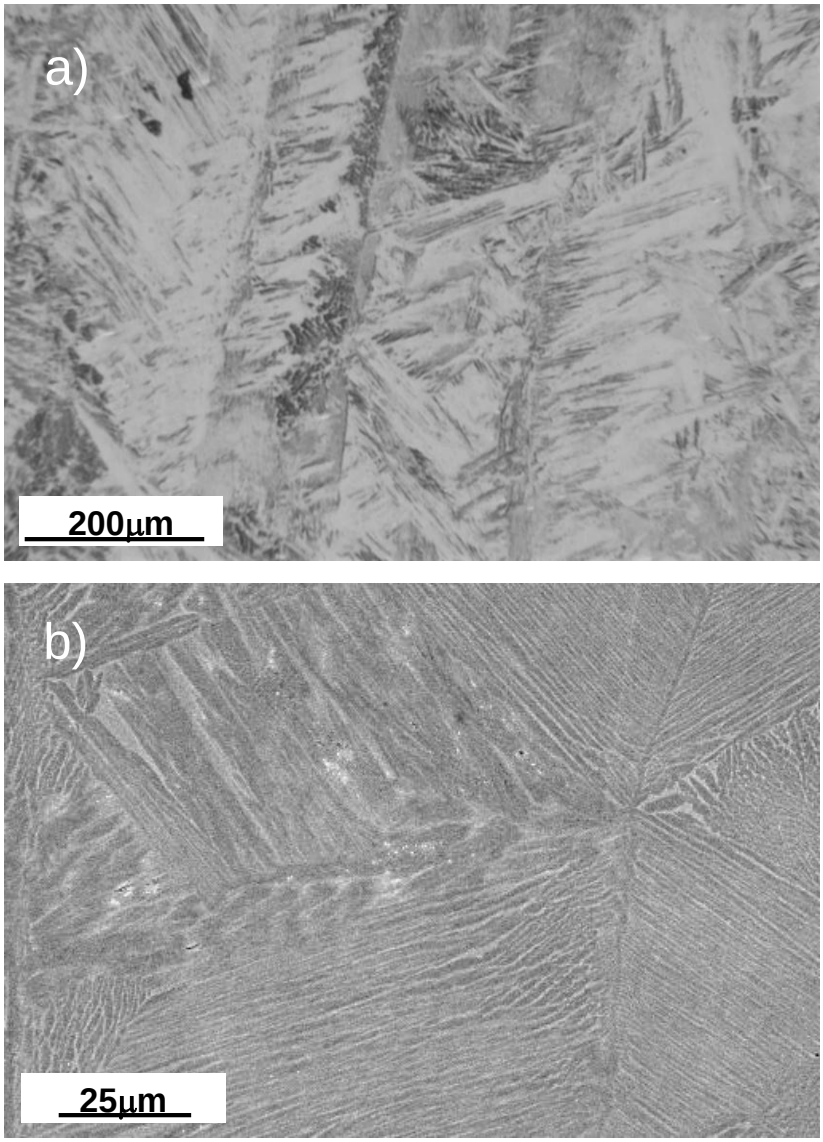

Figure 4-4. Micrographs of as-cast Alloy 11Cr displaying a) large columnar grains (OM); and b) the two-phase β+γ microstructure (BSE) (Courtesy of Michael S. Kesler and Sonalika Goyel)

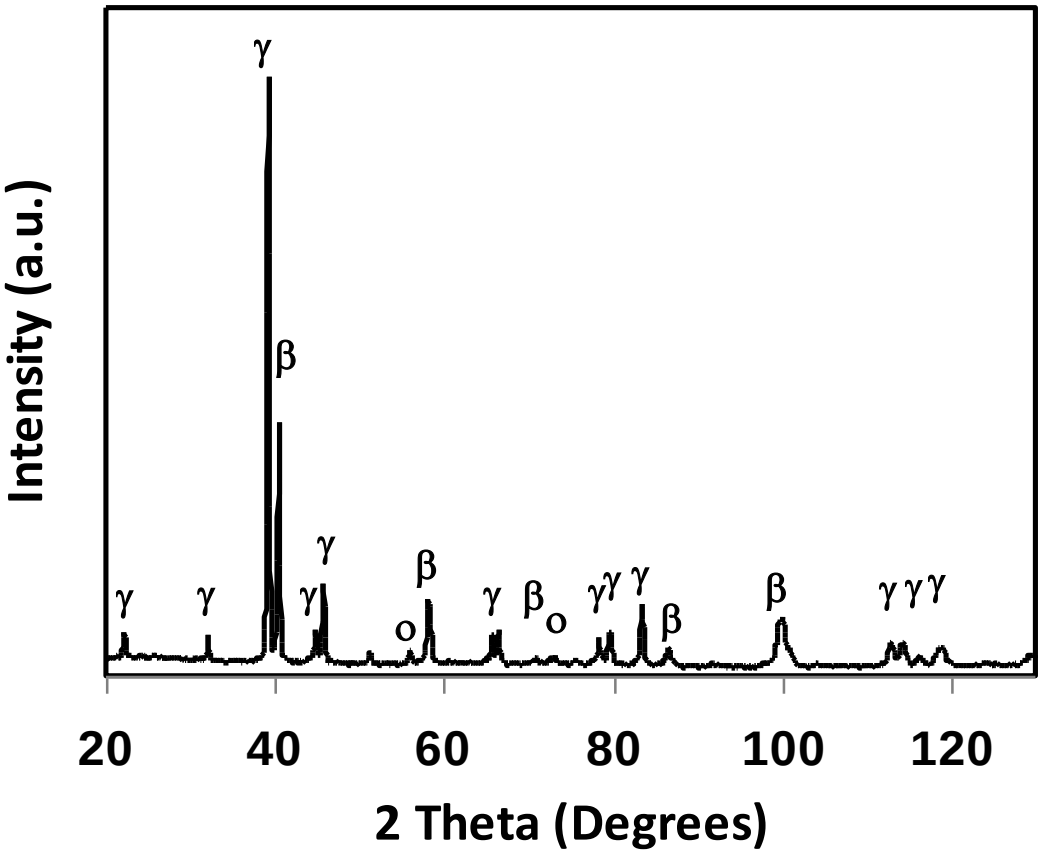

Figure 4-5. The XRD profile of Alloy 11Cr in the as-cast condition (Courtesy of Michael S. Kesler and Sonalika Goyel)

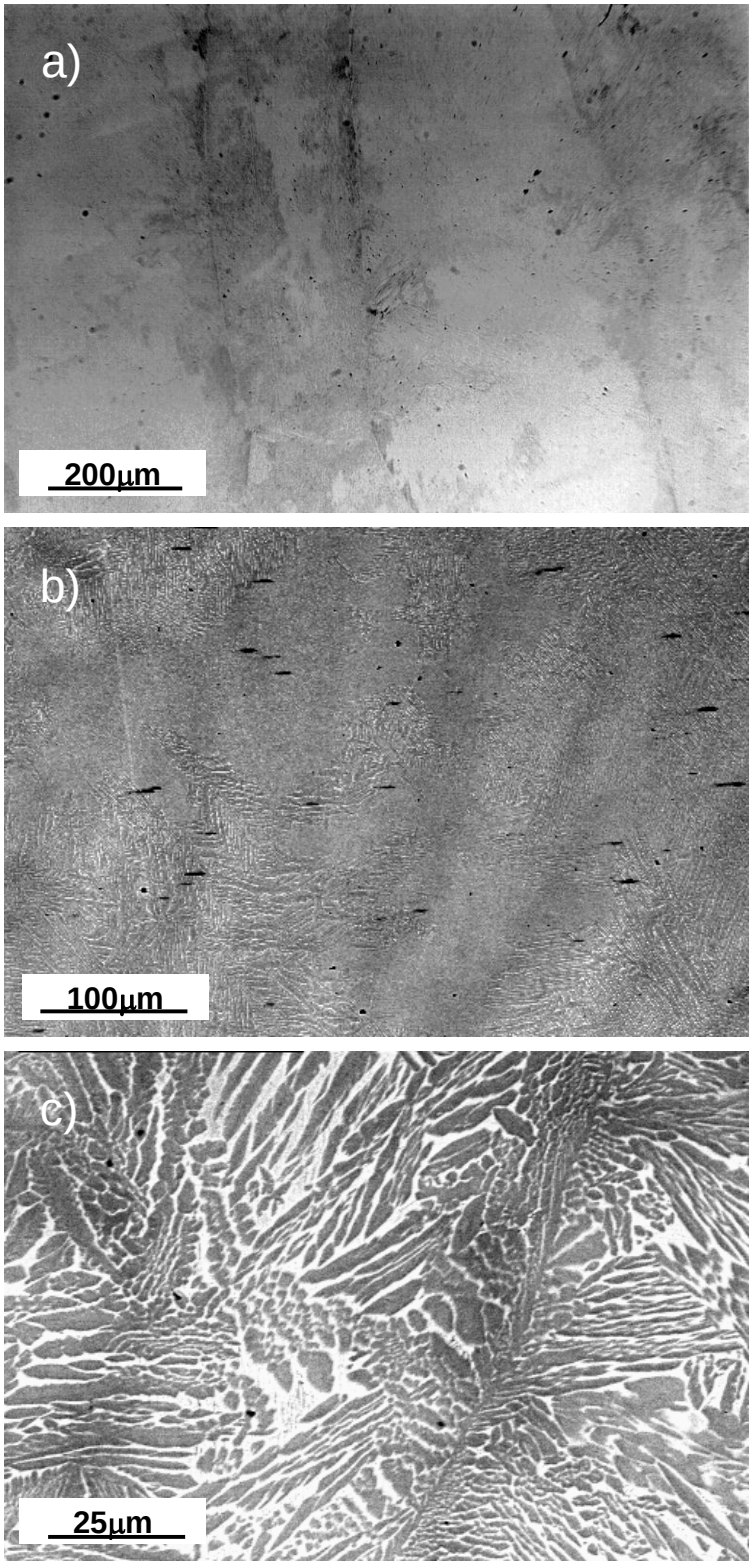

Figure 4-6. Images of as-cast Alloy 12 displaying; a) columnar grains (OM); b) coarse dendritic structure (BSE); and c) the two-phase microstructure (BSE) (Courtesy of Michael S. Kesler)

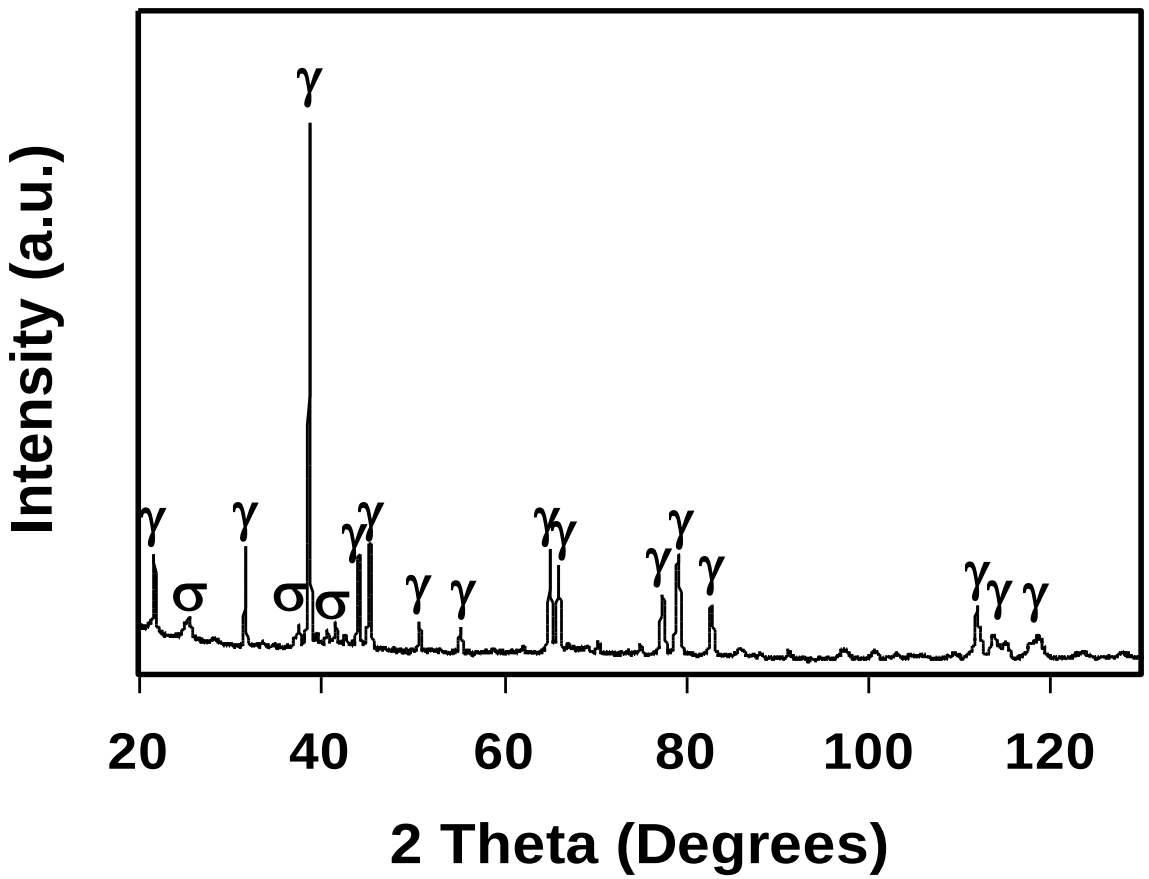

Figure 4-7. The XRD profile of Alloy 12 in the as-cast condition (Courtesy of Michael S. Kesler)

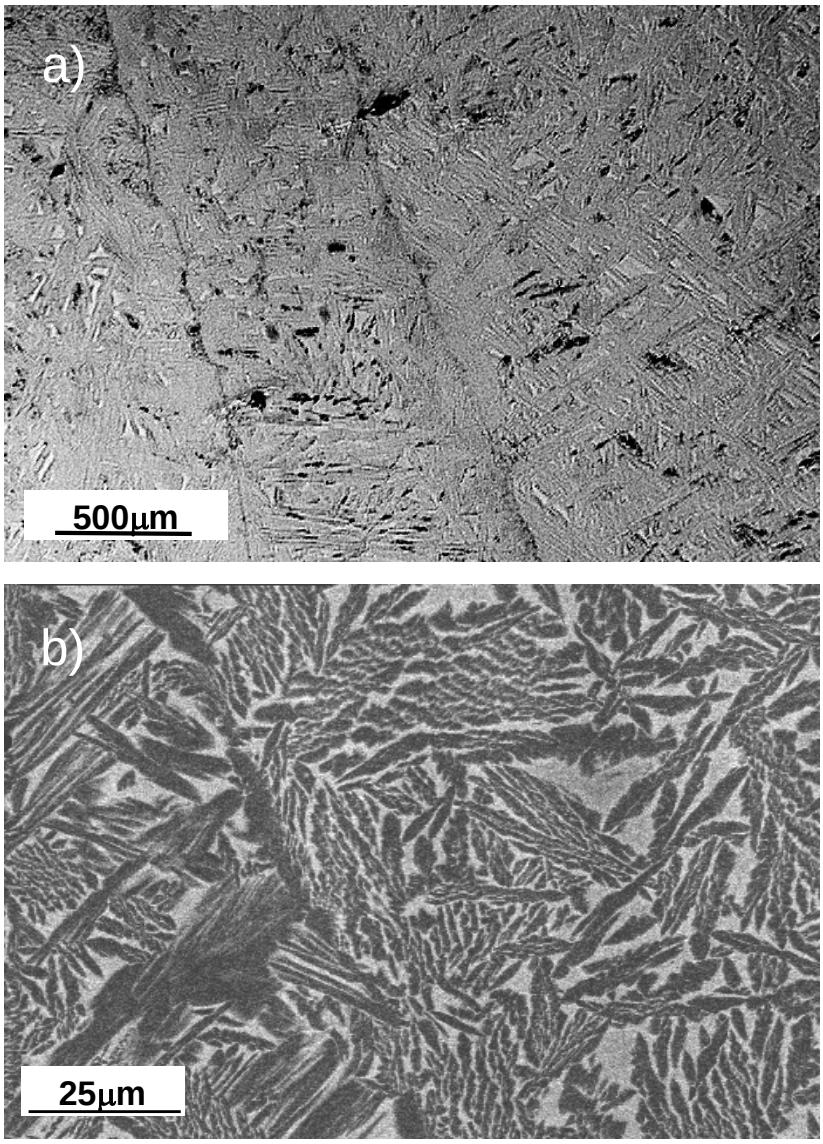

Figure 4-8. Images of as-cast Alloy 12Cr displaying; a) columnar grains (OM); and b) the two-phase microstructure (BSE) (Courtesy of Michael S. Kesler)

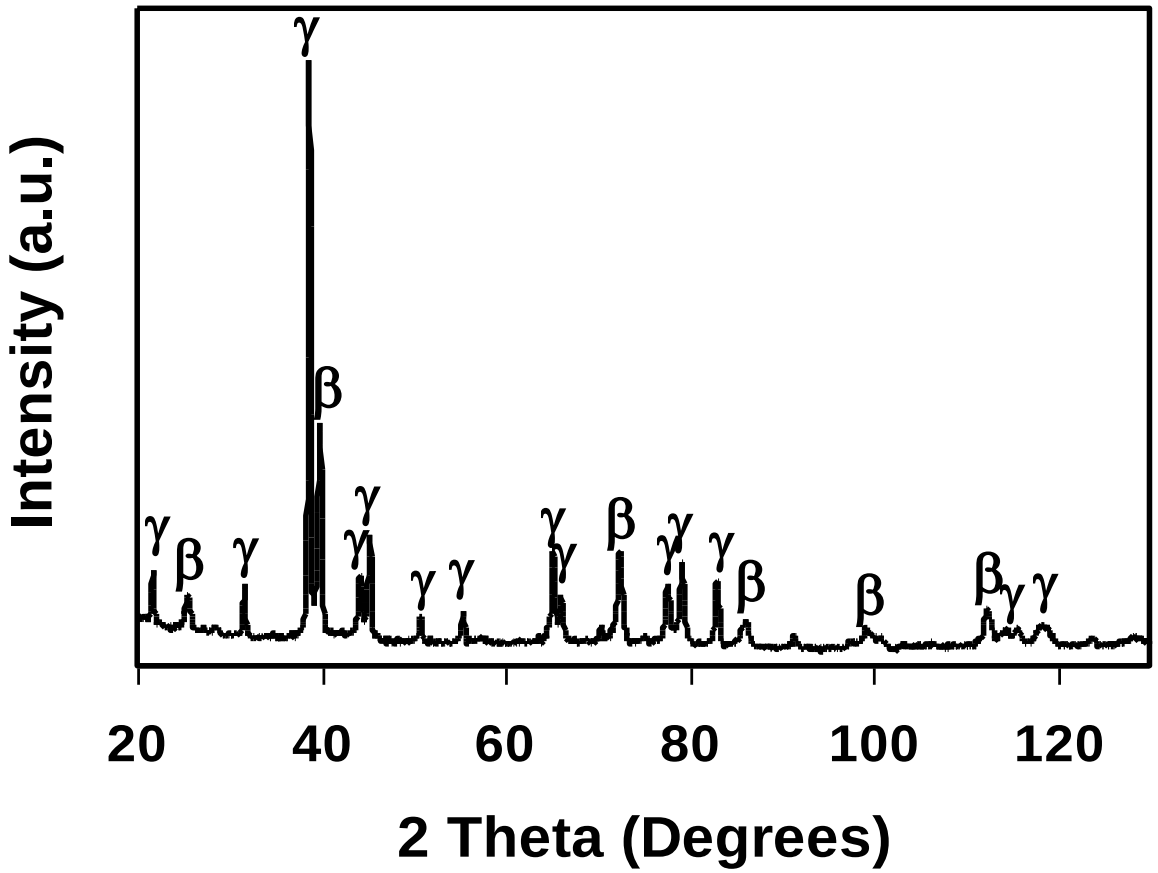

Figure 4-9. The XRD profile of Alloy 12Cr in the as-cast condition (Courtesy of Michael S. Kesler)

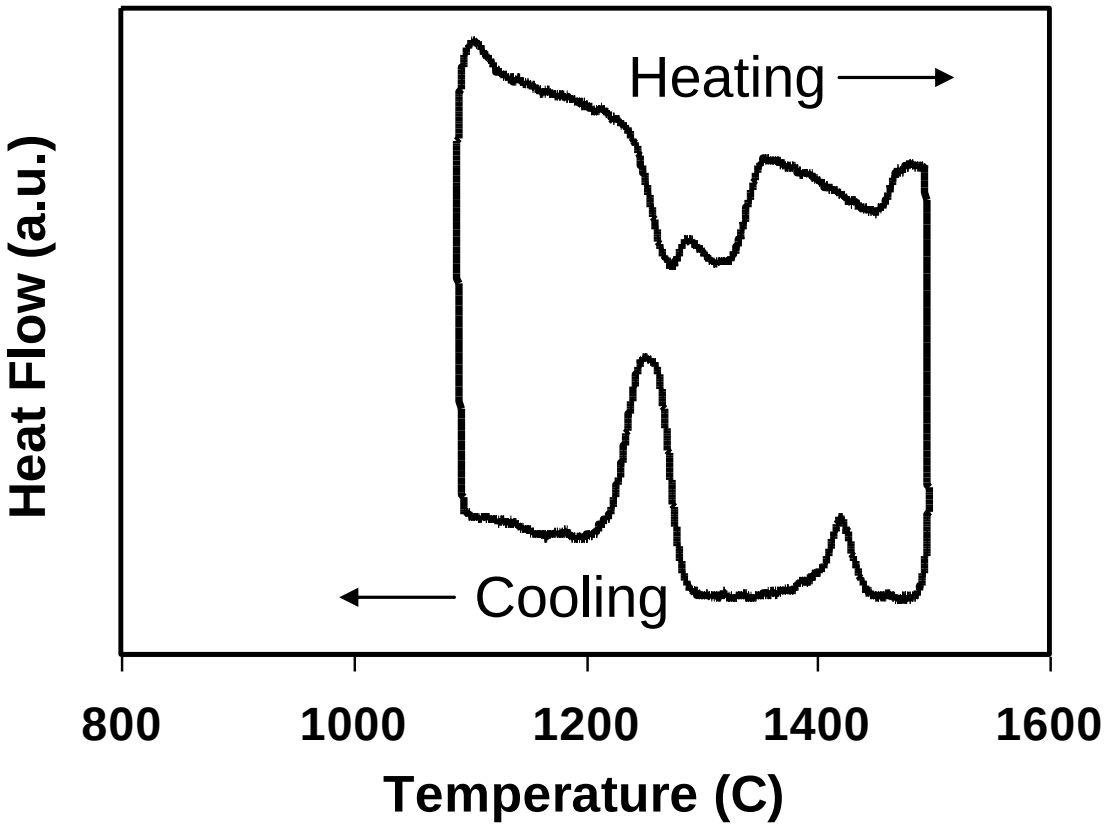

Figure 4-10. DTA plot of Alloy 11 (Courtesy of Michael S. Kesler and Sonalika Goyel)

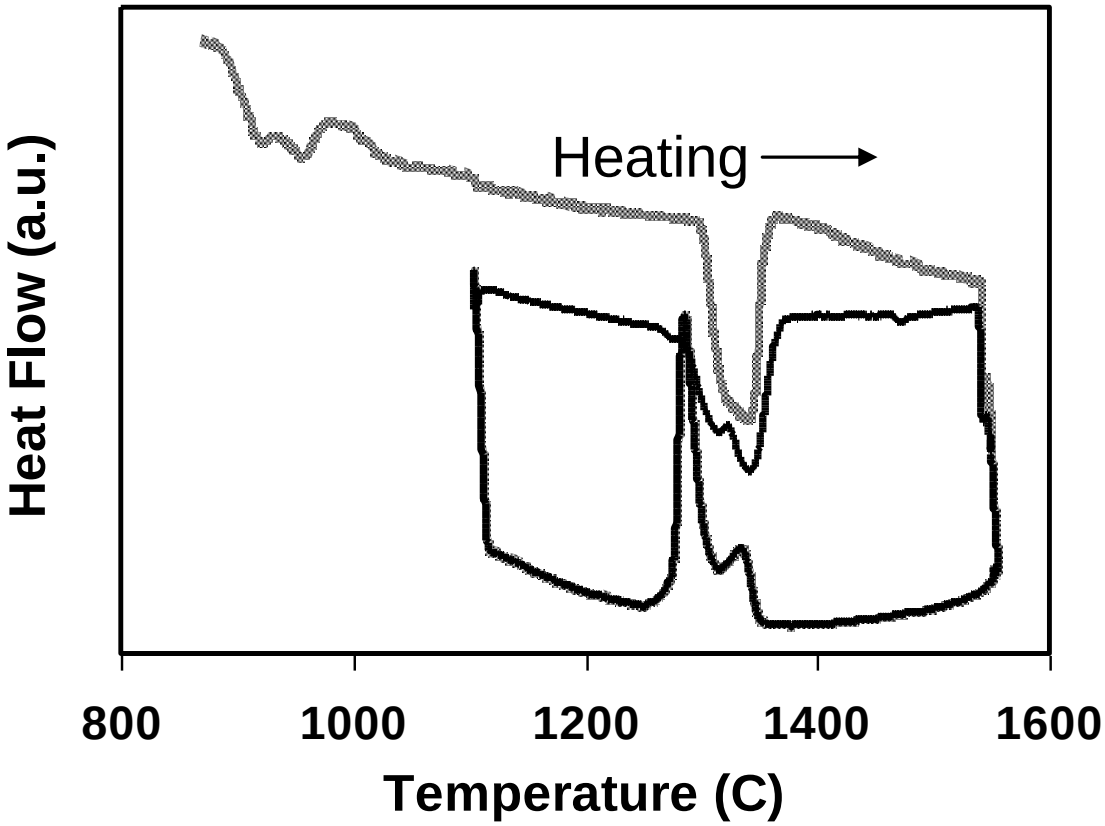

Figure 4-11. DTA plot of Alloy 12 (Courtesy of Michael S. Kesler)

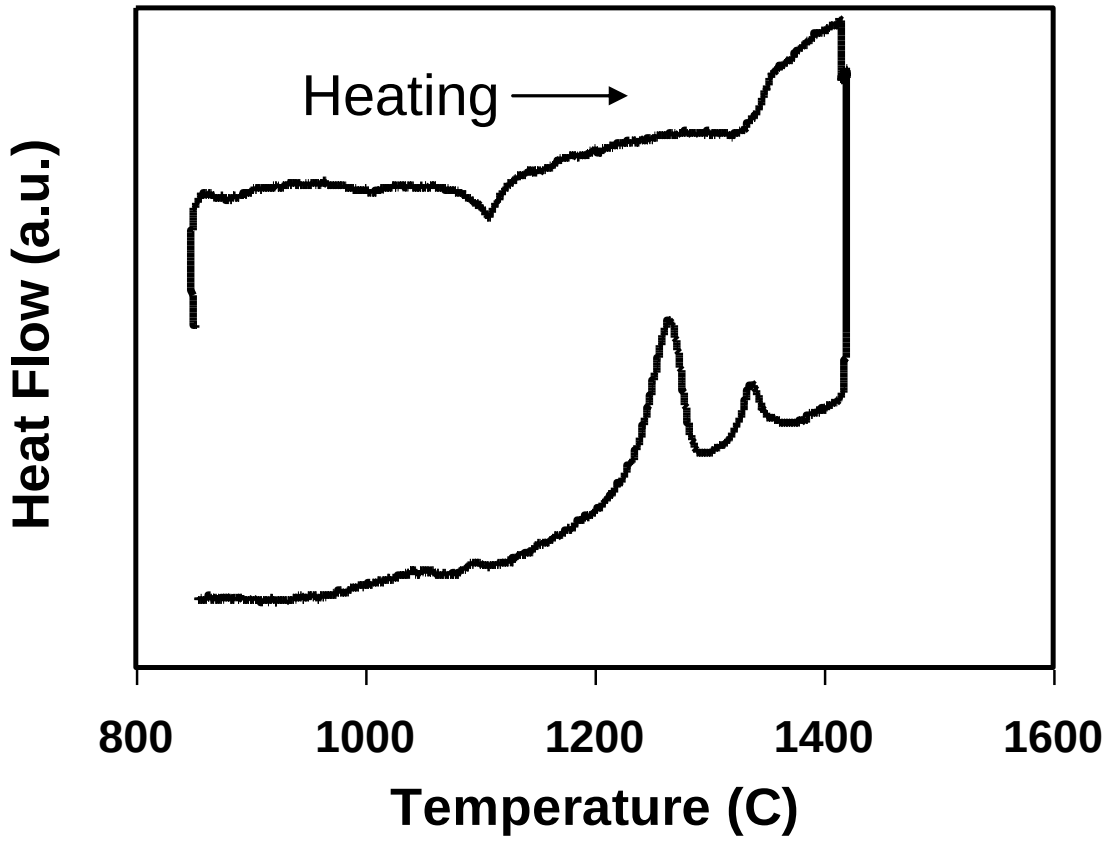

Figure 4-12. DTA plot of Alloy 11Cr (Courtesy of Michael S. Kesler and Sonalika Goyel)

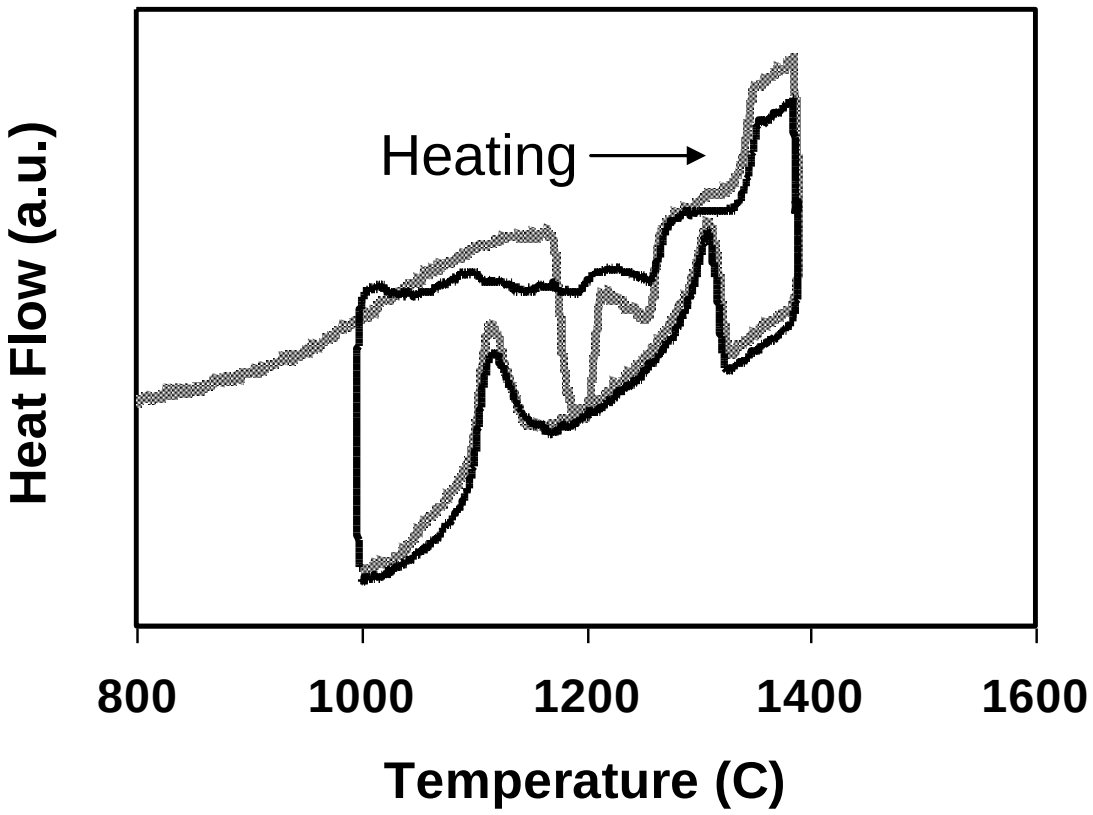

Figure 4-13. DTA plot of Alloy 12Cr (Courtesy of Michael S. Kesler)

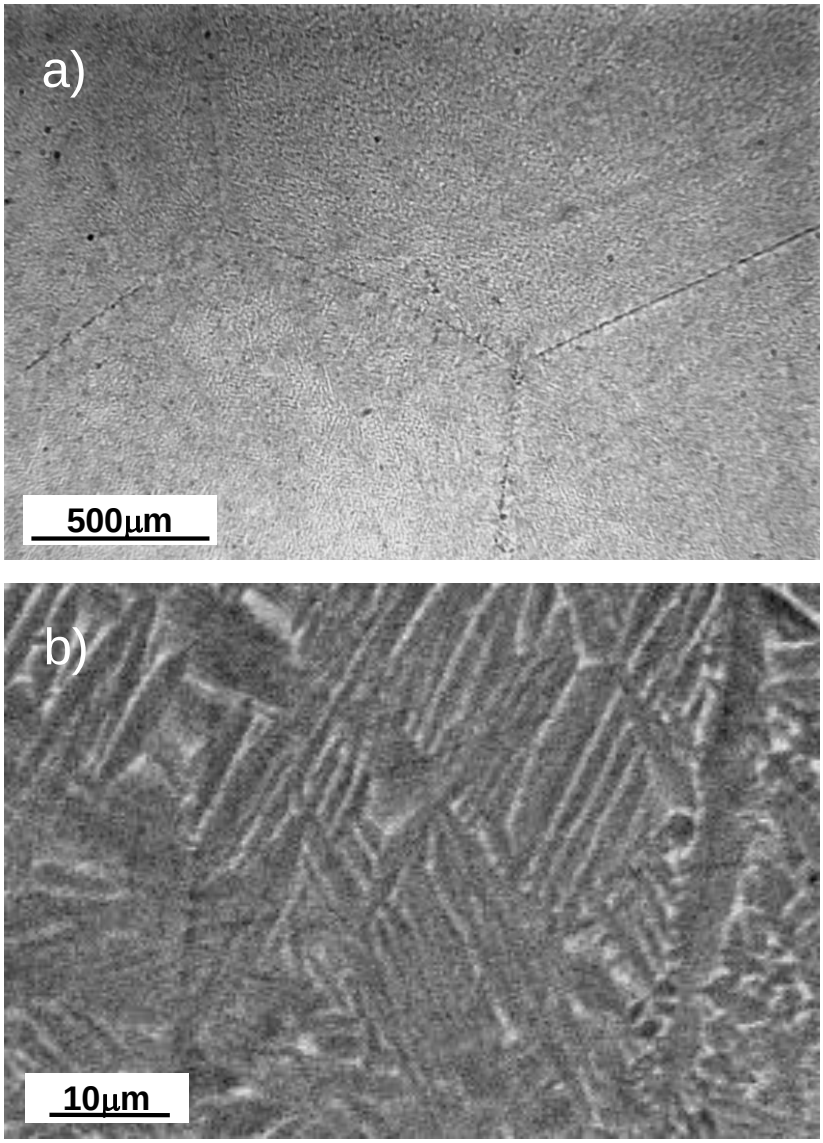

Figure 4-14. Images of Alloy 11 in the soln+WQ condition displaying; a) coarse equiaxed grains (OM); and b) a two-phase microstructure which formed upon WQ (BSE) (Courtesy of Michael S. Kesler and Sonalika Goyel)

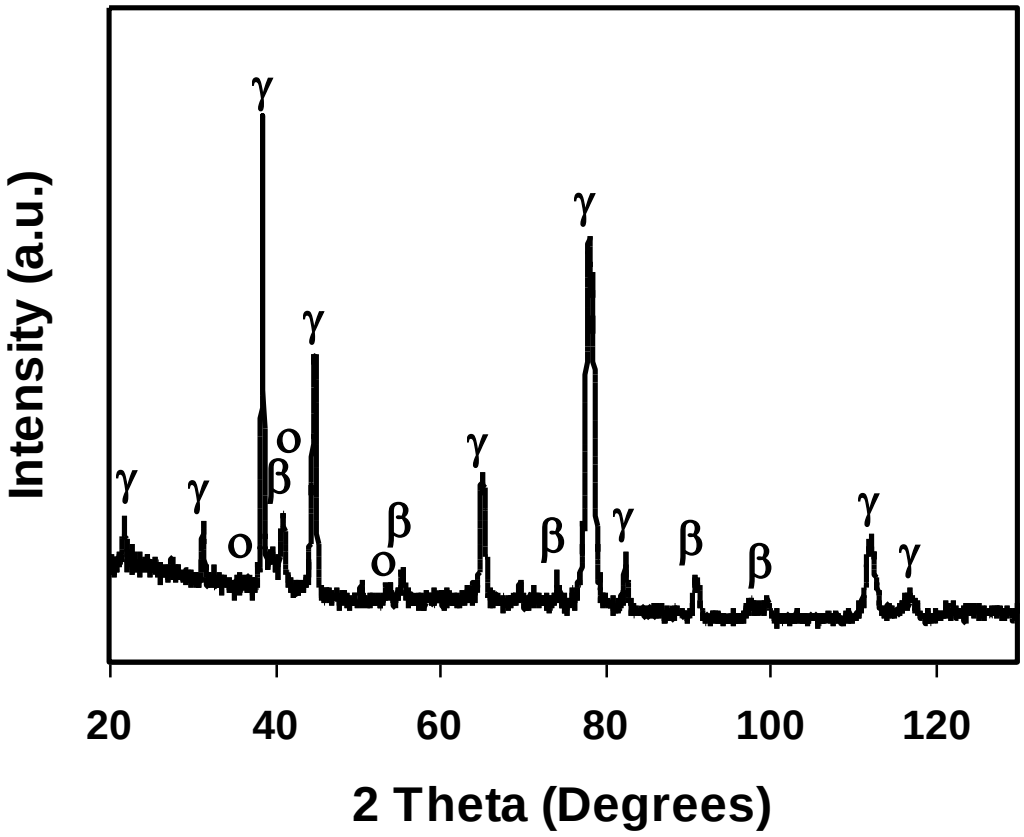

Figure 4-15. The XRD profile of Alloy 11 in the soln+WQ condition (Courtesy of Michael S. Kesler and Sonalika Goyel)

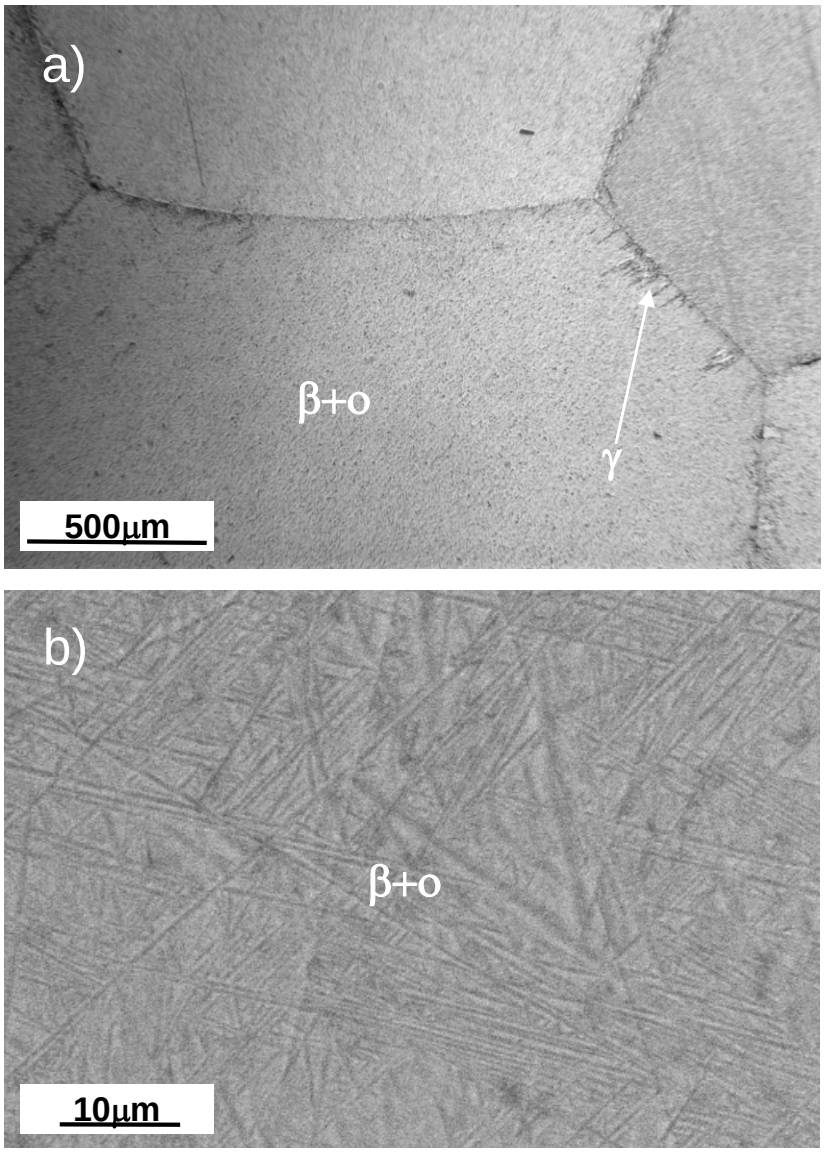

Figure 4-16. Images of Alloy 11Cr in the soln+WQ condition displaying; a) coarse equiaxed grains with Widmanstätten growth emanating from the grain boundaries (OM); and b) a tweed-like microstructure which formed upon WQ in the bulk of the grain (BSE) (Courtesy of Michael S. Kesler and Sonalika Goyel)

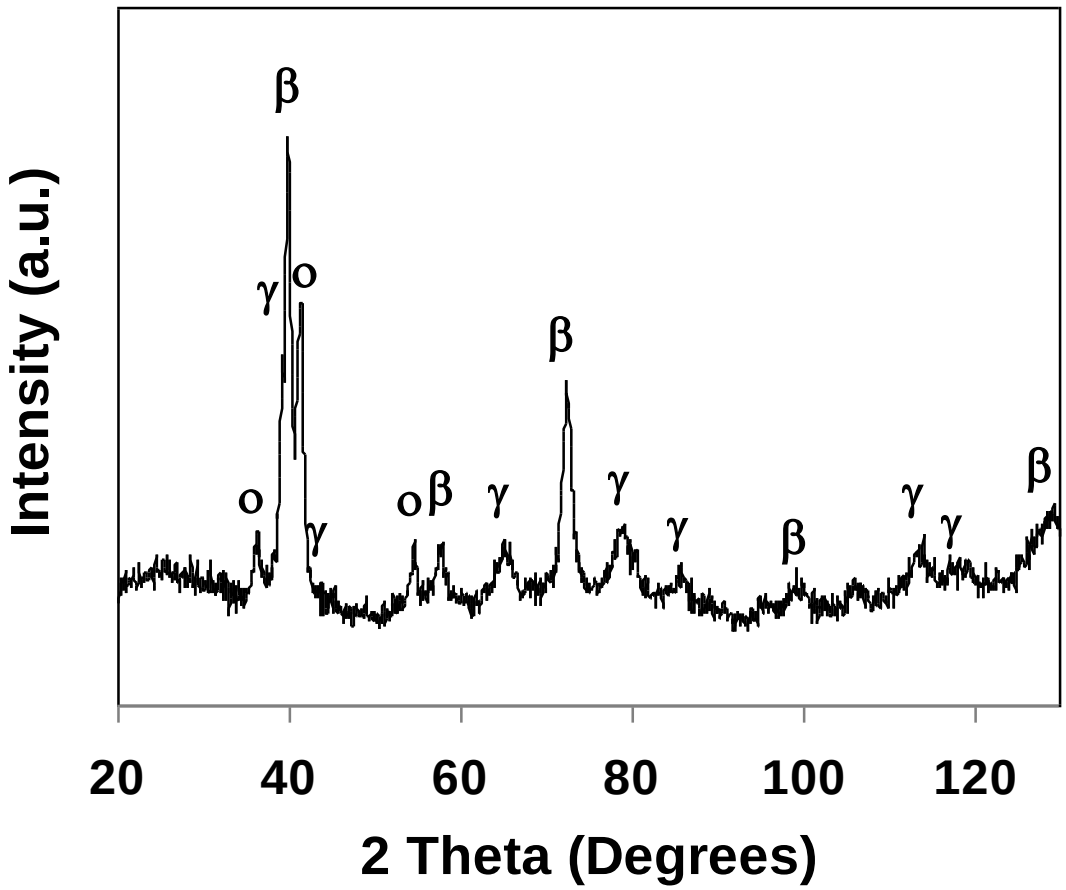

Figure 4-17. The XRD profile of Alloy 11Cr in the soln+WQ condition (Courtesy of Michael S. Kesler and Sonalika Goyel)

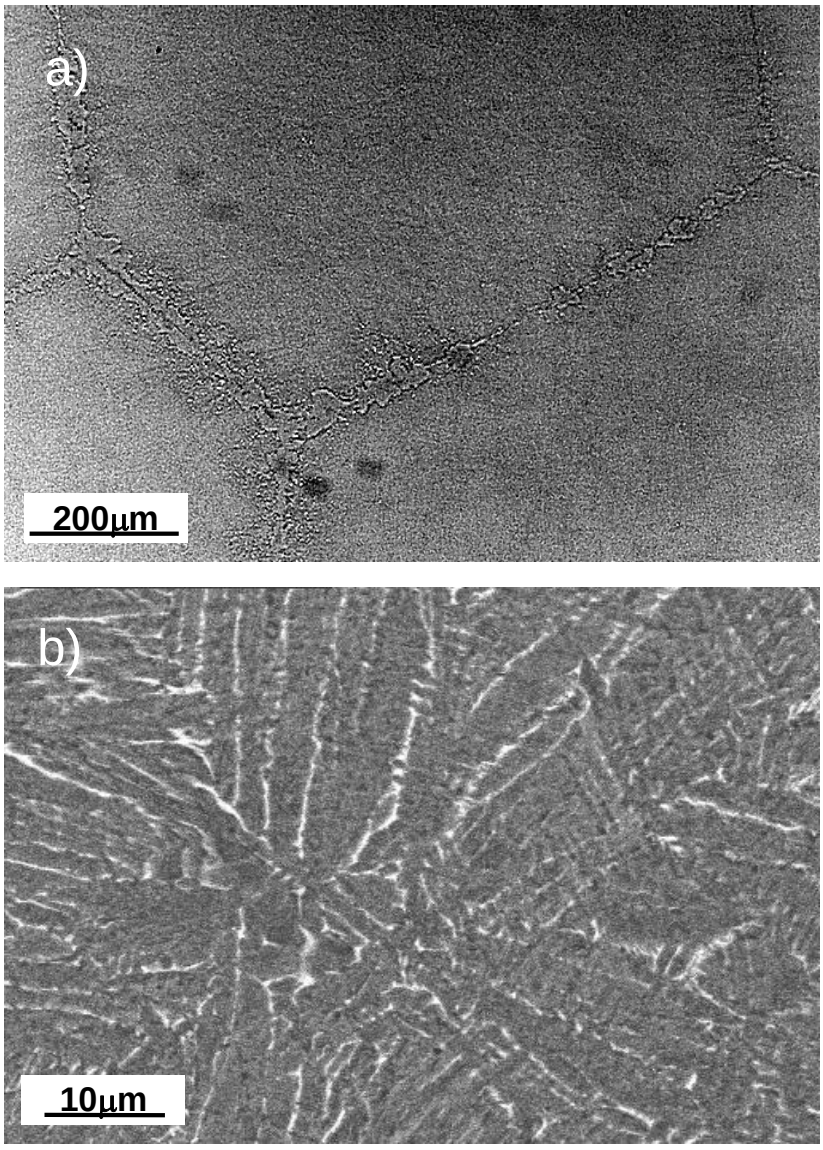

Figure 4-18. Images of Alloy 12 in the soln+WQ condition displaying; a) coarse equiaxed grains (OM); and b) a two-phase microstructure which formed upon WQ in the bulk of the grain (BSE) (Courtesy of Michael S. Kesler)

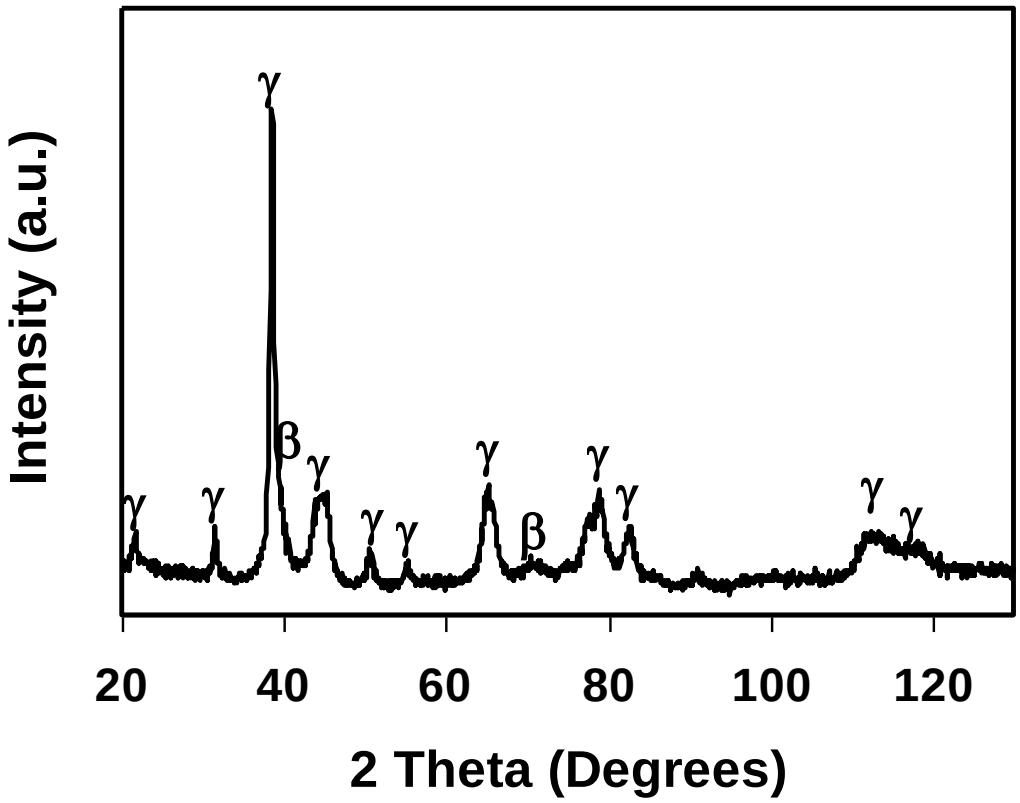

Figure 4-19. The XRD profile of Alloy 12 in the soln+WQ condition (Courtesy of Michael S. Kesler)

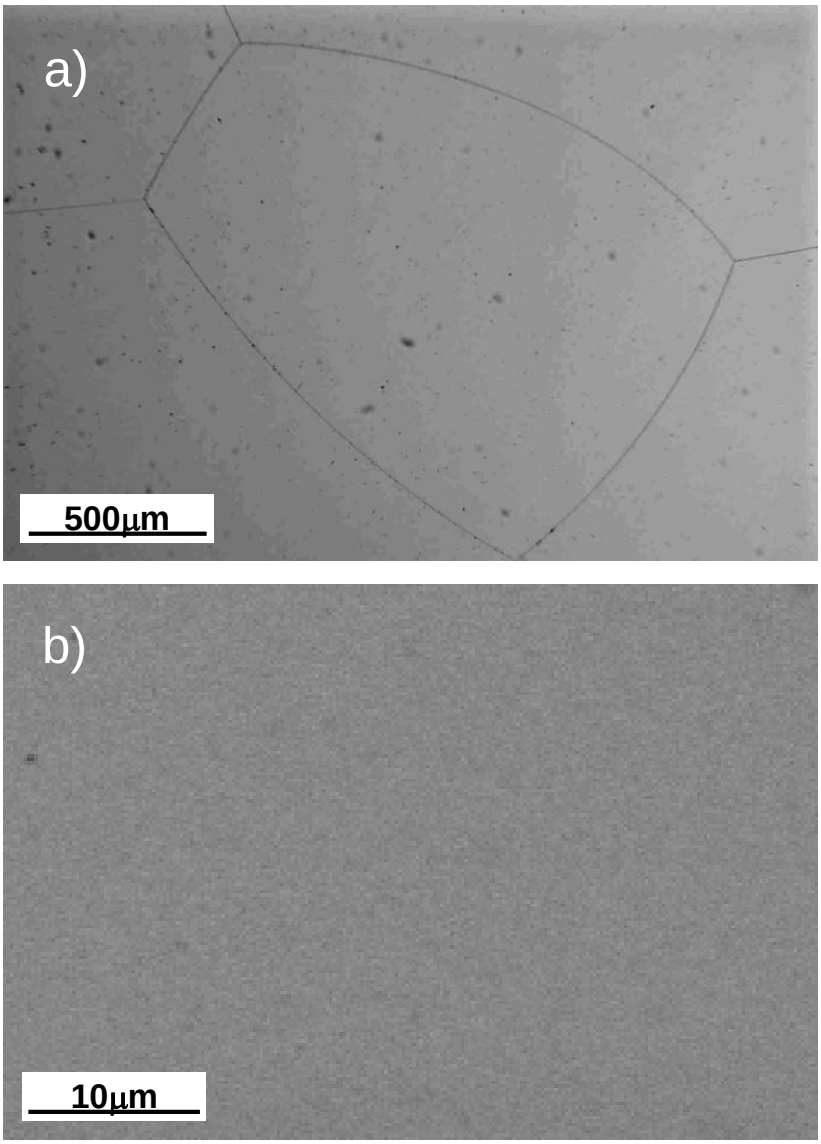

Figure 4-20. Images of Alloy 12Cr in the soln+WQ condition displaying; a) coarse equiaxed grains (OM); and b) a single β-phase that was retained upon WQ (BSE) (Courtesy of Michael S. Kesler)

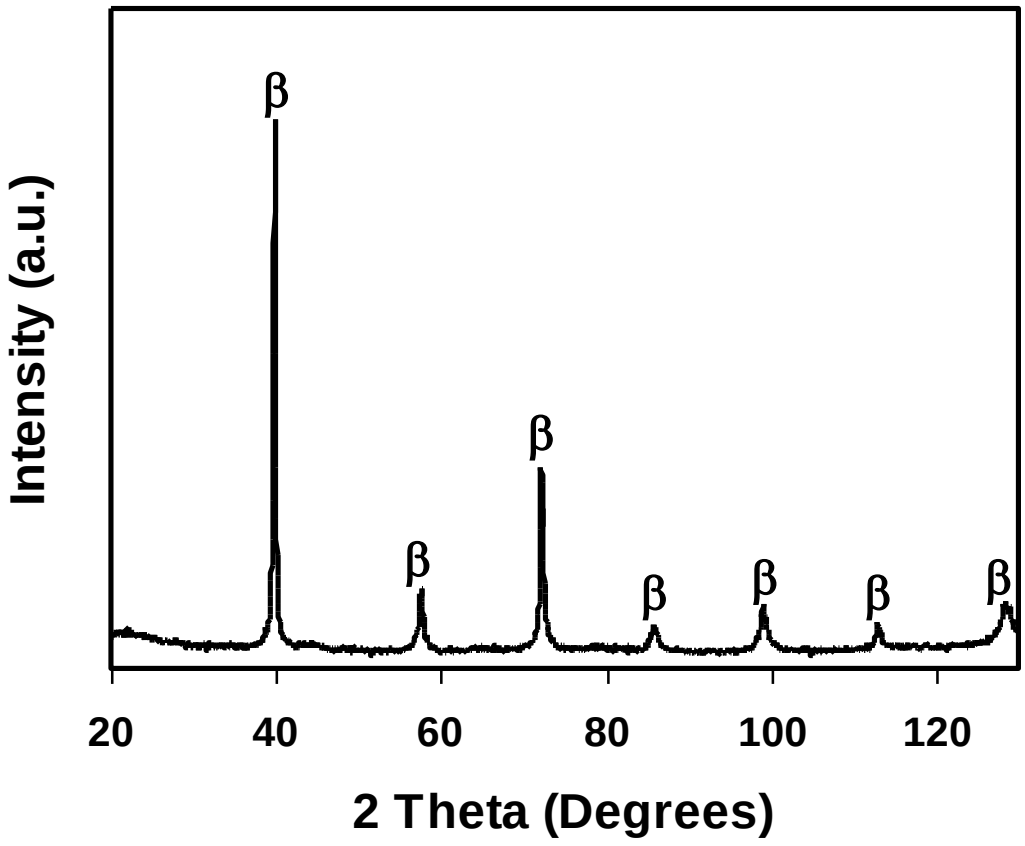

Figure 4-21. The XRD profile of Alloy 12Cr in the soln+WQ condition (Courtesy of Michael S. Kesler)

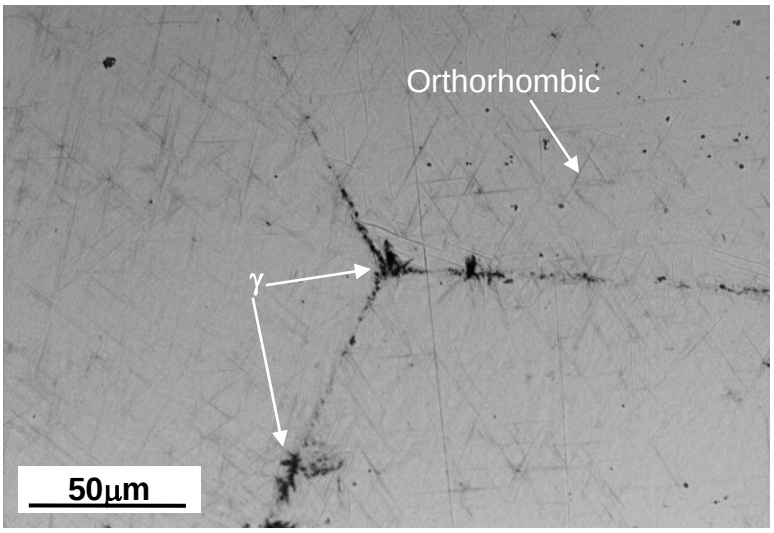

Figure 4-22. Images of Alloy 12.5CrMo in the soln+WQ condition displaying; a) coarse equiaxed grains with Widmanstätten growth emanating from the grain boundaries (OM); and b) a tweed-like microstructure which formed upon WQ in the bulk of the grain (BSE) (Courtesy of Michael S. Kesler)

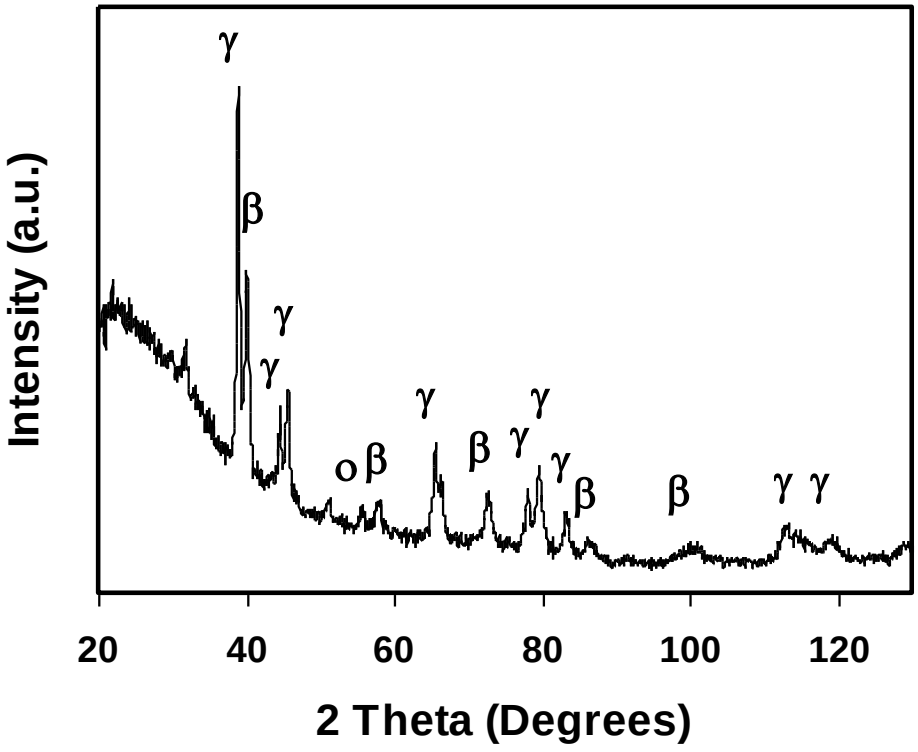

Figure 4-23. The XRD profile of Alloy 12.5CrMo in the soln+WQ condition (Courtesy of Michael S. Kesler)

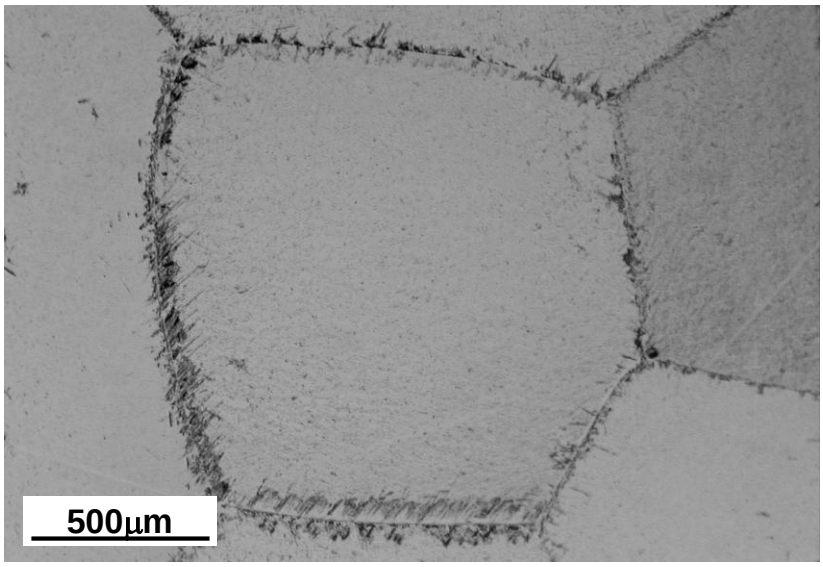

Figure 4-24. Optical micrograph of Alloy 13CrMo in the soln+WQ condition displaying; a) coarse equiaxed grains with Widmanstätten growth emanating from the grain boundaries (Courtesy of Michael S. Kesler)

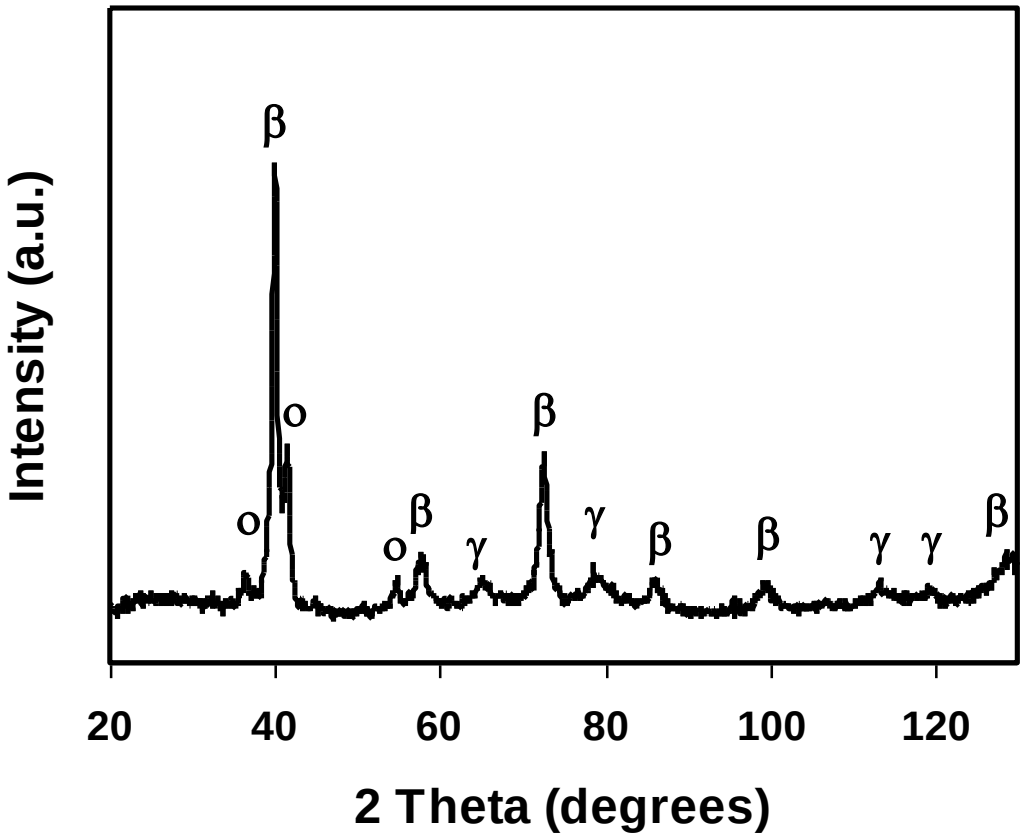

Figure 4-25. The XRD profile of Alloy 13CrMo in the soln+WQ condition (Courtesy of Michael S. Kesler)

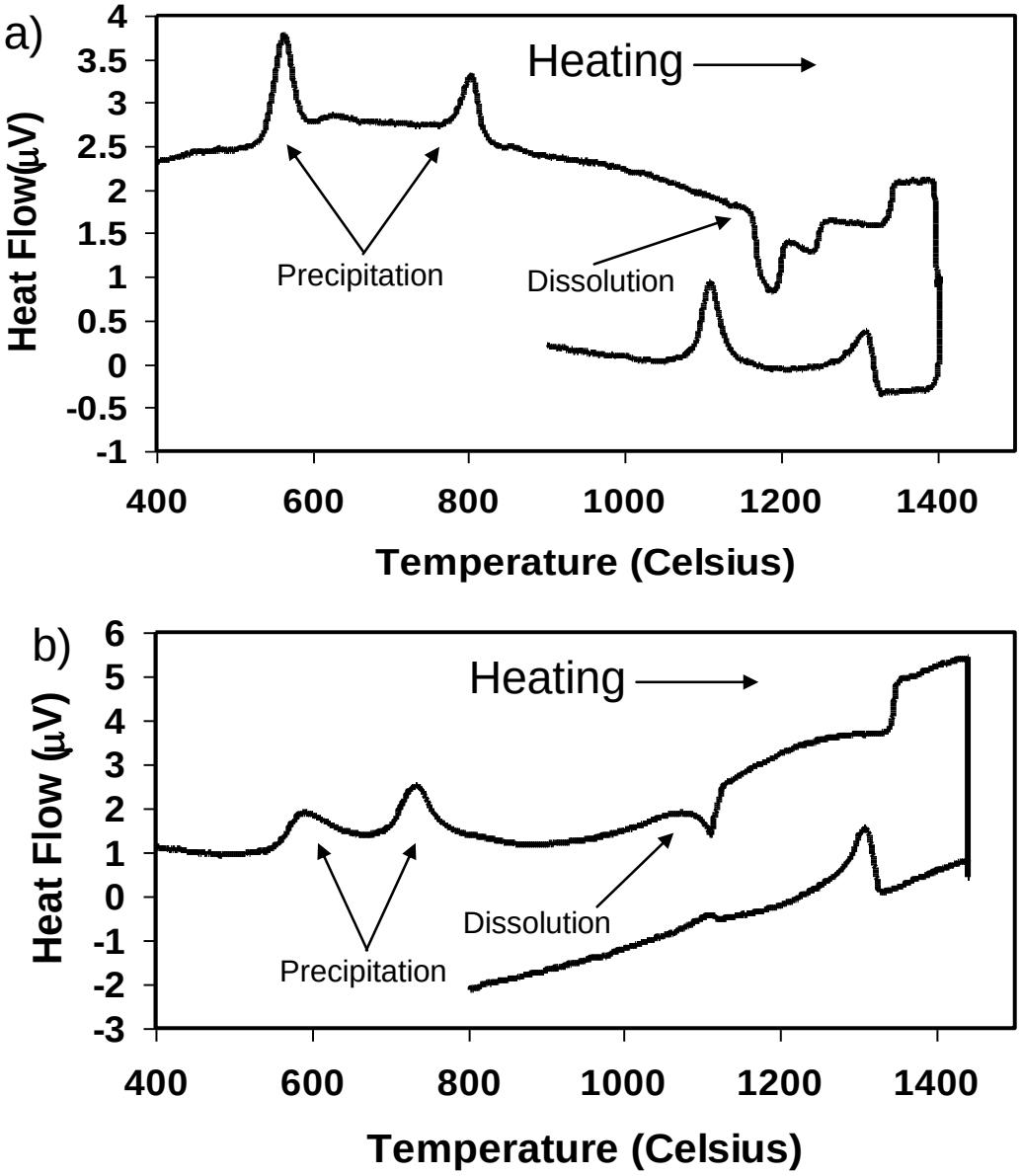

Figure 4-26. DTA curves generated from samples of a) Alloy 12Cr and b) Alloy 13CrMo in the soln+WQ condition revealing transformation temperatures upon heating the meta-stable quenched-in structure (Courtesy of Michael S. Kesler)

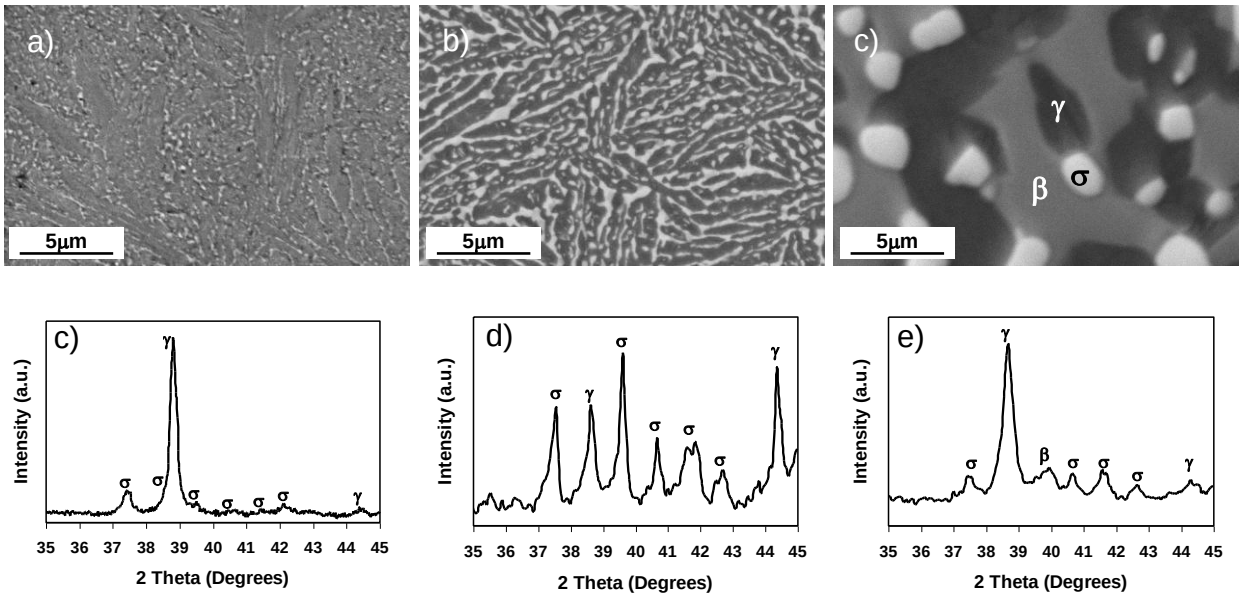

Figure 4-27. BSE micrographs of Alloy 12Cr which had been aged at a) 865ºC, b) 1050ºC and c) 1200ºC, then WQ to room temperature. Analysis of the XRD profiles reveal the phases present at c) 865ºC, d) 1050ºC and e) 1200ºC (Courtesy of Michael S. Kesler)

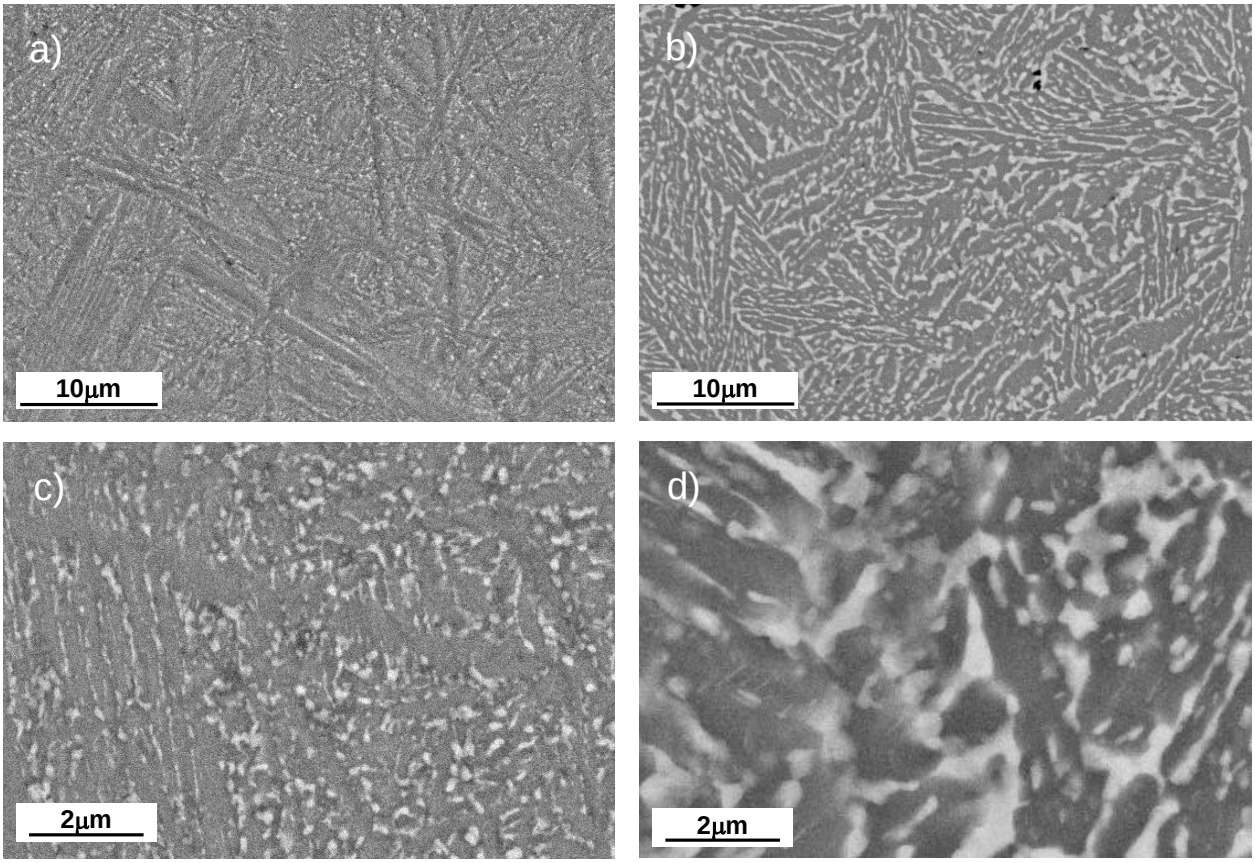

Figure 4-28. BSE micrographs of the two-phase γ+σ microstructures formed in Alloy 12Cr after aging at a,c) 865ºC and b,d) 1050ºC, then furnace cooling to room temperature (Courtesy of Michael S. Kesler)

Table 4-1 Microstructural parameters of alloys aged for mechanical testing

Alloys	Vol%σ	σ_r (μm)	λ (μm)	Mean Diam (μm)
12Cr-865	29.7	0.47	0.33	0.14
12Cr-1050	31.3	0.91	0.62	0.28
12.5CrMo-865	21.5	0.40	0.32	0.09
12.5CrMo-1000	21.8	1.09	0.86	0.24
12.5CrMo-1050	21.7	1.12	0.88	0.24
13CrMo-865	13.1	0.49	0.39	0.06
13CrMo-1000	13.2	1.05	0.91	0.14
13CrMo-1050	12.8	1.66	1.44	0.21
11-1100	12.3	6.02	5.3	0.74

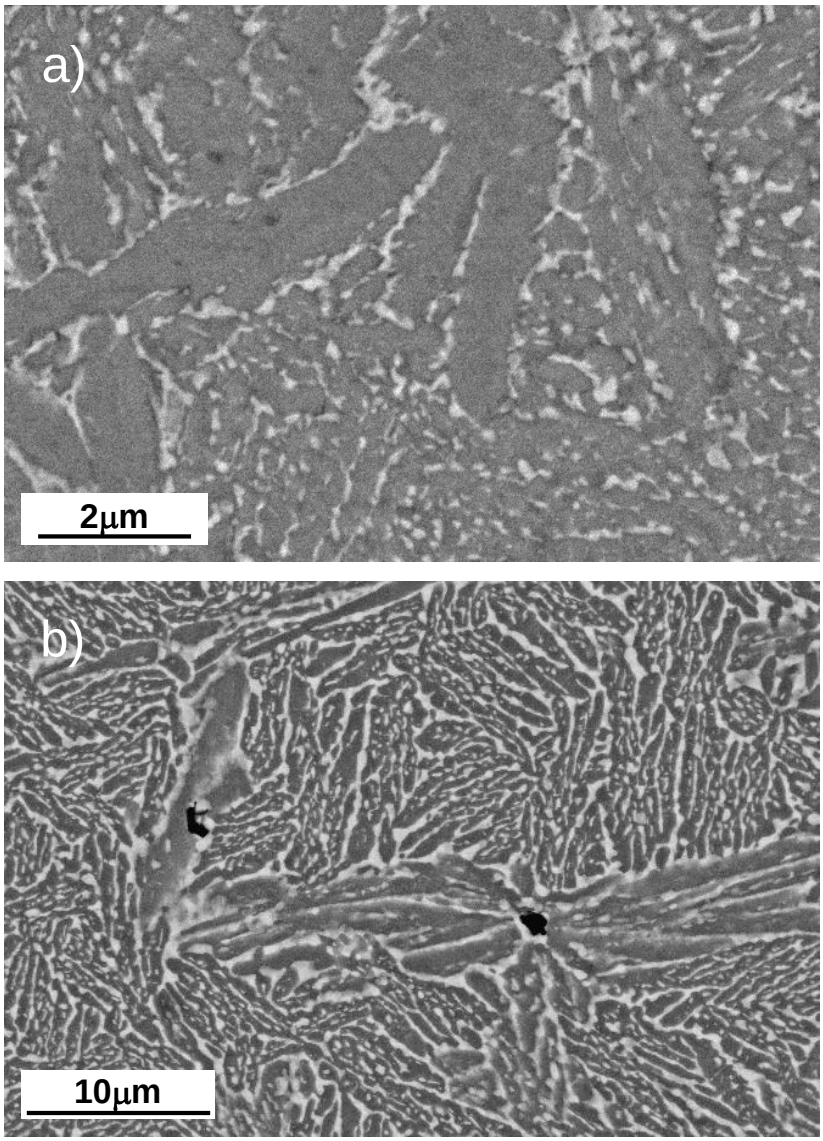

Figure 4-29. BSE micrographs of aged Alloy 12Cr showing regions of relatively coarse γ-phase due to 'early' formation of this phase upon aging at a) 865ºC and b) 1050ºC (Courtesy of Michael S. Kesler)

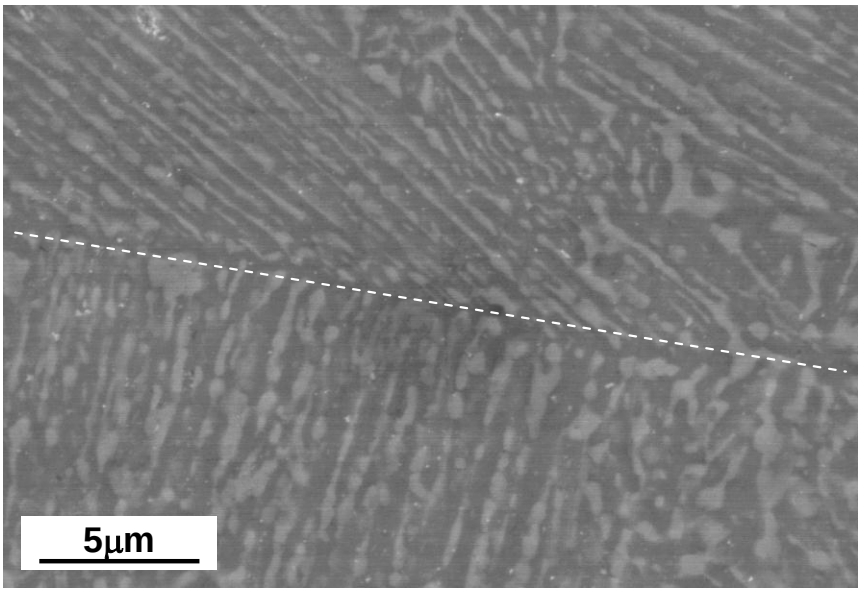

Figure 4-30. BSE micrograph of the Widmanstätten γ-phase formation upon aging at the prior β-phase grain boundaries in Alloy 12Cr-1050 (Courtesy of Michael S. Kesler)

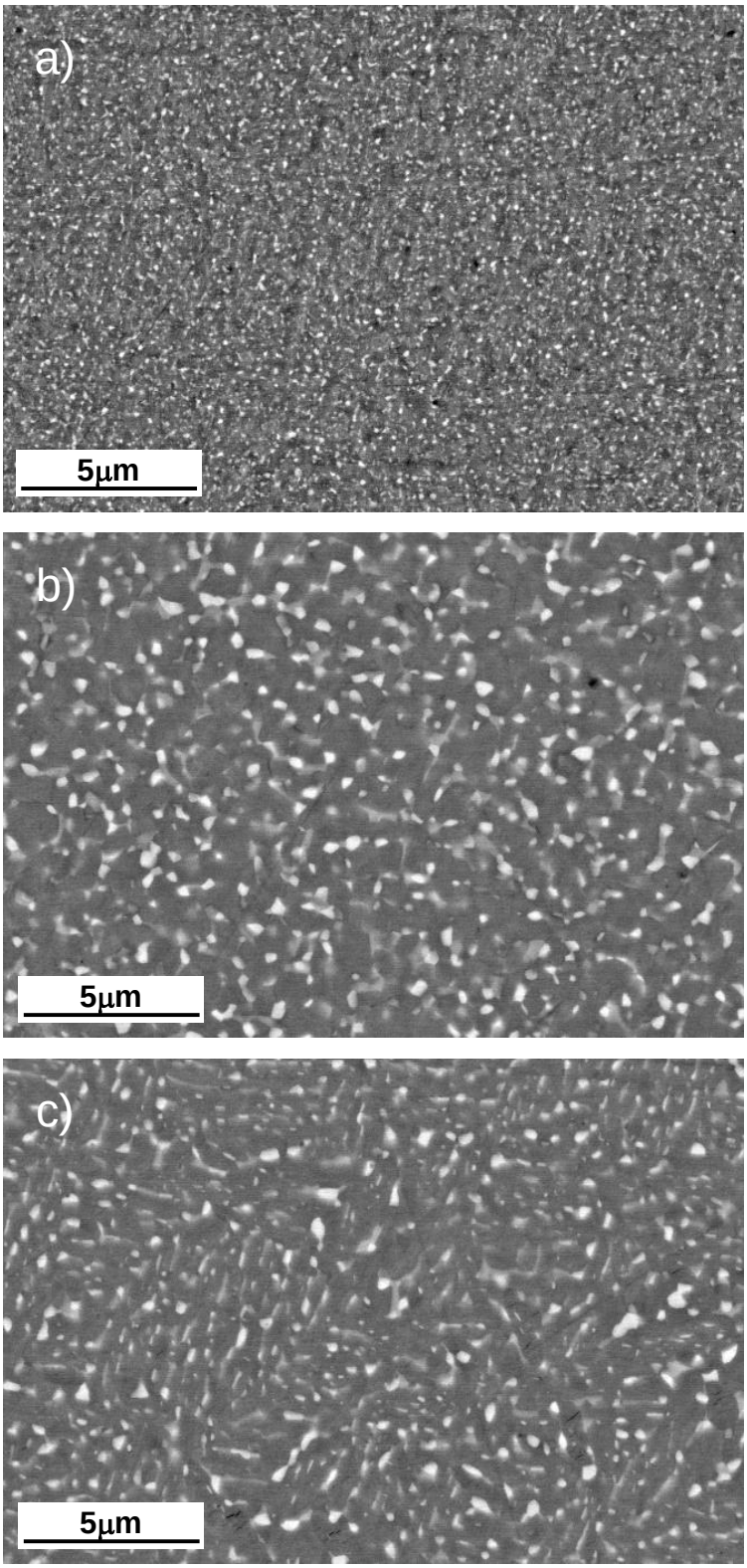

Figure 4-31. BSE micrographs of the two-phase $\gamma+\sigma$ microstructures formed in Alloy 12.5CrMo after aging at a) 865ºC, b) 1000ºC and c) 1050ºC, then furnace cooling to room temperature (Courtesy of Michael S. Kesler)

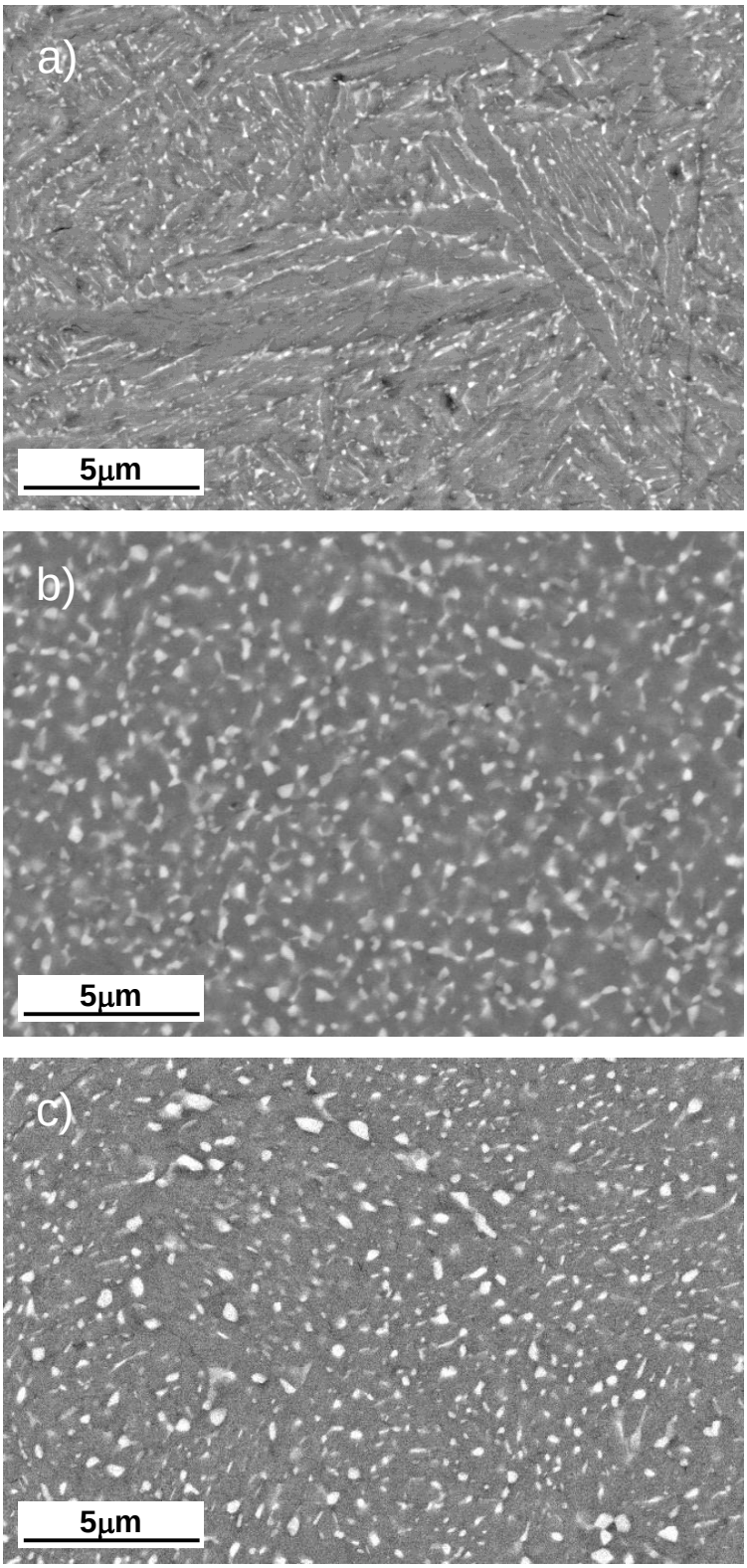

Figure 4-32. BSE micrographs of the two-phase $\gamma+\sigma$ microstructures formed in Alloy 13CrMo after aging at a) 865ºC, b) 1000ºC and c) 1050ºC, then furnace cooling to room temperature (Courtesy of Michael S. Kesler)

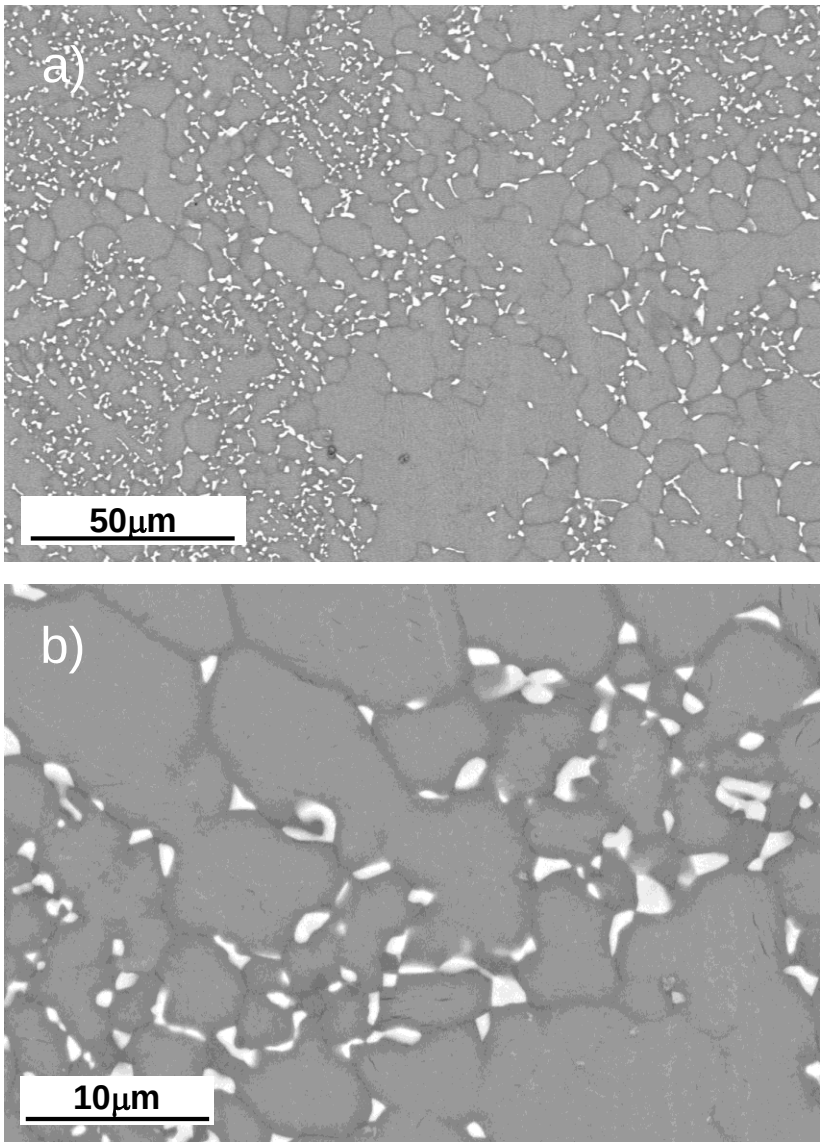

Figure 4-33. a) and b) BSE micrographs of the two-phase $\gamma+\sigma$ microstructures formed in Alloy 11 after aging at 1100ºC, then furnace cooling to room temperature (Courtesy of Michael S. Kesler)

Table 4-2. Transformation temperature estimated from DTA experiments

Heating Path	$\gamma + \sigma \rightarrow \beta + \gamma + \sigma$ (ºC)	$\beta + \gamma + \sigma \rightarrow \beta + \gamma$ (ºC)	$\beta + \gamma \rightarrow \beta$ (ºC)
Alloy 12	1269	1326	1382
Alloy 12 + Cr	1099	1282	1368
Cooling Path	$\beta + \gamma + \sigma \rightarrow \gamma + \sigma$ (ºC)	$\beta + \gamma \rightarrow \beta + \gamma + \sigma$ (ºC)	$\beta \rightarrow \beta + \gamma$ (ºC)
Alloy 12	1243	1309	1349
Alloy 12 + Cr	1058	1179	1330

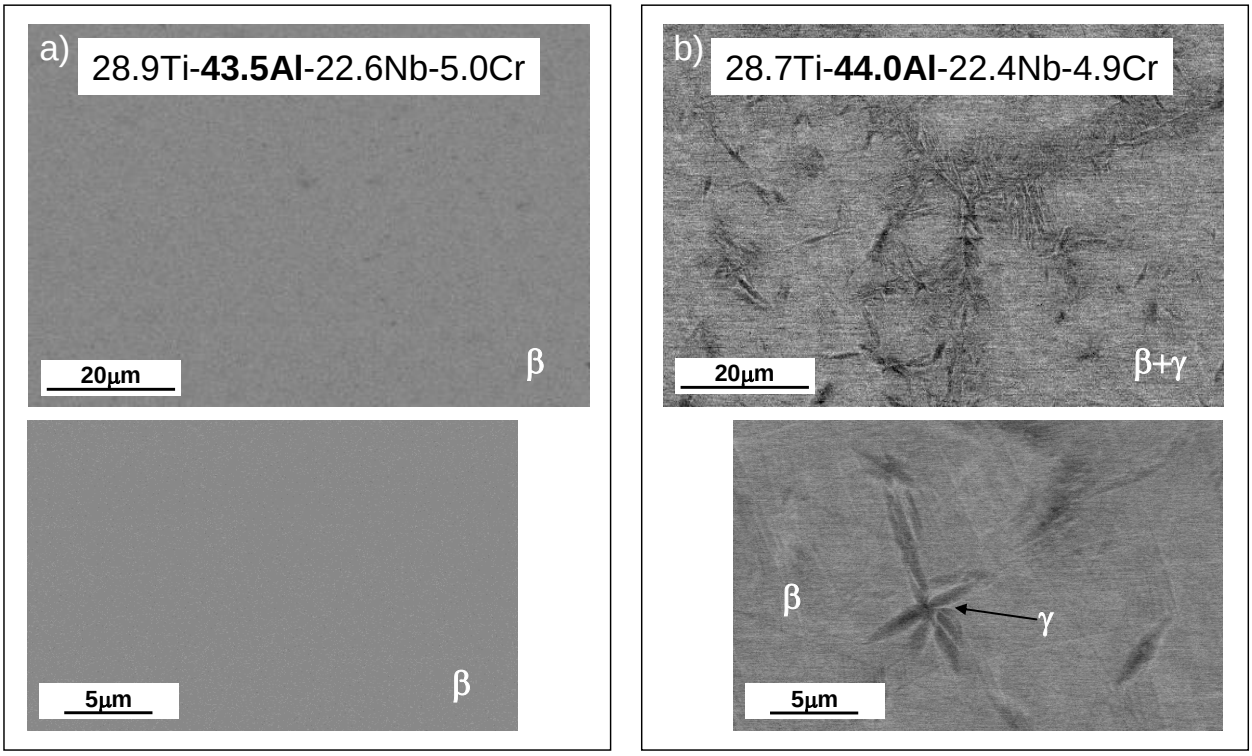

Figure 4-34. BSE micrographs of soln+ WQ Alloy 12Cr with a) low Al-content resulting in a fully quenched-in β-phase and b) higher Al-content resulting in γ-phase formation at the β-phase grain boundaries and select areas in the bulk of the β-grains (Courtesy of Michael S. Kesler)

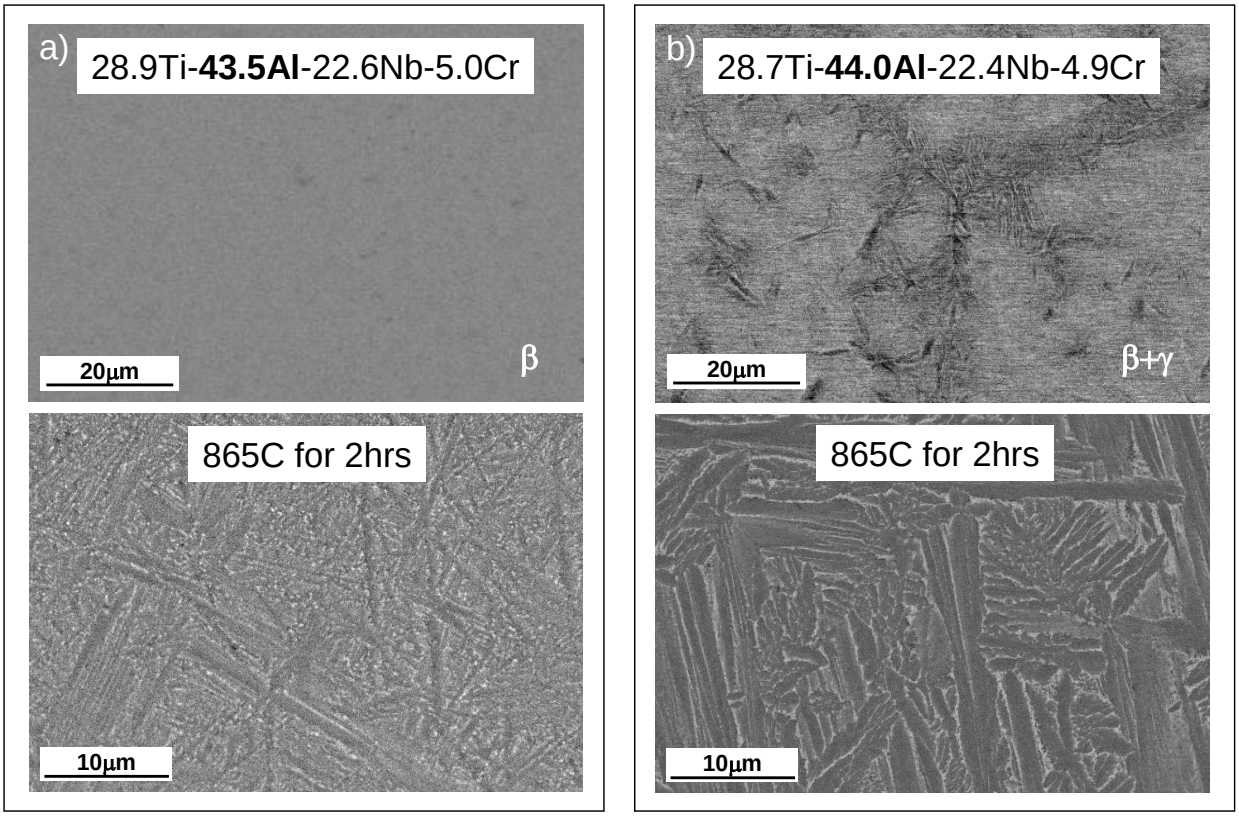

Figure 4-35. BSE micrographs of the soln+WQ microstructures in Alloy 12Cr and shown below are the a) finer and b) coarser aged microstructures as a result of varying Al-content (Courtesy of Michael S. Kesler)

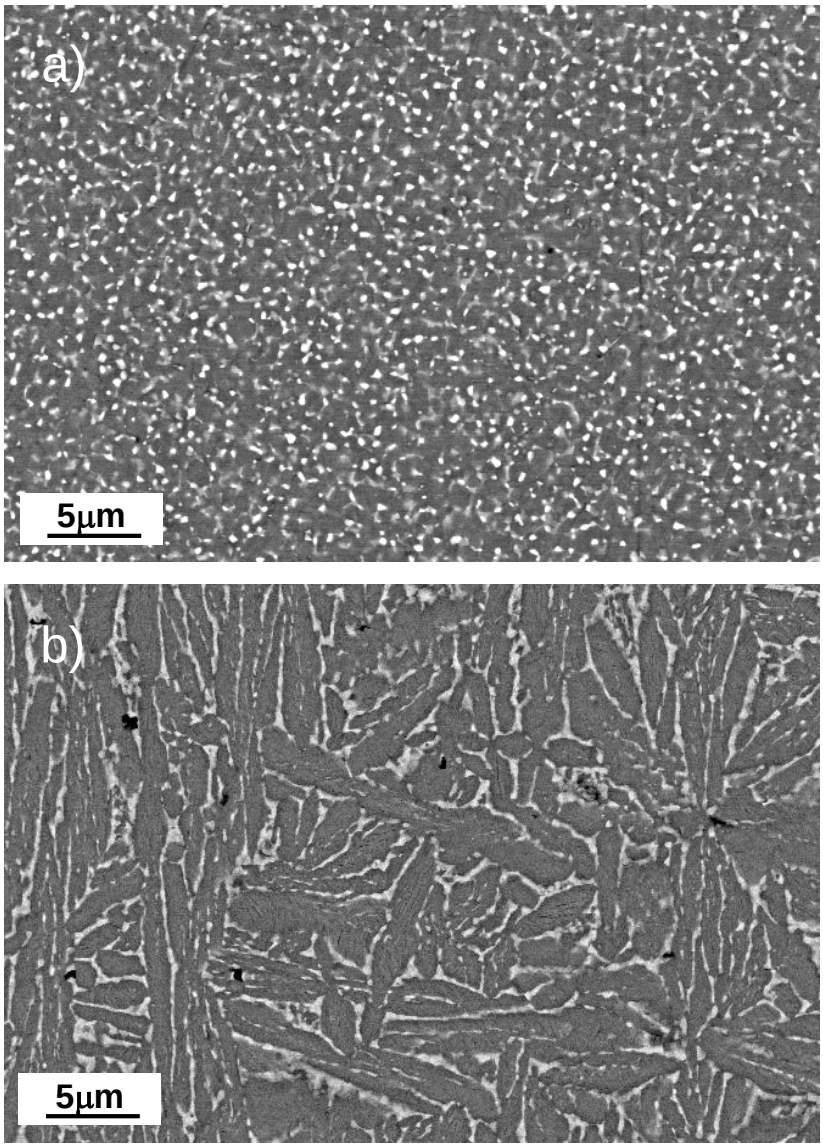

Figure 4-36. BSE micrographs of Alloy 12.5CrMo-1000 revealing fine and coarse microstructures as a result of inconsistent cooling rates upon quenching due to a) smaller and b) larger sample sizes (Courtesy of Michael S. Kesler)

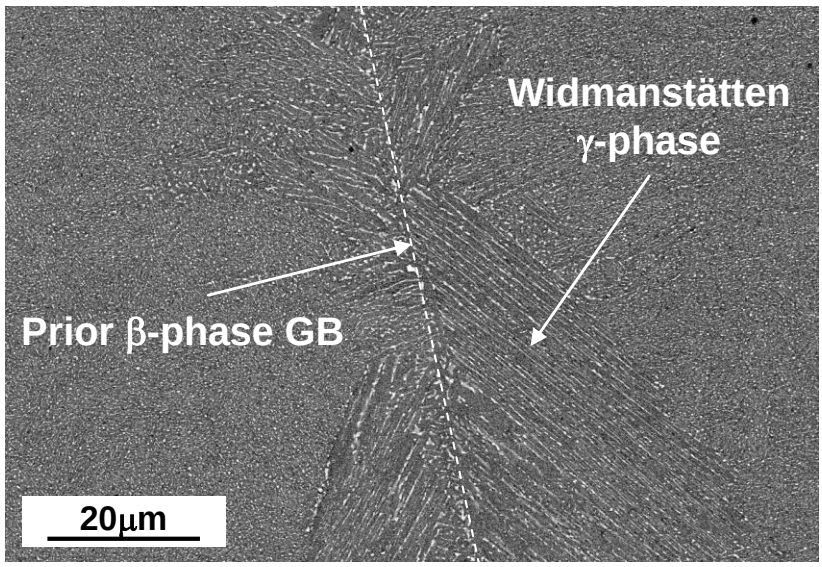

Figure 4-37. BSE micrograph of Alloy 13CrMo revealing the coarse Widmanstätten γ-phase which formed at the prior β-phase grain boundaries upon quenching in this particular sample (Courtesy of Michael S. Kesler)

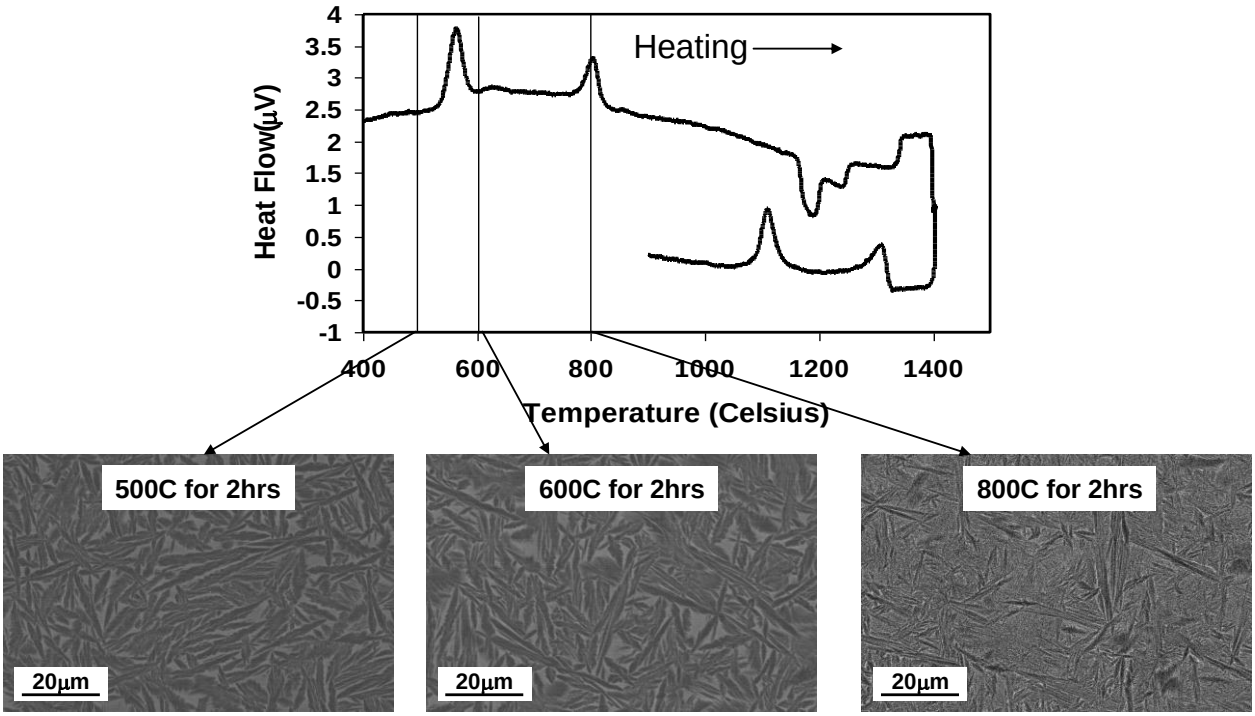

Figure 4-38. The DTA curve of Alloy 12Cr (top) with vertical lines marking the aging temperatures and arrows denoting the resulting microstructures (bottom) from a given aging temperature (Courtesy of Michael S. Kesler)

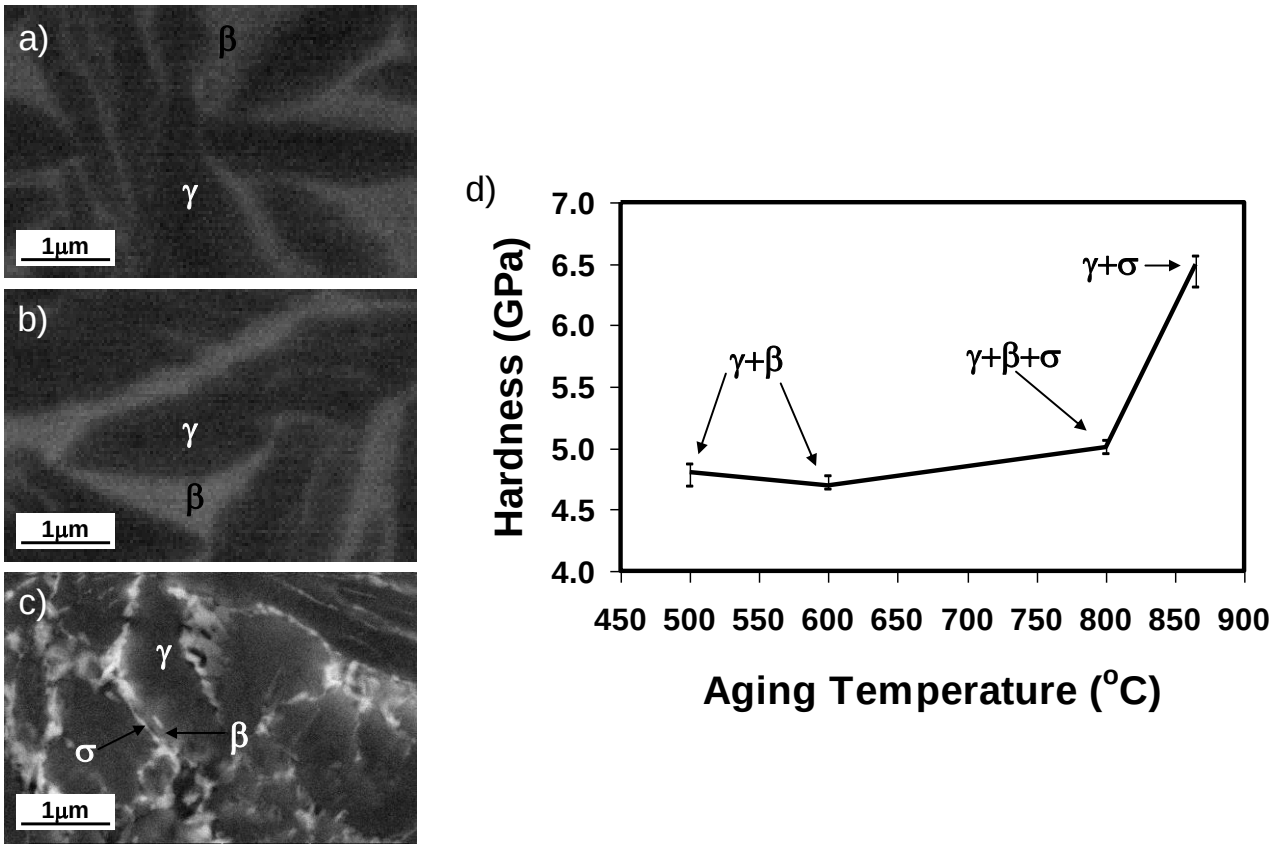

Figure 4-39. Higher magnification BSE micrographs of Alloy 12Cr a,b) aged at 500ºC and 600ºC for 2 hrs resulting in a two-phase β+γ microstructure, and c) aged at 800ºC for 2 hrs resulting in a three-phase β+γ+σ microstructure with the σ-phase forming within the remaining β-phase and at the β/γ interfaces; and d) Vickers hardness versus aging temperature (Courtesy of Michael S. Kesler and Tabea Wilk)

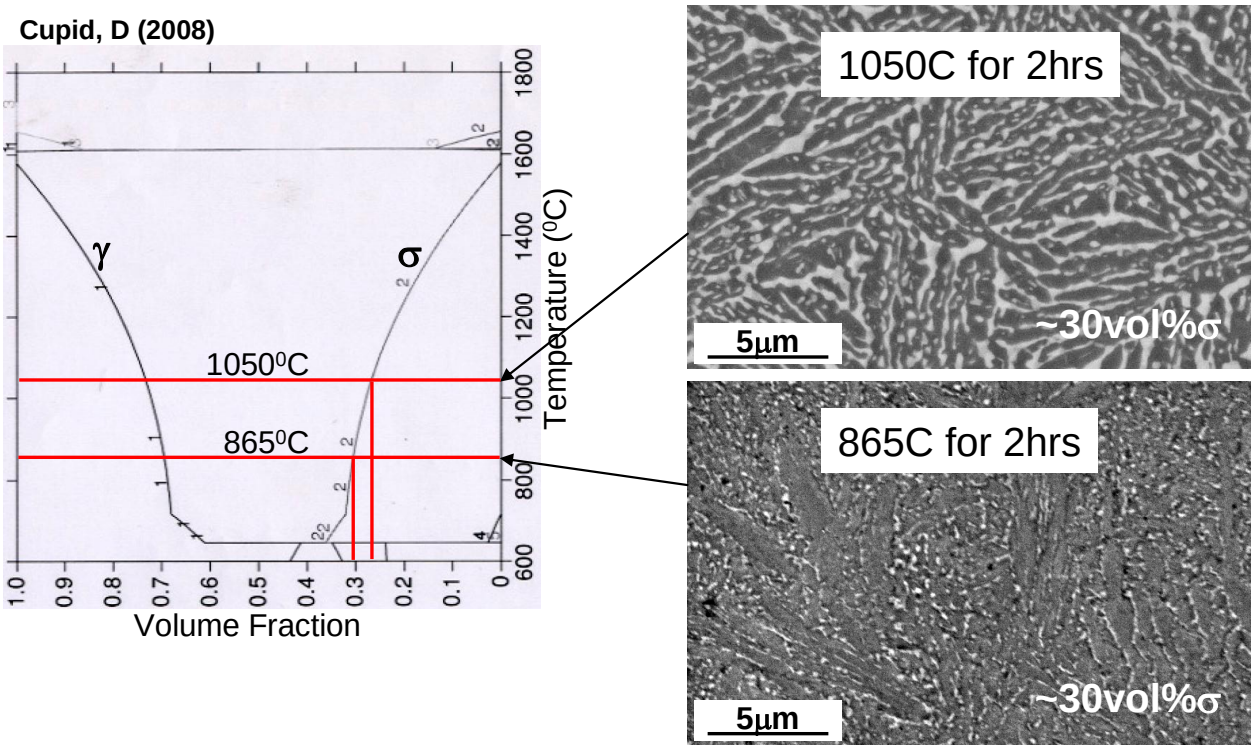

Figure 4-40. A phase fraction diagram (left-Courtesy of Damian Cupid, Ph.D Dissertation, University of Florida, Gainesville, Fla., 2009.) of the base ternary alloy, Alloy 12, revealing limited changes in volume fraction of the γ and σ phases below 1100C, and BSE micrographs (right) of the resulting microstructures of the quaternary alloy, Alloy 12Cr (Courtesy of Michael S. Kesler)

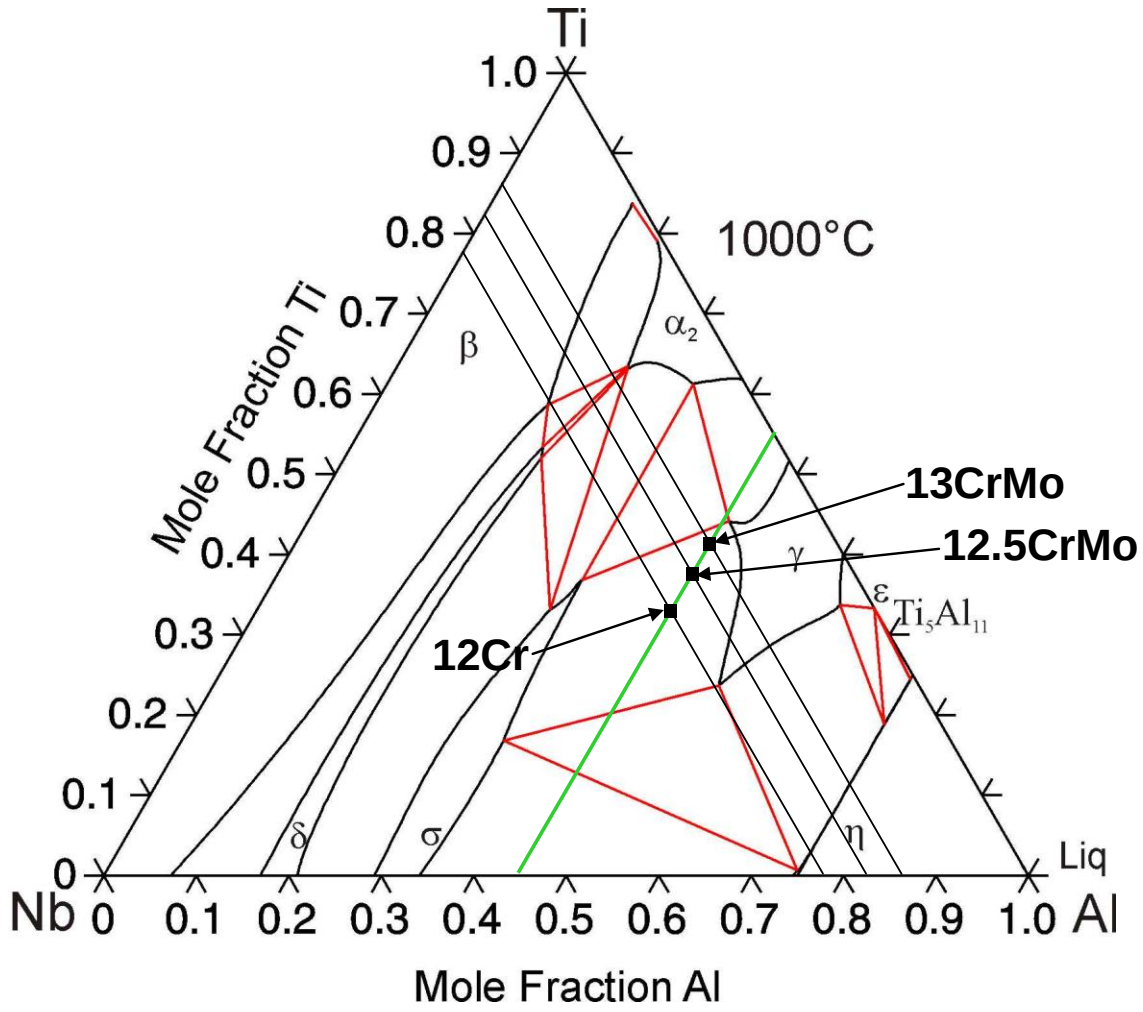

Figure 4-41. 1000ºC isothermal section of the Ti-Al-Nb phase diagram (Courtesy of Damian Cupid, Ph.D Dissertation, University of Florida, Gainesville, Fla., 2009.) with Alloys 12Cr, 12.5CrMo and 13CrMo plotted by nominal Nb-content along the constant 45at%Al line (green)

CHAPTER 5
DEFORMATION AND FRACTURE IN γ+σ ALLOYS AGED FROM A POLYCRYSTALLINE β-PHASE MICROSTRUCTURE

Previous work on Ti-Al-Nb alloys with a high volume fraction of the σ-phase [14, 15, 55, 56] has shown that these materials have attractive high temperature mechanical properties while room temperature properties were lacking due to brittle fracture and no ductility. In an effort to enhance ductility and toughness, alloys with lower volume fractions of the brittle σ-phase were developed as presented in Chapter 4. In addition to lowering the volume fraction of the σ-phase, the scale of the γ+σ microstructure was refined with the intention of imparting both strength and toughness. In this chapter the results of compression testing will be presented and the deformation and fracture behavior as it relates to the microstructure will be discussed.

5.1 Compression Testing on γ+σ Alloys

5.1.1 Compression testing to failure

All compression testing was conducted at room temperature at a constant cross-head speed resulting in strain rates varying between 3.9×10^{-4} and $4.9 \times 10^{-4} s^{-1}$ depending on exact sample dimensions (sample heights ranging from ~5.5-6.5mm). Unless otherwise stated, compression tests were performed until failure, which occurred when the samples either shattered into several large pieces (0-5% plastic deformation) or became unable to bear load any longer due to extensive cracking (5-35% plastic deformation). The stress-strain curves for alloys 12Cr-865 and 12Cr-1050 are displayed in Figure 5-1. Two tests were conducted on each sample condition. The data are very consistent as seen in Figure 5-1a where the two curves virtually overlap. The yield strength (YS), ultimate compressive strength (UCS) and plastic strain (ε_p) values for all

alloys are shown in Table 5-1. A description of how these values were measured can be seen in Appendix B.

Alloys 12Cr-865 and 12Cr-1050 exhibited a limited amount of plasticity prior to fracture, which is evidenced by the deviation from linearity in the stress-strain curves, and exhibited yield stresses approaching 2000MPa and 1500MPa, respectively. Plastic strain was limited to approximately 1% for the finer microstructure (Alloy 12Cr-865) and 5% for the coarsened microstructure (Alloy 12Cr-1050). With the constant 30vol%σ present in these two microstructures, it can be said that the scale of the microstructure has some control over the strength and ductility, though while strength increases with refinement, the ductility has declined for these polycrystalline samples.

As the alloy compositions move toward lower volume fractions of the σ-phase, it is expected that yield strength will drop and ductility will increase due to an increase in the volume of the load-bearing ductile matrix (the γ-phase) and, in turn, a decrease in the number of hard σ-phase particles. Though, interestingly, the stress strain curve for Alloy 12.5CrMo-865 with 22vol%σ (Figure 5-2a) shows an increase in yield strength and greater ductility compared to both aging conditions of Alloy 12Cr with 30vol%σ. Similar to Alloy 12Cr, this alloy with 22vol%σ displayed a trend of decreasing yield strength and increasing ductility as the aging temperature increased (Figure 5-2). It should be noted, that only one data point for Alloy 12.5CrMo-865 is reported here because the second sample fractured in the linear elastic region likely due to faulty sample preparation. During testing a significant amount of chipping of a sizable portion of the sample corner was observed. The test was stopped. Despite the faulty sample preparation, the fracture occurred in the linear elastic region at a stress level above 1900MPa.

Alloy 13CrMo with the lowest volume of hard particles (13vol%σ) resulted in lower YS (Figure 5-3) as compared with the previous alloys at a given aging temperature. When comparing alloys 12.5CrMo and 13CrMo, these two materials followed the expected trend of lower strength as the volume fraction of hard particles was reduced, and again, as the aging temperature increased, the strength decreased and the ductility was enhanced. It should be noted that for alloys 12.5CrMo and 13CrMo, the coarsest microstructures for both alloys exhibited significant increases in plastic strain to failure and decreased yield strengths.

The final alloy tested under compression, Alloy 11-1100, was the materials whose soln+WQ structure contained coarse γ-phase throughout the material which formed upon quenching. As shown in section 4.3.2, the resulting aged structure was far coarser than the previous alloys presented. The 12vol%σ is the lowest volume fraction of the alloys examined in this study, though the two stress-strain curves (Figure 5-4) from this material consistently showed a much lower amount of strain prior to failure, while exhibiting a yield strength comparable to that of alloys 12.5CrMo-1050 and 13CrMo-1050. Along with the relative low ductility and yield strength, the main disadvantage that was evident in Alloy 11 was the inability to control the precipitation of the microstructure.

5.1.2 Interrupted Compression tests

In order to determine when cracking started, interrupted compression tests were performed. In alloys with >50vol%σ the microcracks developed in the brittle σ-phase [16, 29, 55]. The reduced volume fraction of the σ-phase resulting in a more ductile γ-matrix, along with the refinement of the σ-phase may change the mechanisms of fracture initiation. To explore the development of microcracking in an alloy with a low

volume fraction of the σ-phase, a sample of Alloy 13CrMo-1000 was compressed at 1.4% plastic strain and unloaded. The stress-strain curve is shown in Figure 5-5 and, to ensure consistency in these data, it was overlaid on the original curve (light green curve in Figure 5-5) presented in section 5.1.1.

A sample of Alloy 11-1100 was selected for an interrupted compression test to determine if a coarsened σ-phase would play a role in crack initiation. This sample was loaded twice and the curves (dark purple curves) are shown in Figure 5-6. The first test was run up to 0.5% plastic strain. The sample was examined then rerun up to 3.7% plastic strain. The second run was necessary due to an absence of microcracking observed after the initial loading. Further results and microstructural analysis of the samples from these tests will be presented in the following sections as they are relevant to the discussion.

5.2 Deformation and Fracture on the Macroscopic Level

5.2.1 Macroscopic Deformation

The faces of a rectangular compression samples were finely polished and examined with OM and SEM. Figure 5-7a is a compilation of OM images mapping out the surface of the sample of Alloy 13CrMo-1000 which had been loaded to 1.4% plastic deformation. The prior β-grains, which now consisted of the two-phase γ+σ microstructure, were exposed due to what appears to be deformation localizing in the vicinity of the prior grain boundaries. Upon closer observation of a triple point (Figure 5-7b), it was clear that the Widmanstätten γ-phase was present at the prior β grain boundaries and deformed inhomogeneously as compared with the microstructure within the bulk of the prior β-grain. In the region away from the prior β grain boundary each

grain in Figure 5-7b appeared different, but within each respective grain, the deformation was consistent. This suggests the likelihood of an orientation relationship between the prior β crystal and the γ-phase which evolved from it upon aging. In addition, there are few prior β-grains (between 5 and 8) in a given compression sample, so the constraint, and therefore the strain accommodation, varies from grain to grain. The accommodation of neighboring grains also resulted in decreasing severity of the deformation as the prior β grain boundaries got further away, such that the middle portion of the sample contains the majority of the severe deformation. This phenomenon is well documented for single phase polycrystalline materials [79] and in this case, albeit on a macroscopic level, the remnants of the large grained pure β-phase imparted behaviors of a pure single phase polycrystalline material.

5.2.2 Macroscopic Fracture

The compression of these samples resulted in fracture of two types when observing with the naked eye. The alloys 12Cr-1050, 12.5CrMo and 13CrMo remained wholly intact upon compression to failure (failure in this case being a precipitous drop in the ability to bear load), with the exception of some samples where minimal chipping off of a corner occurred due to imperfect sample preparation. The fine microstructure with 30vol%σ (Alloy 12Cr-865) fractured into large pieces and the path of crack propagation was not clearly obvious. As for the intact samples, the fracture occurred in two ways; 1) slabbing, where large vertical cracks span the height of sample and 2) cracking which follow seemingly intergranular fracture paths along the prior β grain boundaries. The nature of fracture is probabilistic and the common observation from these samples leads to the conclusion that when a prior β grain boundary is in a favorable orientation

for fracture then the crack proceeds along the prior boundary. A typical example of this type of fracture is presented in Figure 5-8a where a sample of 12Cr-1050 was compressed to fracture resulting in a large crack which followed a prior β grain boundary until it reached a triple point, where a prior boundary was no longer oriented favorably for propagation, and so the crack proceeded through the bulk of the prior β-grains. Furthermore, it will come to be shown that the majority of catastrophic failure of these samples was a result of fracture initiation near these prior boundaries, whether or not the cracks propagated along them after initiation.

Clues into the macroscopic fracture behavior of Alloy 12Cr-865, which fragmented into several large pieces, revealed themselves when observing the fracture surface. On this fracture surface, shown in Figure 5-8b, the bottom of a large prior β-grain was exposed, revealing that this alloy also fractured in an intergranular-like manner. Upon closer observation, as seen in the higher magnification image in Figure 5-8b, the fracture surface is tortuous which suggests that, in fact, the fracture that occurred in these alloys was a result of crack propagation in the microstructure adjacent to the boundaries and not in a truly brittle manner as is the case with normal intergranular fracture.

5.3 Deformation and Fracture on the Microscopic Level

This section will present the deformation and fracture behavior of the γ and σ phases in polycrystalline samples. Two regions of interest have been identified: 1) near the prior β grain boundaries where the coarse Widmanstätten γ-phase is present; and 2) away from the prior β grain boundaries where the fine γ+σ microstructure formed upon aging.

5.3.1 Deformation Near the Prior β Grain Boundaries

As shown in Section 5.2, there was significant deformation and, in many cases, fracture along prior β grain boundaries. The interrupted compression tests at low plastic strains were designed to observe the localized deformation near the prior β grain boundaries for the purpose of understanding how microcracking developed in these alloys.

Figure 5-9a and Figure 5-9b are OM and SE micrographs taken from the same spot in the region marked '**A**' on the compilation of images in Figure 5-7a. These images revealed significant deformation localized in the vicinity immediately adjacent to the prior boundary. The Widmanstätten γ-phase emanated from both sides of the boundary, but due to the crystallographic nature of the growth, on the right side of the boundary it grew nearly perpendicular and on the left side it grew at a small angle or nearly parallel, to the boundary. The microstructure emanating from the left side seemed to be accommodating a large amount of the strain as compared to the right side and compared to the regions not directly adjacent to the prior boundary. At higher magnification of the left side of the prior boundary (Figure 5-10) slip lines and significant microcracking were observed within the Widmanstätten γ-laths, while on the right side of the boundary no slip lines were apparent and only limited microcracking developed. This is likely do to the particular stress state on the material around this boundary in coordination with the crystallographic orientation of the Widmanstätten laths on either side of the boundary.

A FIB was employed to extract a TEM foil from a similar region in the same sample described above. Figure 5-11a shows an SE image of the exact area from

which the foil was taken. Figure 5-11b shows a BSE image of the FIB trench and a TEM micrograph of the foil is overlaid on the trench. The goal of this extraction was to cross-section the Widmanstätten γ-laths and observe the deformed microstructure therein. A larger image of the TEM foil is shown in Figure 5-12a and the important features for this analysis are the two large, dark regions outlined in the top-middle portion of the micrograph. These samples included cross-sections of the γ-laths. In general, these laths are from 1-2μm in diameter and upwards of 20μm in length. At particular tilting angles in the TEM, the needle-like features shown in Figure 5-12b and Figure 5-12c are visible within the cross-section of the large γ-laths and terminate at the lath boundary. The fact that these needle-like features are apparent at the same tilt angle is evidence that the two lath cross-sections have a common crystallographic orientation which is consistent with the formation of two Widmanstätten laths in the same packet. Several σ-phase particles lie between the two γ-laths and, also, are scattered within the γ-laths. The identity of these particles was confirmed from SAD patterns and an example of this is shown in Figure 5-13. An SAD pattern was taken from an area encompassing a needle and the γ-lath (Figure 5-14a and 5-14b) as well. The analysis of the diffraction pattern confirmed that the needle-like structure was, in fact, a twin boundary of the 1/6 <112]{111} type with beam direction B= <110]. The diffraction pattern has higher and lower intensity spots labeled in red and green, respectively. This matrix/twin pattern contains spots from two crystallographic orientations of the γ-phase and there are coincident lattice reflections that are common between the two orientations. Figure 5-15 shows a different tilt angle of the γ-laths revealing arrays of dislocations. The

dislocations interacted with the twin boundaries and piled up in regions around σ-particles.

5.3.2 Deformation Away From the Prior β Grain Boundaries

While some regions immediately adjacent to the prior boundaries exhibit the most severe deformation, regions away from the prior β grain boundaries also exhibit extensive deformation to a diminishing effect as the distance from the prior boundary increases. Figure 5-16 shows an optical micrograph (left) taken from the area label region '**B**' in Figure 5-7. This area consists of the fine γ+σ microstructure that formed upon aging. In the remaining SE images on the right in Figure 5-16, the degree to which the microstructure was deformed was observed to decrease in severity as the distance from the boundary increases. This is consistent with the heterogeneous deformation of polycrystalline materials.

A look at higher magnification at an area which experienced a relatively large amount of deformation (Figure 5-17) reveals significant strain localization and slip band formation in the γ-phase (SE image in Figure 5-17b). This leads to microcracking as will be discussed in Section 5.3.2. There are two distinct directions that this localized deformation orients itself: 1) perpendicular to the loading axis and at a relatively consistent inclined angle to the loading axis. This is expected to be a result of the textured γ+σ microstructure which evolved from the parent β-phase upon aging. As explained earlier, the appearance and directionality of the localized strain from each β-grain in a given sample was different. In the BSE image in Figure 5-17c, the σ-phase is observed to be unaffected by the impingement of the slip bands on these particles. This phenomenon, while surely leading to enhanced strength in these microstructures, may

promote the formation of microcracks at the interface between the γ and σ phases, as will be discussed further in section 5.3.4.

When moving to a distance of approximately 1mm from the prior boundary, the areas of strain localization are seldom observed, though one such area is shown in Figure 5-18. Here, the nature of the deformation was the same as that observed in Figure 5-17, but to a much lesser extent due to the distance from the highly constrained region near the prior β grain boundary where the majority of the strain is accommodated.

5.3.3 Fracture Near the Prior β Grain Boundaries

It was shown in previous work [29, 55] that in alloys with very high volume fractions of the σ-phase, plasticity in the γ-phase induced intergranular fracture through both γ/σ and σ/σ interfaces. Once the crack tip went beyond the material affected by the plastic zone, the crack propagated primarily transgranularly through the σ-phase and in an interfacial manner when a ductile γ-particle was encountered. In the current work, significant plastic deformation localized in the Widmanstätten γ-laths at the prior boundary appeared to be causing microcracking within the γ-phase itself (Figure 5-10) rather than at the γ/σ interfaces as was observed in the previous study. Figure 5-19a shows an SE image of the same boundary where slip bands and microcracks have developed in a similar manner but were further along in the deformation and fracturing processes. In the high magnification SE image in Figure 5-19b, it shows that the slip bands traversed the microcracks and there were also slip bands which appeared parallel to the microcracking. In addition, the tortuous fracture path of the microcracks (Figure 5-19b appear to be affected by the slip bands present in this region. Here the

interaction of the twin boundaries identified in the coarse γ-laths along with the extensive slip observed on the sample surface cause regions to build extreme localized stresses within this phase. Locking mechanisms in the γ-phase can lead to microcrack formation based on energy calculations [80, 81] and TEM observation [82-85]. While none were able to be identified in the TEM study of this work, the evidence presented here does suggest this to be a likely culprit in the evolution of microcracks in this region of coarse γ-laths.

It should be noted that microcrack development in the coarsened microstructure in Alloy 11 had very similar microcrack morphology in the vicinity of the prior β grain boundary. Figure 5-20a and Figure 5-20b show low magnification SE and BSE micrographs of an identical spot in the vicinity directly adjacent to the prior boundary. Compared to the refined microstructure, the γ-phase at the prior boundary in the coarsened structure was much less elongated and no longer appears to be of Widmanstätten morphology, though like the refined structure, the γ-phase at the boundary is significantly coarser than the microstructure within the bulk of the prior β-grain. As shown in Figure 5-20c, microcracking is significant in this area and almost solely lies within the γ-phase barring the occasional interfacial microcrack.

The coalescence of intense microcracking which had developed within the γ-phase led to much larger microcracks in the microstructure directly adjacent to the prior boundary. This is shown in the OM, SE and BSE images of Alloy 13CrMo-1000 in Figure 5-21. This large crack, if located on a favorably oriented prior grain boundary, would propagate through the intensely microcracked γ-phase and through the γ/σ interfaces adjacent to the prior grain boundary. The only occurrence of fracture through

the σ-phase was when a crack approached an elongated σ-particle close to perpendicular giving the crack no opportunity to circumvent the hard particle.

5.3.4 Fracture Away From the Prior β Grain Boundaries

While the prior β grain boundaries have shown to encompass a large density of the microcracking observed in deformed samples, these boundaries can be engineered in various ways or by-passed altogether by formation of single crystals, so the nature of crack initiation in the bulk of the specimen was of interest. Here, microcrack development in the refined structure of Alloy 13CrMo-1000 which was evolved from the quenched-in β-phase will be introduced and compared to microcrack development in Alloy 11-1100 which was aged from samples containing large amounts of γ-formation upon quenching resulting in a significantly coarsened microstructure (Alloy 11).

5.3.2.1 Refined Microstructure

In contrast to the coarsened Widmanstätten γ-lath microstructure near the prior boundary, the microstructure which formed upon aging fractured in an interfacial manner primarily in the regions of localized deformation displayed in images taken from region '**B**'. This is displayed more clearly in Figure 5-22. Figure 5-23 shows an area closer to the prior boundary that had experienced heavier damage and the interfacial cracks are beginning to coalesce by propagating in a transgranular manner through the γ-phase. Had significant microcracking leading to crack propagation not been dominated by the γ-laths at the prior boundary, these microcracks would likely lead to failure, though it is proposed that this would occur at a much greater final compressive strain value than observed in these polycrystalline samples because strain accommodation would be more uniformly distributed throughout the volume of the sample. In addition, a

proposed added benefit of the refinement of the microstructures would be greater uniform plastic deformation leading to enhanced tensile ductility. Localization of strain is a major factor which limits tensile ductility in TiAl-based alloys [86].As will be shown in Chapter 6, the positive effects of refinement may still be relevant to enhancing tensile ductility, though unsuccessful tensile testing (Appendix C) made it impossible to measure this proposed effect.

5.3.2.1 Coarsened Microstructure

The microcracking at the prior boundaries of Alloy 11 samples were similar to that of the more refined structures, though when observing the bulk of the grain there was a clear difference. Figure 5-24 shows examples of the microcracking present in the bulk of the interrupted compression test sample of Alloy 11. Microcracks were found almost exclusively within the σ-particles and they were cause by cleavage of this brittle phase as evidenced by their smooth crystallographic character. By reducing the size of the σ-particles from ~1μm to <300nm via aging from a successfully quenched-in β-phase, the mode of microcracking has been shifted from cleavage cracks forming in the brittle σ-particles to microcrack formation at the γ/σ interfaces. As a result, the initial crack size in either microstructure is limited to approximately the diameter of the σ-particle, so in the case of a coarsened microstructure the initial crack size is much larger and would likely lead to failure at a lower strain value in the absence of prior β-grain boundaries.

5.4 The Effects of Volume Fraction and Scale on Mechanical Behavior

Analysis of compression testing on polycrystalline samples has resulted in several trends that will be presented in this section and will be followed by a discussion on how

these general trends correlated to the deformation and fracture behavior which these samples exhibit.

5.4.1 Effect of Volume Fraction

When analyzing the effect of volume fraction it is important to limit the comparisons to alloys at constant aging temperatures so that the factors which affect the measured properties are limited. Also, it should be understood that there are many factors which dictate the behavior of these alloys, including composition of phases, particle/matrix coherency and scale, so the following is an attempt to isolate effect of the volume fraction of phases. As a general trend, the yield strength increased as the volume fraction of the σ-phase was increased (Figure 5-25a) and the ductility decreased with increasing volume fraction (Figure 5-25b). The strongest sample at 22vol%σ (12.5CrMo-865 with YS=2140MPa) was the exception to the trend. This apparent inconsistency shows that while the volume fraction of the σ-phase plays a role in the strength, other factors can be employed to optimize the mechanical properties of these alloys. This particular result was attributed to the size of the σ-phase in each sample (0.09μm in 12.5CrMo-865 and 0.14μm in 12Cr-865). The effect of scale will be discussed in Section 5.4.2.

In a previous study [55] where γ+σ alloys had volume fractions of the σ-phase that varied from ~0.5 to 0.7, the alloys fractured in the linear elastic region and the fracture strength was consistent (ranging from 1861 to 1911MPa) over this range of volume fractions. Although these alloys had coarser microstructures than the alloys in this study, the σ-phase was a connected matrix and so the compressive strength of the material seemed to be governed by the strong brittle matrix. Interestingly, when the

volume fraction of the σ-phase was significantly reduced in the current study, the yield strengths were at (Alloy 12Cr-865) or above (12.5CrMo-865) that of the previous study. In addition, the previous study showed that when an alloy has a two-phase β+σ microstructure with comparable σ-phase volume fraction (~0.7), then the yield strength precipitously drops (ranging from 1315 to 1422MPa). The explanation for this drop in fracture strength was associated with the change in composition in the σ-phase. However, like the alloys of the current study, the low relative yield strength of the β-phase which undergoes extensive plasticity maybe the cause of premature fracture in the β+σ alloy. It is proposed here that while the relative high strength of all the alloys mentioned are a result of the presence of the σ-phase, the extent of the strength achieved is governed by the onset of plasticity in the more ductile phase present within the microstructure. As a result, the alloys with high volume fractions of a connected σ-phase fracture soon after the onset of plasticity in the ductile particles because only a small volume of material can accommodate the plastic strain. The alloys in this study have a greater capacity to accommodate the local strains which occur upon the onset of plastic deformation in the γ-phase matrix. In the alloys in the current study, the high strength has been retained, and with the lowering of volume fraction of the brittle phase, the alloys appear more ductile and likely have been toughened significantly.

5.4.2 Effect of Microstructural Scale

Figure 5-26a and Figure 5-26b show the variation of yield strength with σ-particle size and aging temperature, respectively. As a general trend, each alloy in this study exhibited increased strength with the refinement of σ-phase particles, though it is clear that aging temperature plays a roll in the yield strength and ductility of these alloys. The

obvious deviations from the trend in Figure 5-26a were the points of Alloy 12.5CrMo-1000 and 12.5CrMo-1050 (red). These two samples were aged at different temperatures, but resulted in measurably the same particle sizes. The yield strength, however, was not entirely dependent on particle size and, in this instance, the variation of this property with aging temperature seems to have a more predictable dependence in these alloys. This is further evidenced by the presence of the Alloy 11-1100 data in Figure 5-26b. The particle size of 0.74 in this alloy was an outlier in Figure 5-26a as compared to the alloys which were able to successfully be quench-in as the β-phase to room temperature prior to aging. These results suggest that the aging temperature is affecting the yield strength in one or both of the following ways: 1) the composition of the γ-phase is changing with increased aging temperature in Alloy 12.5CrMo resulting in a softer material and 2) the increased aging temperature for all the alloys resulted in more relaxed γ/σ interfaces owing to a change in coherency. So, while smaller particle size was shown to result in increased yield strength, the composition of the γ-phase and coherency of the γ/σ interfaces are likely important factors as well in governing the yielding of these materials.

Figure 5-26c and Figure 5-26d show the variation of ductility (described here as the plastic deformation from the yielding point until fracture) with particle size and aging temperature. For the polycrystalline samples that were aged from a quenched-in β-phase, the trends were generally consistent. As the particle size of a given alloy composition increased, the ductility increased, and akin to the results presented in Figure 5-26a, the samples of 12.5CrMo with larger particles (0.24μm) resulted in vastly different ductility despite the similar scale. Though, when again plotting versus aging

temperature the trend was consistent for alloys 12Cr, 12.5CrMo and 13CrMo. Interestingly, Alloy 11-1100 data (purple) in Figure 5-26d show a low relative ductility despite a higher aging temperature, larger particle size and lower σ-phase volume fraction, all of which correlate with increased ductility in alloys 12Cr, 12.5CrMo and 13CrMo.

The proposed effect of microstructural scale on the ductility of the alloys was challenged by the results produced from these samples. The refined microstructures were expected to result in enhanced ductility. The results from this study suggest that the relative low ductility in refined microstructures was owed to the damage which accumulated in the Widmanstätten γ-phase adjacent to the prior β-phase grain boundaries, the yield strength of the aged material in the bulk of the prior β-grains and the UCS of the samples. The following discussion will show the connection between the microstructure and the resulting mechanical properties.

Yielding, from an engineering standpoint, occurs when slip presides consistently throughout the bulk of a specimen [79]. It is important to understand that localized plastic deformation can occur prior to the conventional yield point which by definition is offset from the proportional elastic limit. For the yield point to be surpassed in these alloys the microstructure comprising the majority of the grains must plastically deform, therefore, the yield strength in these alloys is controlled by the aged microstructure in the middle of the prior β-grains. This study shows the alloys plastically deform in a heterogeneous manner such that small volumes of the material plastically deform most likely prior to the conventional yielding point. This phenomenon occurs adjacent to the prior β-phase grain boundaries in the coarsened γ-laths where the local yield strength is

low compared to the bulk (due to a coarsened microstructure) and local strain is high due to the accommodation of neighboring prior β-grains. The micrographs in Figure 5-9 display the damage that occurred at the prior boundary at just 1.4%ε_p, confirming that severe localized deformation occurred prior to this point.

Generally, as the yield strength increases the ductility decreases (plotted for all alloys in Figure 5-27a). Plotting the ductility versus the UCS, shown in Figure 5-27b, reveals a nearly inverse trend wherein the stress at fracture is high when plastic deformation is high. This is to say that when an alloy has a lower yield strength (coarser microstructure), then the ductility and fracture strength are greater. As samples are compressed in the linear elastic region the local plastic deformation at the prior boundary begins and the extent of the damage that occurs is dependent on the yield strength of the bulk of the microstructure because it is essentially confining the soft planar boundary until the bulk itself can yield. For samples which have lower yield strength the damage would be minimal compared to samples with higher yield strength. The extent of plastic deformation experienced from this point on is governed by the size of the cracks which have formed at the prior boundaries, knowing that these cracks ultimately cause fracture in the majority of samples. The reason why microstructures (i.e. Alloy 12Cr-865, Alloy 12Cr-1050 and Alloy 12.5CrMo-865) have limited ductility is due to the extensive damage which occurred at the soft prior boundary close to the yield point. With the absence of these prior boundaries, the plastic deformation could occur in a more uniform manner resulting in a greater capacity for plastic deformation prior to fracture.

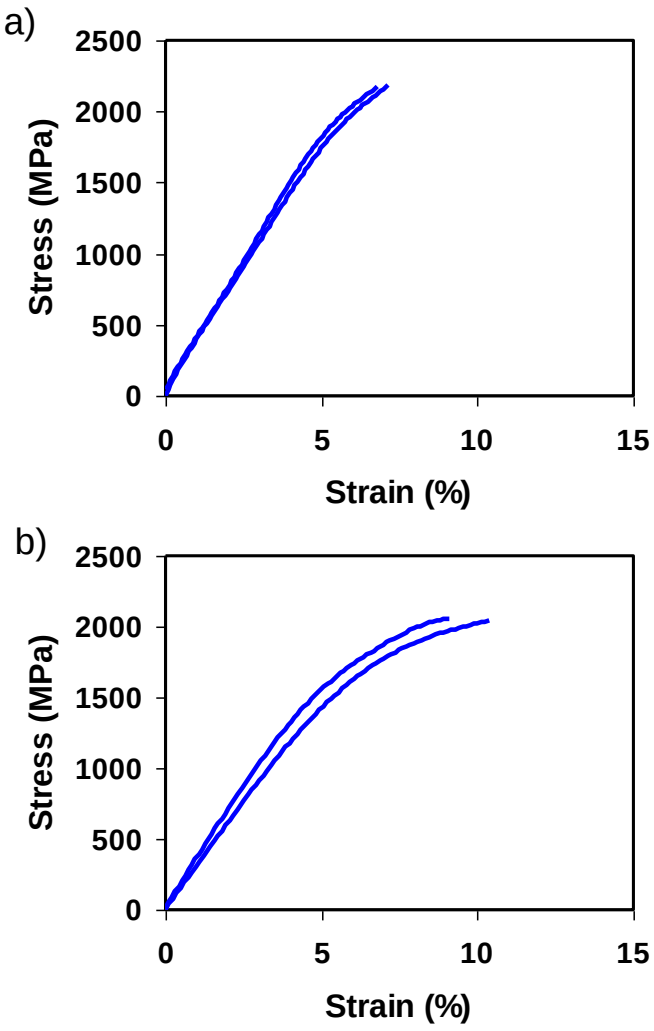

Figure 5-1. Engineering stress vs. strain curves for alloys a) 12Cr-865 and b) 12Cr-1050 tested at room temperature in compression (Courtesy of Michael S. Kesler)

Table 5-1. Mechanical properties of polycrystalline alloys under compression

Alloys	σ_y (MPa)	σ_{UCS} (MPa)	ε_p (%)
12Cr-865	1917	2150	1.5
	1922	2164	1.2
12Cr-1050	1483	2088	4.6
	1468	2037	5.1
12.5CrMo-865	2140	2643	6.7
12.5CrMo-1000	1643	2567	15.6
	1513	2205	13.9
12.5CrMo-1050	1108	2687	27.2
	1011	3075	35.0
13CrMo-865	1653	2514	10.5
13CrMo-1000	1342	2274	12.4
	1336	2139	12.5
13CrMo-1050	909	3106	31.8
11-1100	1112	2321	20.2
	1092	2259	22.0

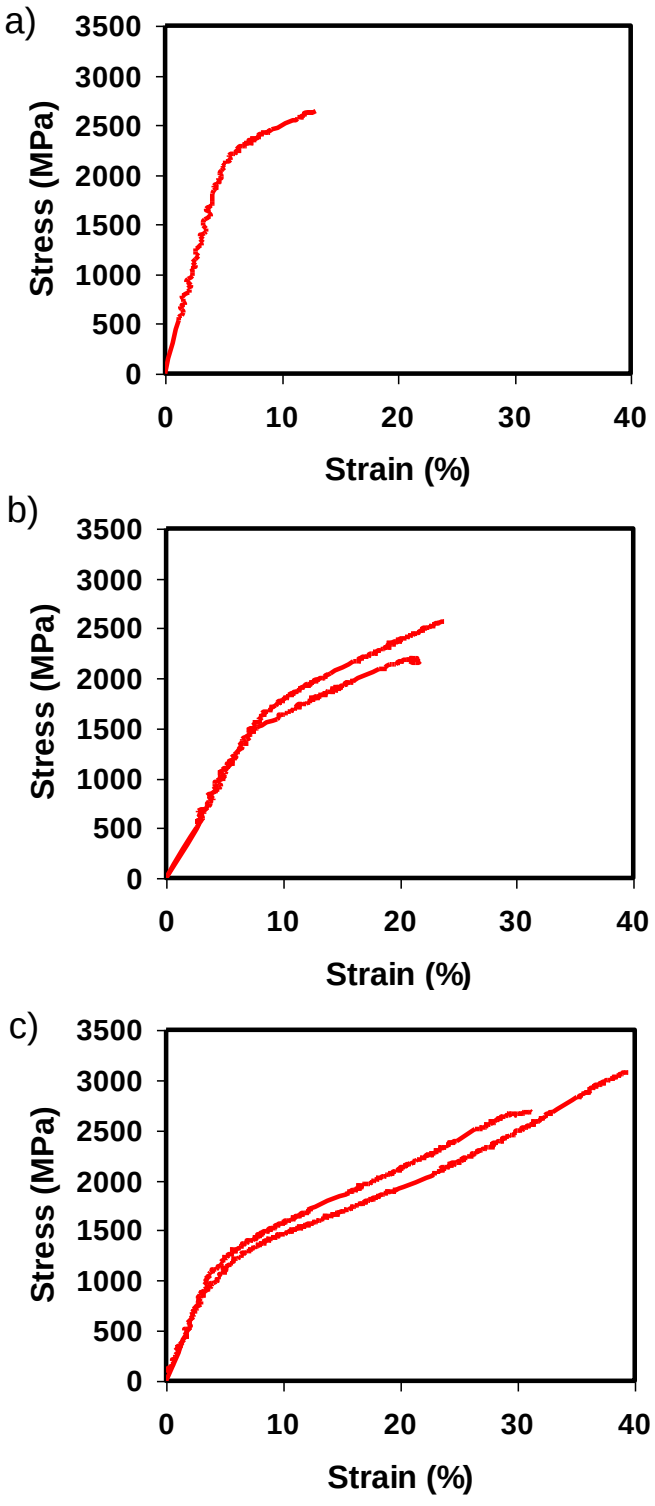

Figure 5-2. Engineering stress vs. strain curves for alloys a) 12.5CrMo-865, b) 12.5CrMo-1000 and c) 12.5CrMo-1050 tested at room temperature in compression (Courtesy of Michael S. Kesler)

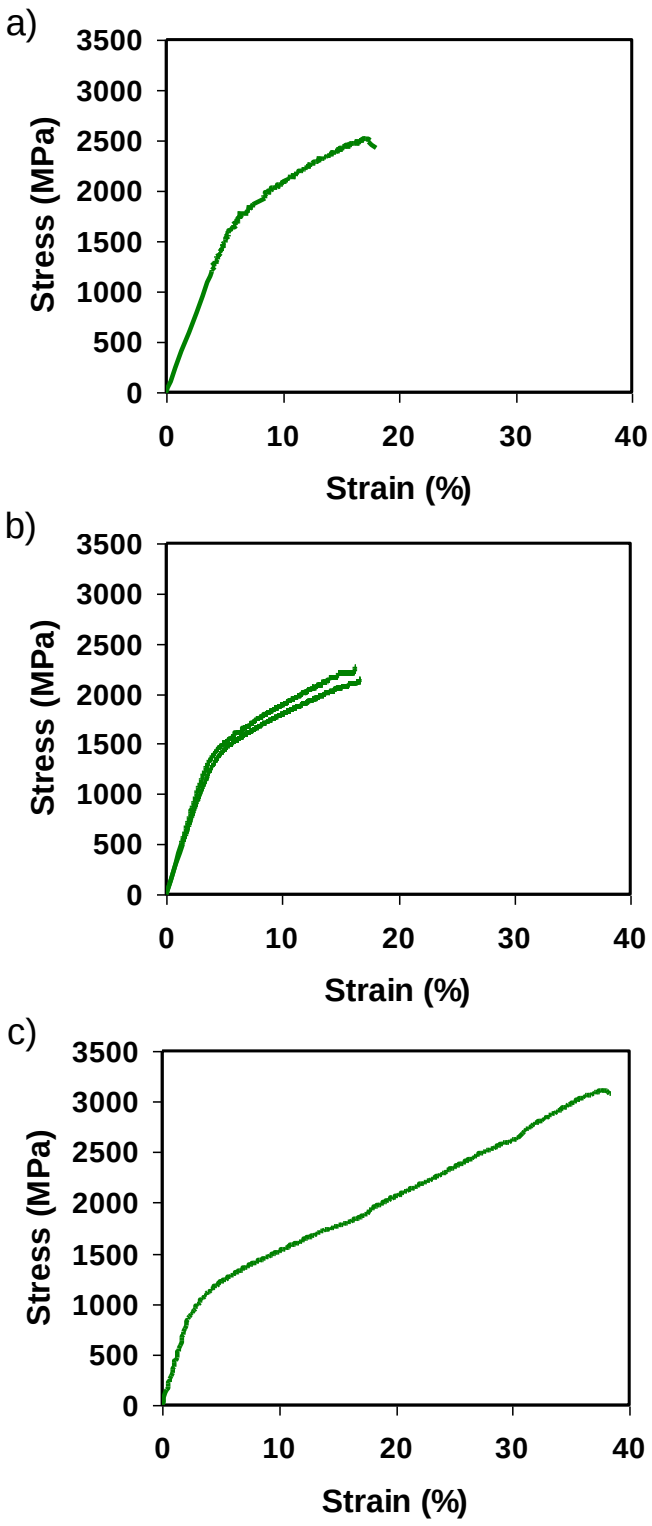

Figure 5-3. Engineering stress vs. strain curves for alloys a) 13CrMo-865, b) 13CrMo-1000 and c) 13CrMo-1050 tested at room temperature in compression (Courtesy of Michael S. Kesler)

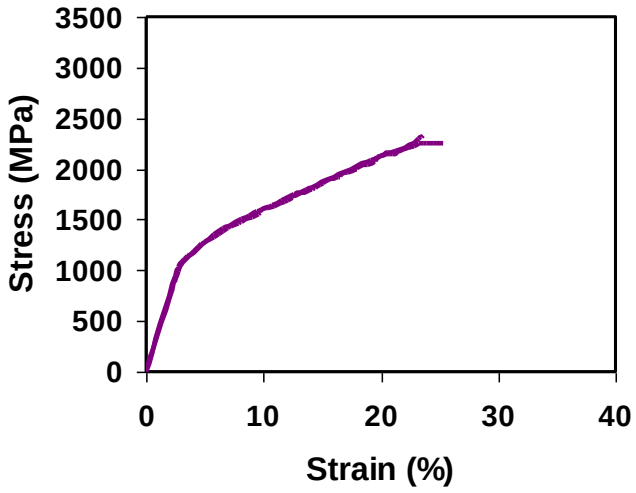

Figure 5-4. Engineering stress vs. strain curve for Alloy 11-1100 tested at room temperature in compression (Courtesy of Michael S. Kesler)

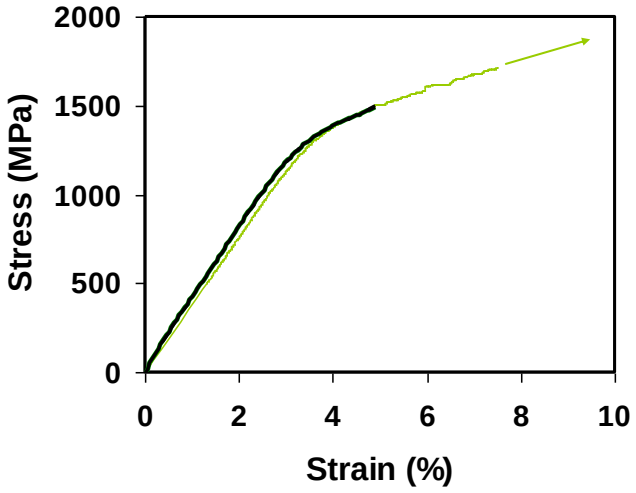

Figure 5-5. Stress strain curve of a room temperature interrupted compression test at 1.4% plastic strain on Alloy 13CrMo-1000 overlaid on curve from a sample loaded to fracture (Courtesy of Michael S. Kesler)

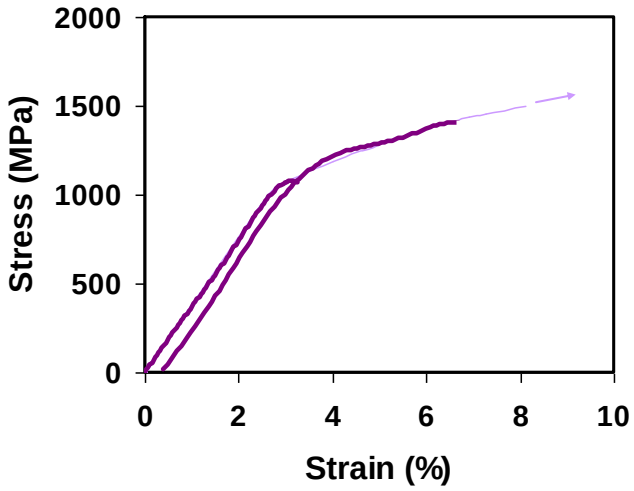

Figure 5-6. Stress strain curve of room temperature interrupted compression tests at 0.5% and at 3.7% plastic strain on Alloy 11-1100 overlaid on curve from a sample loaded to fracture (Courtesy of Michael S. Kesler)

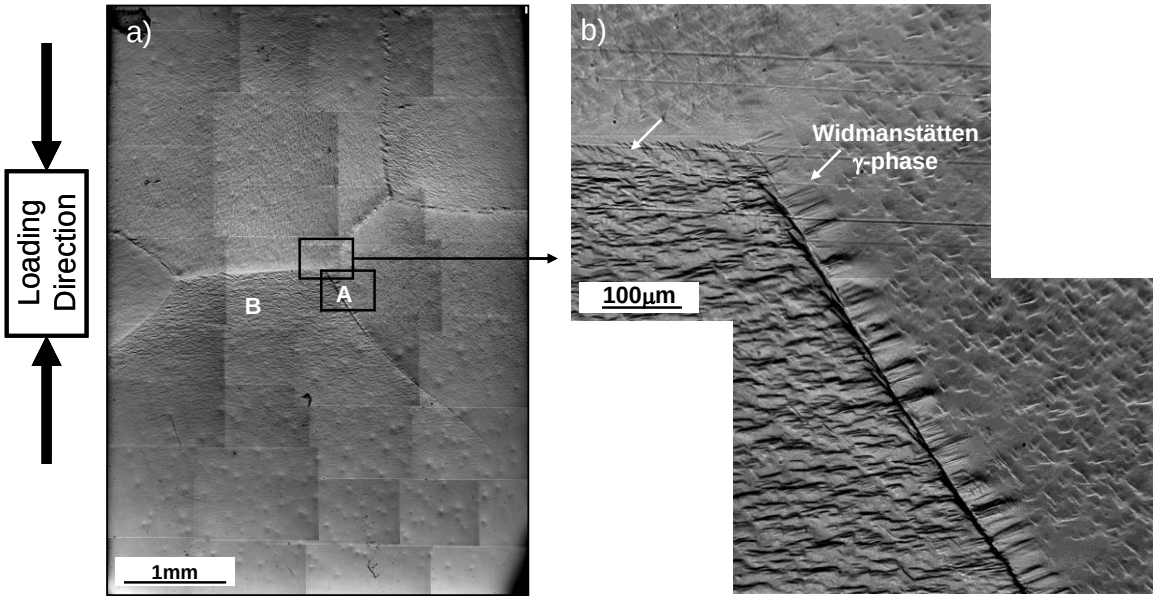

Figure 5-7. Surface deformation after interrupted compression. a) Compilation of OM images from the face of a 4x4x6mm compression sample of Alloy 13CrMo-1000 deformed to 1.4% plastic strain; and b) two adjacent OM images of a deformed triple point (Courtesy of Michael S. Kesler)

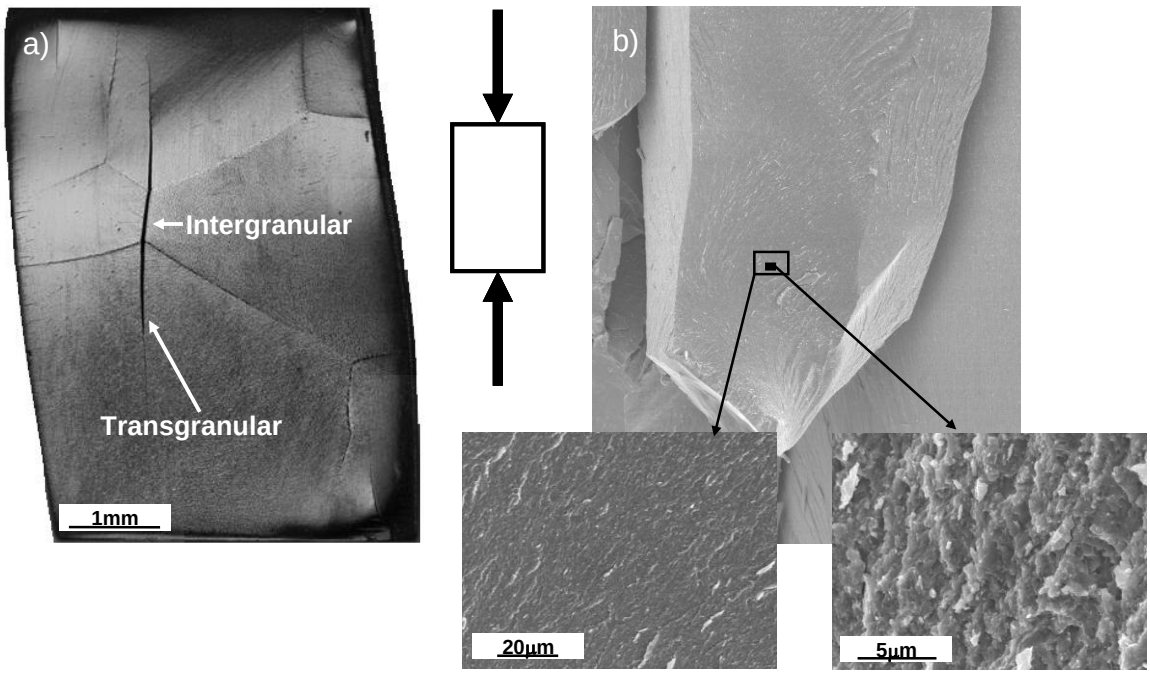

Figure 5-8. Micrographs of fractured compression samples. a) A compilation of OM images from the face of a fractured compression sample of Alloy 12Cr-1050; and b) a SE micrograph of a fracture surface from a fractured compression sample of Alloy 12Cr-865 (Courtesy of Michael S. Kesler)

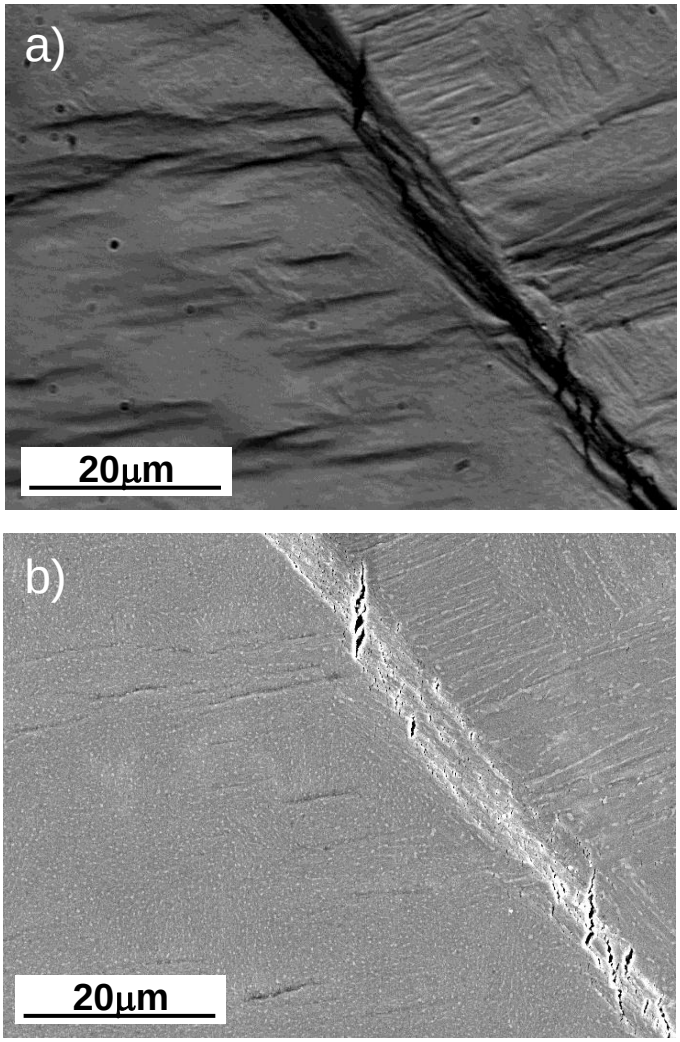

Figure 5-9. Surface deformation after interrupted compression. a) OM and b) SE micrographs taken from the same area in region 'A' from Figure 5-7a showing damage in the vicinity of a prior β-phase grain boundary (Courtesy of Michael S. Kesler)

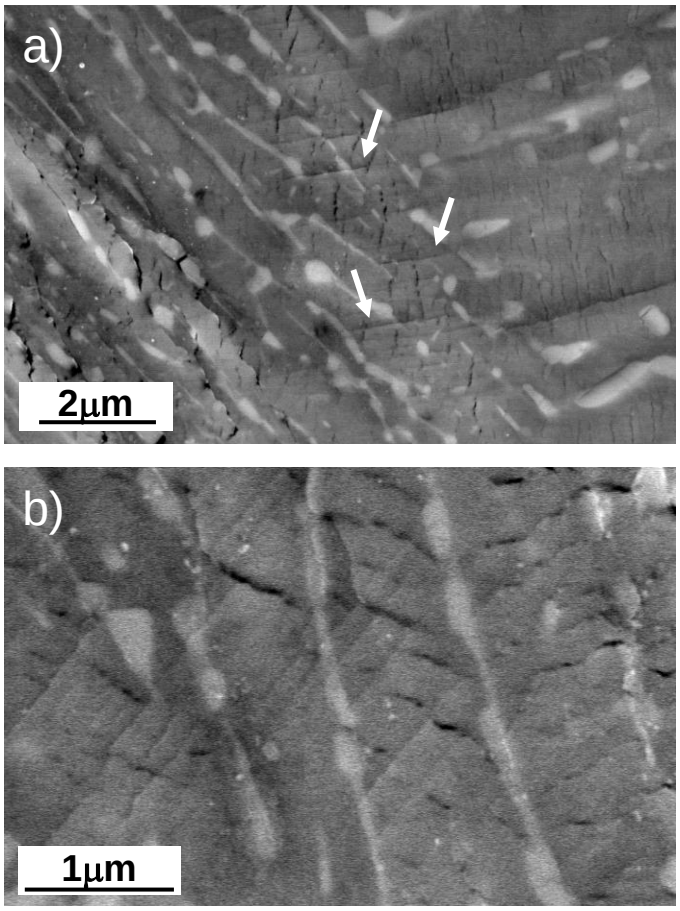

Figure 5-10. SE micrographs showing slip and microcracking in the vicinity of the prior β-phase grain boundary from region 'A' in Figure 5-7a (Courtesy of Michael S. Kesler)

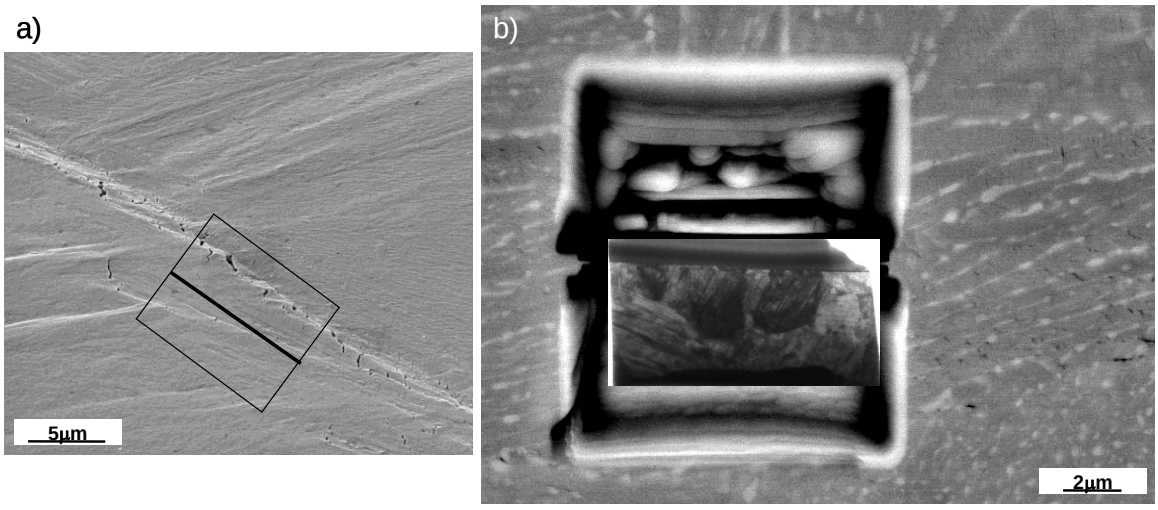

Figure 5-11. SE micrographs of the sample surface after interrupted compression showing a) the region near the prior β-phase grain boundary and b) the FIB trench with an overlaid TEM micrograph of the extracted foil (Courtesy of Michael S. Kesler)

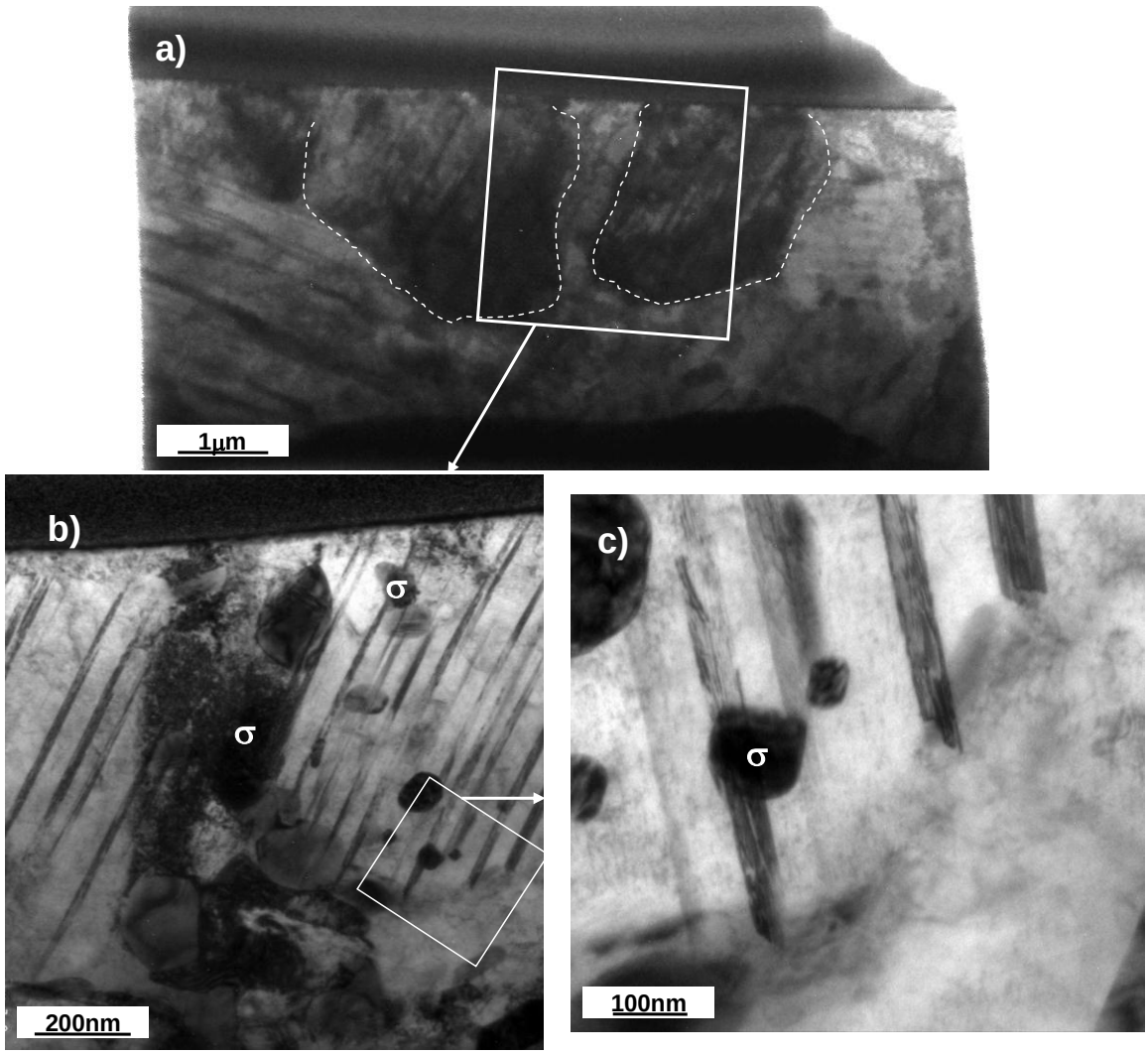

Figure 5-12. TEM micrographs of the FIB foil showing a) the cross-section of two Widmanstätten γ-laths (dotted white lines) (b) containing a needle-like structure while being surrounded by σ-phase particles and c) σ-phase particles were also observed within the cross section of the γ-laths (Courtesy of Michael S. Kesler)

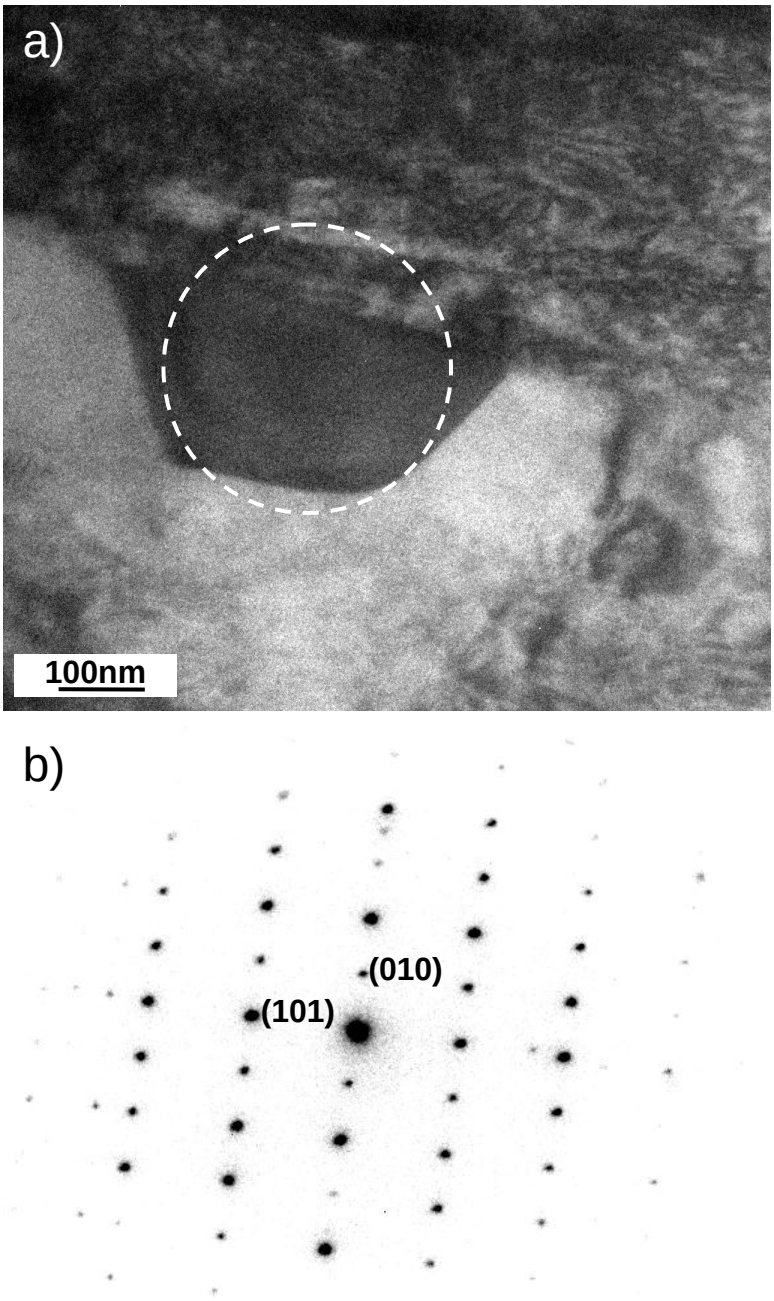

Figure 5-13. TEM micrograph and SAD pattern of a) a σ-phase particle with the white dotted outline of the SAD aperature and b) corresponding SA$\bar{D}$ pattern of the [101] zone axis (Courtesy of Michael S. Kesler and Kerry Siebein)

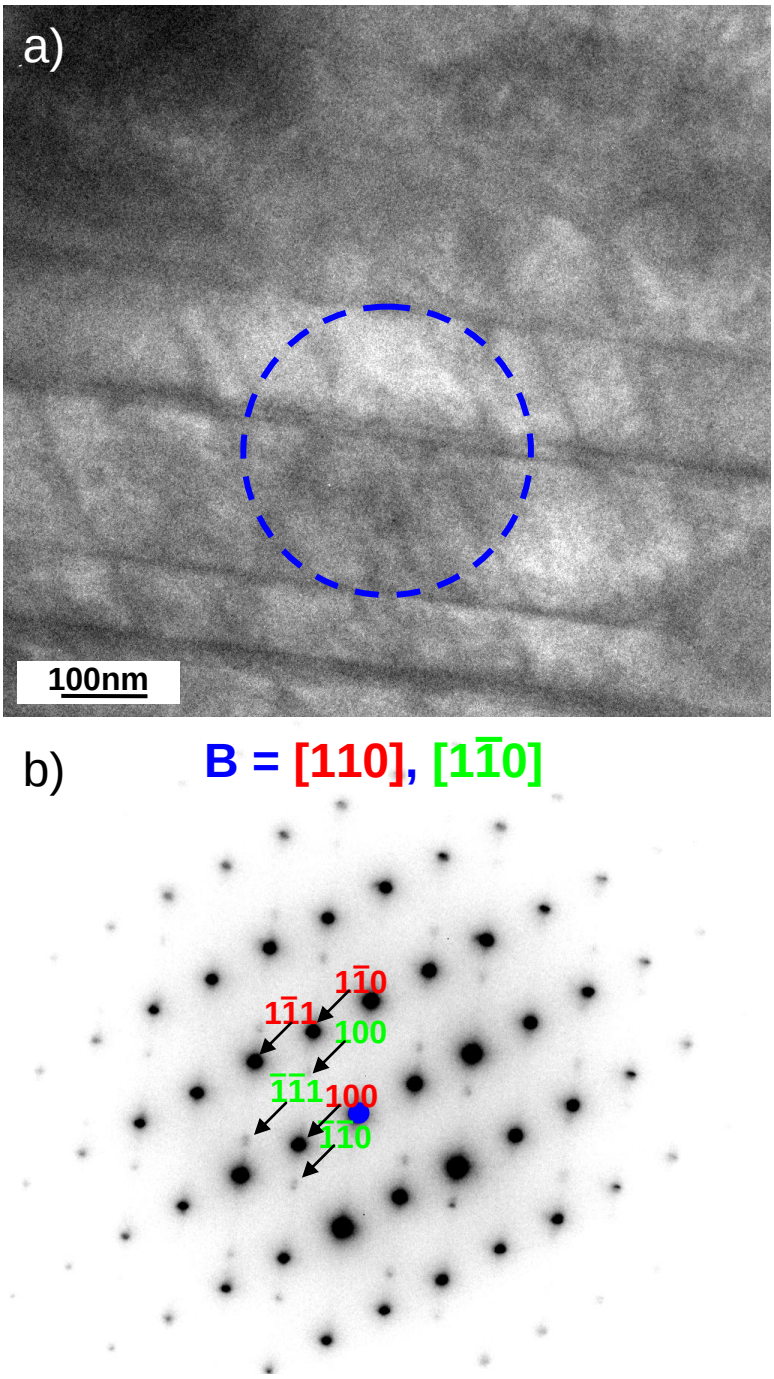

Figure 5-14. A TEM micrograph and SAD pattern taken from a) inside one of the γ-laths shown in Figure 5-12 revealing b) twinning of the 1/6<112]{111} type with beam direction B=<110] (Courtesy of Michael S. Kesler and Kerry Siebein)

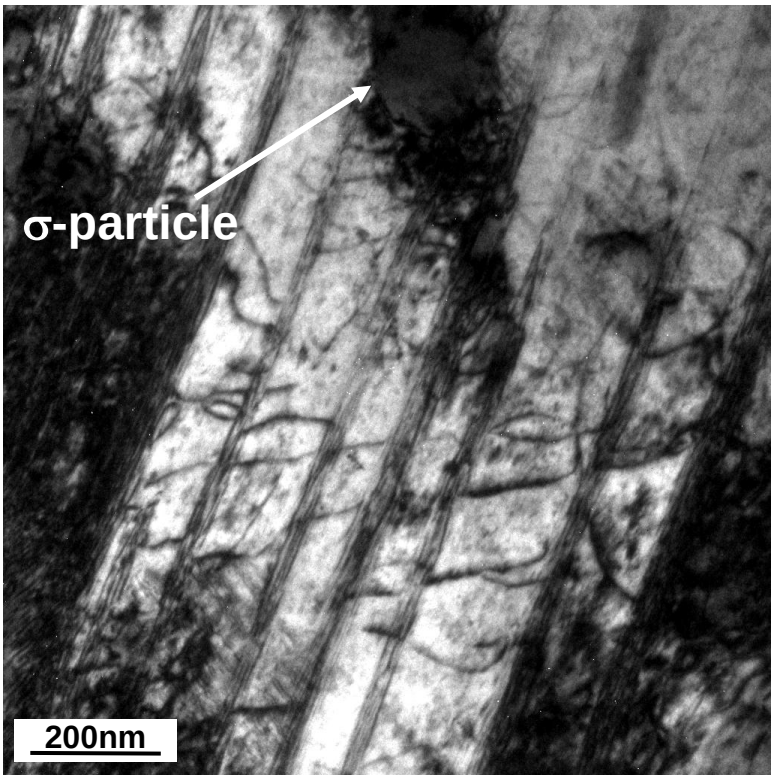

Figure 5-15. TEM micrograph of the inside of a γ-lath showing many dislocations interacting with σ-particles as well as the twin boundaries (needle-like features) which is evidenced by the discontinuous nature of the dislocations when encountering a twin boundary (Courtesy of Michael S. Kesler)

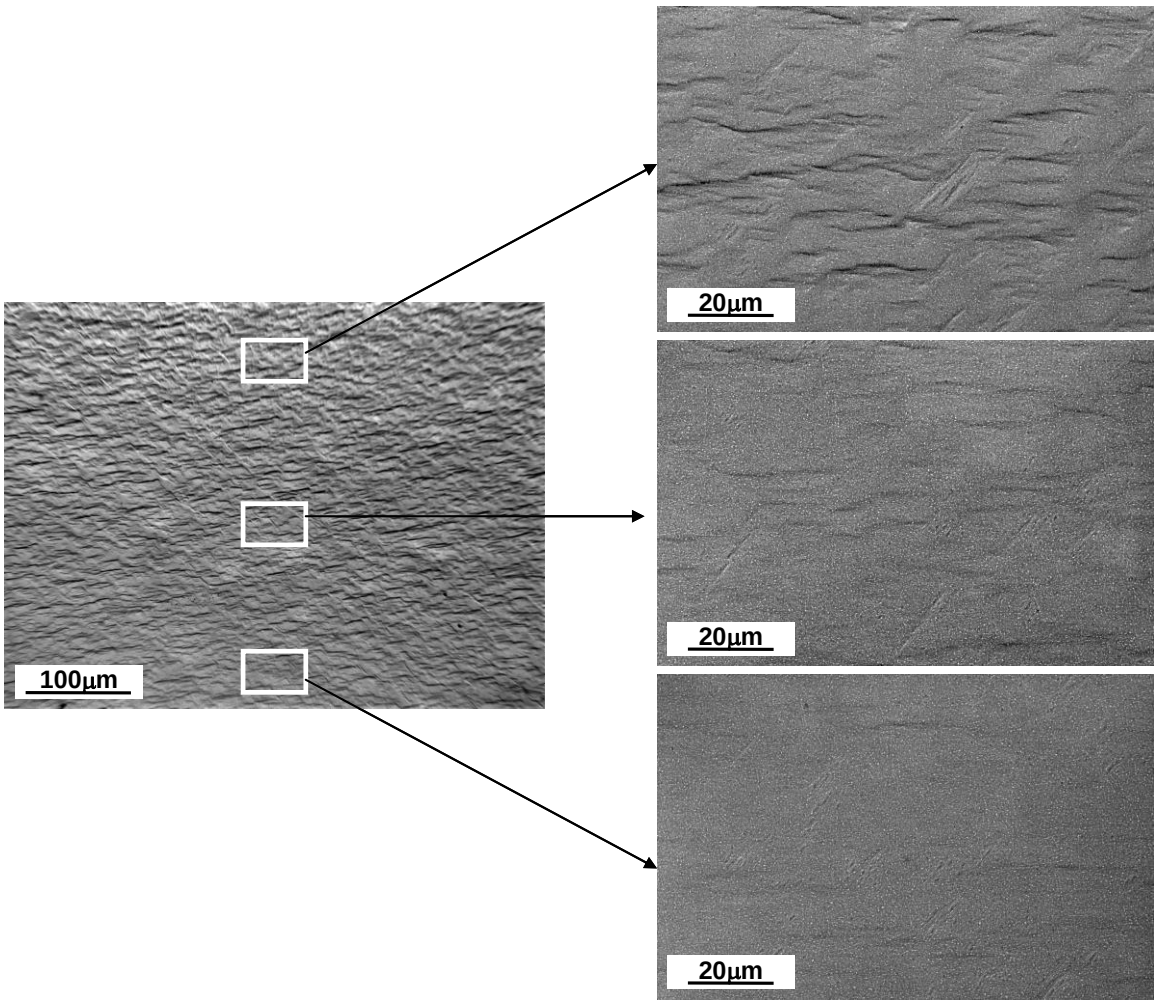

Figure 5-16. An OM image (left) taken from region 'B' from Figure 5-7a showing a decrease in deformation as the prior β-phase grain boundary becomes more distant and the SE micrographs (right) show this phenomenon at a higher magnification (Courtesy of Michael S. Kesler)

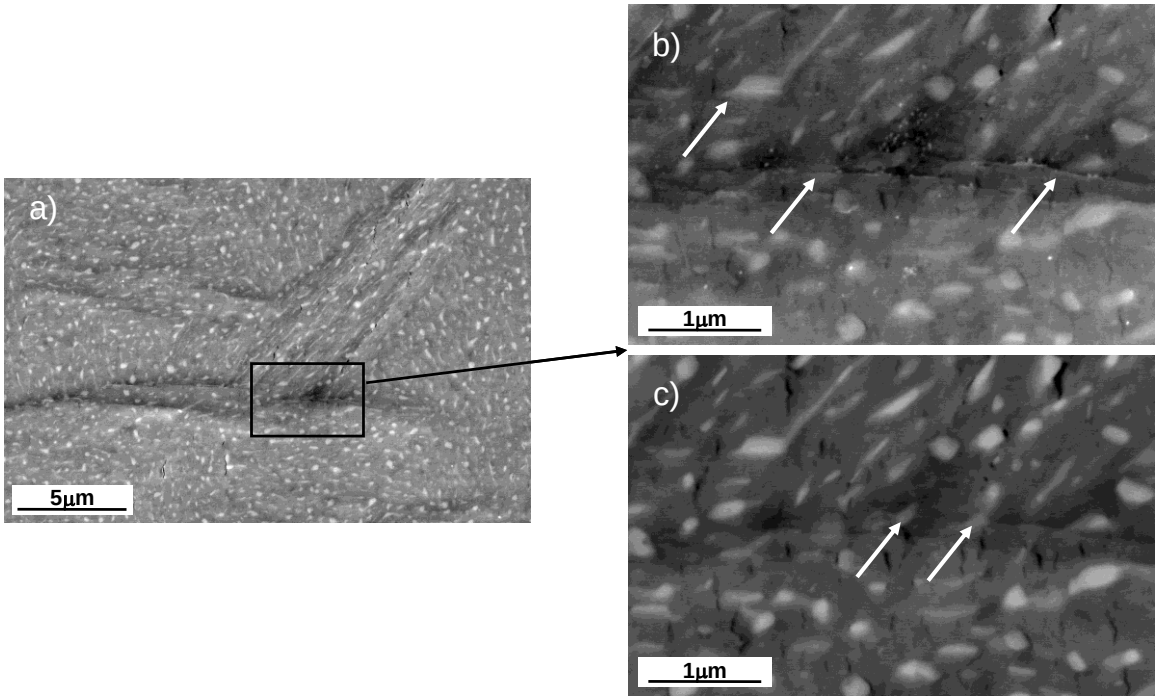

Figure 5-17. SE micrographs of an area of localized deformation from a) region 'B' relatively close to the prior β-phase grain boundary showing b) apparent slip band formation in the γ-phase, while c) the BSE micrograph reveals that the σ-phase is unaffected by the impinging band (Courtesy of Michael S. Kesler)

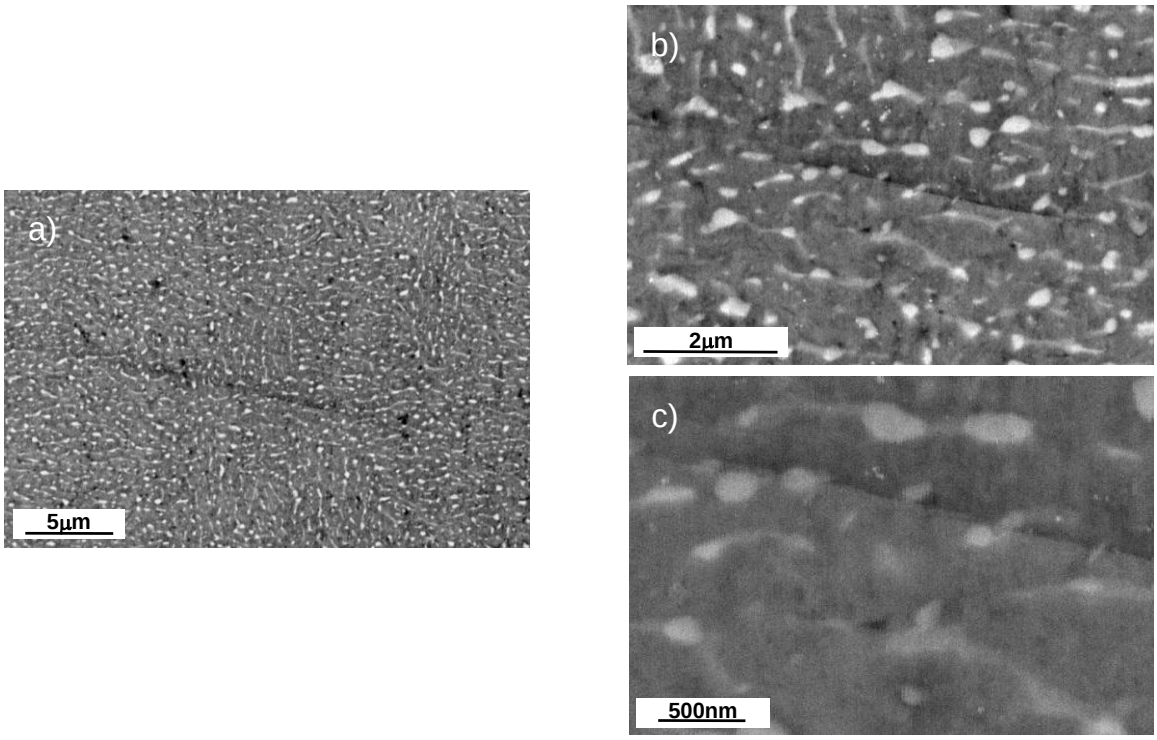

Figure 5-18. SE micrographs of the localized deformation in the a) middle of the prior β-grain below region 'B' from Figure 5-7a showing b) slip band development in the γ-phase and c) seemingly unaffected σ-particles similar to that seen in Figure 5-17b and Figure 5-17c (Courtesy of Michael S. Kesler)

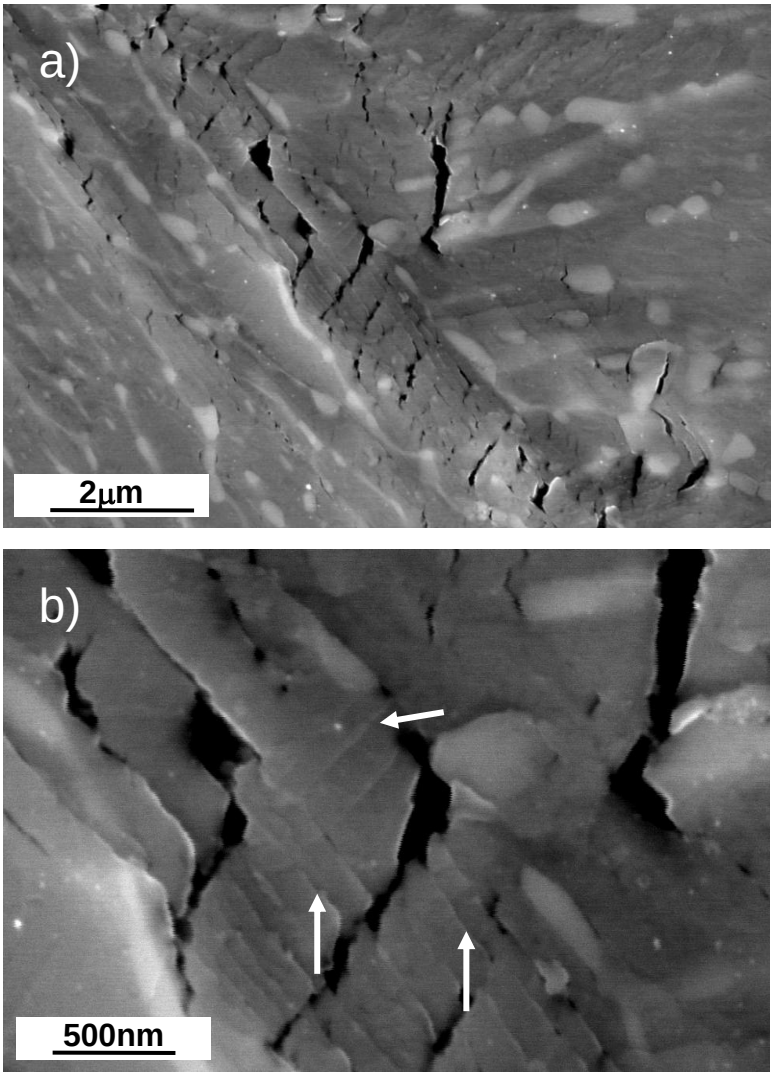

Figure 5-19. SE micrographs showing extensive microcracking a) in the vicinity of the prior β-phase grain boundary where b) slip bands (white arrows) are observed to be traversed and parallel to the microcracks (Courtesy of Michael S. Kesler)

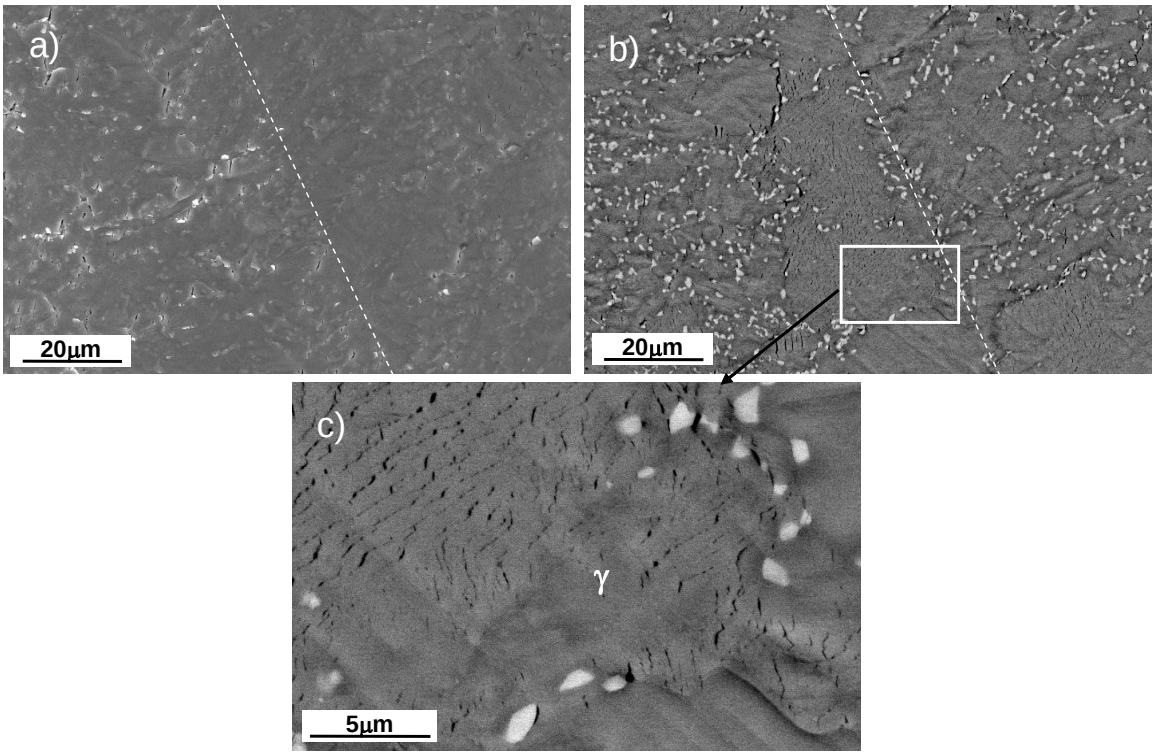

Figure 5-20. SEM micrographs of Alloy 11-1100-3.7%ε_p showing a) SE and b) BSE images taken from the same area of a prior β-phase grain boundary (dotted white line) revealing deformation and c) (BSE) extensive microcracking in the coarsened γ-phase (Courtesy of Michael S. Kesler)

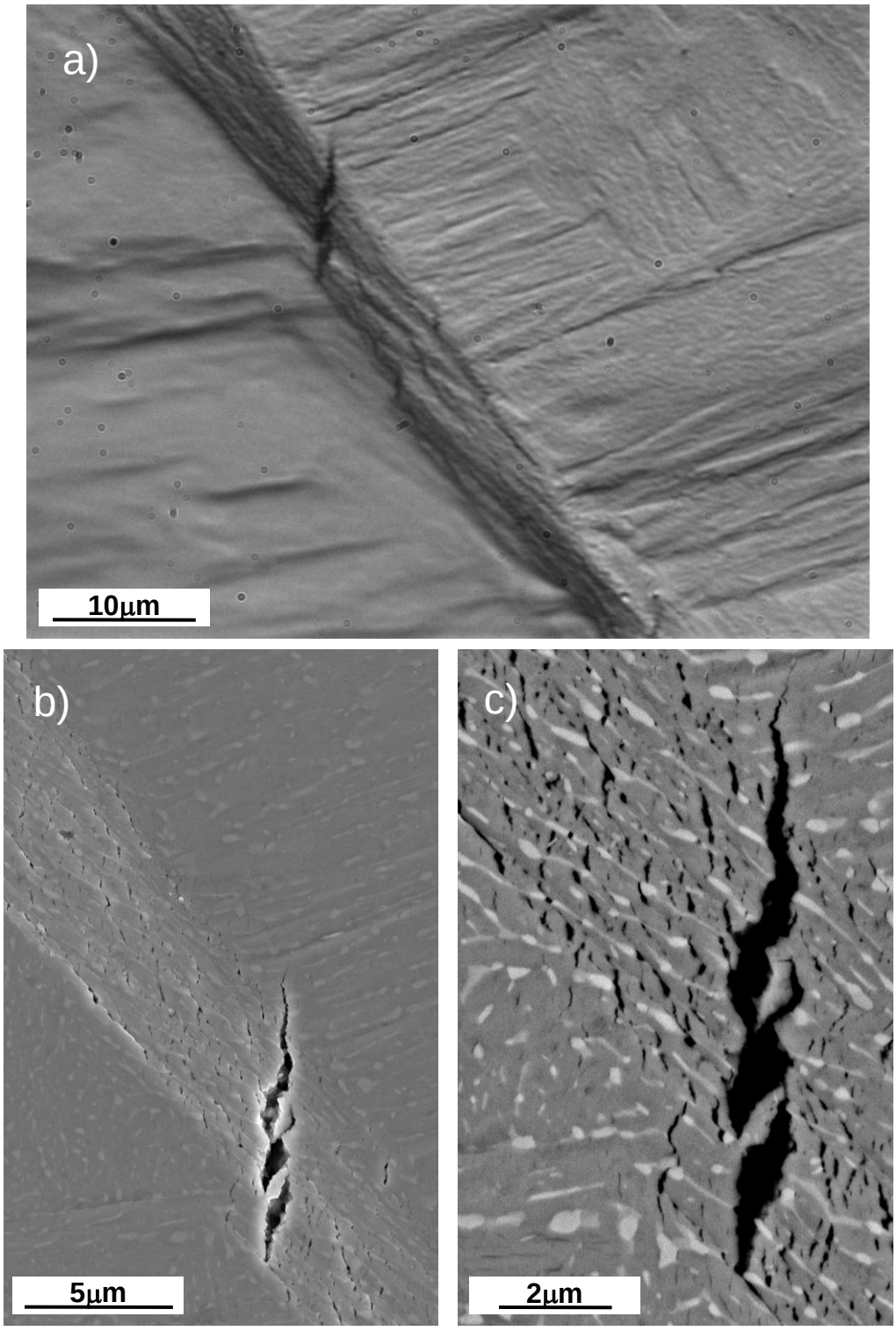

Figure 5-21. Alloy 13CrMo-1000-1.4%ε_p, a) OM, b) SE and c) BSE micrographs show the coalescence of microcracks forming a larger crack which originates near the prior β-phase grain boundary (Courtesy of Michael S. Kesler)

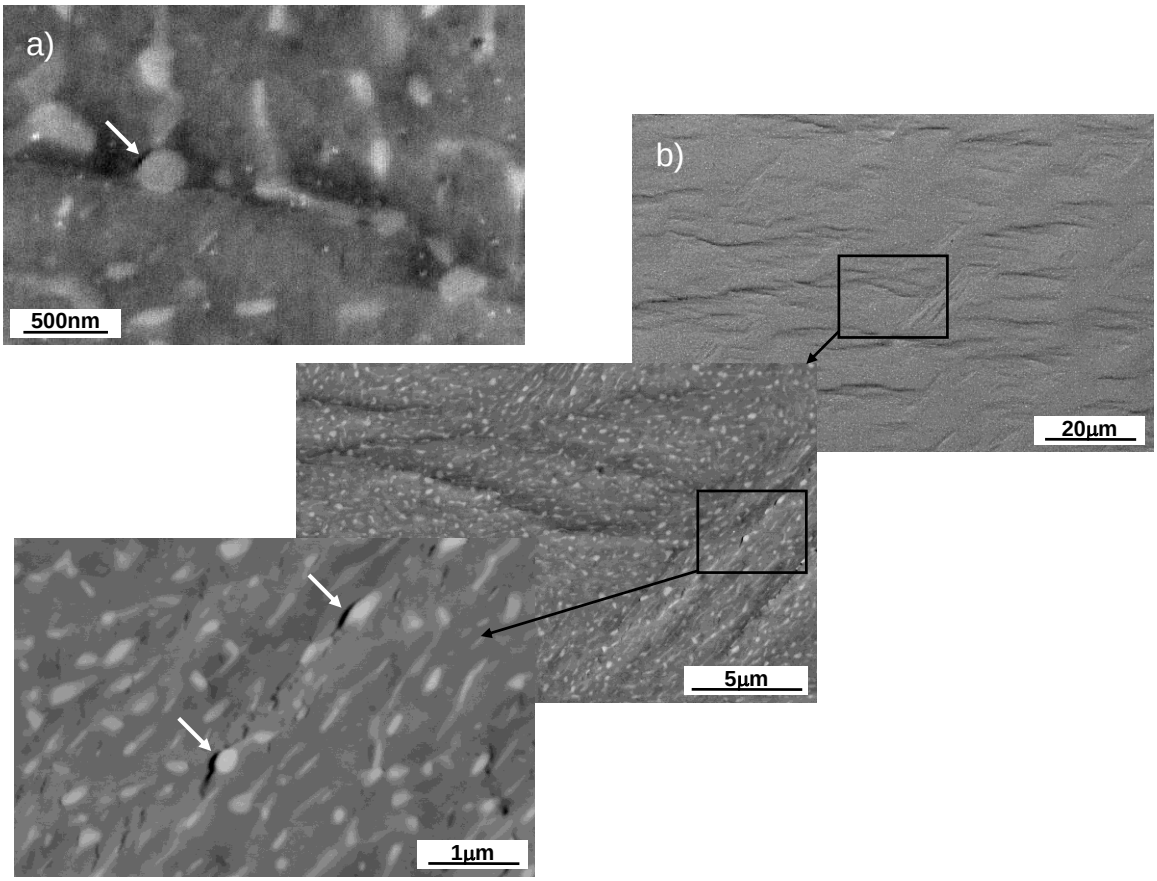

Figure 5-22. SE micrographs showing interfacial microcracks which formed in the areas of localized deformation in region 'B' as described in Section 5.3.2 as a) nearly perpendicular and b) at a consistent inclined angle to the loading axis (Courtesy of Michael S. Kesler)

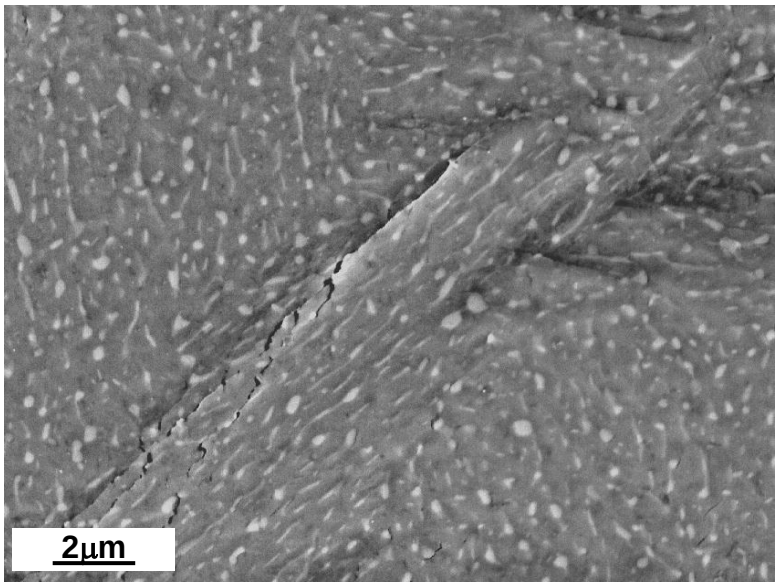

Figure 5-23. An area in region 'B' which has undergone significant microcracking (Courtesy of Michael S. Kesler)

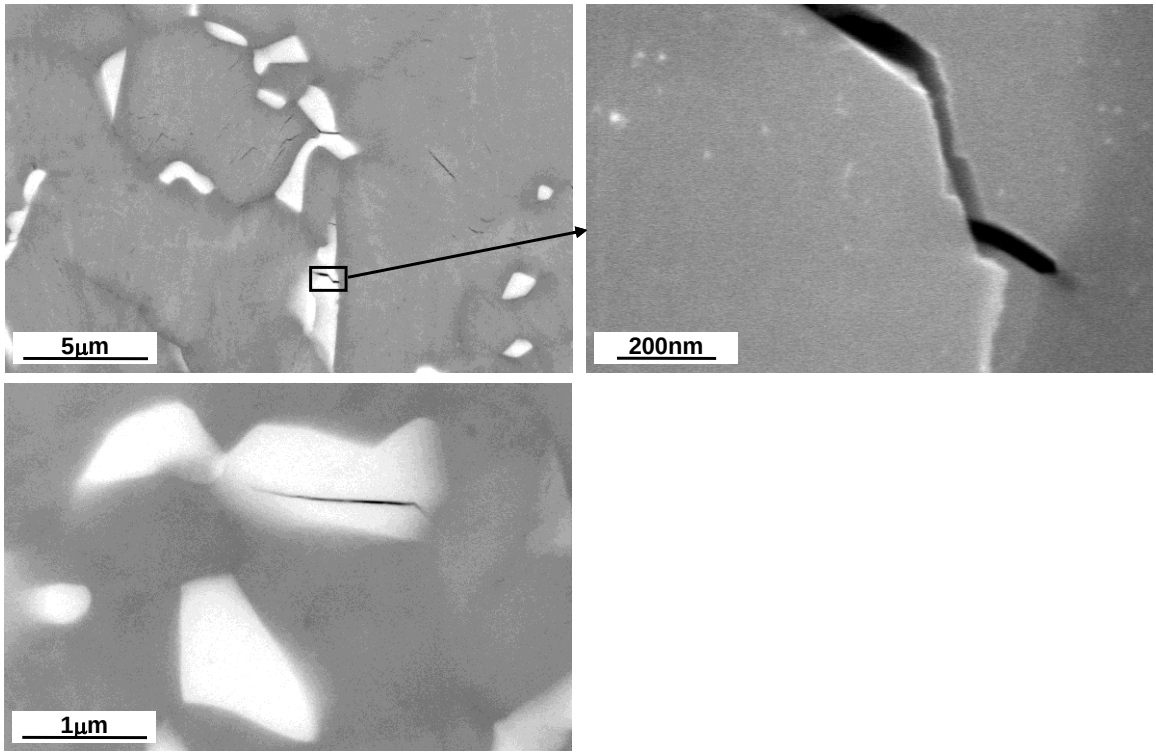

Figure 5-24. The coarsened s-particles in Alloy 11-1100-3.7%ε_p were the primary source of microcracking in this alloy (Courtesy of Michael S. Kesler)

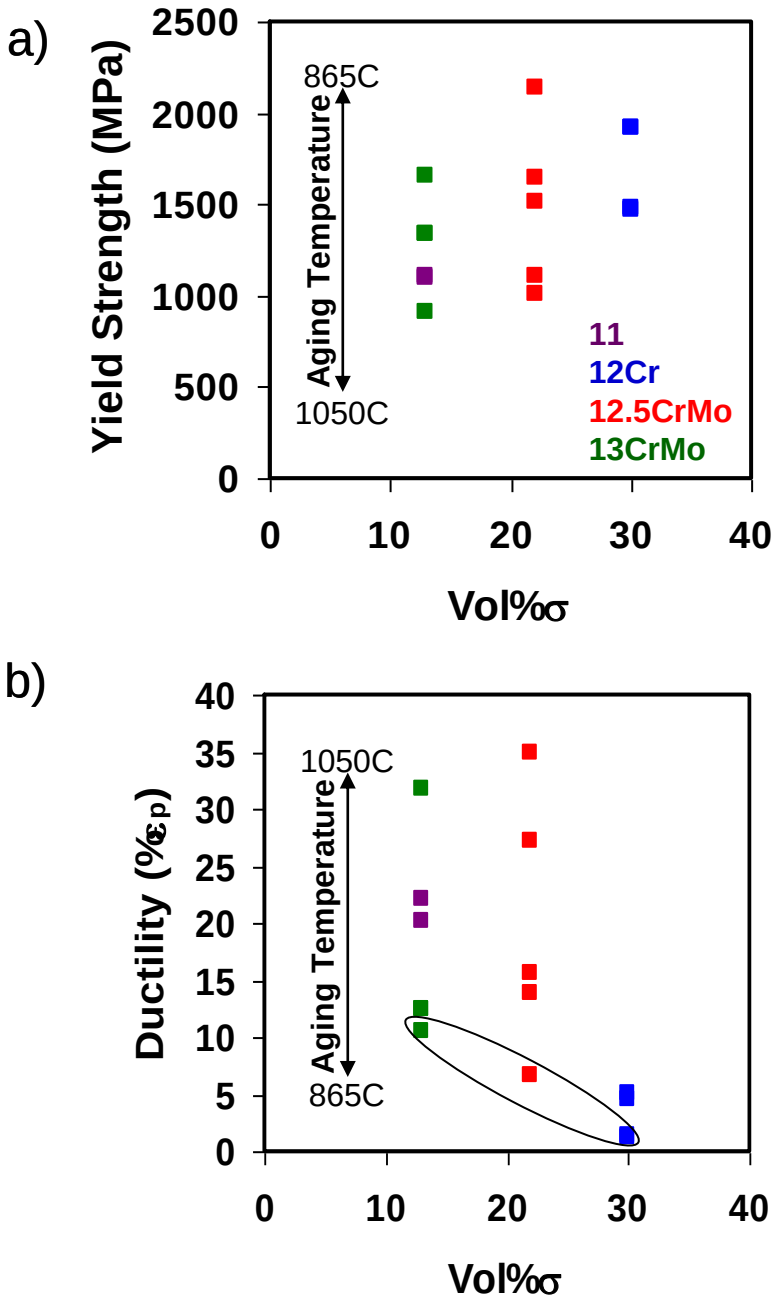

Figure 5-25. The plots of a) yield strength vs. volume fraction of the σ-phase and b) ductility (plastic deformation to failure) vs. volume fraction of the σ-phase for alloys 11 (purple), 12Cr (blue), 12.5CrMo (red) and 13CrMo (green) (Courtesy of Michael S. Kesler)

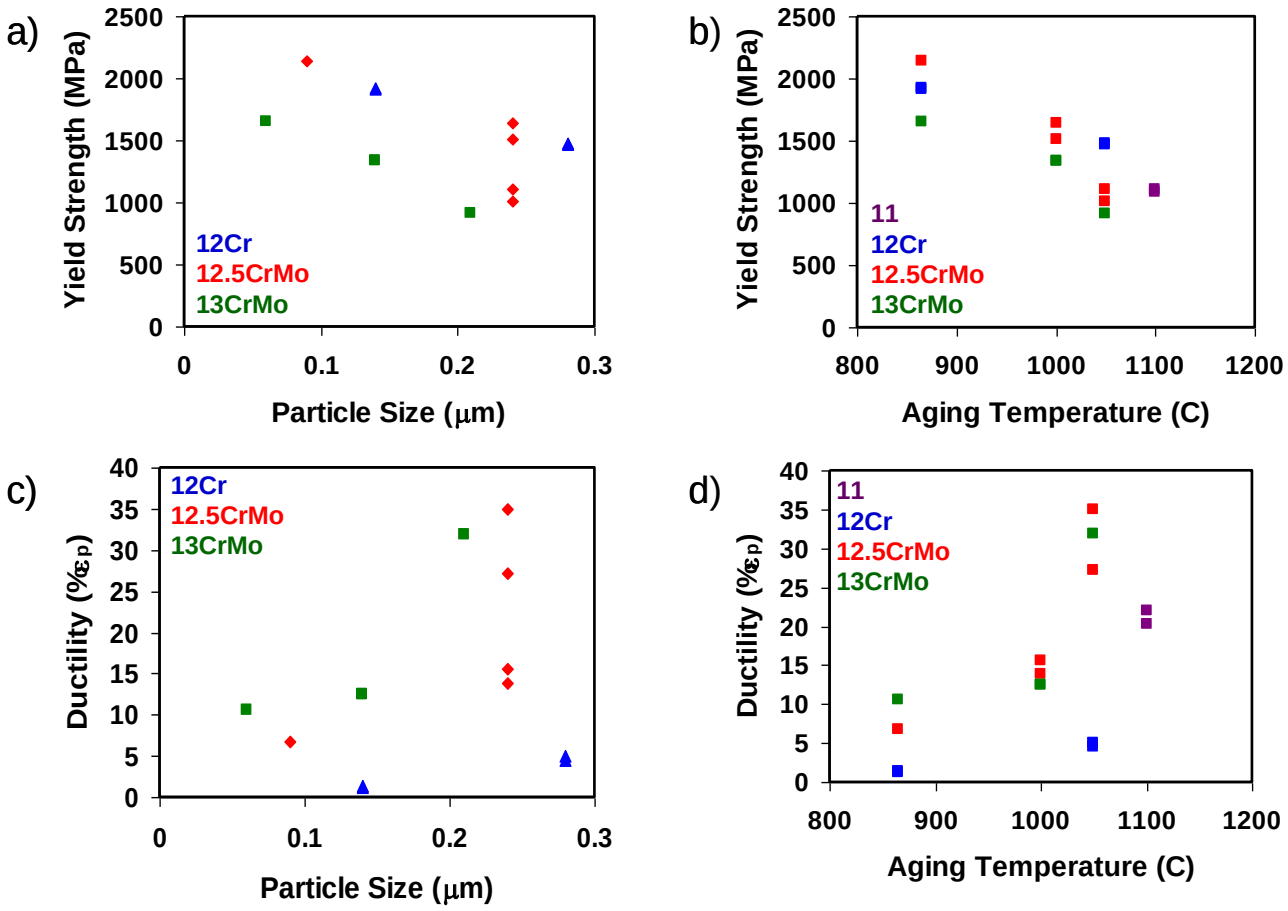

Figure 5-26. The plots of yield strength vs. a) particle of the σ-phase and b) aging temperature; and ductility (plastic deformation to failure) vs. c) particle size of the σ-phase and d) aging temperature for alloys 11 (purple), 12Cr (blue), 12.5CrMo (red) and 13CrMo (green) (Courtesy of Michael S. Kesler)

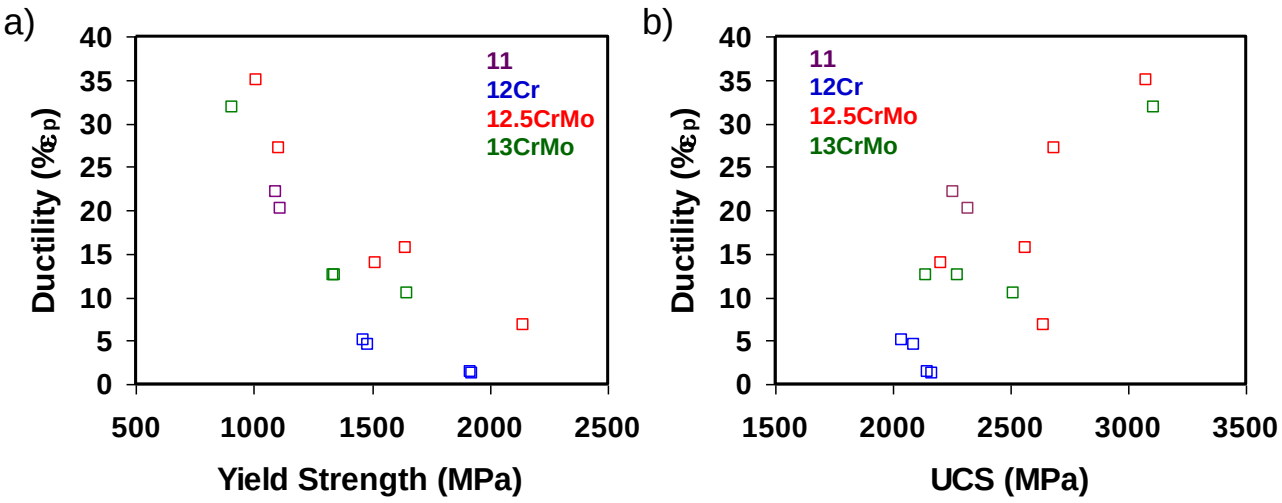

Figure 5-27. The plots of a) ductility (plastic deformation to failure) vs. yield strength and b) ductility vs. ultimate compressive strength for alloys 11 (purple), 12Cr (blue), 12.5CrMo (red) and 13CrMo (green) (Courtesy of Michael S. Kesler)

CHAPTER 6
DEFORMATION AND FRACTURE IN γ+σ ALLOYS AGED FROM SINGLE β-PHASE CRYSTALS

Single crystal metals, when unconstrained during testing, are capable of significant increases in uniform plastic deformation as compared with their polycrystalline counterparts. Due to the significant localized deformation and microcrack formation observed at the prior β-phase grain boundaries, the prior boundaries were eliminated as described in Section 3.5.2. Other than the limited specimen size of samples cut and aged from single β-phase crystals (SX samples), the preparation of these samples was identical to the preparation of polycrystalline (PX) samples, so the microstructural parameters listed in Table 4-1 are directly comparable. The resulting effects on strength and ductility for SX samples were explored with the expectation of an enhancement in ductility.

6.1 Compression Testing on SX γ+σ Alloys

6.1.1 Compression testing to failure

All compression tests on SX alloys were conducted at room temperature at a constant cross-head speed resulting in strain rates varying between $0.8x10^{-3}$ and $1x10^{-3}s^{-1}$ depending on exact sample dimensions (sample heights ranging from ~2.5-3.2mm). The yield strength (YS), ultimate compressive strength (UCS) and plastic strain (ε_p) values for all SX alloys are shown in Table 6-1. Figure 6-1a is an illustration demonstrating where the single crystals were cut from a soln+WQ slice of Alloy 12Cr. Because the eventual microstructure to be tested was an ultra-fine γ+σ microstructure it was important to know whether or not the anisotropic nature of single crystals was apparent in these samples after aging. It was not a focus of this study to determine the

effects of orientation, though recognizing the occurrence of anisotropy was important for the analysis of the results collected. Each SX alloy condition tested was compared with the respective PX data (black curve in Figure 6-1b) and the stress-stain curves for 12Cr-865-SX samples (blue curves) are shown in Figure 6-1b. As illustrated in Figure 6-1a, vertical and horizontal samples were cut from the single β-phase crystal in Alloy 12Cr then aged at 865ºC for 2hrs and the yield strength, UCS and ductility all showed anisotropy (dark blue and light blue curves in Figure 6-1b). What was also evident, and directly relevant to the focus of this study, was the significant increase in ductility (13.5 and 24.2%ε_p) as compared to the PX samples (1.2 and 1.5%ε_p). This was accompanied by a drop in yield strength from 1922 and 1917MPa for the PX samples to 1375 and 1492MPa for the SX samples. The variation of 120MPa in the vertical and horizontal orientations of the SX samples show that there is likely a 'hard' and 'soft' orientation relating back to the parent β-phase. The strain hardening rate for the horizontal orientation (light blue) was observed to be greater than the vertical orientation and possibly was the cause of the significantly lower plastic strain to failure. Though the global UCS was much lower in the horizontal orientation (2427MPa as compared to 2923MPa), the increased strain hardening rate suggests a higher dislocation density at a given strain value and may contribute to greater local stresses in the fine $\gamma+\sigma$ microstructure which would ultimately cause the propagation of cracks that had formed at lower strain levels.

The remaining SX samples presented in this section were cut in the vertical orientation, as shown in Figure 6-1a, though they were cut from different β-grains with unknown orientation, so it should be taken into consideration when analyzing the

results. The stress-strain curve for the coarsened microstructure of Alloy 12Cr-1050-SX (blue curve) is shown in Figure 6-2 along with the PX (black) condition for this alloy. The SX condition again shows a significant increase in ductility from 5.1%ε_p (PX) to 13.2%ε_p (SX). Additionally, Alloy 12Cr-1050-SX displayed relatively high yield strength with respect to the PX condition, suggesting that this specimen happened to have a 'hard' orientation. Despite the similar yield strength (1483MPa for PX and 1415MPa for SX), the ductility had nearly tripled. When the properties of Alloy 12Cr-865-SX and Alloy 12Cr-1050-SX were compared, it was found that the ductility of Alloy 12Cr-865-SX was nearly equal to (13.5%ε_p) or far greater than (24.2%ε_p) that of Alloy 12Cr-1050-SX (13.2%ε_p). These results suggest that in the absence of prior β-phase grain boundaries, the refined $\gamma+\sigma$ microstructures may be intrinsically more ductile than coarsened microstructures which would be consistent with the proposed effect of refinement.

The stress-strain curves generated from samples of alloys 13CrMo-865-SX and 13CrMo-1000-SX (Figure 6-3 and 6-4a, respectively) displayed significant increases in ductility (25.8 and 27.8%ε_p, respectively) compared to the PX conditions (10.5 and 12.5%ε_p, respectively). This was accompanied by significant reductions in yield strength in the orientations tested, though these alloys still have yield strengths which are comparable to the upper limits of the high NB [12, 87] and 4822 [88] alloys discussed in Chapter 5. The photographs in Figure 6-4b were taken from the sample of 13CrMo-1000-SX before and after loading. This visually displays the degree of compressibility of these SX alloys. The stress-strain curve in Figure 6-5 shows the comparison of Alloy 13CrMo-1050 in the SX condition (green) and the PX condition (black). While showing a drop in yield strength, which is consistent, the ductility of the SX condition (27.6%ε_p)

was lesser than that of the PX condition (31.8%ε_p). The direct cause of this inconsistency is difficult to pin point. It could be a result of several factors including crystallographic orientation of the parent β-grain, an increase in strain hardening rate in the SX sample, improper lubrication of the compression platens, or imperfect sample preparation. Despite the apparent premature fracture of this particular sample, extensive plastic deformation was achieved.

6.1.2 Interrupted Compression tests

In Chapter 5 it was determined that strain localization in the vicinity of the prior β-phase grain boundaries was the cause of significant microcrack initiation even at a plastic strain level of 1.4%. As a result, the following questions arose: 1) what is the nature of strain localization and microcrack nucleation at low strain levels in the absence of prior boundaries? and 2) how does microcrack formation differ in coarsened versus refined microstructures in SX alloys?

To address the first question, a sample of 13CrMo-1000-SX was deformed to the same plastic strain level, 1.4%, as the sample of Alloy 13CrMo-1000-PX presented in Section 5.1.2. The resulting stress-strain curves and measurements of achieved strain levels are shown in Figure 6-6. By chance, the orientation of the SX sample resulted in yield strength (1372MPa) comparable to that of the PX sample (1330MPa) as seen in Figure 6-6 and, in fact, greater by 40MPa. A comparison of the nature of macroscopic/microscopic deformation and fracture of these samples will be discussed in Section 6.3.

In order to address the second question, two compression samples were cut from the same β-grain, both in the vertical orientation as shown in the illustration in Figure 6-

7a. The samples were then aged at 865 and 1050ºC resulting in a refined (0.06μm σ-phase mean diameter) and a coarsened (0.21μm σ-phase mean diameter) microstructure, respectively. This allowed for two identically oriented samples to be compared. The samples were both loaded to 3.5%ε_p and the resulting stress-strain curves with the respective yield strengths and measured plastic deformation are shown in Figure 6-7b. The untested microstructures from the exact samples are shown and labeled at the bottom of Figure 6-7. A comparison of the behavior of these specimens will be discussed in Section 6.3.3.

6.2 Fracture Toughness Testing on SX γ+σ Alloys

6.2.1 Vickers Microindentation Technique

Intents were applied to samples within a single prior β-grain using loads of 20 and 30kgf as described in Chapter 3 Section 3.5.1. The goal of this technique was to apply intents such that cracks would develop from the corners of the diamond shaped indenter. The length of these cracks could then be empirically associated to the fracture toughness of the material through Lankford's 'curve fitting model' [57]. This technique was used in previous research [55] on γ+σ alloys and was compared to fracture toughness values gathered by standardized fracture toughness techniques including 4pt bending of chevron-notched samples. A reasonable correlation was found with an over-estimation of approximately 20% for the 'curve fitting model' compared to chevron-notched samples [16, 29, 55]. The ease of sample preparation and evaluation for this technique makes it an attractive option for estimating fracture toughness.

Ten indents at each load were applied to samples of Alloy 12Cr aged at 865ºC and 1050ºC. Examples of 20kgf indents from alloys 12Cr-865 and 12Cr-1050 are shown

in Figure 6-8a and Figure 6-8b, respectively. Indents exhibited significant deformation around the sides and did not yield adequate cracks for fracture toughness estimation (Figure 6-9a bottom). Some indents showed no corner cracks. For adequate estimations of fracture toughness values, crack lengths of approximately half the indent diagonal would be necessary. Some indents had minor cracking at a corner or several corners, mostly observed at the highest loading condition (30kgf) as shown in the OM images in Figure 6-9a and Figure 6-9b, respectively, but not greater than approximately 20μm in length. Figure 6-9c is a BSE image showing a crack at higher magnification. Generally, when cracks formed at the indent corners, the initiation was interfacial in nature as seen in Figure 6-10a and Figure 6-10b and the cracks propagated in a transgranular manner through the γ-phase and interfacially when a σ-particle was encountered as seen in Figure 6-10c. The perimeters of the indents, if present in the images, are marked by dashed lines in Figure 6-10. The microcrack initiation seen in Figure 6-10b was similar to the microcracking observed in the regions of localized deformation in the bulk of the β-grains from the interrupted compression tests (Figure 5-22b) and at this indent corner a deformation band in the γ-phase developed between the interfacial microcracks which is likely the intermediate step between microcrack nucleation and coalescence.

These findings, while not resulting in any quantitative measurements, revealed that the fracture toughness of this alloy (Alloy 12Cr with 30vol%σ) has exceeded the limitations of fracture toughness estimation capabilities for this technique, as this method cannot measure fracture toughness values in these materials beyond approximately 7-8MPam^{½}. This is due to the necessary crack sizes needed for this

technique. A valid crack size for the maximum load available for the indenter would be ~300μm and would result in an estimated fracture toughness of ~8MPam^{½}. The cracks observed did not exceed ~10μm. This was a positive result suggesting that the fracture toughness has been enhanced from previous alloys [16, 29, 55] which contain higher volume fractions of the σ-phase. Because these materials have a larger volume fraction of the more ductile g-phase than previous alloys studied, the results here could be in part due to R-curve behavior. R-curve behavior is a phenomenon observed in elastic-plastic materials where the fracture toughness is overestimated due to plasticity in front of the crack which blunts the crack and provides additional resistance to crack growth. This technique was not conducted on any further alloys in this study due to the expectation that this alloy had the lowest fracture toughness because of the highest σ-phase volume fraction content.

6.2.2 Singe Edge Notch (SEN) 4pt Bending

Table 6-2 shows testing parameters and fracture toughness results for alloys 13CrMo-865-2hrs, 13CrMo-1000-2hrs and 13CrMo-1050-20hrs. Load versus displacement curves and details of notch dimensions are presented in Appendix D. Alloy 13CrMo-865-2hrs exhibited a fracture toughness value of 16.6MPam^{½} though only one of the two tests were valid due to faulty sample preparation during the cutting of the SEN (marked with an asterisk in Table 6-2). The notch in that particular sample was cut asymmetrically such that when measuring the value for the notch length, a, there was a difference of 50μm from one face to the other and the test resulted in a relatively low maximum load and the fracture toughness value was significantly lower (12.3MPam^{½}) than the test with proper dimensions. Samples of Alloy 13CrMo-1000-2hrs resulted in

fracture toughness values of 15.8MPam^{½} and 18.2MPam^{½}. There was not a measurable difference between the samples from alloys 13CrMo-865 and 13CrMo-1000 because of limited data points and no scatter evaluation, so no significant effect of the scale of the $\gamma+\sigma$ microstructure can be commented on. Samples of Alloy 13CrMo-1050 were aged for 20hrs in order to significantly coarsen the $\gamma+\sigma$ microstructure. The micrographs in Figure 6-11 (top) show the relative microstructural scales of the three alloys. Figure 6-11 (bottom) shows the fracture toughness versus aging temperature plot for Alloy 13CrMo. The resulting fracture toughness values for 13CrMo-1050-20hrs of 14.2 and 15.2MPam^{½} were lower than the values for the alloys with finer microstructures (15.8, 16.6 and 18.2MPam^{½} from Table 6-2). Without a larger body of testing, the range of scatter is unknown, though these results reveal a significant improvement in toughness compared with alloys with higher σ-phase volume fraction (50-70vol%σ) [55] and suggest a slight enhancement in toughness in refined $\gamma+\sigma$ microstructures at 13vol%σ.

Fractographic analysis of fracture surfaces of SEN bending samples reveal that some samples fractured from what appeared to be a single point of initiation as seen in the SE images in Figure 6-12a (left is low magnification and right is higher magnification) of Alloy 13CrMo-1000-2hrs-1. Figure 6-12b shows the entire fracture surface of the sample 13CrMo-1000-2hrs-2 revealing a less defined crack initiation site. Sample 13CrMo-1000-2hrs-1 (Figure 6-12a) has defined river marks all seemingly flowing toward a single point in the center of sample (dashed white line in Figure 6-12a left) while sample 13CrMo-1000-2hrs-2 has several possible initiation points as denoted by arrows in Figure 6-12b. Sample 13CrMo-1000-2hrs-2 had a greater toughness value

by 2.4MPam^{½} and could be owed to greater energy absorption due to a more diffuse crack front upon initiation. The calculated toughness values were based on a SEN geometry which would correspond with a wide crack front as was likely the case in sample 13CrMo-1000-2hrs-2, whereas the fracture toughness value calculated for the sample which fractured at a single site likely underestimated the fracture toughness due to the enhanced stress intensity at the single initiation site. The random crystallographic orientation of the prior β-grain that was tested here may also be playing a role in the nature of crack initiation and, thus, the degree of scatter in data observed in these samples. The apparent initial crack sizes were observed to be in the range of 20-50μm (Figure 6-12).

Significant scatter in data of non-precracked SEN samples has been observed when cross comparing studies [27, 89], though it has been largely attributed to inconsistent notch dimensions. Compared to precracked samples, SEN samples without precracks resulted in overestimations of fracture toughness values within 14-30% for notch cutting saw widths of ≤150μm and up to 50% overestimations for a notch cutting saw width of 200μm. With a saw width of 150μm in this study, it is reasonable to suggest a maximum overestimation of 30%. This occurs due to extensive plasticity at the notch root prior to the formation of a sharp crack and results in R-curve behavior due excessive crack tip blunting which requires greater force to extend the crack.

Upon propagation of cracks across the bars, there appears to be a correlation between the tortuosity of the crack path and the size of the 'packets' in the $\gamma+\sigma$ microstructure (regions of common crystallographic orientation attributed to the deformation topography observed in Figure 5-17a). The SE micrograph in Figure 6-13a

reveals the scale of the crack path tortuosity (facets of ~20-50μm marked with arrows) from a side view of the sample, while Figure 6-13b (left) shows similar features from a view normal to the fracture surface. Upon closer observation of a 'valley' on the fracture surface, shown in the BSE image in Figure 6-13 (right), there was a change in the orientation of the γ+σ microstructure from the bottom left to the top right of the image.

6.2.3 Unnotched 3pt Bending Bars

If these materials are to be used in a structural application, it is important to understand how sensitive they are to defects. The introduction of a notch limits the volume of material tested and may avoid a defect that would otherwise result in affectively lower fracture toughness. The sensitivity to defects is most apparent under tensile loading and while testing of tensile specimens was unsuccessful in this study, 3pt bending of an unnotched bar will result in the tensile loading of the portions of the bar above the neutral plane in a bending bar and the top of the bending bar will experience the maximum tensile stress. Identification of a fracture initiation site on the fracture surface would provide an estimate for the critical crack size and, along with the calculation of the maximum applied tensile stress, an estimate of fracture toughness can be calculated. While these values are not necessarily accurate due to a lack of standardization for this type of testing, the results are intended to provide insight into the basic fracture behavior of these materials in tension.

Two bars of Alloy 13CrMo-1000-2hrs were fractured in 3pt bending and the resulting load versus displacement curves are shown in Figure 6-14. Table 6-3 shows testing parameters and fracture toughness results for 3pt bending of the unnotched bars of Alloy 13CrMo-1000-2hrs. The samples fractured at loads of 4805 and 4181N which

corresponded to maximum tensile stresses, σ_{max}, of 1860 and 1646MPa, respectively. The a_{crit} values are approximations based on possible initiation sites observed in the SEM. The load-displacement curves in Figure 6-14 showed a deviation from linearity suggesting possible plastic deformation prior to failure and the calculated maximum tensile stresses were above the yield strengths measured in polycrystalline samples for Alloy 13CrMo-1000 (1336 and 1342MPa). This was an unexpected result as this material was expected to fracture at a tensile stress markedly less than the measured value, closer to or less than the yield strength.

The SE images in Figure 6-15 show the fracture surface of an unnotched sample in successive increasing magnification (left to right) revealing the fracture initiation site which likely led to failure. It was difficult to accurately quantify the size of the initiation site, so the calculated fracture toughness values for possible critical crack sizes (20, 30 and 50μm) are listed in Table 6-3. Fracture toughness values ranging from 8.3MPam^{½} (assume crack size of 20μm) to 14.8MPam^{½} (assume crack size of 50μm) are likely underestimations and overestimations, respectively. When comparing with the SEN specimen of Alloy 13CrMo-1000-2hrs, a fracture toughness value of 15.8MPam^{½} would result in a critical crack size of 23μm. It should be mentioned that the high stress level (>YS) that the unnotched bars reached likely resulted in a significant plastic zone size and if the extent of this plastic zone was on the order of or larger than the critical crack size, it would deem the governance of linear elastic fracture mechanics invalid for this case. What was evident from these data was that, despite these alloys not going through a thorough homogenization process and no HIPping or thermomechanical processing, these alloys still can withstand significantly high levels of tensile stresses

and, while likely sensitive to defects, did not fail in bending due to an obvious inclusion or pore. Additionally, a prior β-phase grain boundary was not identified as the fracture initiation site, though this cannot be ruled out.

6.3 Deformation and Fracture of SX alloys

6.3.1 Macroscopic Deformation and Fracture

The faces of a rectangular compression samples were finely polished and examined with OM and SEM. Figure 6-16a and Figure 6-16b are both compilations of OM images mapping out the surface of samples of Alloy 13CrMo-1000-SX which had been loaded to 1.4% (interrupted) and 27.8% (failure) plastic deformation, respectively. The interrupted sample (Figure 6-16a) had no deformation or cracking apparent to the naked eye, but upon closer inspection (SE micrograph in Figure 6-16c), a fine rippling was observed evenly over the entire surface of the sample. After loading to failure (Figure 6-16b), significant rippling over the entire sample and a large crack were observed and the deformation topography is shown in the SE micrograph in Figure 6-16d.

6.3.2 Microscopic Deformation and Fracture

The evenly dispersed rippling was observed at macroscopic levels in Alloy 13CrMo-1000-SX-1.4%, but, as shown in the SE micrographs in Figure 6-17, small regions of localized deformation were also observed at low strain levels. These features were widely spaced (on the order of hundreds of micrometers) about the sample surface at low plastic strains. Microcracking was observed (Figure 6-17c) in these areas. While these scattered regions of localized deformation encompassed the majority of the microcracking observed, the occasional microcracking at the γ/σ

interfaces was also observed in the rippled region (Figure 6-18) throughout the surface of the sample.

As an SX sample was loaded to higher plastic strains (samples loaded to fracture), the amount of localized deformation, as displayed in Figure 6-17c became more frequent and the severity of microcracking in those regions became extensive to the point of coalescence, leading to the formation of larger cracks as seen in Figure 6-19a. Additionally, the areas which still only consisted of the rippling topography at the fracture strain resulted in extensive interfacial microcrack formation (Figure 6-19b), though coalescence was not observed in the SEM. The changes in deformation topography from localized regions to rippled areas were likely a result of the varying crystallographic orientation of the aged microstructure in those specific regions as the γ-phase is known to orient in several variants from the parent β-phase [68]. Additionally, the anisotropic mechanical properties which remain in the prior β-phase crystal after precipitation of the two-phase $\gamma+\sigma$ microstructure would also suggest crystallographic texturing within the SX samples.

6.3.3 Effect of Microstructural Scale in SX Alloys

The effect of microstructural scale on the deformation and fracture behavior of SX alloys was examined by observing the common sample surfaces of alloys 13CrMo-865-SX and 13CrMo-1050-SX which were cut from the same β-grain and compressed to 3.5% plastic strain (interrupted test described in Figure 6-7). Because the only variation in these samples was the aging temperature/particle size, the behavior could be compared. Shown in Figure 6-20, as the aging temperature/particle size increased (from 0.06 to 0.21μm), the yield strength decreased (from 1466 to 1156MPa). This was the

expected result and was consistent with that observed in the PX alloys. Additionally, the total stress level reached at the point when the test was interrupted was much higher in the sample aged at 865ºC (1980MPa compared to 1472MPa).

Upon observation of a common sample surface from each specimen (SE micrographs in Figure 6-21), the differences in deformation and fracture behavior were evident. The sample aged at 865ºC exhibited a fine distribution of localized deformation, as seen in Figure 6-21a and Figure 6-21b. Compared to the sample aged at 1050ºC (Figure 6-21d and Figure 6-21e), there are more numerous localized regions leading to the presumption that the distribution of strain was more evenly dispersed in the sample with a finer $\gamma+\sigma$ microstructure aged at 865ºC. Figure 6-21c shows a region of localized deformation in 13CrMo-865-SX and no microcracking was observed, though in Figure 6-21f, which shows a region of localized deformation in 13CrMo-1050-SX, microcracking was observed at the γ/σ interfaces. Because both samples underwent an equivalent amount of total plastic strain, an important factor resulting in the formation of microcracks in the coarsened sample was the total volume of material that underwent plastic strain. There were regions in the coarsened sample of 13CrMo-1050-SX that likely experienced greater local strains than in 13CrMo-865-SX due to the fewer sites of localized plasticity. Additionally, the fine microstructure (aged at 865ºC) underwent a higher strain hardening rate (Figure 6-7b), which was expected due to a larger area of interfaces which act as dislocation sources and sinks and barriers to the motion of dislocations. Because of this, the finer microstructure would be expected to develop microcracks more readily as a result of larger local stress buildup at the interfaces, but this was not the case at the plastic strain value of 3.5%.

Additional factors cannot be overlooked, including the coherency of the interfacial boundaries which exist in a given sample. When σ-particles nucleate and grow at phase boundaries, as was suggested in Chapter 4, generally, the smooth rounded sides suggest incoherent interfaces, while the straight angular sides suggest semi-coherent or coherent interfaces. Microcracking was observed primarily at apparent semi-coherent or coherent interfaces of the σ-phase particles and the γ-matrix shown in Figure 6-21f. This phenomenon can also be observed more clearly in Figure 6-18. These straight surfaces were also observed on σ-particles in the samples aged at 865ºC where no microcracking was observed. Due to these observations, the microcracking observed in the coarsened microstructure was attributed to localized strain distribution over a smaller volume of material. The larger applied stress without crack formation in the finer sample aged at 865ºC would also suggest a greater distribution of stress throughout this sample, limiting points of stress intensity at particle interfaces.

6.3.4 PX vs SX: A Comparison

It was shown in Chapter 5 that the damage in the bulk of the prior β-grains with the fine γ+σ microstructure lessened as the distance from the prior grain boundaries and neighboring grains increased (Figure 5-16). The nature of the damage was observed to be the same, but to a lesser extent. It was suggested that in the absence of the constraint from neighboring grains, the damage would be more uniform, allowing for larger global strains prior to fracture.

With the absence of the prior β-phase grain boundaries in SX samples, significantly greater compressive strains were realized. This was owed to the more uniform distribution of strain throughout the compression samples. The comparison of

sample surfaces from alloys 13CrMo-1000-PX-1.4% (Figure 6-22a) and 13CrMo-1000-SX-1.4% (Figure 6-22b), shows a visual representation of the damage accumulated in the respective samples. The PX sample has visible deformation lining the prior β-grains while the SX sample does not appear to have any damage at this low magnification. It can also be noted that the face of SX sample shown here is 2mm x 3mm and the face of the PX sample is 4mm x 6mm, so despite the higher magnification in the SX image (Figure 6-22b) still no visible deformation was observed.

At higher magnification, regions of localized plastic deformation were observed. Figure 6-23 shows SE micrographs comparing the deformation in the respective samples (PX on the left and SX on the right) at increasing magnification. Despite the greater level of damage in the region of the PX sample (Figure 6-23b and Figure 6-23c), the way in which the damage developed was the same in both samples (compare Figure 6-23c with 6-23g). Additionally, as mentioned in both Chapter 5 and Chapter 6, microcracking initiated at the γ/σ interfaces in the fine $\gamma+\sigma$ microstructures (Figure 6-23-d and Figure 6-23h) in the regions of localized deformation.

The PX samples followed a trend of decreasing ductility with increasing yield strength (Figure 5-27a) in coordination with refinement/aging temperature of the $\gamma+\sigma$ microstructure (Figure 5-26a, Figure 5-26b and Figure 5-26c). A proposed explanation for the unexpected loss of ductility with refinement was discussed in Section 5.4.2 and the results of compression on SX samples could provide further information regarding this behavior. Figure 6-24 shows plots of ductility versus particle size (Figure 6-24a), aging temperature (Figure 6-24b) and yield strength (Figure 6-24c) for Alloy 12Cr (blue) and Alloy 13CrMo (green). The hollow squares are data from PX samples and filled

squares are data from SX samples. For Alloy 12Cr, the data show that the ductility switched from decreasing with refinement in PX samples to increasing with refinement though the evidence was limited to just 3 tests (Figure 6-1 and Figure 6-2). For Alloy 13CrMo, the ductility seemed to be independent of the particle size in SX alloys and, additionally, there was a limited variation in the yield strength for the unknown orientations tested. While these results do not conclusively link enhanced ductility with the refinement of the microstructure, they do suggest that the trend observed in PX samples was due to the damage that developed at the prior β-phase grain boundaries. The direct effect of refinement of the $\gamma+\sigma$ microstructure on ductility could be evaluated by testing samples aged from common orientations similar to the interrupted tests at 3.5%ε_p, described in Section 6.1.3, where a direct effect of particle size on yield strength could be observed (Figure 6-20).

6.4 Comparing $\gamma+\sigma$ Alloys to Other Novel γ-based Alloys

It is important to understand where the properties of these alloys lie with respect to other γ-based alloys being explored for advancement of aerospace turbines. Figure 6-25a and Figure 6-25b are plots of plastic strain versus strength under compression for several TiAl-based alloys [8, 10, 12, 87, 88] including alloys from this study in the PX (hollow colored squares) and SX (filled colored squares) conditions. The compressive strength of the $\gamma+\sigma$ alloys are in the upper range of mechanically alloyed TiAl composites (dashes and dots in Figure 6-25) and are approaching the compressive ductility of some advanced 4822 and high Nb alloys (diamonds and triangles, respectively, in Figure 6-25) [8, 10, 12, 87, 88]. It is important to note that the 4822 and High Nb alloys in Figure 5-28 have been thermomechanically processed and the alloys

in this study are directly tested from as-cast material. The ability to enhance $\gamma+\sigma$ alloys has several attractive dimensions, including the capability of being thermomechanically processed due to the presence of the β-phase at elevated temperatures, further microstructural control through varying aging times and temperatures, means of microstructural refinement such as straining prior to aging, and growing of single crystals.

Table 6-1. Mechanical properties of SX alloys under compression

Alloys	σ_y (MPa)	σ_{UCS} (MPa)	ε_p (%)
12Cr-865-SX	1492 (Vert) 1375 (Hor)	2933 2427	24.2 13.5
12Cr-1050-SX	1415	2468	13.2
13CrMo-865-SX	943	2803	25.8
13CrMo-1000-SX	1083	2722	27.8
13CrMo-1050-SX	820	2499	27.6

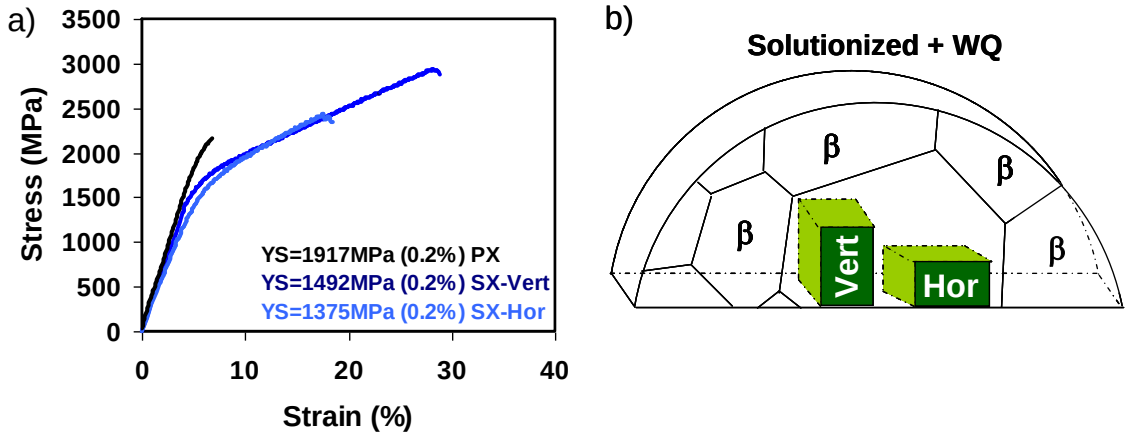

Figure 6-1. a) The engineering stress-strain curves generated from compression of Alloy 12Cr-865 in the following conditions: PX (black), SX-Vertical (dark blue) and SX-Horizontal (light blue). b) An illustration of the slice and relative orientation from which the vertical and horizontal SX samples were cut (Courtesy of Michael S. Kesler)

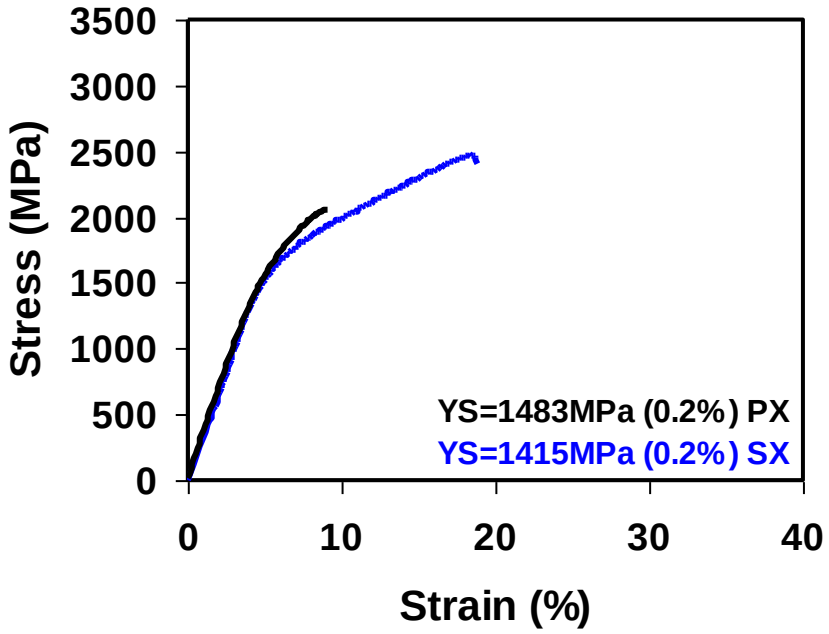

Figure 6-2. The engineering stress-strain curves generated from compression of Alloy 12Cr-1050 in the PX (black) and SX (blue) conditions (Courtesy of Michael S. Kesler)

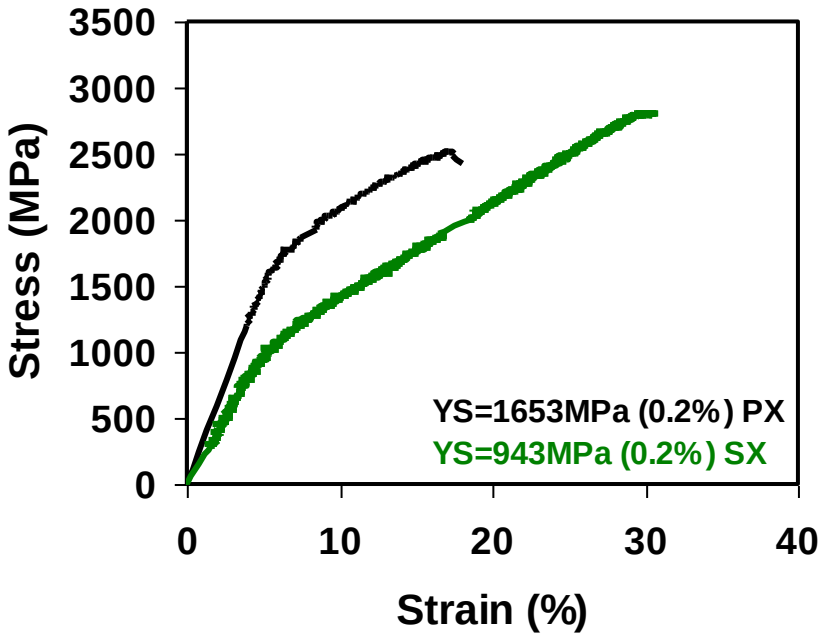

Figure 6-3. The engineering stress-strain curves generated from compression of Alloy 13Cr-865 in the PX (black) and SX (green) conditions (Courtesy of Michael S. Kesler)

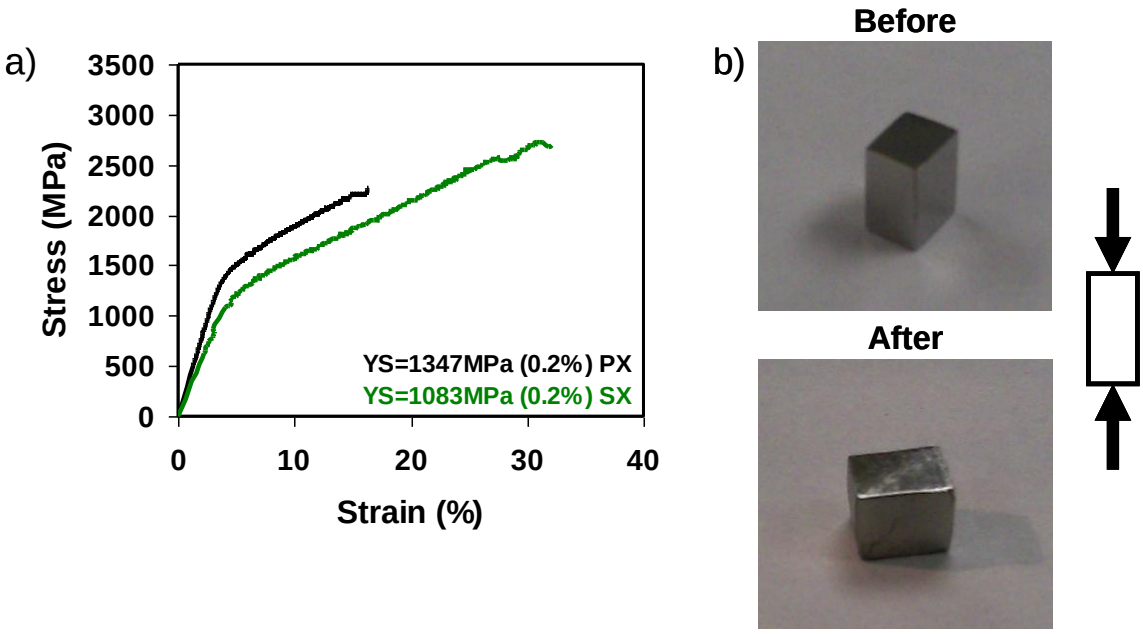

Figure 6-4. The a) engineering stress-strain curves generated from compression of Alloy 13Cr-1000 in the PX (black) and SX (green) conditions and b) before and after photographs if the SX compression sample (Courtesy of Michael S. Kesler)

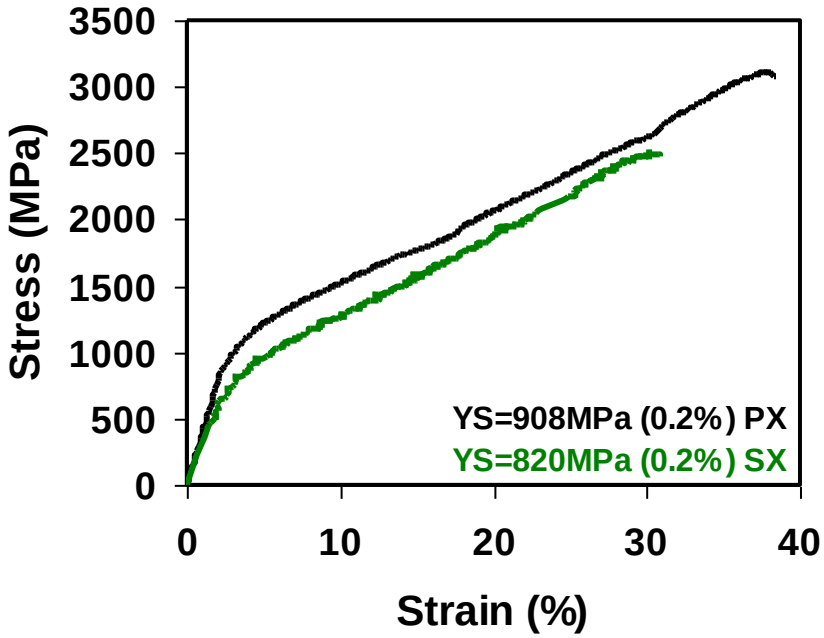

Figure 6-5. The engineering stress-strain curves generated from compression of Alloy 13Cr-1050 in the PX (black) and SX (green) conditions (Courtesy of Michael S. Kesler)

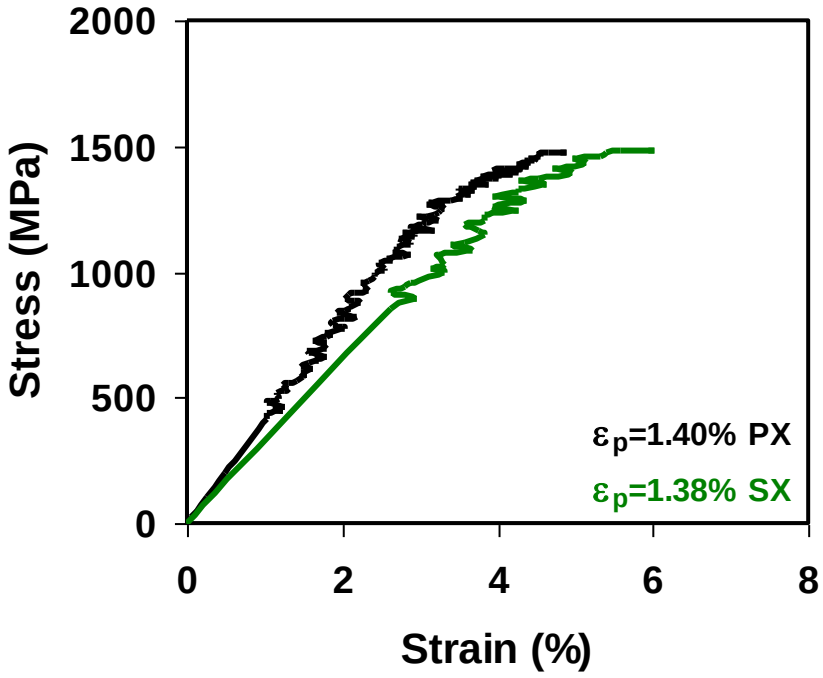

Figure 6-6. Stress-strain curves of room temperature interrupted compression tests at 1.4% plastic strain on alloys 13CrMo-1000-PX (black) and 13CrMo-1000-SX (green) with exact respective plastic strains (Courtesy of Michael S. Kesler)

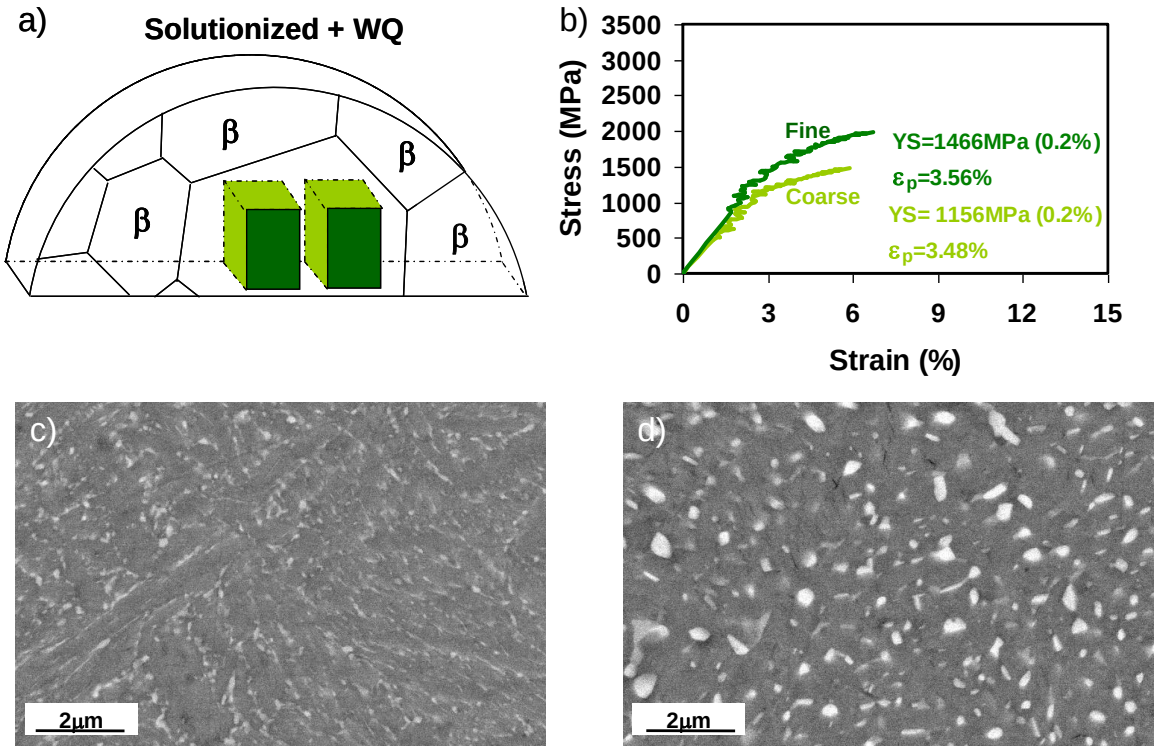

Figure 6-7. Interrupted compression tests on a) two identically oriented samples of Alloy 13CrMo aged at 865ºC (fine) and 1050ºC (coarse) for 2hrs. b) The stress-strain curves and measured yield strength and plastic strains achieved and c,d) MSE micrographs of the fine and coarse microstructures, respectively (Courtesy of Michael S. Kesler)

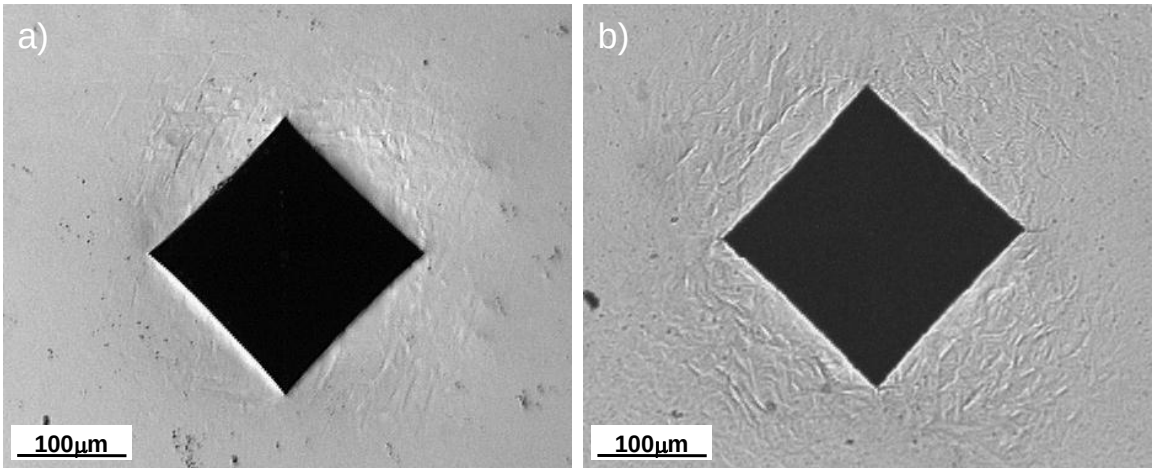

Figure 6-8. OM images of Vickers indents applied with 20kgf on alloys a) 12Cr-865 and b) 12Cr-1050 (Courtesy of Michael S. Kesler)

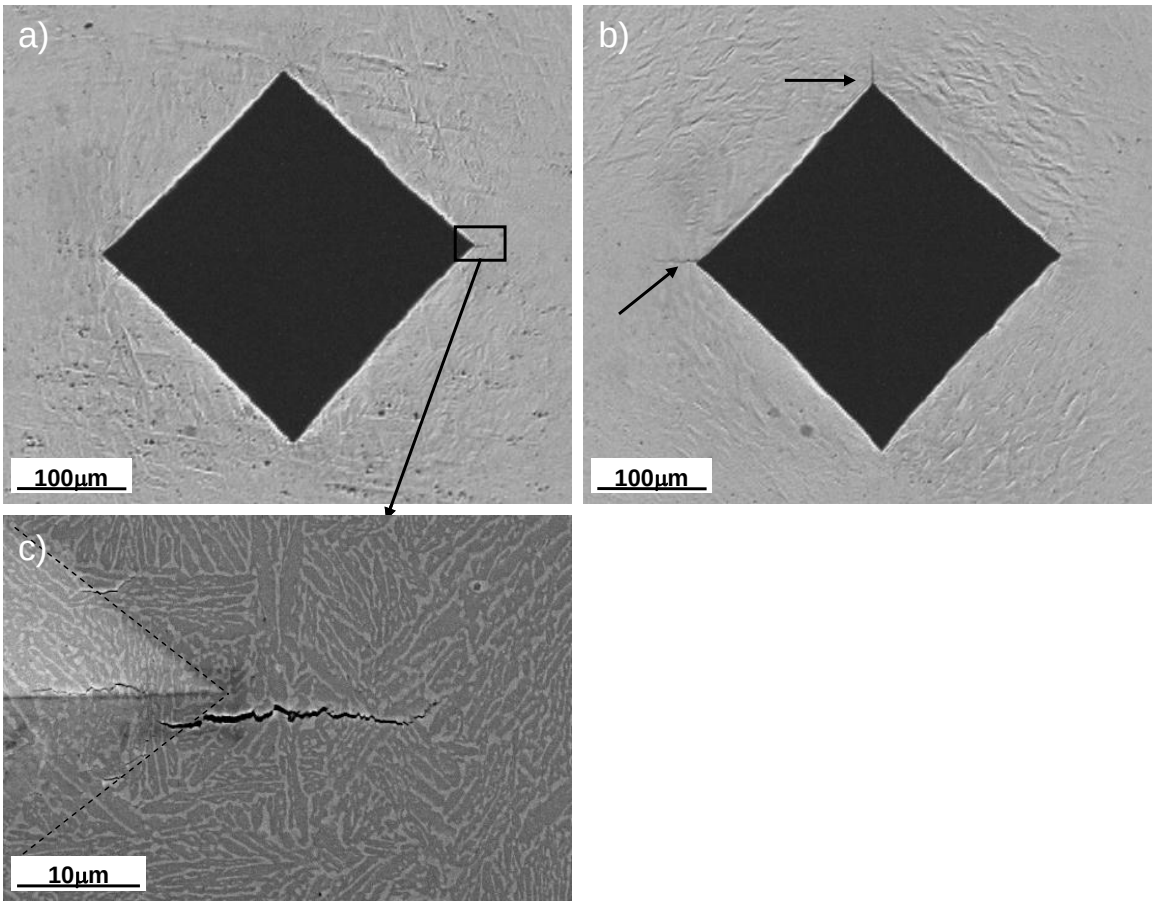

Figure 6-9. OM images of Vickers indents applied with 30kgf on alloy a,b) 12Cr-1050 revealing small cracks emanating from some corners and c) an SE image revealing the scale of the crack (Courtesy of Michael S. Kesler)

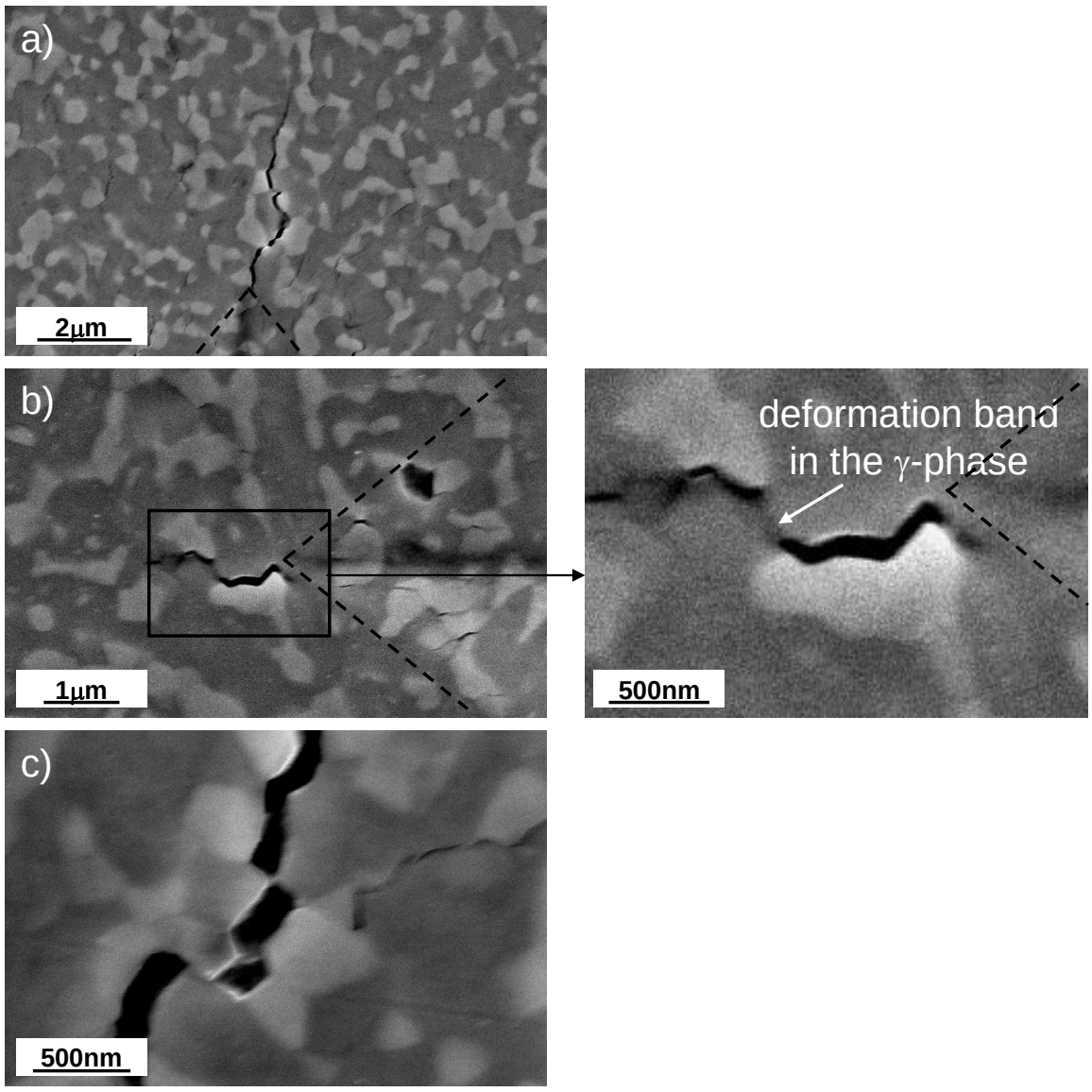

Figure 6-10. SE images from Alloy 12Cr-1050 revealing a,b) interfacial crack formation at the corners of an intent and c) the propagation of the crack travelling thougth γ/σ interfaces and transgranularly through the γ-phase (Courtesy of Michael S. Kesler)

Table 6-2. Sample dimensions and SEN fracture toughness results

Alloys	B (mm)	W (mm)	P (N)	S_1 (mm)	S_2 (mm)	α(a/W)	Y(α)	K_{1C} (MPam^{½})
13CrMo-865-2hrs-1*	2.17	3.86	264*	20	10	0.505	6.28	12.3*
13CrMo-865-2hrs-2	2.18	4.49	395	20	10	0.468	6.14	**16.6**
13CrMo-1000-2hrs-1	2.2	4.25	383	20	10	0.461	5.90	**15.8**
13CrMo-1000-2hrs-2	2.19	4.38	433	20	10	0.459	6.07	**18.2**
13CrMo-1050-20hrs-1	2.29	3.94	290	20	10	0.523	7.38	**15.2**
13CrMo-1050-20hrs-2	2.15	4.15	286	20	10	0.513	7.01	**14.2**

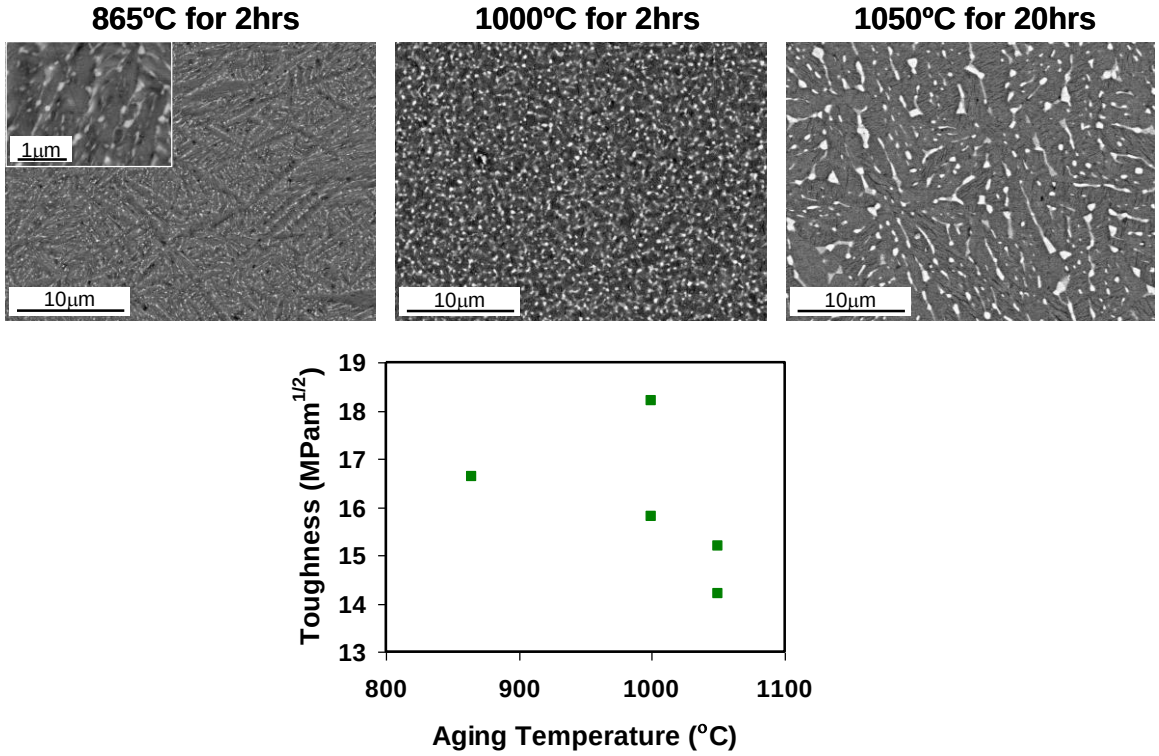

Figure 6-11. (top) SEM micrographs revealing the scales of the microstructures in Alloy 13CrMo at different aging temperatures and times and (bottom) fracture toughness versus aging temperature plot for alloys containing the above microstructures (Courtesy of Michael S. Kesler)

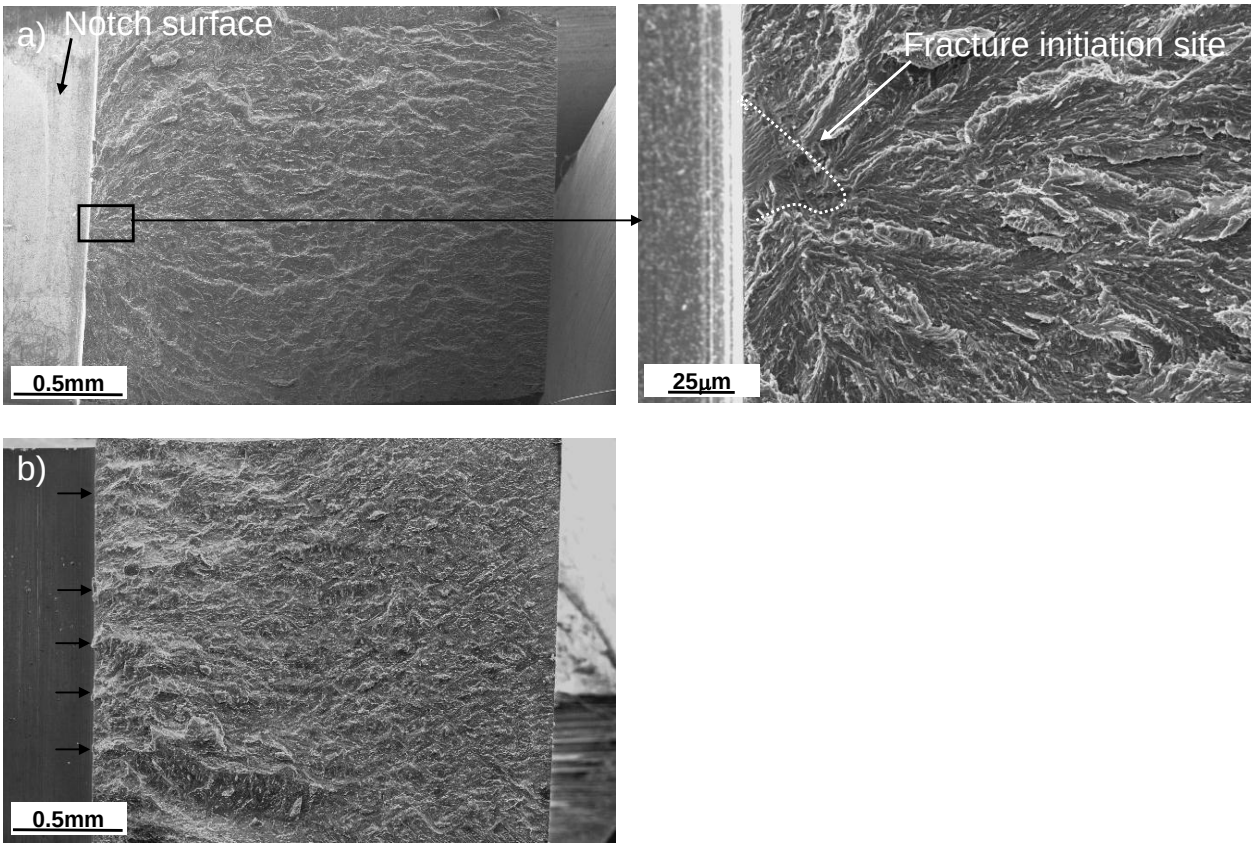

Figure 6-12. Fracture surfaces from SEN bending samples a) 13CrMo-1000-2hrs-1 and b) 13CrMo-1000-2hrs-2 showing likely crack initiation sights (Courtesy of Michael S. Kesler)

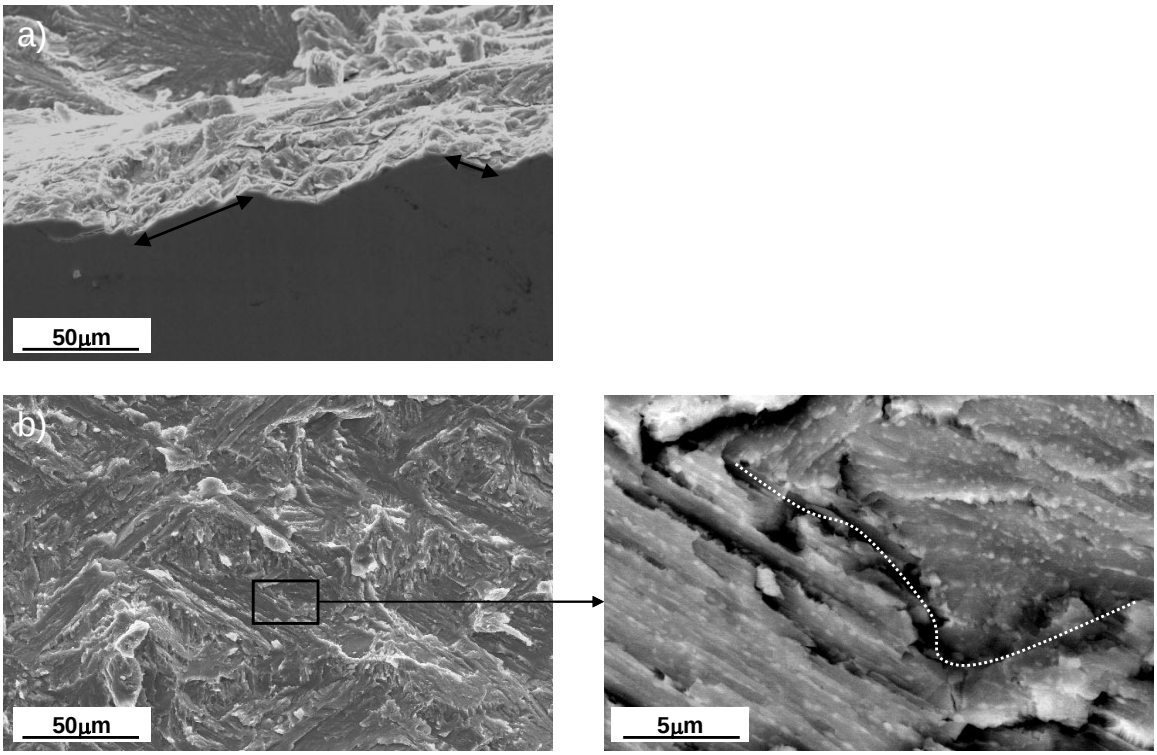

Figure 6-13. SE micrographs from Alloy 13CrMo-1000 of the a) crack path and b) fracture surface showing tortuosity on the scale of the γ+σ packets revealed by BSE imaging (right) (Courtesy of Michael S. Kesler)

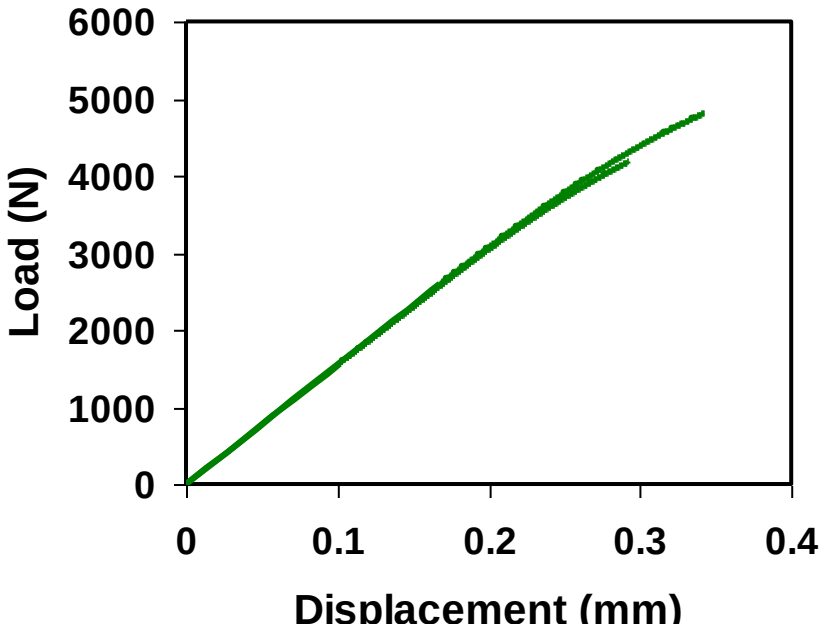

Figure 6-14. Load-displacement curves for bending of unnotched samples of Alloy 13CrMo-1000-2hrs (Courtesy of Michael S. Kesler)

Table 6-3. Sample dimensions and unnotched 3pt bend test results

Alloy	B (mm)	W (mm)	P (N)	S (mm)	σ_{max} (MPa)	a_{crit} (μm)	K_1 (MPam^{½})
13CrMo-1000-2hrs-1	2.11	4.28	4804	10	1860	20	9.3
						30	11.5
						50	14.8
13CrMo-1000-2hrs-2	2.10	4.26	4181	10	1646	20	8.3
						30	10.1
						50	13.1

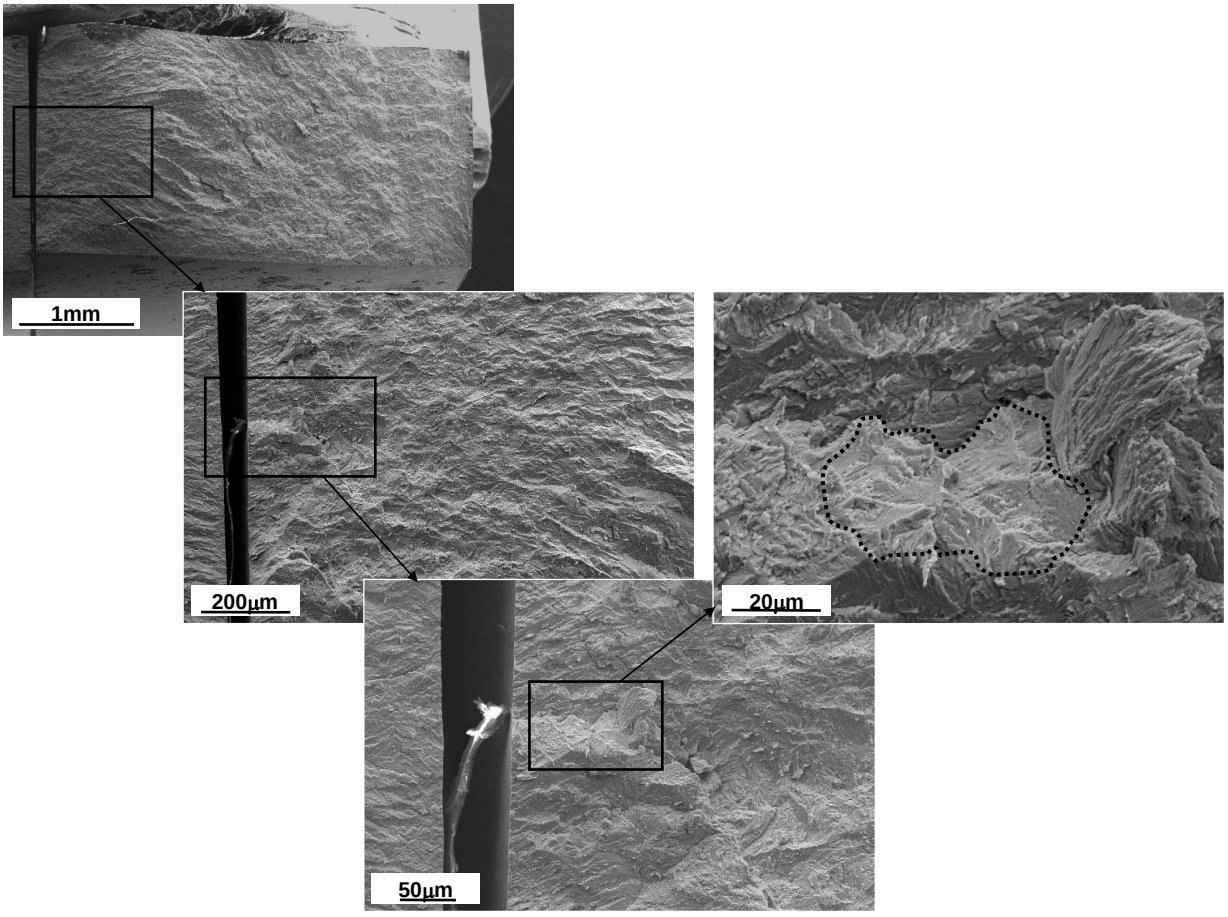

Figure 6-15. The fracture surface of an unnotched sample of Alloy 13CrMo-1000-2hrs at increasing magnification (left to right) showing the crack initiation site which likely led to fracture (Courtesy of Michael S. Kesler)

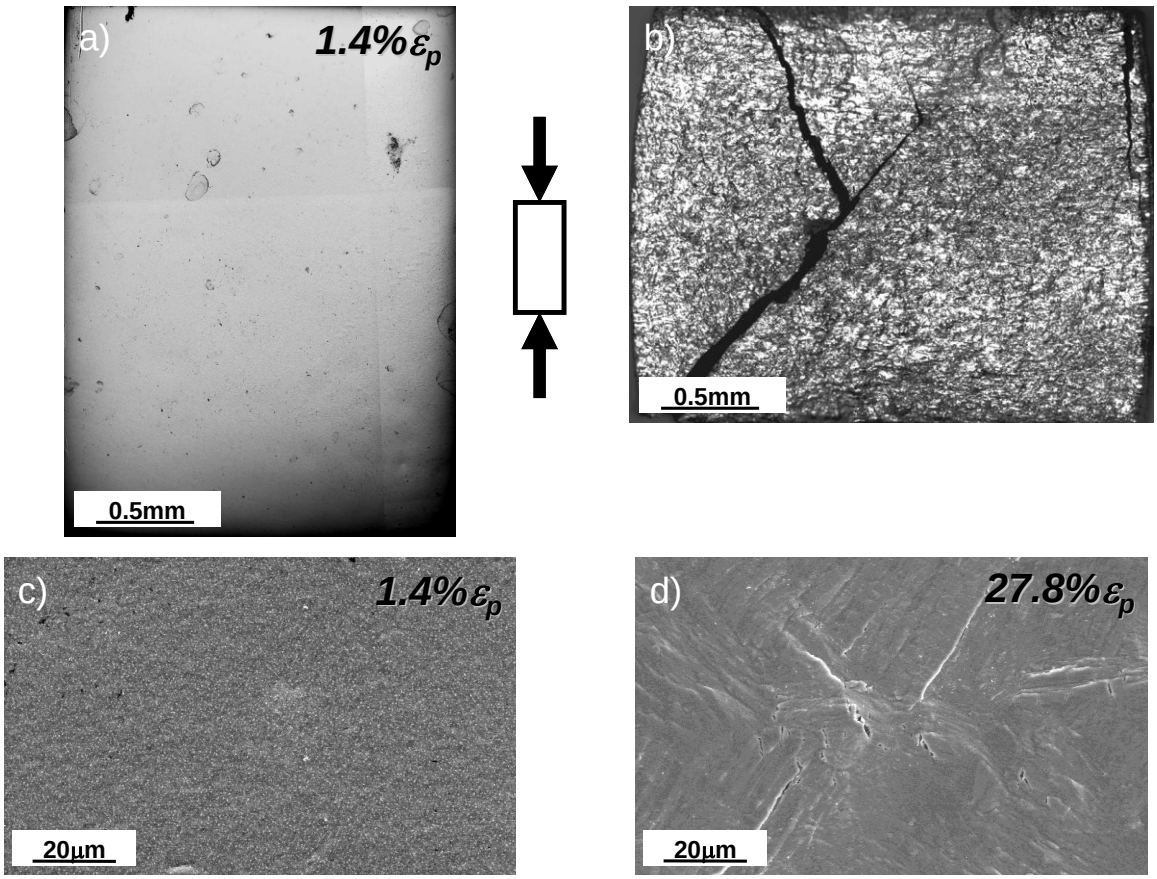

Figure 6-16. Compilations of OM images of Alloy 13CrMo-1000-SX revealing surface damage after loading to a) 1.4%ε_p and b) to failure (27.8%ε_p) and c,d) SE micrographs of the respective surface damage at higher magnification (Courtesy of Michael S. Kesler)

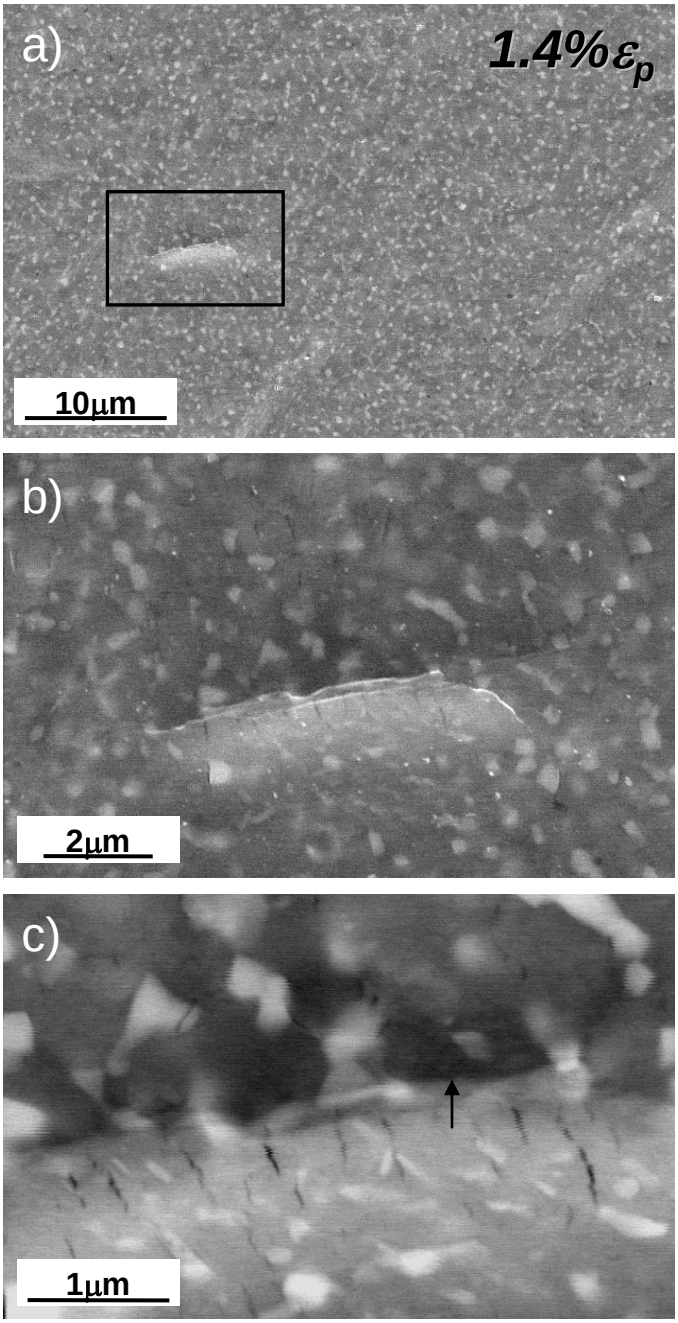

Figure 6-17. SE micrographs from a,b) the surface of Alloy 13CrMo-1000-SX-1.4% of a region of localized deformation and c) showing microcracking adjacent to the apparent slip bands (arrow) (Courtesy of Michael S. Kesler)

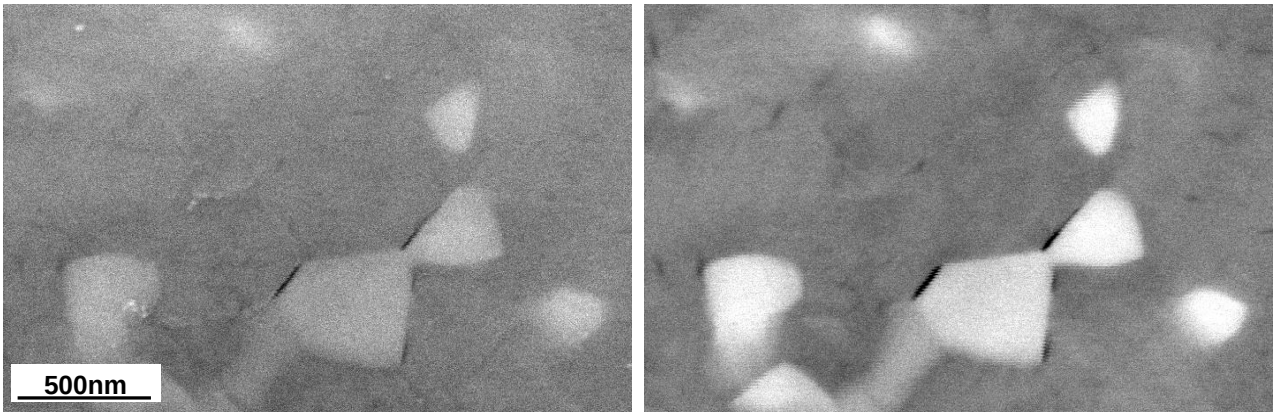

Figure 6-18. SE (left) and BSE (right) micrographs from Alloy 13CrMo-1000-SX-1.4% showing the interfacial microcrack formation at the σ-particles in the 'rippled' region (Courtesy of Michael S. Kesler)

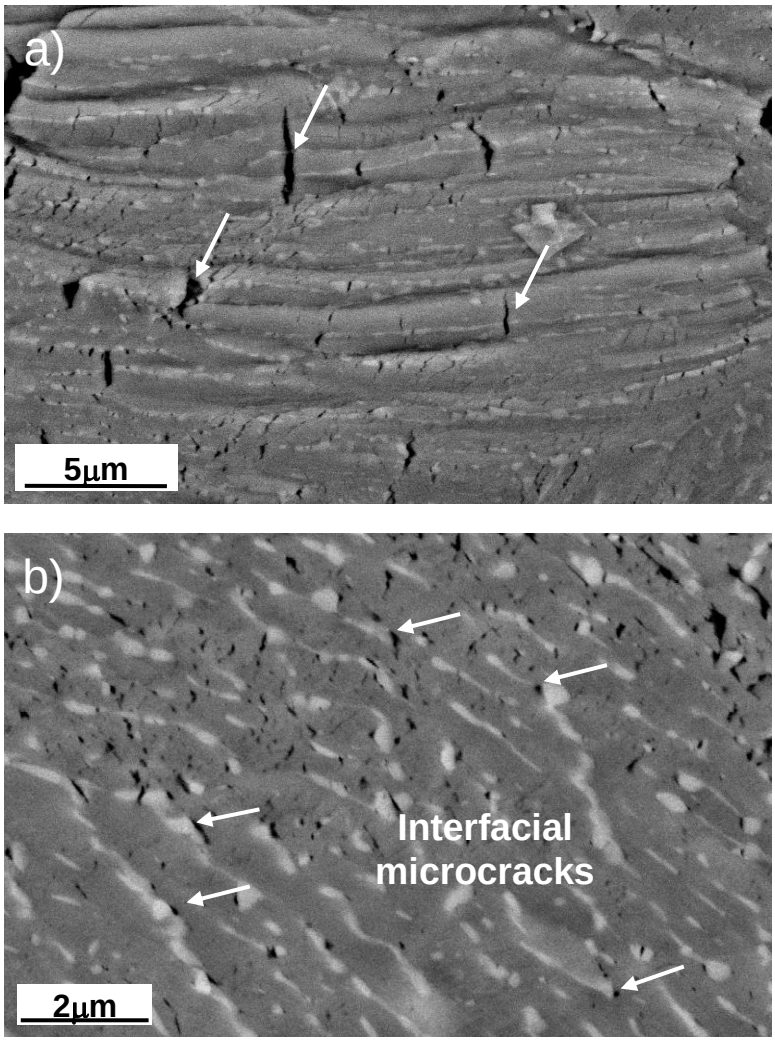

Figure 6-19. SEM micrographs taken from Alloy 13CrMo-1000-SX loaded to fracture showing a) microcrack coalescence adjacent to regions of localized deformation and b) extensive interfacial microcracking in the 'rippled' region (Courtesy of Michael S. Kesler)

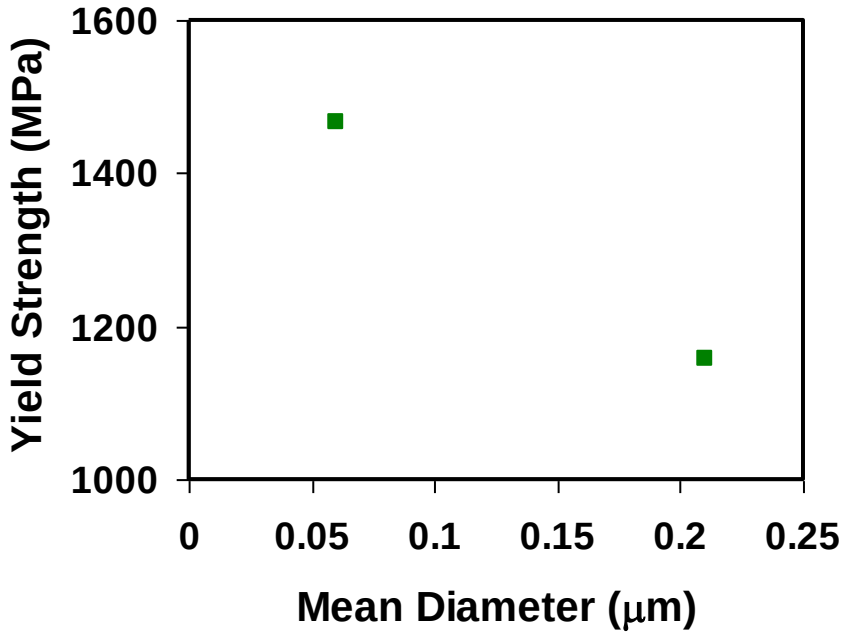

Figure 6-20. Plot of yield strength versus mean diameter of σ-particles for samples of Alloy 13CrMo-SX aged at 865ºC (finer) and 1050ºC (coarser) taken from the same β-grain and compressed in the same orientation (Courtesy of Michael S. Kesler)

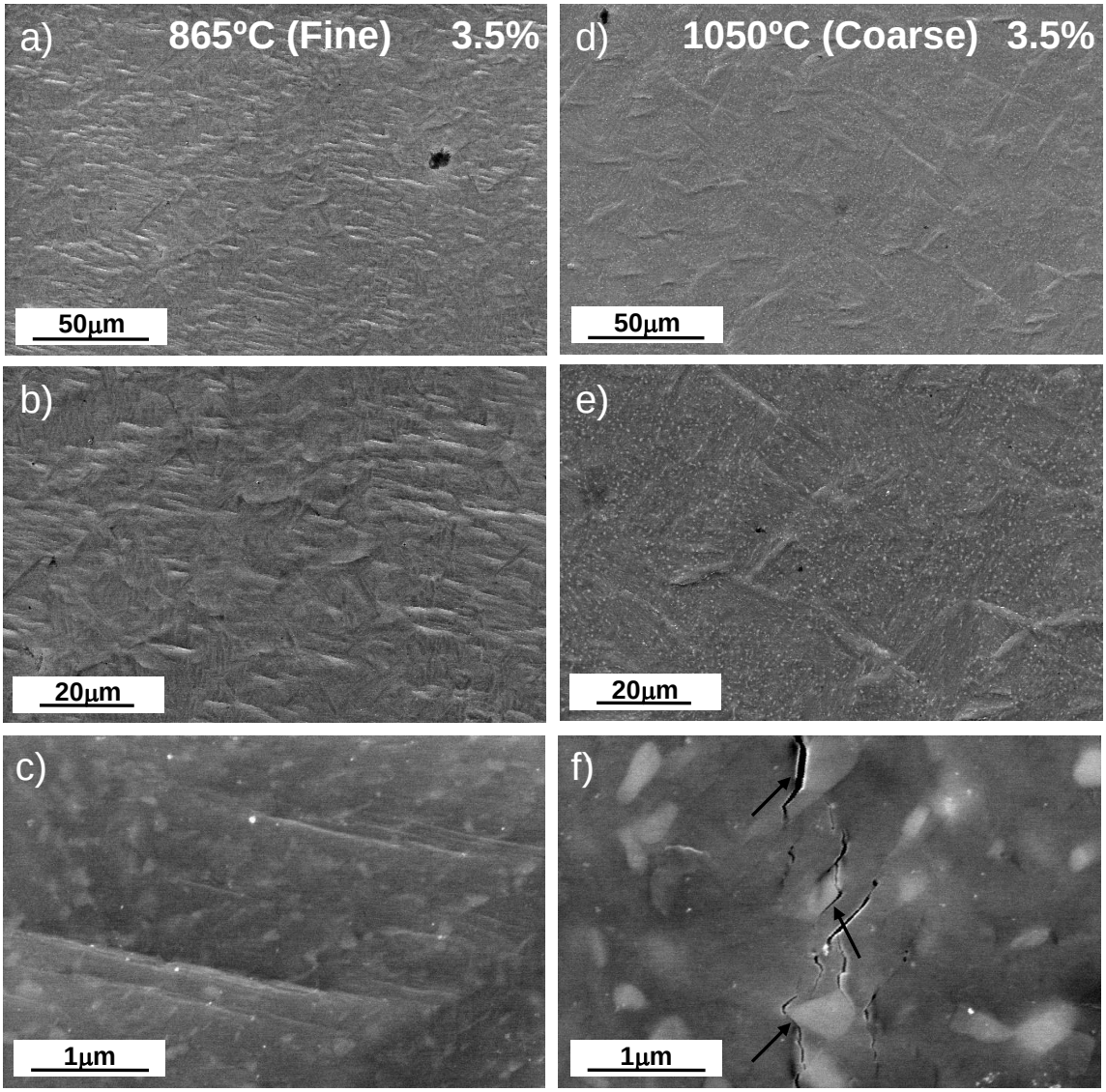

Figure 6-21. SE micrographs of surface damage to samples with a,b) fine and d,e) coarse microstructures from Alloy 13CrMo-SX after interrupted compression testing to 3.5%ε_p and high magnification SE micrographs showing c) no microcracking in the fine microstructure and f) significant interfacial microcracking in the coarsened microstructure (Courtesy of Michael S. Kesler)

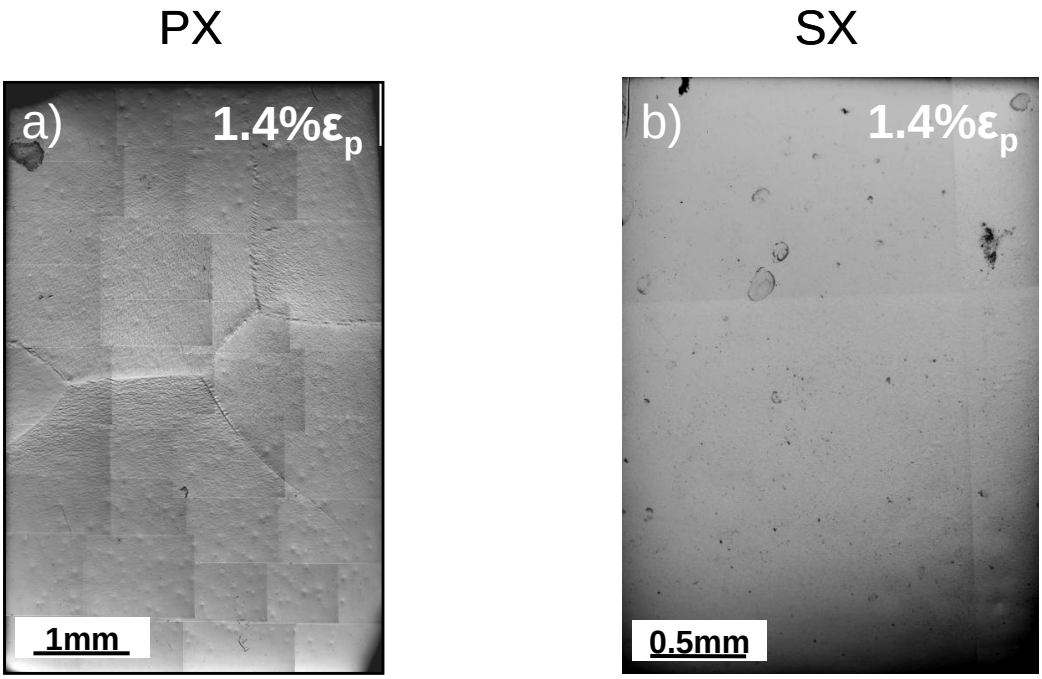

Figure 6-22. Compilations of OM images from the sample surfaces of a) 13CrMo-1000-PX-1.4% and 13CrMo-1000-SX-1.4% (Courtesy of Michael S. Kesler)

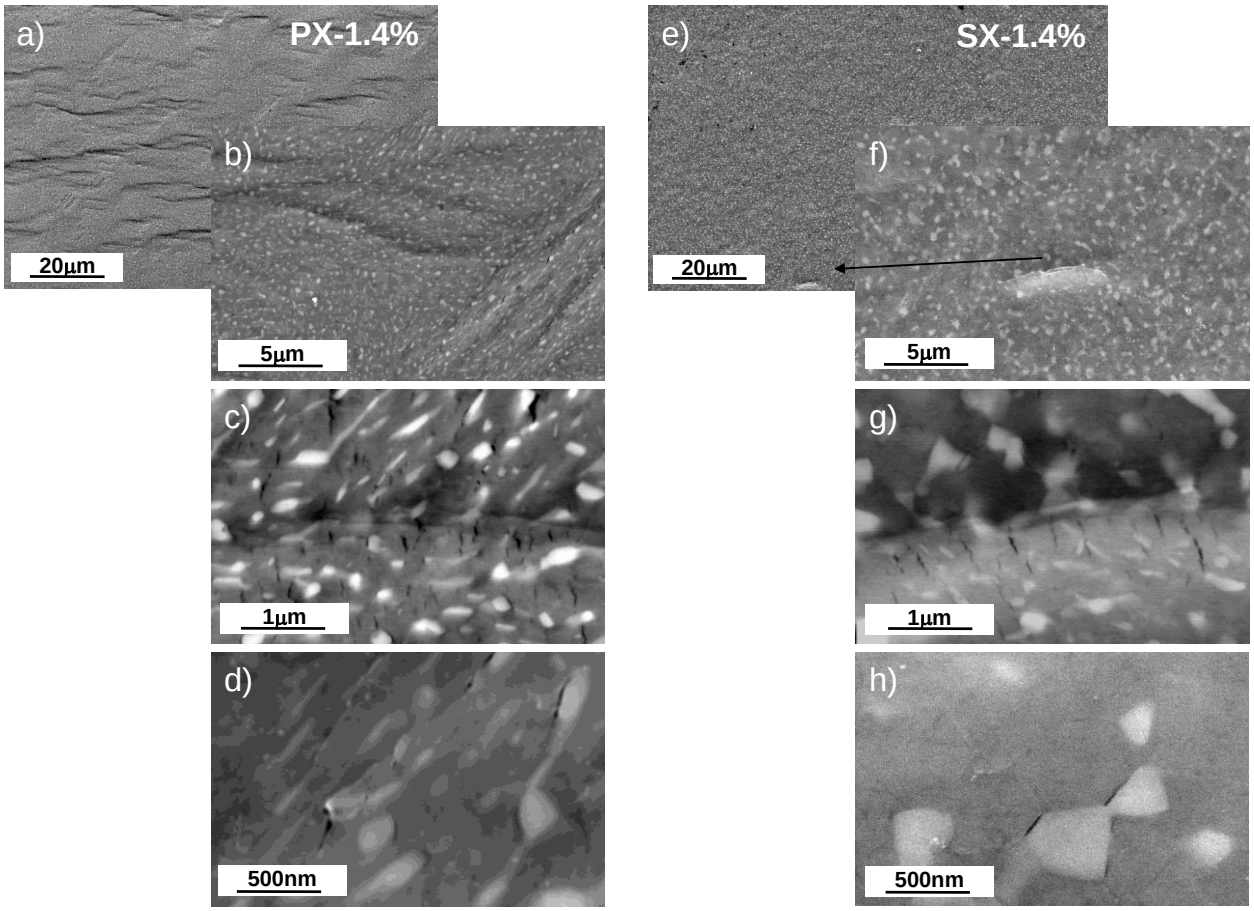

Figure 6-23. SE micrographs comparing the surface damage from a,b,c,d) Alloy 13CrMo-1000-PX-1.4% and e,f,g,h) Alloy 13CrMo-1000-SX-1.4% (Courtesy of Michael S. Kesler)

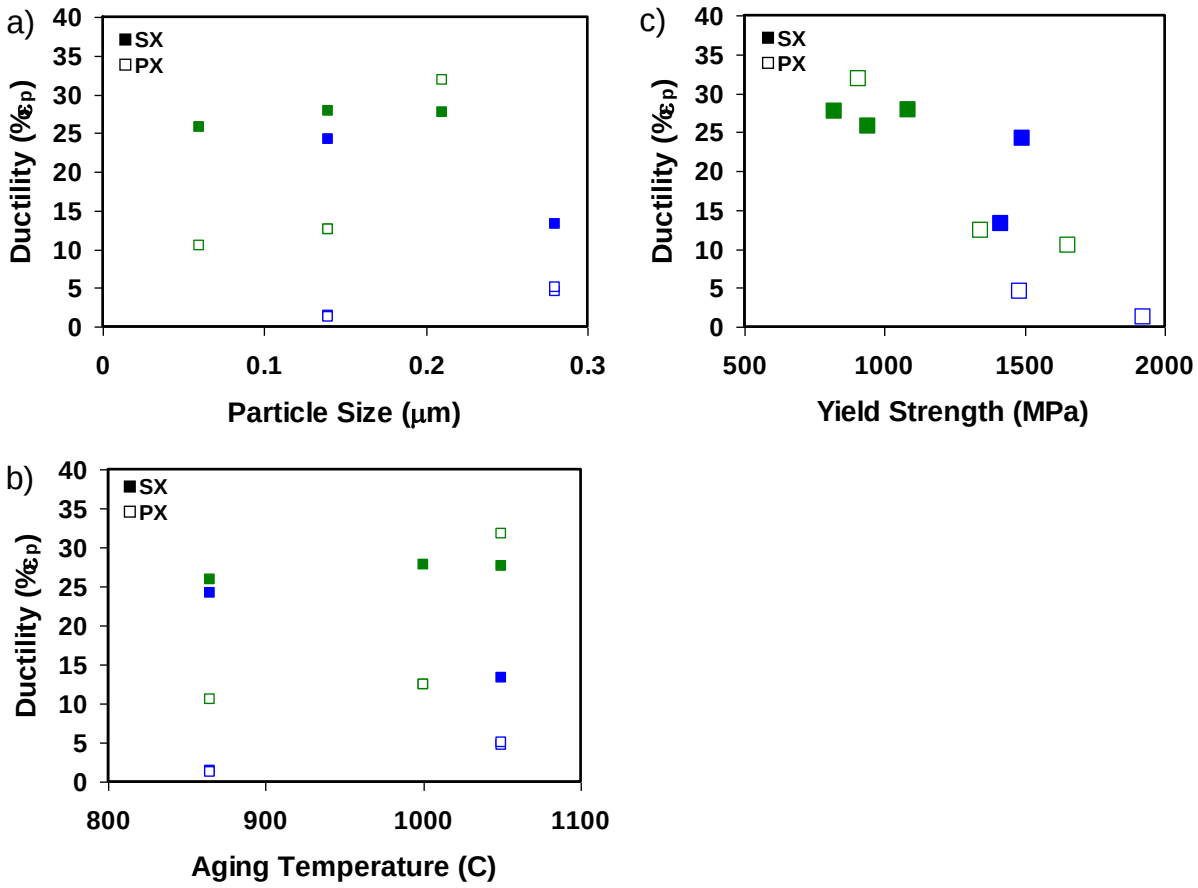

Figure 6-24. Plots of ductility versus a) particle size, b) aging temperature and c) yield strength comparing data from PX (hollow squares) and SX (filled squares) for Alloy 12Cr (blue) and Alloy 13CrMo (green) (Courtesy of Michael S. Kesler)

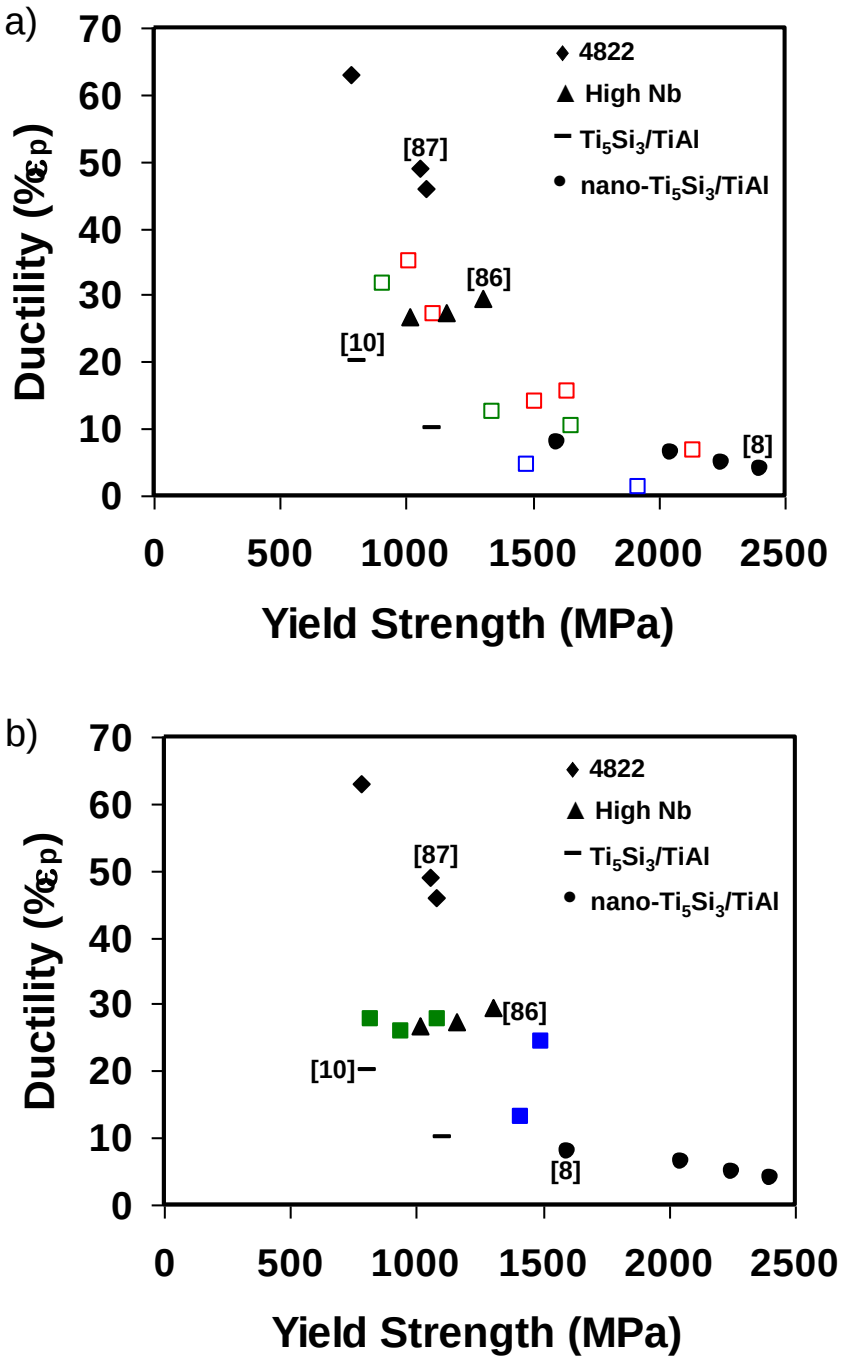

Figure 6-25. A comparison of the compressive ductility (plastic deformation to failure) vs. yield strength data from a) Alloy 12Cr-PX (hollow blue), Alloy 12.5CrMo-PX (hollow red) and Alloy 13CrMo-PX (hollow green) with other novel TiAl-based alloys and b) Alloy 12Cr-SX (solid blue) and Alloy 13CrMo-SX (solid green) with other novel TiAl-based alloys (Courtesy of Michael S. Kesler)

CHAPTER 7
SUMMARY

The goal of this research was to study the effects of σ-phase volume fraction and microstructural scale on the strength, ductility and fracture toughness of TiAlNb alloys with a two-phase γ+σ microstructure. Based on the results from previous work, it was proposed that a low volume fraction (<30vol%) of disconnected σ-phase in a refined γ-phase matrix would result in enhancements in ductility and toughness. In order to control the precipitation of the two-phase γ+σ microstructure, a single high temperature meta-stable parent phase (the β-phase) had to be fully retained to room temperature prior to the aging. The following are a summary of the findings of this study:

1. Ternary alloys with compositions which lie in the two-phase γ+σ region between 1000-1200ºC that would result in a low volume fraction of the σ-phase do exist as a single β-phase at higher temperatures. Upon water quenching from the single β-phase field, these ternary alloys rapidly transformed to two-phase β+γ microstructures. Aging then resulted in coarsened two-phase γ+σ microstructures (Alloy 11-1100). This finding revealed the need to incorporate β-stabilizing alloying elements in an attempt to fully retain the β-phase in the sample sizes for this study.

2. The results of the substitution of Nb with 5at%Cr were that alloys either fully retained the β-phase (Alloy 12Cr), or retained the β-phase with the exception of Widmanstätten γ-phase formation in the vicinity of the β-grains. The addition of Cr also resulted in a lower melting temperature for the alloys.

3. Upon aging, the Widmanstätten γ-phase formation at the β-phase grain boundaries could not be suppressed.

4. In the bulk of the prior β-grains, the refinement of the microstructure could be controlled by the aging temperature. The finest microstructure could be obtained at the lowest temperature that both the γ and σ phases formed nearly simultaneously due to the impingement of the σ-phase on the γ-phase, thereby retarding growth. When the aging temperature was too low, the γ-phase would precipitate and grow uninhibited, resulting in a coarsened γ-phase.

5. The volume fraction of the σ-phase could be controlled by altering the Nb content in the range of 14-22at% resulting in vol%σ ranging from 13-30%.

6. The prior β-phase grain boundaries were detrimental to ductility in compression due to localized deformation and extensive microcracking in the relatively coarse γ-phase that grew in Widmanstätten morphology from the boundaries. This damage led to either fracture along favorably oriented prior β-grain boundaries, or initiated fracture at the boundaries which then propagated transgranularly through prior β-grains.

7. In polycrystalline samples, as the aging temperature/microstructural scale decreased, the yield strength increased while ductility decreased. The decreasing ductility as particle size decreased was attributed to the damage which accumulated at the prior β-phase grain boundaries at low global strain values in alloys with relative high yield strength. The limited damage in the refined γ+σ microstructure in the bulk of the prior β-grains did not lead to fracture of polycrystalline compression samples.

8. In alloys with 5at%Cr addition, as the volume fraction of the σ-phase was reduced, the ductility increased significantly and, generally, the yield strength decreased, with the exception of one alloy condition (12.5CrMo-865).

9. In the absence of prior β-phase grain boundaries in SX samples, greater ductility was realized and the effect was more significant for alloys aged at 865ºC and 1000ºC. This was a result of greater differences in the relative yield strength of the bulk and grain boundary microstructures which limited ductility in PX samples aged at these lower temperatures.

10. At constant σ-phase volume fraction, refined microstructures (aged at 865ºC) in SX alloys exhibited a more uniform distribution of localized strain as compared with coarser microstructures (aged at 1050ºC). The result was microcrack formation at lower plastic strain values in coarsened microstructures. The absence of microcracking at 3.5%ε_p in compression in the most refined microstructure (13CrMo-865-SX) suggests that this alloy would have the greatest likelihood of exhibiting tensile ductility.

11. Yield strength in SX alloys was dependent on orientation, though higher strengths were generally observed with refinement of the γ+σ microstructure.

12. Fracture toughness values improved significantly compared to previously tested σ+γ alloys by the reduction in volume fraction and microstructural scale of the σ-phase. The refinement resulted in crack initiation occurring at γ/σ interfaces and in the γ-phase at prior β-phase grain boundaries rather than within a coarse σ-phase as seen in the previous study. This is an indication that the refinement of the σ-phase is adequate for avoiding crack initiation. Additionally, cracks propagated through γ/σ interfaces and transgranularly though the γ-matrix rather than transgranularly through the continuous σ-phase observed previously.

13. The results suggest that in alloys with the same volume fraction of the σ-phase, refined microstructures exhibit greater fracture toughness, though a more thorough evaluation of scatter is necessary in order to accurately quantify this material property as it relates to the microstructural scale.

CHAPTER 8
FUTURE WORK

This study focused on developing TiAlNb(Cr,Mo) alloys in an effort to the evaluate mechanical properties at room temperature as they relate to the parameters of the two-phase $\gamma+\sigma$ microstructure. As questions were answered, more questions arose. Due to limited time and resources, many pertinent questions go unanswered. The following is a list of unexplored aspects of this topic which are important for understanding these materials:

1. Perhaps the greatest obstacle in moving these materials closer to a practical application is the rigorous water quenching process necessary in order to ultimately arrive at the ultra-fine aged microstructures presented in this study. The limitations are two-fold: 1) water quenching of larger samples results in γ-phase formation, and 2) only uniform samples were able to be quenched without cracking, so preformed samples are not viable. The former could be addressed by exploring additional alloying elements and by limiting internal defects including grain boundaries, pores and other preferential nucleation sites for the γ-phase. The latter could be addressed by producing an alloy which could be quenched at a slower rate, thus limiting the severity of the thermal gradient.

2. Single crystal samples provided significant improvements in ductility, but strength was lost as a result of crystallographic texturing of the aged $\gamma+\sigma$ microstructure which formed out of the single β-grain. The orientation relationship of the γ and σ phases with the parent β-phase could be explored. The evaluation of the mechanical properties as they relate to the crystallographic orientation of the prior β-grain would be an interesting topic of exploration.

3. As outlined in Appendix C, the fabrication of tensile samples of these materials is not trivial and the results would be invaluable for the furthering of this work. This and a more detailed evaluation of fracture toughness are perhaps the most significant results that would complement this work.

This study serves as groundwork to build on for the furthering of this class of materials. Many more aspects of the mechanical properties need to be explored to know if these materials are viable, including fatigue and creep.

APPENDIX A
EPMA STATISTICS AND QUANTITATIVE MICROSCOPY

A-1 EPMA

The following are tables listing the composition of alloys (at%) as measured by EPMA taken from random spots from a cross-section of each button as described in Section 3.4.3. The compositions in Table 3-1 are taken from the average and the standard deviations (STDEV) of each measurement are given.

A-2 Volume Fraction Measurements

The images of Alloy 11(Figure A-1) at higher and lower magnifications (top left and top right, respectively) and the corresponding threshold enhanced images (bottom) resulting in a two-tone black and white image that allows the ImageJ software to conduct area fraction measurements. These are two of several images from which measurements were averaged in order to estimate the final volume fraction values listed in Table 4-1. Table A-6, Table A-7, Table A-8 and Table A-9 list the actual measured values taken from each image, averaged values and standard deviations for each alloy condition.

A-3 Particle Size Measurements

Figure A-2 shows images of Alloy 13CrMo aged at 865ºC, 1000ºC and 1050ºC, respectively, with lines of a given length and the number of intercepted σ-particles for each line. Table A-10 shows an example of the data gathered from three images of 13CrMo-1000 at different magnifications.

The inverse of the average number of intercepts per unit length, N_L, gives the mean random spacing, σ_r, or center-to-center spacing of σ-particles [60]. The calculation of the mean free path, λ, or edge-to-edge spacing could then be calculated.

Figure A-3 is a schematic showing how the mean particle diameter was estimated by (σ_r-λ).

Table A-1. EPMA from random spots on Alloy 11

Alloy 11	Ti	Al	Nb
	37.09	44.35	18.56
	37.1	44.76	18.14
	37.13	44.55	18.32
	37.31	44.67	18.02
	36.97	44.54	18.49
	36.79	44.8	18.41
	36.84	44.83	18.33
	36.79	44.75	18.46
	37	44.82	18.18
	37.14	44.48	18.37
Average	37.02	44.66	18.33
STDEV	0.171	0.166	0.169

Table A-2. EPMA from random spots on Alloy 12

Alloy 12	Ti	Al	Nb
	28.2	43.59	28.21
	28.46	43.72	27.83
	28.31	43.94	27.75
	28.42	43.68	27.9
	28.39	44.25	27.36
	28.15	43.94	27.91
	28.04	44.55	27.42
	28.48	43.92	27.6
	28.32	43.98	27.7
	28.38	43.91	27.71
Average	28.32	43.94	27.74
STDEV	0.143	0.281	0.248

Table A-3. EPMA from random spots on Alloy 12Cr

12Cr	Ti	Al	Nb	Cr
	29.1	43.35	22.52	5.02
	28.52	43.33	23.22	4.93
	29.02	43.51	22.5	4.97
	29.17	43.79	22.16	4.88
	28.73	43.58	22.66	5.03
	28.86	43.4	22.59	5.15
	28.91	43.47	22.61	5.01
	28.79	42.95	23.24	5.02
	29.18	43.5	22.37	4.95
	29.07	43.82	22.2	4.9
Average	28.94	43.47	22.61	4.99
STDEV	0.213	0.247	0.368	0.078

Table A-4. EPMA from random spots on Alloy 12.5CrMo

12.5CrMo	Ti	Al	Nb	Cr	Mo
	30.82	45.48	18.22	4.73	0.9
	30.72	45.81	17.71	4.89	0.88
	30.63	45.65	18	4.91	0.81
	30.87	45.35	17.94	4.87	0.96
	30.84	45.68	17.54	5.05	0.9
	30.57	45.36	17.89	5.1	1.08
	30.63	45.39	18.01	5.13	0.84
	30.98	45.58	17.41	5.08	0.94
	30.42	45.39	18.09	5.09	1.01
	30.73	45.75	17.71	4.87	0.95
Average	30.72	45.54	17.85	4.97	0.93
STDEV	0.164	0.172	0.254	0.135	0.080

Table A-5. EPMA from random spots on Alloy 13CrMo

13CrMo	Ti	Al	Nb	Cr	Mo
	34.83	44.5	14.52	5.03	1.12
	34.88	44.88	14	5.17	1.07
	34.95	44.56	14.43	5.15	0.9
	34.78	44.46	14.54	5.18	1.04
	34.95	44.55	14.32	5.14	1.04
	35	44.55	14.4	5.14	0.92
	34.72	44.88	14.33	5.06	1
	34.79	44.75	14.2	5.19	1.07
	34.82	44.72	14.63	4.85	0.98
	34.94	45.03	13.88	5.15	1
Average	34.87	44.69	14.33	5.11	1.01
STDEV	0.092	0.194	0.239	0.103	0.069

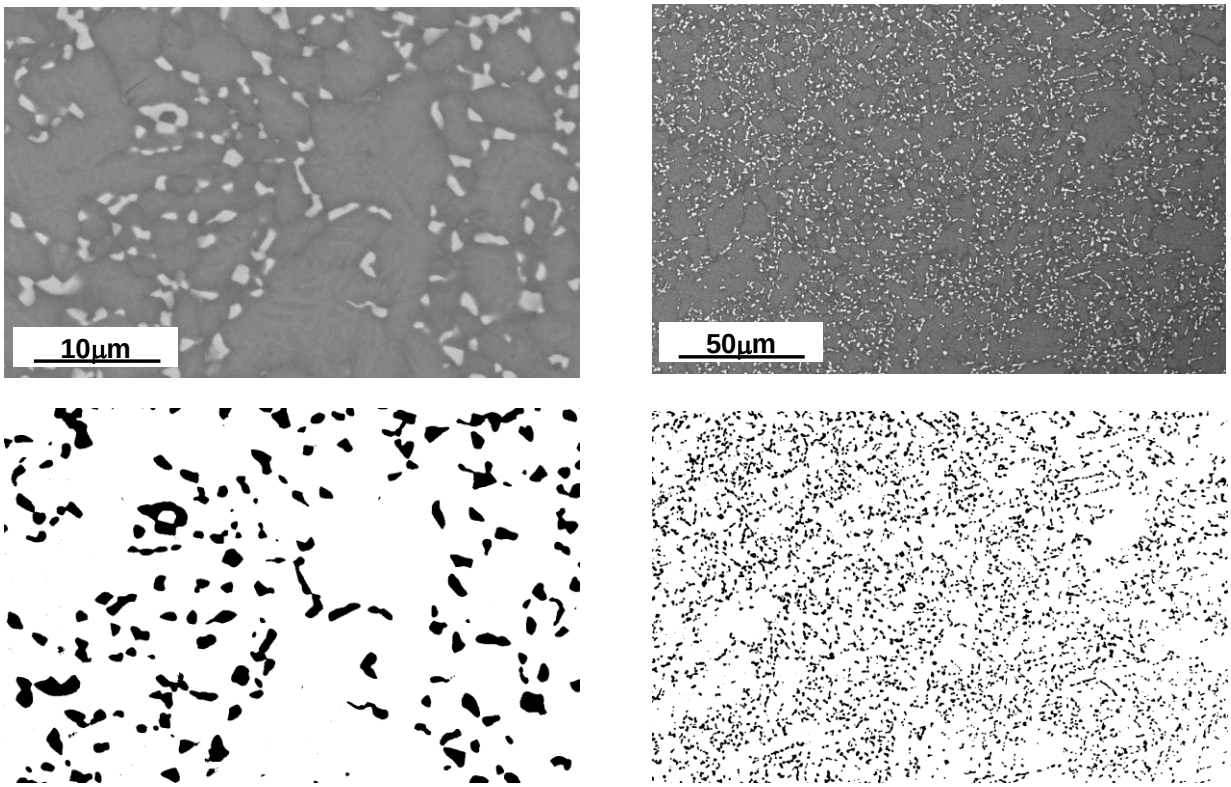

Figure A-1. BSE (top) and corresponding threshold enhanced (bottom) images of Alloy 11 for volume fraction measurements (Courtesy of Michael S. Kesler)

Table A-6. Volume fraction measurements from Alloy 11

11-1100	Vol%σ
	11.8
	12
	13.9
	11.5
	12.4
Average	**12.32**
STDEV	0.942

Table A-7. Volume fraction measurements from Alloy 12Cr

12Cr-865	Vol%σ	**12Cr-1050**	Vol%σ
	25.7		33.3
	27.1		34.2
	32.9		29.7
	31.3		28.4
	27.5		30.7
	35.6	Average	**31.26**
	27.7	STDEV	2.436
Average	**29.69**		
STDEV	3.633		

Table A-8. Volume fraction measurements from Alloy 12.5CrMo

12.5CrMo-865	Vol%σ	**12.5CrMo-1000**	Vol%σ	**12.5CrMo-1050**	Vol%σ
	22.1		22.5		20.2
	21.4		20.9		20.5
	21.9		20.6		22.7
	21.3		24.1		22.6
	20.9		20.9		20.1
Average	**21.52**	Average	**21.8**		23
STDEV	0.481664	STDEV	1.486607		22.5
				Average	**21.65714**
				STDEV	1.315114

]Table A-9. Volume fraction measurements from Alloy 13CrMo

13CrMo-865	Vol%σ	**13CrMo-1000**	Vol%σ	**13CrMo-1050**	Vol%σ
	14		14.1		14.4
	12.3		12.1		12
	14.2		14.1		13.3
	11.4		13.4		13.2
	13.6		13.1		12.3
Average	**13.1**		12.5		11.6
STDEV	1.204		13.1	Average	**12.8**
		Average	**13.2**	STDEV	1.030
		STDEV	0.751		

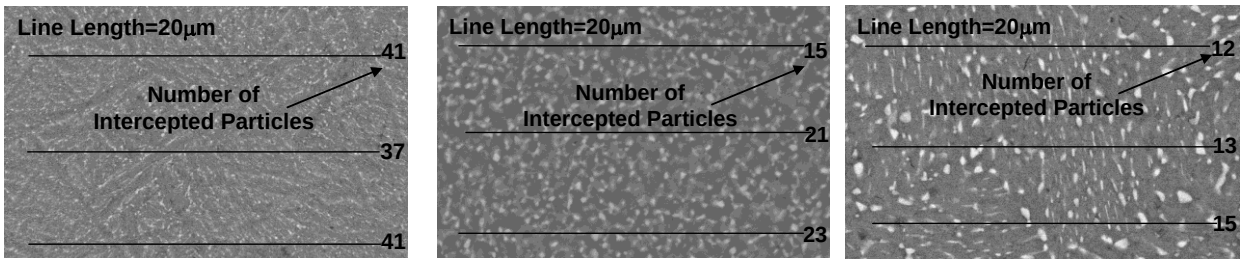

Figure A-2. BSE images with lines intersecting σ-phase particles in Alloy 13CrMo (Courtesy of Michael S. Kesler)

Table A-10. Particle size measurements from Alloy 13CrMo

13CrMo-1000	Line Length (μm)	Intersections	σ_r (μm)
	10	8	
	10	12	
	10	8	
	40	38	
	40	35	
	40	40	
	20	**15**	
	20	**21**	
	20	**23**	
Average	23.33	22.22	**1.05**

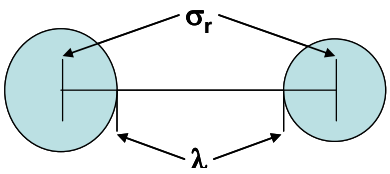

Figure A-3. Schematic showing that (σ_r-λ) equals the mean diameter (Courtesy of Michael S. Kesler)

APPENDIX B
DETERMINATION OF YIELD STRENGTH AND PLASTIC STRAIN VALUES FROM EVALUATION OF STRESS-STRAIN CURVES

All yield strength and plastic strain to failure values were gathered from raw compression stress-strain data. As shown in Figure A-4, the linear-elastic portion of the stress-strain curves were enhanced (right) and a line was constructed though the middle of the data scatter (sloped line on the left). A parallel line was off-set to 0.2% (sloped line on the right) and a horizontal line was placed such that it intersected the off-set line where it intersected the middle of the raw data curve. The exact data point at this intersection was identified resulting in the measured yield strength value. The plastic strain to failure was then measured by taking the corresponding strain value (4.9%) and subtracting it from the strain value at the point of failure (10.0%).

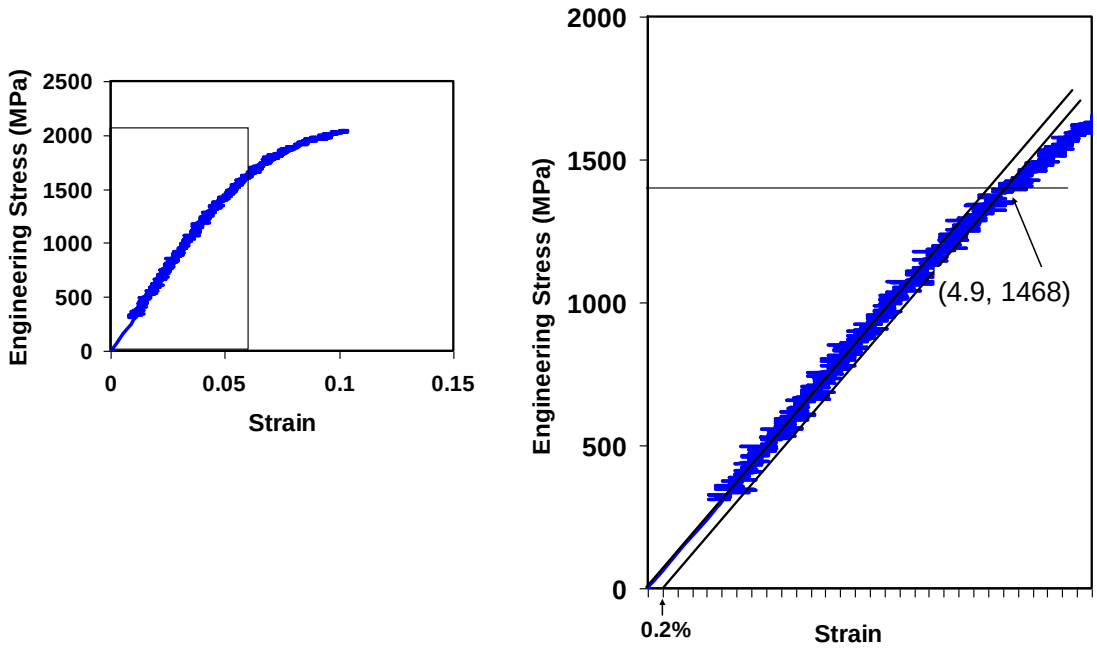

Figure A-4. Raw compression stress-strain curves showing the procedure for measuring 0.2% off-set yield strength and plastic strain to failure (Courtesy of Michael S. Kesler)

APPENDIX C
TENSILE SAMPLE FABRICATION

It was a goal of this research to determine whether or not reducing the volume fraction of the σ-phase would result in enhanced toughness and greater ductility in $\gamma+\sigma$ alloys. In Chapter 5 and Chapter 6, significant enhancements in compressive ductility and toughness were realized when comparing to alloys with higher σ-phase volume fraction (50-70vol%σ) [55]. The alloys from this study are comparable in compressive ductility (25-30%ε_p) and strength (around 1000MPa) to $\gamma+\alpha_2$ alloys with high Nb content (8.5-10at%Nb) [87]. These $\gamma+\alpha_2$ alloys exhibit tensile elongation in the range of 0-2%ε_p and depended strongly on processing routes and microstructure. Duplex (DP) microstructures (a combination of equiaxed γ-grains and lamellar γ/α colonies) routinely exhibited the greatest tensile elongation and this was attributed to the fine equiaxed γ-grains and lamellar colony-containing grains. The fully lamellar (FL) microstructure was expected to exhibit superior properties, but in order to develop this microstructure, higher heat treatment temperatures are necessary resulting in larger grain and colony sizes. It was determined from those studies that refined γ-phase and lamellar grain sizes (<4mm) yielded the greatest tensile elongation [20, 30]. The alloys in this study are refined to a greater extent with γ-grains generally on the order of 0.5-2μm and σ-particles in the ultrafine and nano-sized regime (Table 4-1). The refinement was intended to impart greater strain accommodation between grains and result in more uniform deformation. The results in Chapter 6 suggest this to be true for compression testing and the toughness results, while inconclusive, do suggest enhanced toughness in the refined microstructures. It is important to note, that compressive properties do not

always translate proportionately to tensile properties as these properties are highly dependant on localization of strain and microcrack development which leads to fracture at very low plastic strains, particularly in γ-based alloys.

Because very low plastic strains (or no plastic strain) are likely, it is imperative to have near perfect alignment of the samples and of the fixtures on the testing apparatus because any off-set would place a moment on the sample resulting in premature fracture. Firstly, fixtures were selected from the options in the lab which included free-hanging collar for cylindrical or rectangular dog bone, cylindrical threaded fixtures and hydraulic clamps. In selecting a fixture, ease of use/fabrication and sample size and geometry are the primary considerations. The use of the free-hanging collared fixture is ideal because it is self aligning as long as the instrument itself is already in good alignment. The versatility of being able to use a rectangular shaped dog bone sample would allow for the use of EDM for fabricating the sample geometry. This was the first option for fixtures. The samples were cut into the final form from 25g bars using EDM, as shown in Figure A-5. The double reduction of the cross-sectional area of the gauge length was necessary because there was a need to limit the length of the narrowest region of the cross-section to limit the moment on the gauge length. In addition, the upper reduction was necessary due to the maximum cross-sectional area that could fit in the collared fixture. The issue with this geometry/sample preparation route was quickly recognized, as water quenching, during soln+WQ, resulted in significant cracking primarily in the region where the heads of the dog bones met the reduced cross-section. This was an obvious result of inconsistent cooling rates on different parts of the sample and deemed this process of tensile sample fabrication unusable.

The next step was to move to a cylindrical shaped tensile sample (Figure A-6). The main benefit of this geometry was maximizing the total number of samples obtained from a single 25g bar (5 instead of 3 for the bar-shaped samples). Several challenges were presented including maintaining uniform cylinders upon water quenching from the solutionizing temperature, achieving a reduced cross-section (not possible with EDM) and threading the heads of the samples. As mentioned in Section 3.5.3.1, surface grinding was a viable option for these materials, so turning on a lathe (courtesy of MTE) with a carbide bit (a more rigorous process) was successfully attempted on soln+WQ cylinders. Because of the slight warping experienced during water quenching, the EDMed cylinders needed to be 'center-pointed' on the lathe and turned to the designed maximum diameter (3.5mm). Prior to reducing the gauge length cross-section via grinding, threading with a die on the lathe was attempted unsuccessfully. The result was catastrophic failure of the cylindrical bar in the to-be-threaded region. The next method of threading attempted was to incrementally cut the threads with the lathe using a carbide bit. This allowed for a less rigorous process. As the threading process went on, a small volume of material (the thread itself) was continually exposed to the stress applied by the carbide bit and the result was that the material hardened and ultimately pieces of the thread chipped off. A third idea for fabricating threading was devised, where a grinding bit would be used to grind the threading in an incremental manner, but this method was unable to be attempted due to the lack of a precision grinding bit. To clarify, the carbide bit used during lathing has a fine sharpened edge and is considered cutting which is far more damaging to the surrounding material, whereas grinding is often more localized, thus not affecting as large a volume of material.

In the final attempt at fabricating a viable tensile specimen, a sample geometry was designed to be fitted to the hydraulic clamps (Figure A-7). For these samples, a rectangular bar was EDMed, soln+WQ and planed by the surface grinding technique. At this point in the research, results from single crystal compression tests had shown an increase in ductility. Based on these results, it was of interest to maximize the possible tensile elongation in tensile samples. Therefore, a single β-grain was identified near the center of the bar in the soln+WQ condition. The gauge length was ground (via surface grinding) such that the entire reduced cross-section was made up of a single β-grain, as seen in Figure A-7. The sample was polished to 0.3mm and placed in the hydraulic grips. The standard procedure for sample insertion was undertaken which involved opening and closing of each grip to insure proper alignment. Upon running the test, the sample fractured above the reduced cross-section due to misalignment. This was evident after the sample fractured because the two sides of the sample (one in each grip) were slightly off-set from each other. Because of the late relative date at which this test was conducted, no further testing was attempted in the interest of time. It is suggested based on the experience from this study that this is the most viable option for tensile sample fabrication. It is entirely possible to fabricate such sample geometries with EDM, but soln+WQ treatments much be conducted on uniform samples and then final sample geometries can be machined.

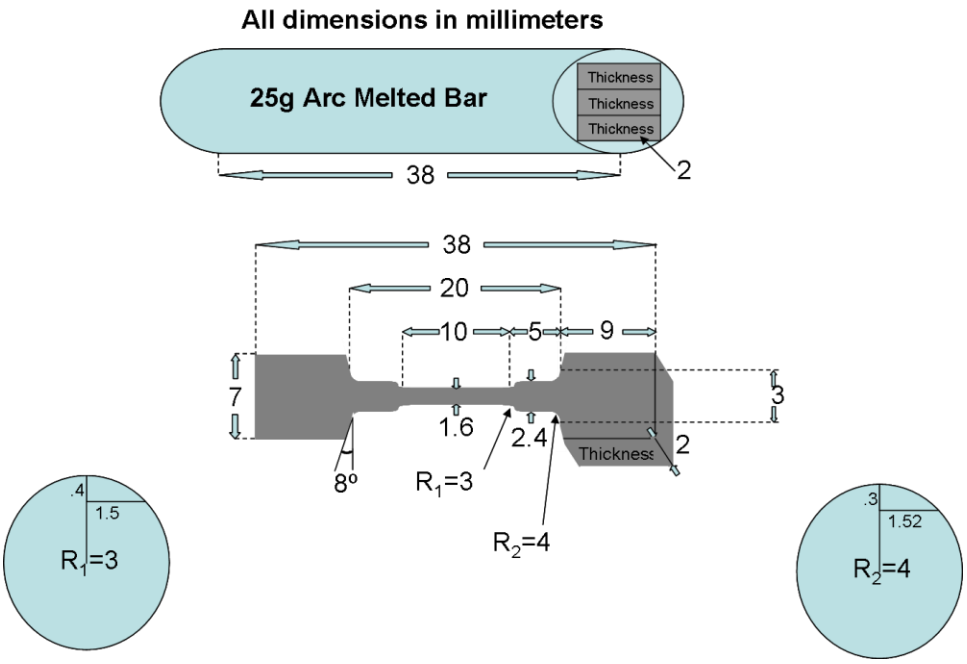

Figure A-5. Schematic of the tensile specimen designed for the collared fixture (Courtesy of Michael S. Kesler)

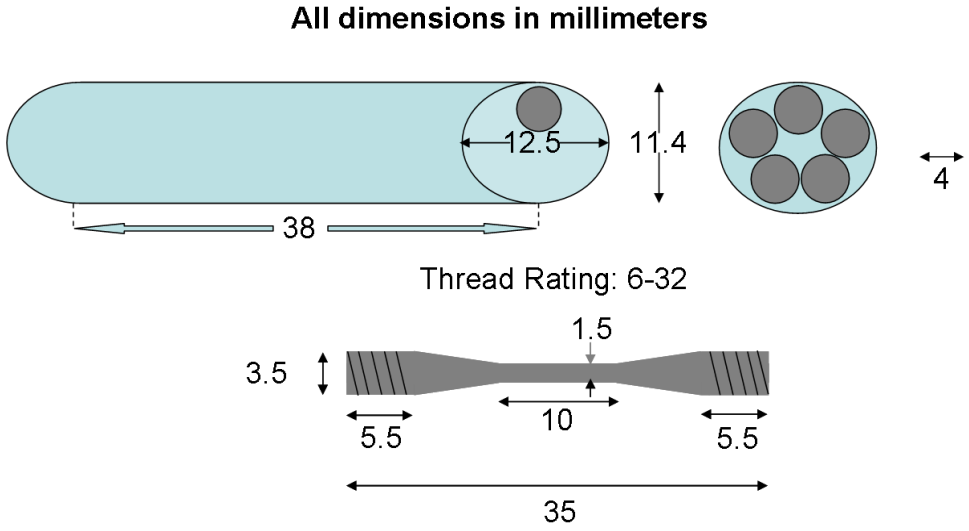

Figure A-6. Schematic of the tensile specimen designed for the cylindrical threaded fixture (Courtesy of Michael S. Kesler)

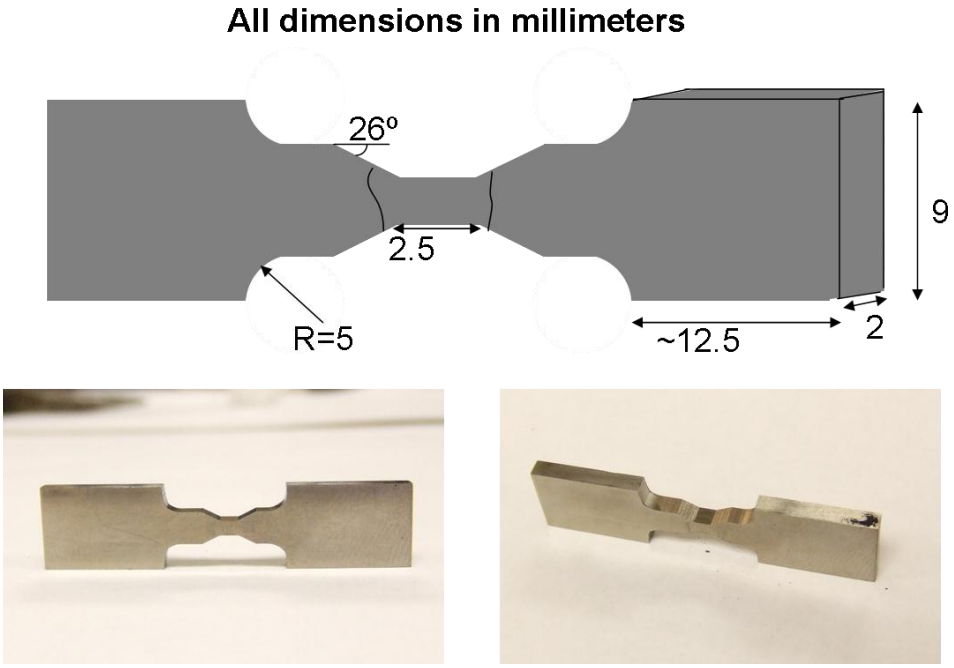

Figure A-7. Schematic (top) of the tensile specimen designed for the hydraulic grips and images of the fabricated tensile sample (bottom) (Courtesy of Michael S. Kesler)

APPENDIX D
NOTCH DIMENSIONS AND LOAD-DISPLACEMENT CURVES

Uniform notch dimensions in SEN bar samples are vital in order to yield consistent results upon testing. Figure A-8 shows the SEN which was cut into sample Alloy 13CrMo-1000-2hrs-1. The notch was imaged using OM from both sides and precisely measured. Because the notch was cut with a round diamond blade, the alignment of the bar on the saw was not a trivial process. If the sample was placed at the slightest angle, the length of the notch on one side of the sample could measure significantly different that the other side. All samples had precise notches that did not vary more that ~10μm from side to side, barring one, Alloy 13CrMo-865-2hrs-1. The erred sample had notch measurements which varied ~50μm from side to side and the result was a significant drop in the maximum load achieved upon bending and, thus, a drop in the calculated fracture toughness value (Table 6-2). Additionally, the width of the notch plays a roll in the stress intensity at the notch root and with a notch root width of 190μm (cut with a 150μm blade width), in the absence of a precrack, the plastic zone size, r_p, had a significant impact on the fracture toughness values calculated from the maximum stress (~15-30% overestimation). Figure A-9a shows the fracture surface of Alloy 13CrMo-1000-2hrs-2 and Figure A-9b shows a side view of the fractures specimen revealing a change in fracture path after ~400μm which would be consistent with the estimation of the plastic zone size ahead of a blunted crack tip, $r_p \approx 1.9\delta$ [62].

The load-displacement curves for samples of Alloy 13CrMo-865-2hr, Alloy 13CrMo-1000-2hrs and Alloy 13CrMo-1050-20hrs are shown in Figure A-10 Figure A-11 and Figure A-12, respectively.

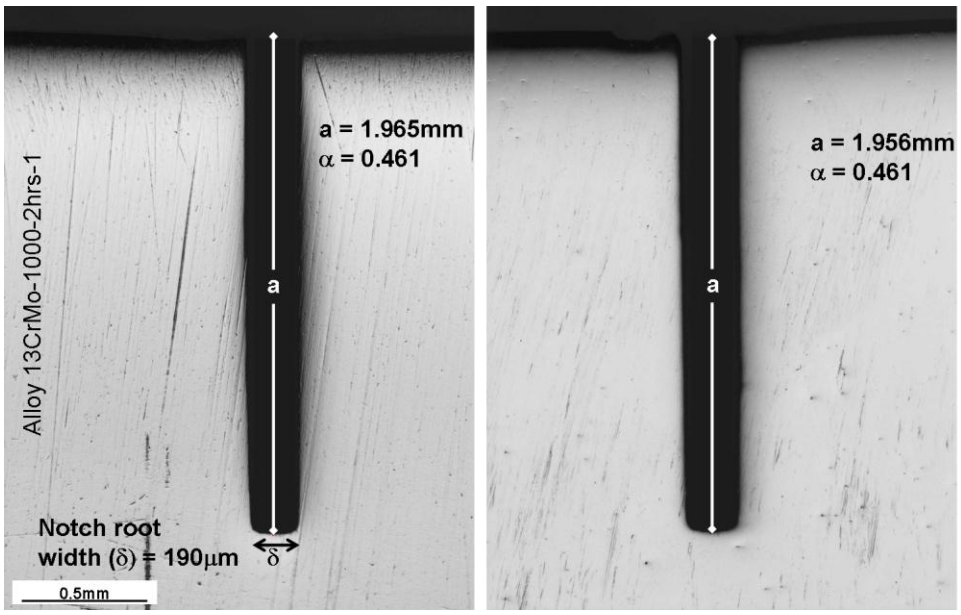

Figure A-8. OM images of the notch cut into the sample Alloy 13CrMo-1000-2hrs-1 with labeled dimensions (Courtesy of Michael S. Kesler)

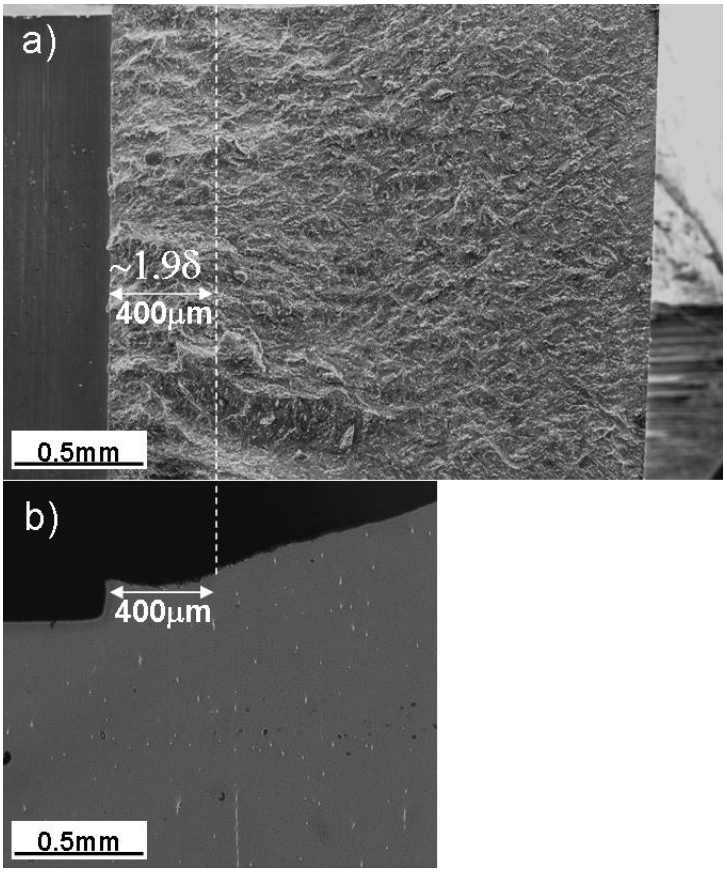

Figure A-9. Images showing a) the fracture surface and b) side view of the fracture path from the sample Alloy 13CrMo-1000-2hrs-2 (Courtesy of Michael S. Kesler)

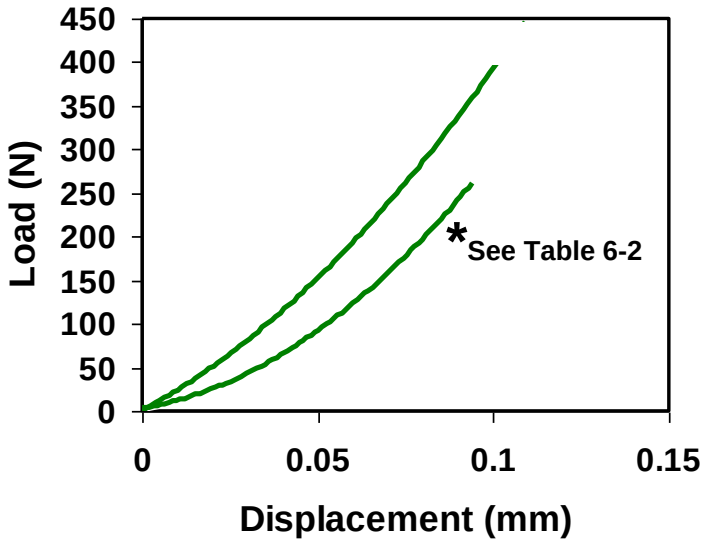

Figure A-10. Load-displacement curve of Alloy 13CrMo-865-2hrs (Courtesy of Michael S. Kesler)

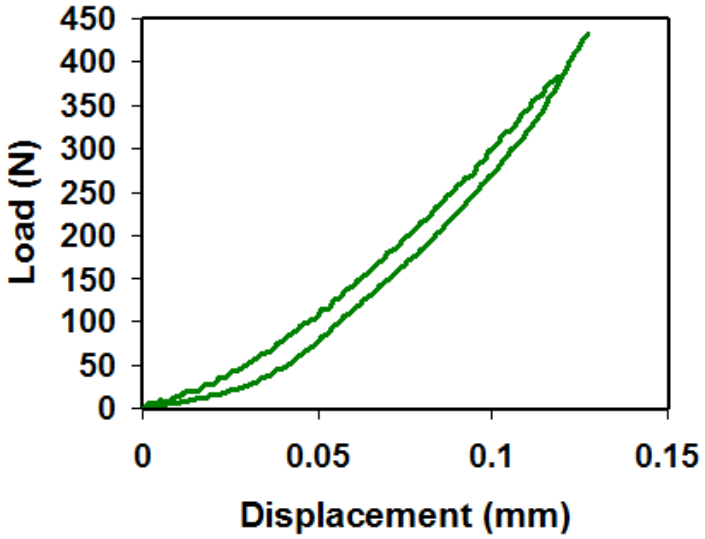

Figure A-11. Load-displacement curve of Alloy 13CrMo-1000-2hrs (Courtesy of Michael S. Kesler)

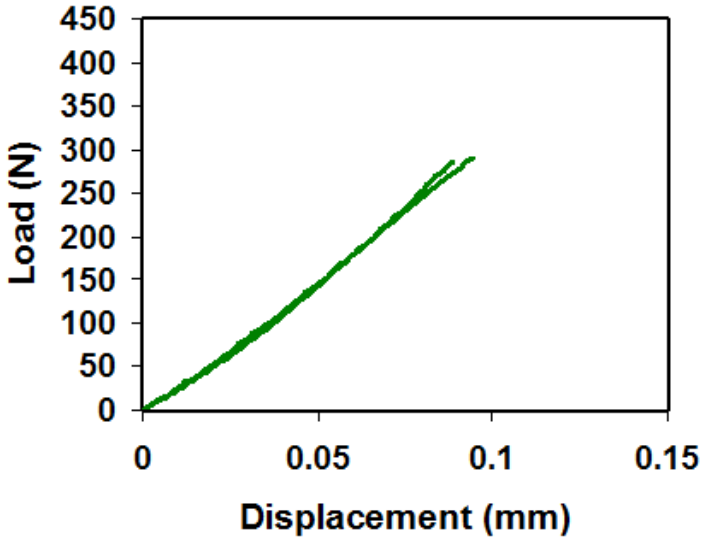

Figure A-12. Load-displacement curve of Alloy 13CrMo-1050-20hrs (Courtesy of Michael S. Kesler)

LIST OF REFERENCES

[1] R. C. Reed, The Superalloys: Fundamentals and Applications, Cambridge University Press, 2006.

[2] Y. W. Kim, Jom-Journal of the Minerals Metals & Materials Society 46 (1994) 30-39.

[3] F. Appel, R. Wagner, Materials Science & Engineering R-Reports 22 (1998) 187-268.

[4] J. P. Lin, X. J. Xu, Y. L. Wang, S. F. He, Y. Zhang, X. P. Song, G. L. Chen, Intermetallics 15 (2007) 668-674.

[5] M. Yamaguchi, H. Inui, K. Ito, Acta Materialia 48 (2000) 307-322.

[6] W. Zhang, G. Chen, Z. Sun, Scripta Metallergica 28 (1993).

[7] W. J. Zhang, F. Appel, Materials Science and Engineering a-Structural Materials Properties Microstructure and Processing 329 (2002) 649-652.

[8] R. Bohn, T. Klassen, R. Bormann, Acta Materialia 49 (2001) 299-311.

[9] J. Lapin, L. Ondrus, O. Bajana, Materials Science and Engineering a-Structural Materials Properties Microstructure and Processing 360 (2003) 85-95.

[10] K. P. Rao, J. B. Zhou, Materials Science and Engineering a-Structural Materials Properties Microstructure and Processing 356 (2003) 208-218.

[11] K. P. Rao, J. B. Zhou, Materials and Manufacturing Processes 21 (2006) 513-517.

[12] Y. H. Wang, J. P. Lin, Y. H. He, X. Lu, Y. L. Wang, G. L. Chen, Journal of Alloys and Compounds 461 (2008) 367-372.

[13] T. T. Ai, Chinese Journal of Aeronautics 21 (2008) 559-564.

[14] B. J. G. DeAragao, F. Ebrahimi, Materials Science and Engineering a-Structural Materials Properties Microstructure and Processing 208 (1996) 37-46.

[15] F. Ebrahimi, J. R. Castillogomez, Acta Metallurgica Et Materialia 40 (1992) 1409-1416.

[16] F. Ebrahimi, D. T. Hoelzer, J. R. Castillogomez, Materials Science and Engineering a-Structural Materials Properties Microstructure and Processing 171 (1993) 35-45.

[17] K. S. Chan, Y. W. Kim, Metallurgical Transactions a-Physical Metallurgy and Materials Science 23 (1992) 1663-1677.

[18] K. S. Chan, Y. W. Kim, Acta Metallurgica Et Materialia 43 (1995) 439-451.

[19] Y. W. Kim, Materials Science and Engineering a-Structural Materials Properties Microstructure and Processing 193 (1995) 519-533.

[20] Y. W. Kim, Intermetallics 6 (1998) 623-628.

[21] R. Gnanamoorthy, Y. Mutoh, Y. Mizuhara, Materials Science and Engineering A 197 (1995) 69-77.

[22] S. Kumar, W. A. Curtin, Materials Today 10 (2007) 34-44.

[23] R. Cao, Y. Z. Lin, D. Hu, J. H. Chen, Engineering Fracture Mechanics 75 (2008) 4343-4362.

[24] R. Cao, H. J. Yao, J. H. Chen, J. Zhang, Materials Science and Engineering: A 420 (2006) 122-134.

[25] J. H. Chen, R. Cao, J. Zhang, G. Z. Wang, Journal of Materials Science 42 (2007) 2820-2829.

[26] R. T. Zheng, G. A. Cheng, X. J. Li, G. X. Cao, L. F. Fu, Y. G. Zhang, C. Q. Chen, Journal of Materials Science 42 (2007) 1251-1260.

[27] B. Dogan, D. Schöneich, K. H. Schwalbe, R. Wagner, Intermetallics 4 (1996) 61-69.

[28] J. H. Chen, R. Cao, G. Z. Wang, J. Zhang, Metallurgical and Materials Transactions a-Physical Metallurgy and Materials Science 35A (2004) 439-456.

[29] F. Ebrahimi, B. J. G. Dearagao, J. R. Castillogomez, Materials Science and Engineering a-Structural Materials Properties Microstructure and Processing 177 (1994) L7-L10.

[30] Y. W. Kim, D. M. Dimiduk, Jom-Journal of the Minerals Metals & Materials Society 43 (1991) 40-47.

[31] V. Paidar, Materials Science and Engineering A 387-389 (2004) 977-980.

[32] M. Yamaguchi, Y. Umakoshi, Progress in Materials Science 34 (1990) 1-148.

[33] H. A. Lipsitt, D. Shechtman, R. E. Schafrik, Metallurgical Transactions a-Physical Metallurgy and Materials Science 6 (1975) 1991-1996.

[34] X. J. Xu, J. P. Lin, Y. L. Wang, J. F. Gao, Z. Lin, G. L. Chen, Journal of Alloys and Compounds 414 (2006) 175-180.

[35] H. Zhu, D. Y. Seo, K. Maruyama, P. Au, Materials Science and Engineering: A 483-484 (2008) 533-536.

[36] F. Appel, U. Christoph, M. Oehring, Materials Science and Engineering A 329-331 (2002) 780-787.

[37] T. Matsuo, T. Nozaki, T. Asai, M. Takeyama, Materials Science and Engineering A 329-331 (2002) 774-779.

[38] S.-C. Huang, E. L. Hall, Acta Metallurgica et Materialia 39 (1991) 1053-1060.

[39] R. Uemori, T. Hanamura, H. Morikawa, Scripta Metallurgica et Materialia 26 (1992) 969-974.

[40] J. Kumpfert, Y. W. Kim, D. M. Dimiduk, Materials Science and Engineering A 192-193 (1995) 465-473.

[41] J. M. K. Wiezorek, H. L. Fraser, Philosophical Magazine a-Physics of Condensed Matter Structure Defects and Mechanical Properties 77 (1998) 661-674.

[42] W. J. Zhang, Z. C. Liu, G. L. Chen, Y. W. Kim, Materials Science and Engineering A 271 (1999) 416-423.

[43] R. M. Imayev, O. A. Kaibyshev, G. A. Salishchev, Acta Metallurgica et Materialia 40 (1992) 589-595.

[44] V. M. Imayev, R. M. Imayev, G. A. Salishchev, Intermetallics 8 (2000) 1-6.

[45] K. S. Chan, JOM-Journal of the Minerals Metals & Materials Society 44 (1992) 308.

[46] H. E. Dève, A. G. Evans, Acta Metallurgica et Materialia 39 (1991) 1171-1176.

[47] A. Dlouhý, K. Kucharová, J. Brezina, Materials Science and Engineering A 319-321 (2001) 820-826.

[48] S. Azad, R. K. Mandal, A. K. Singh, Materials Science and Engineering a-Structural Materials Properties Microstructure and Processing 429 (2006) 219-224.

[49] D. Banerjee, Progress in Materials Science 42 (1997) 135-158.

[50] S. Das, J. M. Howe, J. H. Perepezko, Metallurgical and Materials Transactions a-Physical Metallurgy and Materials Science 27 (1996) 1623-1634.

[51] I. S. Jung, H. S. Jang, M. H. Oh, J. H. Lee, D. M. Wee, Materials Science and Engineering a-Structural Materials Properties Microstructure and Processing 329 (2002) 13-18.

[52] A. K. Singh, D. Banerjee, Metallurgical and Materials Transactions a-Physical Metallurgy and Materials Science 28 (1997) 1735-1743.

[53] T. Tetsui, Intermetallics 10 (2002) 239-245.

[54] W. J. Zhang, Z. C. Liu, G. L. Chen, Philosophical Magazine 79 (1999) 1073-1078.

[55] J. R. Castillogomez, Development of high temperature niobium based alloys, in: Materials Science and Engineering, Masters Thesis, University of Florida, Gainesville, Fla., 1990.

[56] B. J. G. deAragao, High temperature deformation of Nb-Ti-Al alloys with sigma plus gamma microstructure, in: Materials Science and Engineering, Masters Thesis, University of Florida, Gainesville, Fla., 1993.

[57] J. Lankford, Journal of Materials Science Letters 1 (1982) 493-495.

[58] S. Ochiai, Mechanical Properties of Metallic Composites, Marcel Dekker, Inc., New York, NY, 1994.

[59] O. Rios, Examination of the high temperature equilibrium in the Ti-Al-Nb ternary alloy system, in: Materials Science and Engineering, PhD Dissertation, University of Florida, Gainesville, Fla., 2009.

[60] E. E. Underwood, Quantitative Stereography, Addison-Wesley Pub. Co., Reading, Mass., 1970.

[61] M. Sakai, R. C. Bradt, International Materials Reviews 38 (1993) 53-78.

[62] J. F. Knott, Fundamentals of fracture mechanics, Wiley, 1973.

[63] O. Rios, S. Goyel, M. S. Kesler, D. M. Cupid, H. J. Seifert, F. Ebrahimi, Scripta Materialia 60 (2009) 156-159.

[64] D. M. Cupid, O. Fabrichnaya, O. Rios, F. Ebrahimi, H. J. Seifert, International Journal of Materials Research 100 (2009) 218-233.

[65] D. M. Cupid, Thermodynamic assessment of the Ti-Al-Nb, Ti-Al-Cr, and Ti-Al-Mo systems, in: Materials Science and Engineering, Ph.D Dissertation, University of Florida, Gainesville, Fla., 2009.

[66] D. Music, J. M. Schneider, Physical Review B 74 (2006).

[67] S. Goyel, The study of the beta to gamma phase transformation in high-Nb Ti-Al-Nb alloys, in: Materials Science and Engineering, PhD Dissertation, University of Florida, Gainesville, Fla., 2011.

[68] D. T. Hoelzer, Phase transformations in the central portion of the Nb-Ti-Al ternary system / by David Timothy Hoelzer, 1996.

[69] K. J. Leonard, V. K. Vasudevan, Intermetallics 8 (2000) 1257-1268.

[70] C. Servant, I. Ansara, Calphad 25 (2001) 509-525.

[71] C. Servant, I. Ansara, Berichte Der Bunsen-Gesellschaft-Physical Chemistry Chemical Physics 102 (1998) 1189-1205.

[72] A. Zdziobek, M. Durandcharre, J. Driole, F. Durand, Zeitschrift Fur Metallkunde 86 (1995) 334-340.

[73] M. S. Kesler, S. Goyel, O. Rios, D. M. Cupid, H. J. Seifert, F. Ebrahimi, Materials Science and Engineering a-Structural Materials Properties Microstructure and Processing 527 (2010) 2857-2863.

[74] E. O. Hall, S. H. Algie, Journal of the Institute of Metals 94 (1966) 61-&.

[75] S. Tournier, M. Barth, D. M. Herlach, B. Vinet, Acta Materialia 45 (1997) 191-199.

[76] K. Hashimoto, M. Kimura, Y. Mizuhara, Intermetallics 6 (1998) 667-672.

[77] F. S. Sun, C. X. Cao, S. E. Kim, Y. T. Lee, M. G. Yan, Metallurgical and Materials Transactions a-Physical Metallurgy and Materials Science 32 (2001) 1573-1589.

[78] e. a. W. Wallgram, Int. J. Mat. Res. 100 (2009).

[79] M. F. Ashby, Philosophical Magazine 21 (1970) 399-424.

[80] I. H. Katzarov, A. T. Paxton, Philosophical Magazine 89 (2009) 1731-1750.

[81] I. H. Katzarov, A. T. Paxton, Acta Materialia 59 1281-1290.

[82] F. Gregori, P. Veyssiere, Materials Science and Engineering: A 309-310 (2001) 87-91.

[83] F. o. Louchet, B. Viguier, Scripta Metallurgica et Materialia 31 (1994) 369-374.

[84] K. J. Hemker, B. Viguier, M. J. Mills, Materials Science and Engineering: A 164 (1993) 391-394.

[85] F. Appel, Philosophical Magazine 85 (2005) 205-231.

[86] N. E. Biery, M. De Graef, T. M. Pollock, Materials Science and Engineering: A 319-321 (2001) 613-617.

[87] X. Lu, X. B. He, B. Zhang, L. Zhang, X. H. Qu, Z. X. Guo, Intermetallics 17 (2009) 840-846.

[88] M. Usta, H. Wolfe, D. J. Duquette, N. S. Stoloff, R. N. Wright, Materials Science and Engineering a-Structural Materials Properties Microstructure and Processing 359 (2003) 168-177.

[89] J. K. M. Mizuno, Japan Fine Ceramics Center (1997).

BIOGRAPHICAL SKETCH

Michael Steiner Kesler was born in Gainesville, Florida and is the second child of Alex Kesler and Sherry Steiner. Michael attended a small private school throughout his childhood. He went on to P.K. Yonge Developmental Research School where he excelled in the classroom as well as in several sports, including Baseball, Tennis, Basketball and Soccer.

Michael is passionate about travelling and following high school he attended Santa Fe Community College part-time while working and saving money for various international adventures. At the age of 22 he received his associate degree and transferred to the University of Florida. Based on his interest in both chemistry and mechanical engineering, Michael chose the natural path of materials science and metallurgy as a focus of his studies. He made the Dean's list on several occasions and completed his senior research on slip band formation in single crystal superalloys. Michael was recruited by his senior research advisor to work on a collaborative project in his field of interest. He made the decision to join the group as a graduate assistant and was awarded an alumni fellowship. Throughout his PhD work, Michael was a laboratory technician at the MAIC facility and was responsible for training graduate students in analytical techniques such as electron microscopy and X-ray diffraction. Michael went on to defend his dissertation in the fall of 2011 and earned a Ph.D. from the University of Florida.